UNIVERSITY OF SHEFFIELD

DEPARTMENT OF MATERIALS SCIENCE AND ENGINEERING

PHASE EQUILIBRIA STUDIES IN Nb-RICH SYSTEMS

IOANNIS PAPADIMITRIOU

Supervisors: Prof. Panos Tsakiropoulos and Dr Claire Utton

Στον πατέρα μου

ὣς οὐδὲν γλύκιον ἦς πατρίδος οὐδὲ τοκήων
γίγνεται, εἴ περ καί τις ἀπόπροθι πίονα οἶκον
γαίῃ ἐν ἀλλοδαπῇ ναίει ἀπάνευθε τοκήων.

Contents

Abstract

In this thesis the Nb-Ti-Si-Al-Sn-Cr system was investigated. Literature on relevant phase equilibria and the ab initio theory is reviewed. Details about the experimental and theoretical techniques used in the current study are outlined. Data for thermodynamic and elastic properties, phase equilibria and phase stabilities are given. The Nb-Si, Nb-Sn, Nb-Al binary systems along the A15 $Nb_3(X,Y)$ (X,Y=Si, Sn, Al, Ge) compounds and tetragonal TM_5Sn_2Y (TM=Nb, Ti, Y=Si, Al) phases were studied with ab initio calculations. The Nb-Si-Sn, Nb-Al-Sn, Nb-Ti-Sn, Nb-Ti-Si-Sn and Nb-Cr-Sn ternary systems were studied experimentally. Alloys with codes from IP1 to IP12 and actual compositions (at. %) Nb-24Ti-18Si-5Sn (IP1), Nb-16Si-13Sn (IP2), Nb-18Si-17Sn (IP3), Nb-17Al-17Sn (IP4), Nb-33Al-13Sn (IP5), Nb-16Al-20Sn (IP6), Nb-10Ti-18Sn (IP7), Nb-13Ti-3Sn (IP8), Nb-40Ti-23Sn (IP9), Nb-39Ti-40Sn (IP10), Nb-15Cr-11Sn (IP11) and Nb-65Cr-18Sn (IP12) were studied in the as cast and heat treated conditions (at 900 °C, 1000 °C, 1100 °C, 1200 °C or 1400 °C).

The stable intermetallics in the Nb-Si binary system were investigated and their elastic and thermodynamic properties (enthalpy of formation versus temperature, Debye temperature) were obtained. The most ductile phases are βNb_5Si_3 and Nb_3Si with the latter being the most ductile while the less ductile are αNb_5Si_3 and $NbSi_2$ (with the latter being the most brittle). Also the transition temperatures of $Nb_3Si \rightarrow Nb+\alpha Nb_5Si_3$ and $\beta Nb_5Si_3 \rightarrow \alpha Nb_5Si_3$ and the stability of the $NbSi_2$ at low and elevated temperatures were investigated and found to be in good agreement with the phase diagram.

The enthalpy of formation versus temperature, Debye temperatures and elastic properties of the intermetallics in the Nb-Sn system were calculated. The Nb_3Sn was found to be the less brittle compound, while the temperature dependence of its moduli and Poisson's ratio, along with the corresponding properties of Nb were calculated and found to be in good agreement with the literature.

The elastic properties, enthalpies of formation and Debye temperatures of intermetallics in the Nb-Al binary system were calculated. The temperature dependence of their enthalpy of formation, along with the temperature dependence of the elastic properties of the Nb_3Al were calculated and reported for the first time. The Nb_3Al has the highest bulk modulus value, while the $NbAl_3$ is the stiffest and most brittle phase.

A comparative study of the A15 intermetallics containing Nb and Sn, Si, Al, Ge was carried out. Their linear thermal expansion coefficients were obtained and found to be in good agreement with the available literature. The temperature dependence of their enthalpy of formation along with their Debye temperatures were also calculated. The Nb_3Si phase has the highest bulk, shear and Young's modulus values and is the stiffest and less ductile of the four binary A15 intermetallics of the present study. The Sn and Al additions in the Nb_3Si stabilise the A15 structure over the competing *tP*32, while the Ge addition has the opposite effect.

An investigation of the ternary W_5Si_3 type $TMSn_2X$ compounds (TM=Nb, Ti and X=Al,Si) was done. Useful data for the temperature dependence of the enthalpies of formation of the $TMSn_2X$ phases (TM=Nb, Ti and X=Al,Si) that would allow the construction and optimisation of the Nb-Si-Sn, Nb-Al-Sn, Ti-Si-Sn, Ti-Al-Sn phase diagrams, were obtained. Aluminium and Nb improve ductility, while Ti and Si enhance brittleness. When the transition metal is Nb the moduli of the ternary phase are considerably higher compared with the case of Ti.

Phase equilibria in the Nb-Si-Sn system at 900 °C and 1200 °C and the solidification paths of the alloys Nb-16Si-13Sn (IP2) and Nb-18Si-17Sn (IP3) were studied. The Nb_5Sn_2Si is a thermodynamically stable phase forming between 900 °C and 1200 °C. In Nb_3Sn the Si/Sn ratio reached up to ~1.

Phase equilibria at 900 °C and 1200 °C, along with the solidification paths of the Nb-Al-Sn alloys were studied using the alloys Nb-17Al-17Sn (IP4), Nb-33Al-13Sn (IP5) and Nb-16Al-20Sn (IP6). Tin showed high solubility in Nb_2Al, reaching up to 21 at. % in the Sn-rich areas, substituting Al atoms. Tin and Al substituted each other in the A15 phase (Nb_3Al and Nb_3Sn), while Sn showed limited solubility in $NbAl_3$, not exceeding ~3.6 at. %. as it substituted Al atoms. The solubility of Al in $NbSn_2$ varied from ~4.8 to ~6.8 at. %. The Nb_5Sn_2Al is a stable ternary intermetallic stable in the range between ~900 °C and ~1200 °C and it can be treated as a line compound.

In the Nb-Ti-Sn system phase equilibria at 900 °C and 1200 °C and the solidification paths of the alloys Nb-10Ti-18Sn (IP7), Nb-13Ti-3Sn (IP8), Nb-40Ti-23Sn (IP9) and Nb-39Ti-40Sn (IP10) were studied. In Nb_3Sn, the Ti substituted Nb, whereas in Ti_3Sn Nb substituted Ti. In Ti_6Sn_5 Nb substituted both Ti and Sn, with primary preference to the former.

Phase equilibria in Nb-Ti-Si-Sn system at 1000, 1100 and 1300 °C were studied using the alloy Nb-24Ti-18Si-5Sn (IP1). Above a certain content of Ti (possibly 25-30 at. %) the γNb_5Si_3 phase becomes stable. Titanium showed higher solubility in the γNb_5Si_3 intermetallic of all the Nb_5Si_3 silicides and reduced the solubility of Si in the Nb_3Sn.

In the Nb-Cr-Sn system the corresponding phase equilibria at 900 °C and 1200 °C were studied. The solidification paths of the alloys Nb-15Cr-11Sn (IP11) and Nb-65Cr-18Sn (IP12) were deduced. Chromium substitutes Nb in the Nb_3Sn and Nb_6Sn_5 phases. Tin on the other hand substitutes Cr and Nb in the Laves phase. Finally, Nb and Sn showed very small solubility in Cr_{ss}.

The results from the present study can prove very beneficial to the Nb silicide based alloys synthesis, as a very concise “map” of the as yet uncharted Nb-Ti-Si-Sn-Al-Cr territory, containing elastic properties, phase stabilities and phase equilibria data is produced, helping towards significant minimization of cost of the future alloy design.

1

Introduction

Since the 1950's high-temperature materials have been intrinsically linked to the development of gas turbines used in transport and energy industries. This has been due to their excellent resistance to chemical and temperature degradation at temperatures close to their melting points. They are employed in the very hottest sections of the turbines (Fig. 1.1) under heavy loads and are expected to retain their structural integrity.

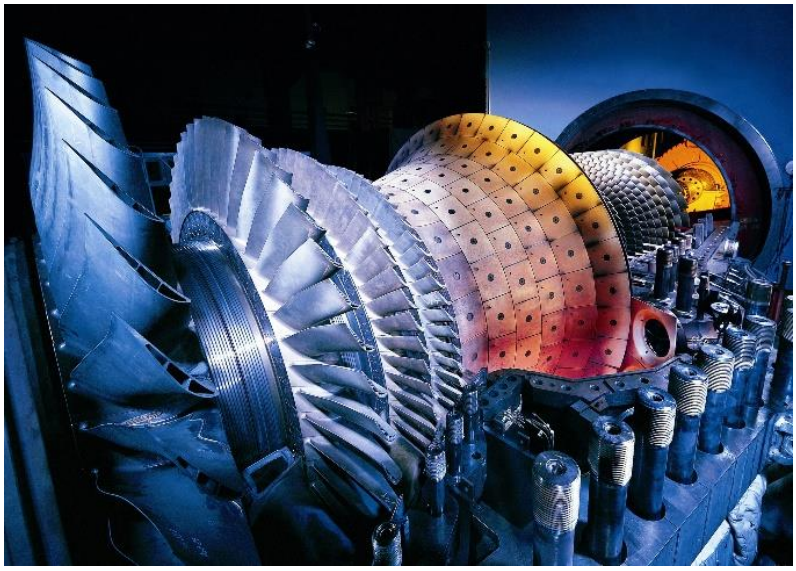

Fig.1.1. Modern day gas turbine (Image taken from power-technology.com)

The first desirable characteristic of a high-temperature alloy is the ability to withstand loading at an operating temperature near to its solidus point. A second characteristic is a substantial resistance to mechanical degradation over long periods of time. As time increases creep strain is accumulated and it is desirable for this accumulation to be as low as possible. Furthermore, yield stress, ultimate tensile strength and fracture toughness should be maintained over time. Operating at high temperatures may enhance the possibility of corrosion and oxidation leading to reduction of the life of the component. Hence the final desirable characteristic is resistance to any kind of surface degradation.

As the economies and populations of the developing countries keep growing at a fast pace, the need for further improvements in high temperature capabilities of structural alloys of aircraft gas turbines is increasing. The most advanced Ni-based superalloys used in state of the art gas turbine engines have reached the limit of their temperature capabilities as they are currently operating with surface temperatures around 1150 °C in their hottest areas and their melting occurs around 1350 °C [1]. Thus, there is need for new alloys in order for the gas turbine technology to advance. Higher temperature

capabilities would mean significant improvement of efficiency, which in turn would mean reduction of fuel consumption and carbon emissions.

Alloys based on refractory metal intermetallic compounds can achieve a balance of mechanical and environmental properties with low density and thus are considered as candidate materials for high temperature applications. Niobium silicide based alloys have attracted much interest as the next generation ultra-high temperature alloys owing to their excellent creep, high temperature strength and ambient temperature fracture toughness [1, 2]. The microstructure consists of ductile Nb solid solution phase in which are embedded high strength silicide(s) and other intermetallic phase(s) or vice versa, depending on alloy composition [1-3]. The choice of the latter intermetallics is influenced by considerations about achieving a balance of high and ambient temperature properties [1, 2, 4].

Additions of Al, Ti, Cr and Sn in the Nb-silicides are reported to benefit their oxidation behaviour, room-temperature toughness, and oxidation resistance and are important for their high-temperature creep performance [1, 3, 5-11]. The design of Nb silicide based alloys requires better understanding of the effects of each alloying element as well as their synergy in the microstructure of the Nb silicide alloys. Thus, it is important that data for thermodynamic and mechanical properties of alloys and specific phases is obtained. Limited data exist for the Nb-Si-Sn, Nb-Sn-Al, Nb-Ti-Sn and Nb-Cr-Sn ternary systems, as well as elastic and thermodynamic properties of several important intermetallics containing Nb. This is mostly due to the difficulty to produce alloys of the aforementioned systems because of the large differences between the elements' melting temperatures.

In this study the aim is to explore the Nb-Ti-Si-Sn-Al-Cr system in order to obtain data that will be used in the future to support the design of Nb silicide based alloys. The objectives of the current study are:

(a) To investigate phase equilibria and phase stabilities in Nb-Ti-Si-Al-Cr-Sn subsystems, which have not been reported in the past;

(b) To investigate the mechanical and thermodynamic properties of intermetallics in this system.

The strategy adopted to achieve these objectives included the use of XRD, SEM/EDS and EBSD to characterise the alloys produced in the present study, and ab initio

calculations to predict the thermodynamic and mechanical properties of the elemental and intermetallic phases involved in this study.

The thesis starts with a review of literature on the existing data for the binary and ternary Nb containing systems in chapter 2. This chapter focuses on phase equilibria in the Nb-Ti-Si-Sn-Al-Cr system and the theory of the ab initio method. The experimental and theoretical methods are described in chapter 3. The results of the theoretical research are presented in chapters 4 to 8, while the experimental research results are shown in chapters 9 to 13. The conclusions of this work and suggestions of future work are presented in chapter 14. In chapter 15 the Appendices containing formulae used in the present work, schematics of crystal structures of phases assessed in the current work, details of the characterisation of the alloys and the papers published from this work are given.

2

Literature Review

2.1 Niobium

The high melting metals are divided in the group of noble metals, namely Ru, Rh, Os, Ir and Pt, and the group of refractory metals (RM), namely Zr, Hf, Nb, Ta, Cr, Mo, W, Tc and Re. Besides the high melting point other properties like high temperature strength, creep and corrosion resistance, Young's modulus and vapour pressure are critical for their high temperature applications.

Refractory metals, namely Nb, Ta, Mo and W are considered to be suitable candidates for high temperature applications. Niobium has very attractive physical properties as high melting point, the lowest density of the RM, the lowest Young's modulus (which means better ductility compared with another RM) high corrosion resistance, good workability at room temperature, a low Ductile/Brittle Transition Temperature (DBTT) (ductility at lower temperatures) and high vapour pressure (suitable for high temperature applications) [1, 2]. Some of the properties of RM are shown in Table 2.1.

Table 2.1

Physical and mechanical properties of Nb, Ta, Mo and W [12].

	Niobium	Tantalum	Molybdenum	Tungsten
Melting Point (^{0}C)	2470	2996	2610	3410
Density (g/cm^3)	8.57	16.6	10.2	19.3
Young's Modulus (GPa)	110	186	290	358
Workability at Room Temperature	Good	Good	Middle [a]	Bad [a]
Corrosion Resistance	High	Very high	Low	Low
Ductile/Brittle Transition Temperature (^{0}C)	-150	-260	-20	300

[a] Depending on degree-of-deformation and dimension.

2.2 Niobium silicides

Niobium-silicide based alloys are suitable candidates for next generation gas turbine components. They have high melting points (> 1700 ^{0}C), low densities (6.6 - 7.2 g/cm^3) [8] and contain mainly high strength intermetallic phases toughened by Nb solid solution (Nb_{ss}) [13]. The Nb-Si system allows for a range of possible combinations of phases to exist [9], as is shown in the phase diagram (Fig. 2.1 (a)).

One of the attractive features of the Nb-Si system is the wide Nb_{ss} and αNb_5Si_3 two phase field. Different versions of the Nb-Si binary phase diagram have been proposed that essentially have different transformation temperatures and eutectic compositions. For example in the phase diagram shown in Fig. 2.1 (a) there is a eutectic reaction at 1916 °C (2189 K) (Liquid ↔ Nb_{ss} + Nb_3Si) and a eutectoid at 1673 °C (1946 K) (Nb_3Si ↔ Nb_{ss} + αNb_5Si_3). Thus there is a variety of ways to reach the region of Nb_{ss} and αNb_5Si_3 and have different volume fractions of Nb_{ss}, Nb_3Si, αNb_5Si_3 and βNb_5Si_3. Four intermetallic compounds are reported in the equilibrium Nb-Si phase diagram [14], namely the Nb_3Si (*tP*32-Ti_3P), which is stable above 1765 °C (2038 K), the αNb_5Si_3 (*tI*32, Cr_5B_3, $D8_1$), which transforms to βNb_5Si_3 (*tI*32, W_5Si_3, $D8_m$), with upper and lower transformation temperatures of 1934 °C (2208 K) and 1645 °C (1918 K) (this temperature is lower than that in Fig. 2.1 (a)) and the $NbSi_2$ (*hP*9, $CrSi_2$, C40) which is stable below 1934 °C (2208 K), where the structures were denoted using Pearson Symbols, crystal structure prototypes and Structurbericht Symbols (See appendix). As already mentioned different values for the aforementioned temperatures have been reported in the literature. The lowest temperature above which the Nb_3Si has been reported to be stable is 1670 °C (1943 K) [15], the lowest and highest values of the upper and lower transformation temperature of αNb_5Si_3 to βNb_5Si_3 have been 1642 °C (1915 K) [16] and 1947 °C (2220 K), respectively [16] and the highest value for $NbSi_2$ has been 1963 °C (2236 K) [17]. The stability of the Nb_3Si can be extended to lower temperatures [18] or its formation can be suppressed by alloying [19]. Alloying is also crucial for the transformation of βNb_5Si_3 to αNb_5Si_3 [20]. The stability range of $NbSi_2$ is important for the temperature capability of oxidation resistant silicide based bond coat alloys for Nb silicide based alloys [21, 22]. Thus, it is important to know the thermal and physical properties of the Nb_3Si, βNb_5Si_3, αNb_5Si_3 and $NbSi_2$ intermetallic phases in order to

improve the Nb-silicide based alloys and silicide based coatings. A first principles study of the Nb-Si system, excluding the $NbSi_2$ phase, has been reported in [23].

Niobium-silicide based alloys, also known as Nb-silicide in-situ composites which consist of a bcc Nb_{ss} with Nb_5Si_3 and/or Nb_3Si exhibit excellent creep strength, but often have poor fracture toughness and oxidation resistance. [2, 24]. The effect of various alloying additions including Ti, Cr, Al, Hf, Sn, Ta, Mo and Ge as well as the synergy of them has been studied in order to achieve balance between room-temperature toughness, high-temperature creep performance, and oxidation resistance.

2.2.1 Titanium addition

Titanium reduces the density of Nb silicide alloys and improves their oxidation resistance and fracture toughness [9-11, 24-26]. For better understanding of the effect of titanium on the microstructure of Nb silicide based alloys the ternary Nb-Ti-Si system has been assessed [27] (Fig. 2.2). The tetragonal Nb_3Si phase (*tP*32 structure) is present and stable above 1673 ^{0}C (1946 K) in the Nb-Si system [13], (Fig. 2.1 (a)) while in the Ti-Si system a tetragonal Ti_3Si phase with the same structure is stable below 1170 ^{0}C (1443 K) [28] (Fig. 2.1 (b)). The above silicides are isomorphous and it has been reported [19, 29], that the addition of Ti in Nb-Si-Ti ternary alloys leads to the stabilisation of the $(Nb,Ti)_3Si$ phase at lower temperatures. This stabilisation can be enhanced by the synergy of Ti with Fe [30]. This isomorphism however does not apply to the Nb_5Si_3 and Ti_5Si_3 silicides, hence there is a limited solubility of Nb in Ti_5Si_3 (~20 at. %) and Ti in Nb_5Si_3 (~ 30 at. %) [31]. According to Bewlay et al. [24] the addition of Ti leads to lowering of the eutectic temperature from 1880 ^{0}C (2153 K) to 1330 ^{0}C (1603 K). In order to maintain a eutectic temperature above 1700 ^{0}C (1973 K) in Nb-Si-Ti silicide based alloys the Ti content should be less than 25 at. % [24].

According to Geng et al. [5, 32] the Ti addition enhances the eutectoid decomposition of Nb_3Si to Nb_{ss} and αNb_5Si_3 and decreases the lattice parameter of bcc Nb_{ss} especially with increase of the Mo content. Grammenos and Tsakiropoulos [18] showed that the synergy of Ti with Hf can stabilise the Nb_5Si_3 while replacing the eutectoid transformation $Nb_3Si \leftrightarrow Nb_{ss} + \alpha Nb_5Si_3$ by an alternate eutectoid transformation in which the 5-3 silicide has the hexagonal (hP16) structure, instead of the tetragonal one

(*tI*32). It has also been reported that the addition of Ti resulted to macrosegregation (variation in compositions that occur in the alloy and range in scale
from several millimeters to centimeters or even meters) (of Si in the Nb-24Ti-18Si-5Sn (at. %) [19] , as well as in the Nb-18Si-5Cr-5Ge (at. %) and Nb-24Ti-18Si-5Cr-5Ge (at. %) alloys, especially in synergy with Cr [32].

In the Nb–24Ti–18Si-5Cr (at. %) alloy [29] microsegregation (variation in compositions that occur in the alloy and range in scale comparable to the size of the dendrite arm spacing) of Ti was particularly evident, increasing the solubility of Cr in the solid solution. In the Nb-24Ti-18Si-5Al (at. %) alloy [29] the solubility of Al in the solid solution increased with Ti content and the solubility of Al in αNb_5Si_3 decreased [29].

Apart from its influence on the microstructure of the Nb silicide alloys, Ti also has an impact on the mechanical properties of their constituent phases. A significant improvement of the fracture toughness and ductility of the Nb_{ss} and the Nb_5Si_3 has been noted in the presence of Ti [33, 34] as well as improvement of oxidation resistance [8, 24]. However, when the Ti content is increased beyond 30 at. % the Nb_5Si_3 transforms into Ti_5Si_3 [31]. The latter is not desirable due to its low creep strength. Titanium can have a strong effect on Nb_{ss} and Nb_5Si_3 causing solid solution strengthening of the former and decrease in the hardness of the latter [32].

2.2.2 Tin addition

Niobium silicide based alloys exhibit desirable creep properties at higher temperatures than Ni based superalloys but their oxidation resistance must be improved. Wainer [35], in 1957 discovered that two groups of elements can benefit the oxidation resistance of Nb-based alloys. The first group consists of Be, Ti, Al, Zr, Cr, Si and V. These elements have atomic volumes or radii smaller than that of Nb and thus their ions or atoms will diffuse as fast as the base metal and are classified as retarders of oxidation (suppressing the rate of oxidation). The second group includes Ca, Ce, Er, La, Nd, Pr, Pb, Th and Sn which are characterised as diffusion barriers (can form thin layer on the surface of the alloy) as their atomic volumes are smaller than that of the first oxide that develops on the surface of the Nb alloy when it is oxidized. Tin is one of the elements that has been shown to benefit the oxidation resistance of Nb silicide based alloys [24, 36] when present at low concentrations and in synergy with specific alloying additions.

Tin suppresses the formation of Nb_3Si [19], in synergy with Ti and with Ti, Fe and Cr encourages respectively the transformation of βNb_5Si_3 to αNb_5Si_3 [19] and the formation of the metastable Nb_3Si [37] and oxidation improvement seems to be linked with the formation of Nb_6Sn_5 below the scale [36, 38]. In order to understand alloy behaviour in ternary and higher order systems, knowledge of thermal and physical properties of the intermetallic compounds that are key to the development of the new alloys is critical.

No intermetallics exist in the Si-Sn binary system [39] (Fig. 2.3 (a)). In the Nb-Sn system there are three stable intermetallics [28] (Fig. 2.3 (b)). The Nb_3Sn has the A15 structure which is a close-packed structure whose stability is largely governed by size [40], has a primitive cell of 8 atoms and belongs to the space group P*m*3*n*, its Pearson symbol is *cP*8 and is of the Cr_3Si type and its melting temperature is 2374 °C (2647 K). The Nb_6Sn_5 has a D2H-25 orthorhombic structure with a primitive cell of 22 atoms and belongs to the I*mmm* space group with *oI*45 Pearson symbol and is of the Ti_6Sn_5 type and its melting temperature is 907 °C (1180 K). The $NbSn_2$ has the D2H-24 orthorhombic structure, Pearson symbol *oI*48, space group F*ddd* and is of the $CuMg_2$ type with its primitive cell containing 12 atoms and its melting temperature is 827 °C (1100 K). The Nb_3Sn has attracted interest due to its superconducting properties [41], with a transition temperature of -254.25 °C (18.9 K) and its high melting temperature. The transition temperatures of the other two intermetallics are -270.47 °C (2.68 K) and -271.08 °C (2.07 K) for $NbSn_2$ and Nb_6Sn_5, respectively [42]. The crystal structures can be seen in the Appendix.

The resistivity [43], heat capacity [44], electron-phonon interaction [45] and magnetic susceptibility [46] of the Nb_3Sn compound have been studied but there is limited data [44, 47] about its thermodynamic properties. The elastic properties of the Nb_3Sn have also been calculated [48], but to the best of the author's knowledge no data exists for the other two intermetallics in the Nb-Sn system. There is experimental and theoretical data for the vibrational and elastic properties of Nb [49] and Sn [50] and their Debye temperatures [51, 52].

According to Geng et al. [5, 38] the addition of Sn in the Nb-24Ti-18Si-5Al-5Cr-5Hf-5Sn-2Mo (at. %) caused the formation of Sn-rich and Sn-poor areas in the $(Nb,Ti)_{ss}$, while it significantly increased the solubility of Si in the solid solution. Subsequent research in the group confirmed the former as Nb_3Sn. On the other hand the Ti solubility in Nb_5Si_3 increased slightly in the presence of Sn, compared with the

Nb-24Ti-18Si-5Al-5Cr-2Mo-5Hf (at. %) alloy. Significant improvements were noticed [36] in the oxidation of the Nb-24Ti-18Si-5Al-5Cr-2Mo-5Hf-5Sn alloy (at. %) at 800 ^{0}C and 1200 ^{0}C by the addition of Sn. Geng et al. [36] reported that pest damage after 100 hours at 800 ^{0}C of this alloy was successfully eliminated by alloying with 5at. % Sn.

Vellios and Tsakiropoulos [37] reported that in the presence of Sn macrosegregation of Si occurred in the Nb-24Ti-18Si-5Cr-5Fe-5Sn (at. %) alloy, whereas in the Nb-24Ti-18Si-5Cr-5Fe (at. %) alloy macrosegregation of Si was not evident. Also the addition of Sn increased the solubity of Ti in the solid solution, while it had no influence on the solubility of Cr in the $(Nb,Ti)_5Si_3$. In the presence of Sn the hardness was reported to be decreased as the hardness of the Nb-24Ti-18Si-5Cr-5Fe-5Sn (at. %) alloy was approximately 15 at. % lower compared with that of the Nb-24Ti-18Si-5Cr-5Fe (at. %) alloy.

2.2.3 Aluminium addition

Another important alloying element in Nb silicide based alloys that can improve their oxidation resistance [53], lower their density and possibly be beneficial for their room temperature ductility is Al which tends to substitute Si. As the oxidation temperature increases, Al plays an increasingly important role. Zelenitsas and Tsakiropoulos [29] suggested that Al destabilises the Ti_3Si and may have the same effect on the Nb_3Si and that Al additions in Nb-Ti-Si based alloys stabilise the βNb_5Si_3 to lower temperatures and lower the Si content of the eutectic composition.

2.2.4 Chromium addition

Chromium is another important alloying addition that can form the $NbCr_2$ Laves phase that can aid the oxidation resistance of Nb silicide based alloys. The $NbCr_2$ is very brittle. Thus in order to control the fracture toughness of the alloys, the Laves phase volume fraction must be kept in low levels. Zelenitsas and Tsakiropoulos [29] reported that in the Nb–24Ti–18Si–5Cr–5Al (at. %) alloy the Cr addition retarded the diffusion of Al from the 5-3 silicide and decelerated the transformation of the βNb_5Si_3 to αNb_5Si_3 and Nb_{ss}. The synergy of Al and Cr additions has been reported [54] to

improve the oxidation resistance without the solid solution becoming severely brittle, when the concentration was within 2-6 at. % for Al and 2-8 at. % for Cr. The synergy of Cr and Ta retarded the transformation $\beta Nb_5Si_3 \rightarrow \alpha Nb_5Si_3 + (Nb,Ti)_{ss}$ [55].

2.3 Niobium aluminides

The Nb-Al binary phase diagram consists of three intermetallics. The Nb_3Al has a primitive cell of 8 atoms, A15 cubic structure and belongs to the space group P*m*3*n* with Pearson symbol is *cP*8 and is of the Cr_3Si type. The $NbAl_3$ has a primitive cell of 4 atoms, $D0_{22}$ tetragonal structure and belongs to the space group *I*4/*mmn*, while its Pearson symbol is *tI*8 and is of the Al_3Ti type. The Nb_2Al has a primitive cell of 30 atoms, $D8_b$ tetragonal structure and belongs to $P4_2/mnm$, whereas its Pearson symbol and structure type are *tP*30 and σCrFe, respectively. Images of the crystal structures are given in the Appendix

These Nb aluminide based alloys have been investigated as potential candidate materials for high performance turbine applications. The Nb_2Al intermetallic has desirable strength above 1000 ^{0}C but poor ductility and oxidation resistance. It shows a high melting temperature (1940 °C (2213 K)) and low density, thus making it interesting structural material for high temperature applications [56, 57]. The $NbAl_3$ compound is regarded as a promising material for use at high temperatures due to its high melting temperature (1605 °C (1878 K)), low density and exceptional oxidation resistance, with its only disadvantage being its room temperature brittleness. The most promising of the niobium aluminides appears to be the Nb_3Al because of its high melting temperature (2127 °C (2400 K)) [58] and creep properties. However it shows poor oxidation resistance. Alloying with elements like Ti, Cr, Sn or Si can improve oxidation resistance for Nb_3Al alloys. Due to its low symmetry as a result of the A15 crystal structure though, it shows limited ductility and poor fracture toughness at ambient temperatures [59]. It has also been reported [58, 60, 61] that additions of Mo, W and Ta increase its high temperature strength.

To date and to the best of the author's knowledge work has been carried out on the enthalpies of formation of all the Nb-Al intermetallic phases [62, 63] and the mechanical properties of the Nb_3Al [48, 64] and the $NbAl_3$ [65-67]. Furthermore, work on the heat capacity and Debye temperature of $NbAl_3$ can be found in [65].

2.5 Ternary systems

2.5.1 The Nb-Si-Ti system

One of the most important binary systems including Nb is Nb-Si. Its latest assessment was by David et al. [13] and was based on Liang and Chang [68] and Fernandes et al. [17]. Liang and Chang [68] modelled the αNb_5Si_3 and βNb_5Si_3 as the same stoichiometric phase. Fernandes et al. [17] presented separate descriptions for those phases, considering the solubility of Si in the βNb_5Si_3. David et al. [13] modelled the αNb_5Si_3 and $NbSi_2$ as non-stoichiometric compounds with a very small (<1 at. %) solubility. The phase diagram of Nb-Si is shown in Fig. 2.1 (a). Three eutectic and one eutectoid transformations are clear in the phase diagram. The first eutectic, Liquid ↔ Nb_{ss} + Nb_3Si occurs at 1916 ^{0}C (2189 K), the eutectoid Nb_3Si ↔ Nb_{ss} + αNb_5Si_3 at 1673 ^{0}C (1946 K), the second eutectic Liquid ↔ βNb_5Si_3 + $NbSi_2$ at 1873 ^{0}C (2146 K) and the third eutectic Liquid ↔ $NbSi_2$ + Si at 1407 ^{0}C (1680 K). Thus, four stable intermetallic compounds exist in the binary Nb-Si phase diagram [13] (Fig. 2.1 (a), see section 2.2).

The Ti-Si binary phase diagram has been calculated by Seifert et al. [69] (Fig. 2.1 (b)). The Ti_5Si_3, which is isomorphous to the Nb_5Si_3, is present around 37.5 at. % Si. Its melting point is significantly lower, and has wider solubility range in Si than Nb_5Si_3. Four other intermetallic compounds are shown in Fig. 2.1 (b), all of them modelled as stoichiometric. They are Ti_3Si, Ti_5Si_4, TiSi and $TiSi_2$. The peritectoid reaction at 1170 ^{0}C (1443 K) between βTi and Ti_5Si_3 produces the Ti_3Si. At 1920 ^{0}C (2193 K) and 1572 ^{0}C (1845 K) two peritectic transformations, Liquid + βTi_5Si_3 ↔ Ti_5Si_4 and Liquid + Ti_5Si_4 ↔ TiSi, take place respectively, while at 1485 ^{0}C the congruent transformation Liquid ↔ $TiSi_2$ occurs.

The phase diagram of the Nb-Ti system modelled by Zhang et al. [70] is shown in Figure 2.1 (c). It is much simpler than the Nb-Si and Ti-Si binaries, as it does not show any compounds formed between Nb and Ti. The αTi (HCP) is stable to 860 ^{0}C (1133 K) and has a small solubility range of Nb (<3 at. %) beyond which βTi (BCC) co-exists with the Nb (BCC) and form the BCC (Nb,Ti) solid solution.

Based on the assessments of the binary Nb-Si, Ti-Si and Nb-Si systems the optimisation of the Nb-Ti-Si system was conducted by Geng et al. [27]. In the aforementioned study no differentiation between the αNb_5Si_3 and βNb_5Si_3 was made. A good agreement between the experimental results of Geng et al. and of previous research, and the calculated data was accomplished. The isothermal section at 1200 ^{0}C (1473 K) from [27] is shown in Fig. 2.2.

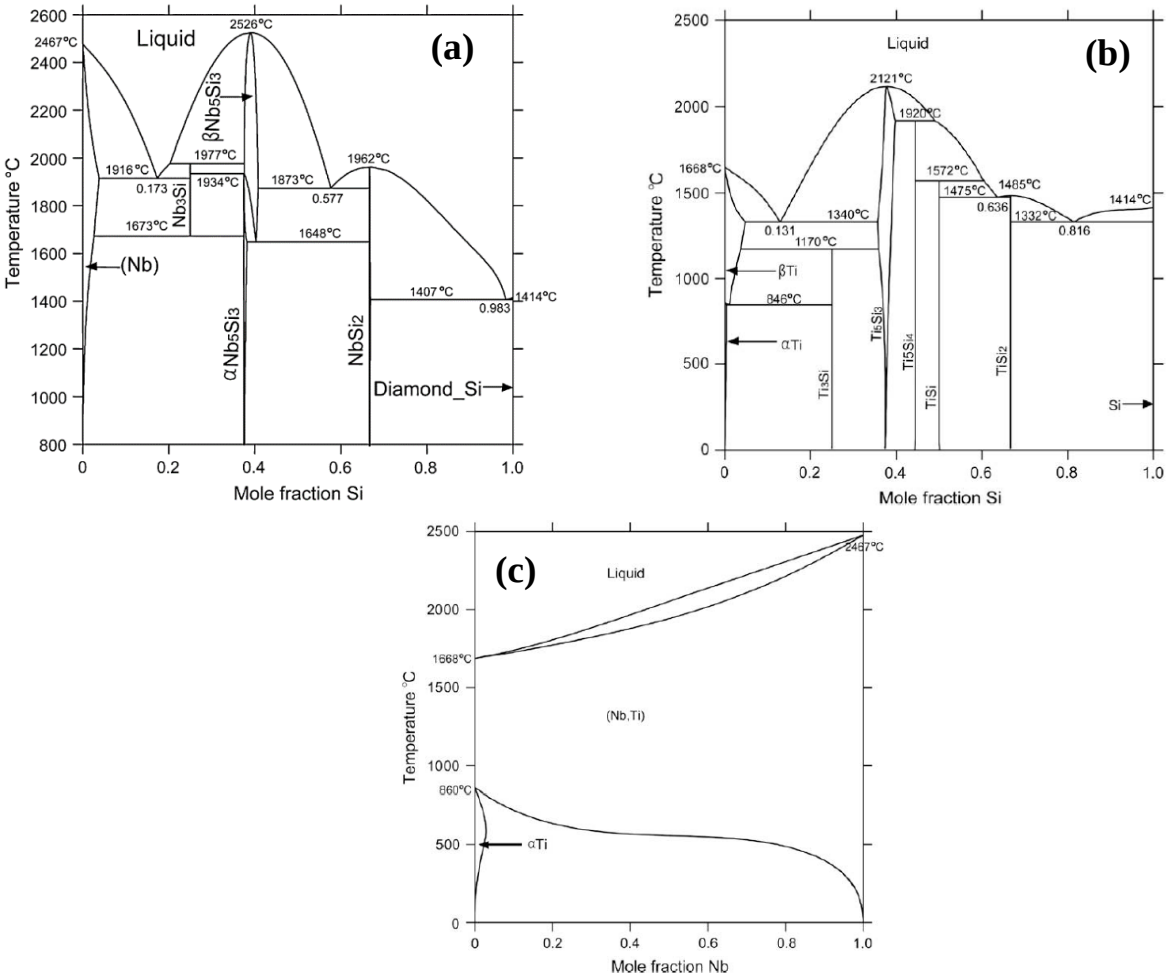

Fig. 2.1. Calculated phase diagrams of (a) Nb-Si [13], (b) Ti-Si [69], (c) Nb-Ti [70]

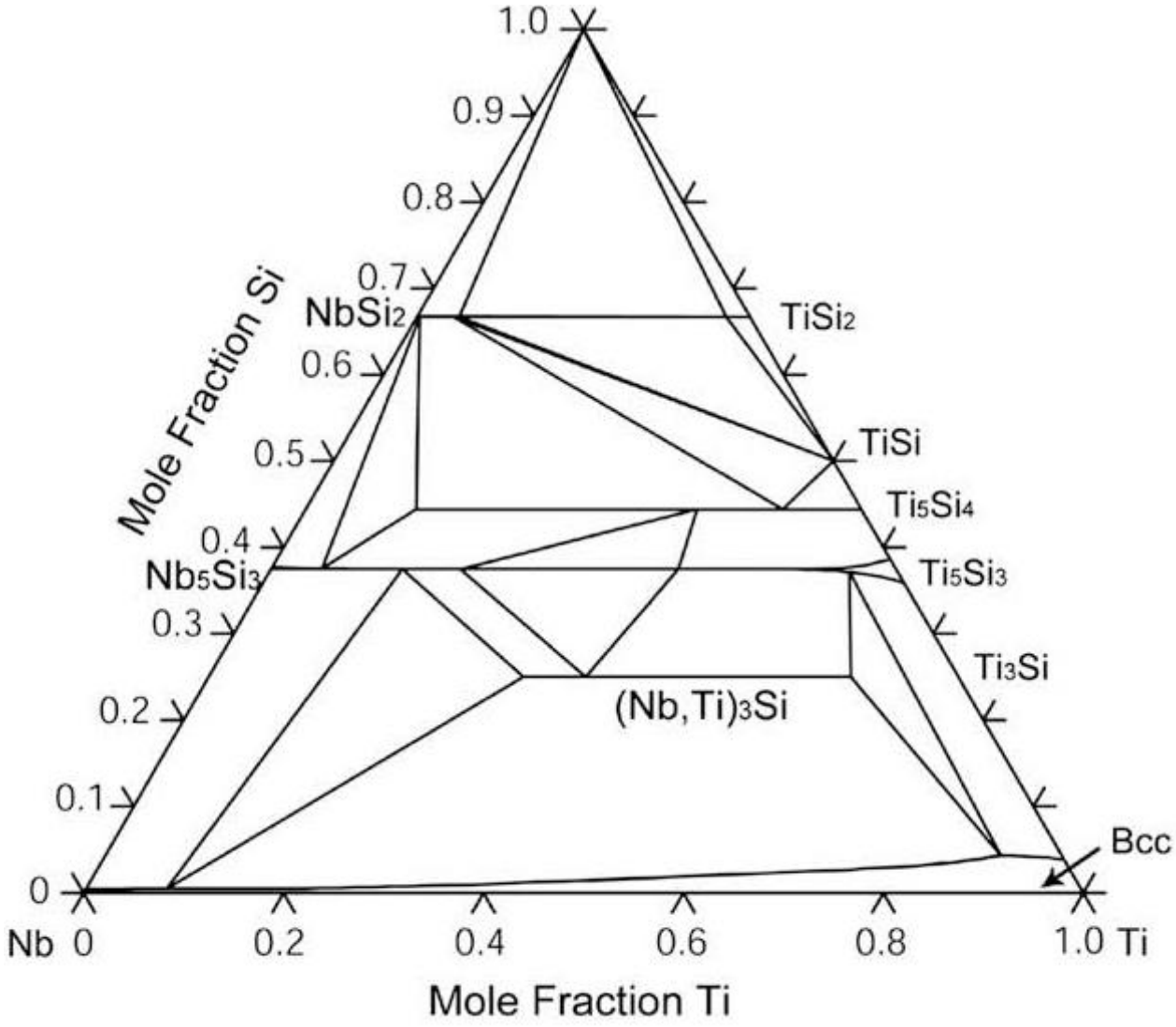

Fig. 2.2. Isothermal section at 1200 °C of the Nb–Si–Ti system [27]

2.5.2 The Nb-Si-Sn system

The Nb-Si system was discussed in section 2.2. The Si-Sn system was recently remodelled by Sun et al. [71] based on the work done by Meng et al. [39] (Fig. 2.3 (a)). The assessment of the Nb-Sn system was done by Toffolon et al. [28] who took into account enthalpy of formation data for the Nb_3Sn. The obtained phase diagram was in good agreement with the experimental data as shown in Figure 2.3 (b). Three intermetallic compounds are observed as the Sn content increases. The first is Nb_3Sn with a significant solubility in Sn, Nb_6Sn_5 and $NbSn_2$, which are both treated as line compounds.

Sun et al. produced a thermodynamic description of the Nb-Si-Sn system based on previous work by Waterstrat and Muller [72], Vellios and Tsakiropoulos [19] and Horyn and Lukaszewicz [73]. The Nb_5SiSn_2 is a ternary compound which was treated as stoichiometric and was calculated to be stable between 900 ^{0}C (1173 K) and 1200 ^{0}C (1473 K), consistent with the findings of Horyn and Lukaszewicz [73]. The crystal structure of the ternary compound is tetragonal W_5Si_3 structure type and of the I4/*mcm* space group. No comprehensive experimental evidence about the temperature range of the stability of this compound exist. Figure 2.4 shows the 900 ^{0}C (1173 K) Nb-rich isothermal section of the Nb-Si-Sn system [71].

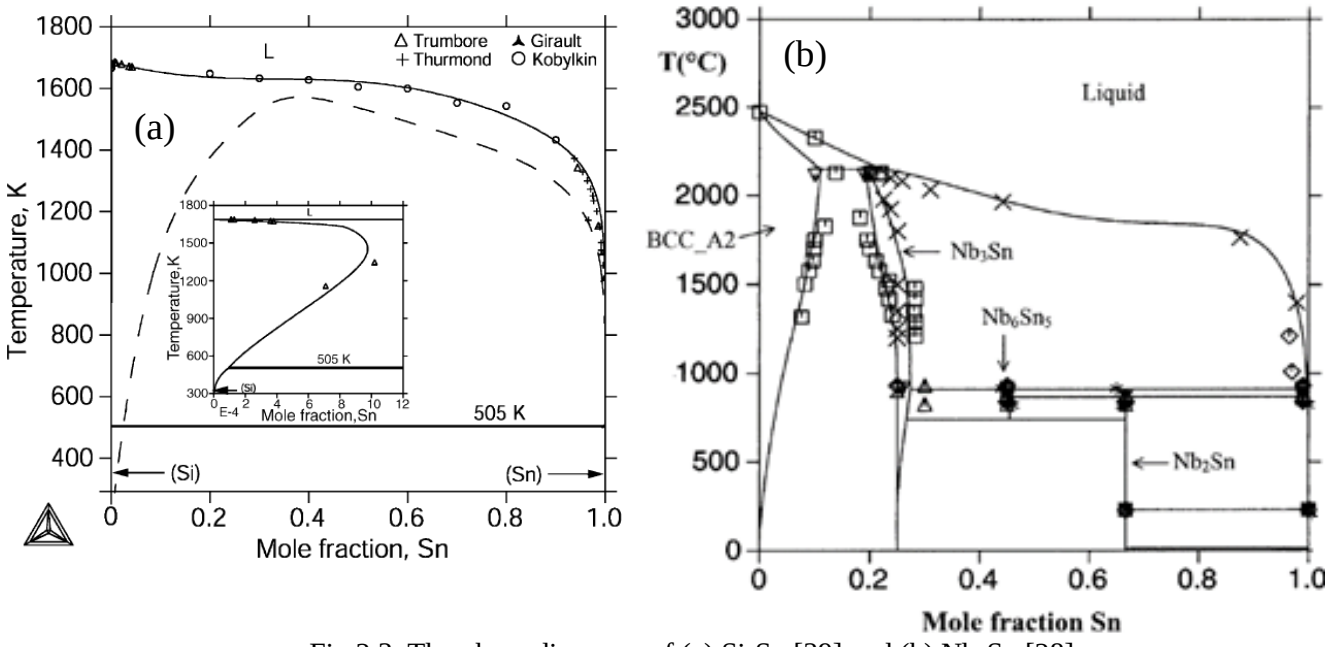

Fig 2.3. The phase diagrams of (a) Si-Sn [39] and (b) Nb-Sn [28].

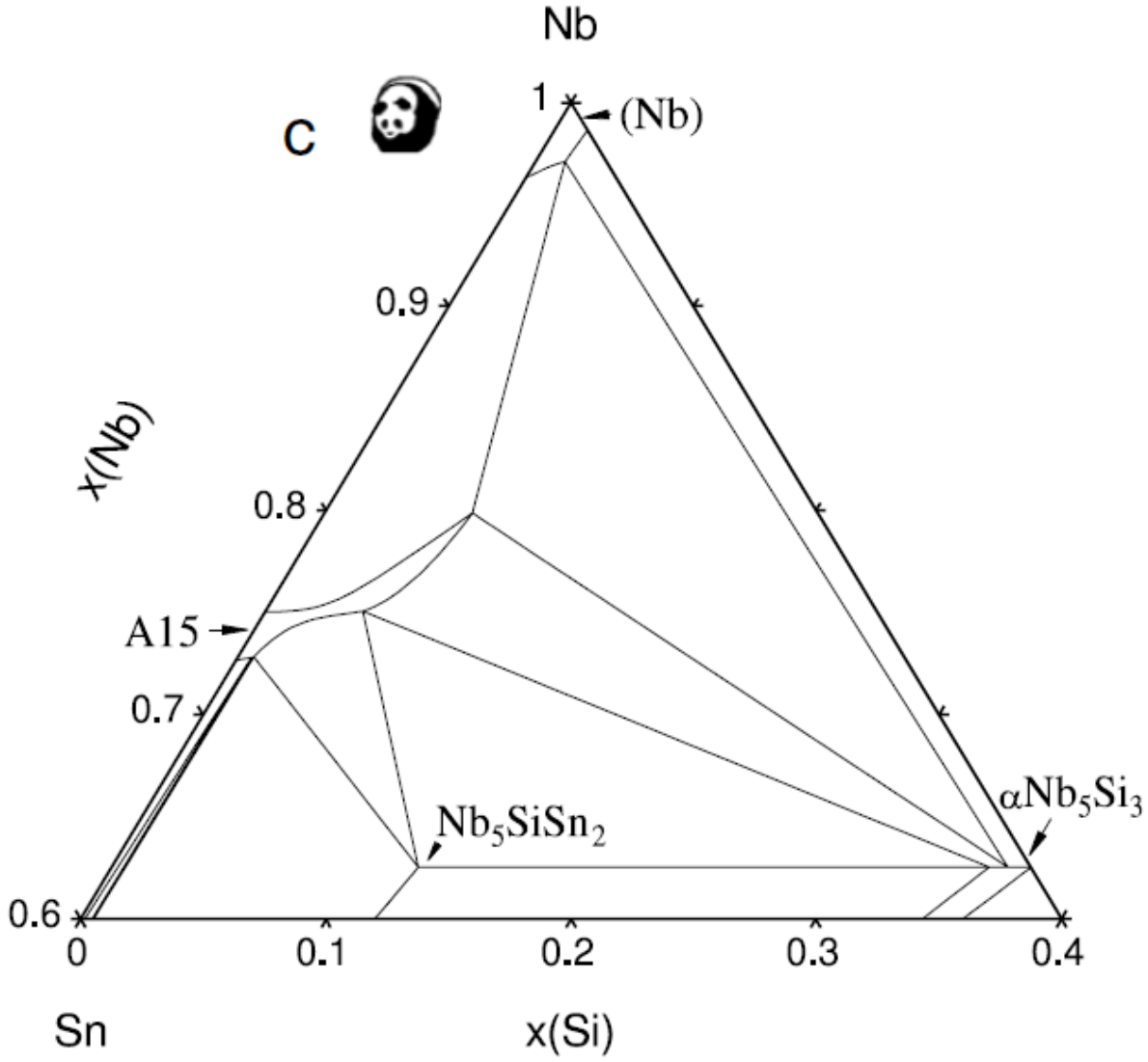

Fig. 2.4. Nb-rich isothermal section of Nb-Si-Sn system at 900 ^{0}C [71]. A15 is the Nb_3Sn phase.

2.5.3 The Nb-Al-Sn system

A description of the ternary Nb-Al-Sn system does not exist as yet in the literature. The Nb-Sn, Nb-Al and Al-Sn binary phase diagrams are shown in Figures 2.3 (b), 2.6 (b) and [74], respectively. The Nb-Al phase diagram consists of the elemental phases and three intermetallics (Fig. 2.6 (b)), section 2.3). As it can be seen in Fig. 2.7 (b), there are no intermetallics in the Al-Sn system. There is no thermodynamic data except the work done by Pietzka and Schuster [75] who reported a series of ternary aluminides including the Nb_5Sn_2Al ternary compound. Its crystal structure was shown to be tetragonal W_5Si_3 structure type and of the I4/mcm space group. Hence, it is isomorphous with the Nb_5SiSn_2 in the Nb-Si-Sn ternary system [71]. Pietzka and Schuster reported that the Nb_5Sn_2Al phase has lattice parameters α=1.0629(2) nm, c=0.5216(2) nm, c/a=0.490 and V=0.5892 nm^3 [75]. Also, Bachner et al. [76] reported that the Nb_3Al and Nb_3Sn compounds show complete solid solubility.

2.5.4 The Nb-Ti-Sn system

The Nb-Ti-Sn system has also not been thermodynamically assessed to date. The Nb-Ti (Fig. 2.1 (c)) [69] and Nb-Sn (Fig. 2.3 (b)) [28] phase diagrams were described previously. The most recent description for Ti-Sn is from Yin et al. [77] in which the compounds Ti_2Sn and Ti_3Sn were considered as non-stoichiometric. The phase diagram is shown in Figure 2.5 [77]. In order to proceed to a robust description of this ternary system experimental data is needed.

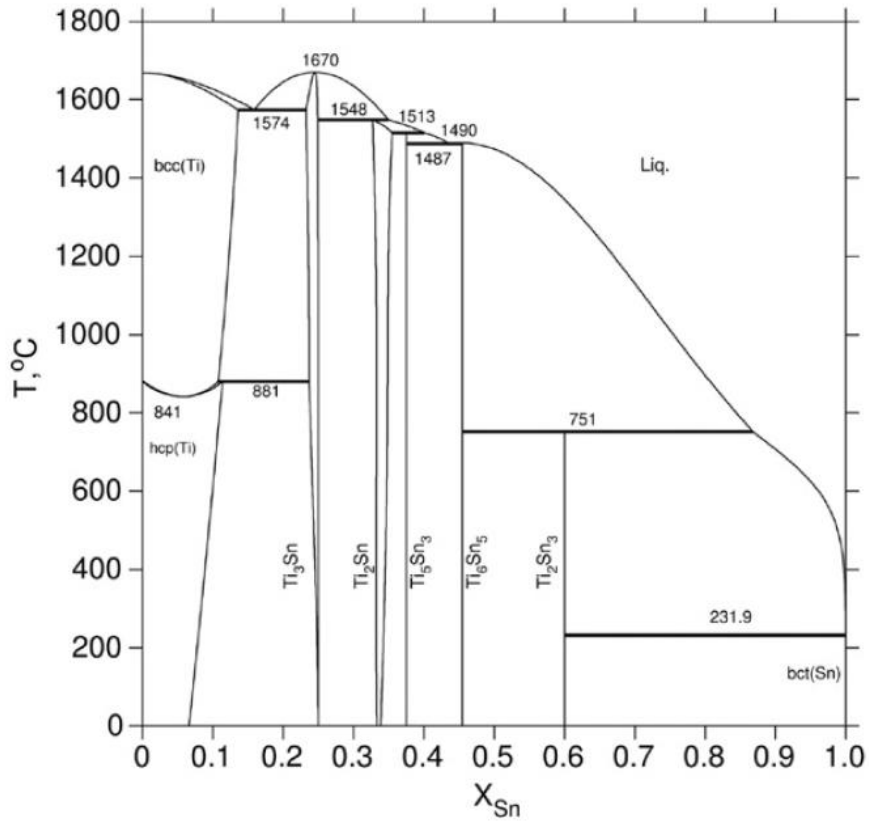

Fig. 2.5. The Ti-Sn phase diagram [77].

2.5.5 The Nb-Ti-Al system

Another important ternary system is the Nb-Ti-Al. It has been extensively studied since the 1970's, owing to the emerging of the titanium aluminide alloys as aerospace materials. The latest assessment of the Nb-Al, Ti-Al and Nb-Ti-Al systems was conducted by Witusiewicz et al. [78, 79]. The Ti-Al and Nb-Al phase diagrams and the Nb-Al-Ti 1060 ^{0}C (1333 K) isothermal are presented in Figure 2.6 (a) (b) and (c) respectively. In Figure 2.6 (c) it can be seen that Ti exhibits high solubility in Nb_3Al (up to about 25 wt. %), in Nb_2Al (up to about 40 wt. %), while the $TiAl_3$ and $NbAl_3$ phases are isomorphous and Nb has a solubility in TiAl up to ~30 wt. %.

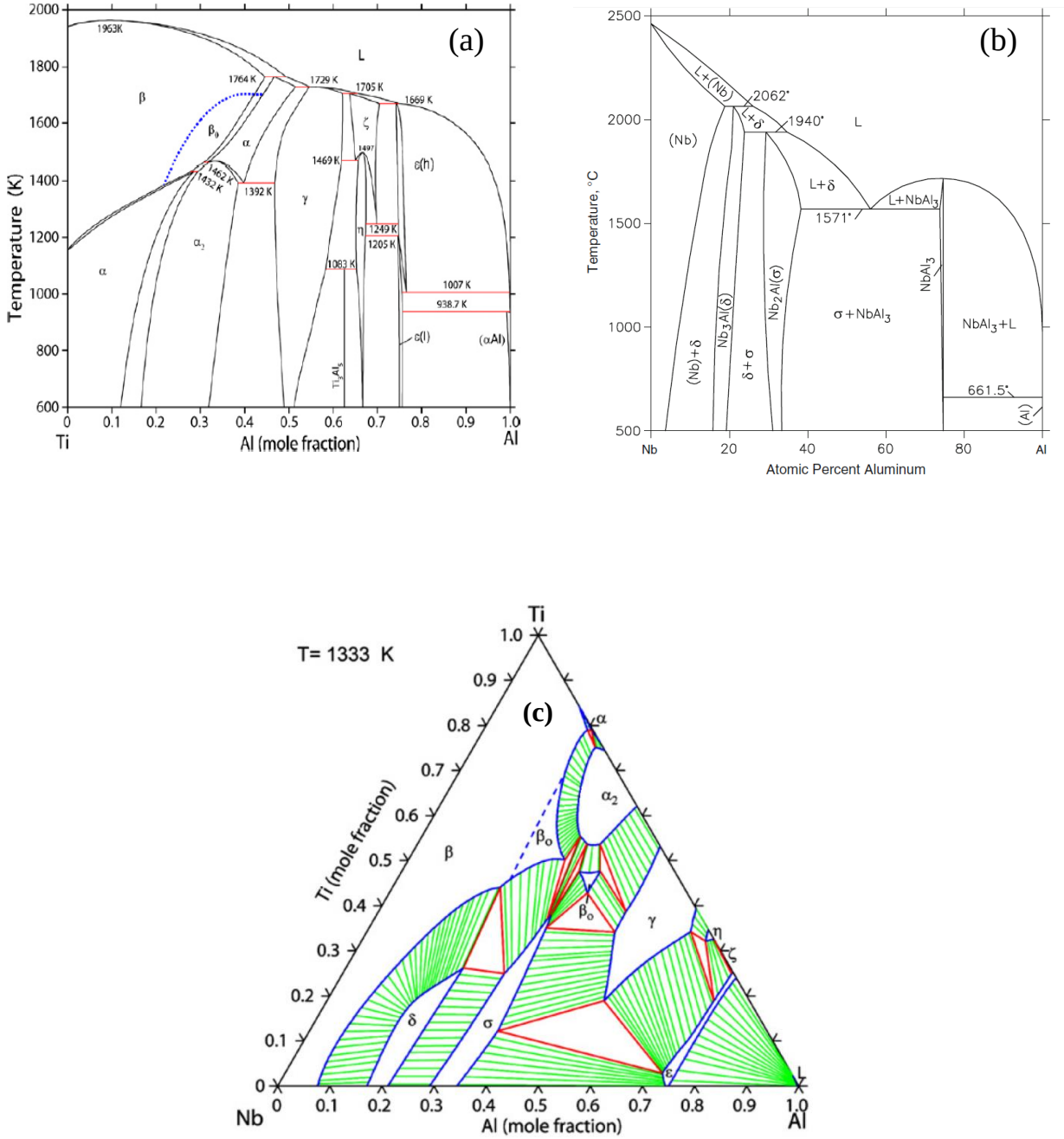

Fig. 2.6 (a) Al-Ti phase diagram [78], (b) Nb-Al phase diagram [79], and (c) Nb-Ti-Al 1060 ^{0}C isothermal section [79]. β:BCC_A2 Ti (disordered), β_0:BCC_B2 Ti (ordered), δ: Nb_3Al, σ: Nb_2Al, ε: $NbAl_3$, γ: TiAl, α_2: Ti_3Al, η:Ti_2Al.

2.5.6 The Nb-Si-Al system

Understanding of the Nb-Si-Al system is essential in order to study thoroughly the effect of Al additions to the Nb-Si system. The Nb-Al binary is shown in Fig. 2.6 (b) and the Nb-Si in Fig. 2.1 (a). The Al-Si binary is based on the data from Dinsdale and is presented in Fig. 2.7 (a) [74]. Brukl et al. [80] reported the presence of two ternary compounds $Nb_3Si_5Al_2$ and $Nb_{10}Si_3Al_3$ which were in equilibrium with each other. Pan et al. [81] contradicted this and reported that these ternary phases were not in equilibrium, instead the $NbAl_3$ and αNb_5Si_3 were in equilibrium with each other. The Al solubility in αNb_5Si_3 was reported differently in each research. Brukl et al. [80] and Murakami et al. [82] agreed on it being near zero, while Pan et al. reported it being ~10 at. %. Zelenitsas and Tsakiropoulos [29] reported the Al solubility in αNb_5Si_3 and βNb_5Si_3 to be 2.2 - 3.8 at. % and 3.3 - 3.8 at. %, respectively. The most recent effort of integrating the experimental data to a model was done by Shao et al. [53]. The isothermal section at 900 °C (1173 K) by Murakami et al. [82] is shown in Fig 2.8.

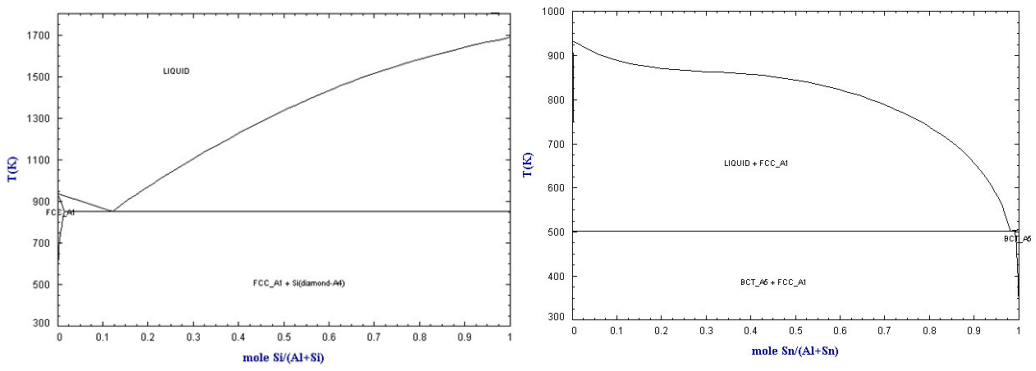

(a) (b)

Fig. 2.7. The phase diagrams of (a) Si-Al [74] and (b) Al-Sn [74]

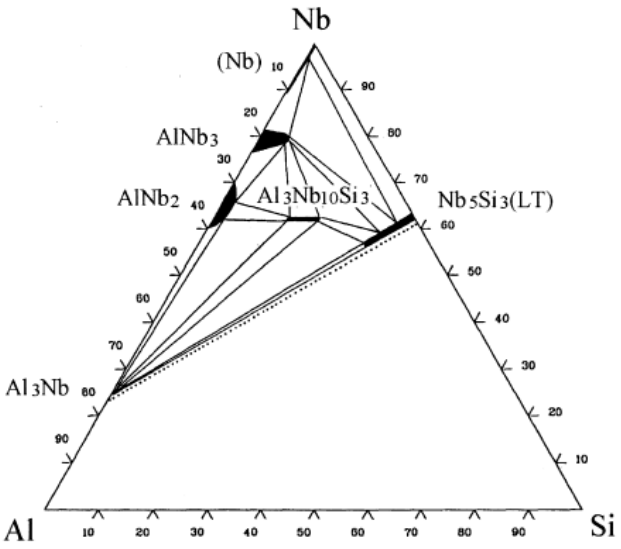

Fig. 2.8. Isothermal section of Nb-Si-Al at 1173 K [82]

2.6 Cubic A15-structure phases

The Nb_3Si and Nb_5Si_3 silicides can be present in the microstructure of Nb silicide based alloys [1, 2]. Both silicides can form as stable and metastable compounds [14]. In the Nb-Si binary phase diagram the equilibrium (stable) 5-3 silicide has the βNb_5Si_3 tetragonal structure at high temperatures and the αNb_5Si_3 tetragonal structure at low temperatures, and the tetragonal (stable) Nb_3Si transforms via a eutectoid reaction to Nb_{ss} and αNb_5Si_3 [14] which can be used to generate desirable microstructures in the alloys [2]. Metastable Nb_3Si can form with the A15 cubic structure. There is no data about phase transformations involving the A15-Nb_3Si.

Additions of Al, Ge and Sn in Nb-18Si (at. %) based alloys have been shown to benefit their oxidation behaviour [3, 5-7] and to influence the transformation of βNb_5Si_3 to αNb_5Si_3 [1]. These elements suppress the formation of the tetragonal (stable) Nb_3Si [19, 55, 83] and Sn plays a key role in the elimination of pest oxidation [3, 6]. The effectiveness of Sn depends on its concentration and its synergy with other elements in the alloy and on whether the A15-Nb_3Sn is stable in the microstructure. Furthermore, Sn can stabilise metastable forms of the Nb_3Si when it is in synergy with Fe and Cr [30]. The formation of A15-Nb_3Al in Nb silicide based alloys is possibly depending on the Ti/Al ratio in the alloy [84].

In the equilibrium Nb-Si binary phase diagram the Nb_3Si has a tetragonal Ti_3P-type crystal structure. In Nb-Si-Ti based alloys the formation of the A15 Nb_3Sn destabilises the tetragonal Nb_3Si [19]. Some intermetallic phases with the A15 cubic structure have also attracted interest because of their superconducting properties. Niobium forms a number of superconducting A15 compounds that exhibit high transition temperatures (T_c), namely Nb_3Ge (-249.55 °C (23.6 K)), Nb_3Ga (-252.95 °C (20.2 K)), Nb_3Sn (-254.25 °C (18.9 K)) and Nb_3Al (-254.35 °C (18.8 K)). It has been suggested that the A15 Nb_3Si phase would have a T_c above that of Nb_3Ge, of the order of -248.15 °C (25 K) [41], owing to its small lattice parameter.

The A15 structure is a close-packed structure whose stability is largely governed by cell size [41]. It has a primitive cell of 8 atoms and belongs to the space group P*m*3*n*, its Pearson symbol is *cP*8 and is of the Cr_3Si type. The A_3B cubic unit cell has two B atoms at (0, 0, 0) and (0.5, 0.5, 0.5) sites and six A atoms at (0.25, 0, 0.5), (0.5, 0.25, 0), (0, 0.5, 0.25), (0.75, 0, 0.5), (0.5, 0.75, 0) and (0, 0.5, 0.75) sites. In the current study the A atoms are Nb while the B atoms are Sn, Al, Ge or Si. In the case of the ternary compounds, two different atoms occupy either the (0, 0, 0) or (0.5, 0.5, 0.5) sites.

The resistivity [43, 85], heat capacity [44, 47], electron-phonon interaction [45] and magnetic susceptibility [46] of A15 compounds have been studied. There is limited data about enthalpies of formation and Debye temperature of the A15-Nb_3X (X=Sn, Al, Si, Ge) compounds [44, 47]. The elastic properties of Nb_3Sn and Nb_3Al have been calculated [48, 64], but to the best of the authors' knowledge no data exists for the A15 Nb_3Si and Nb_3Ge intermetallics.

2.7 Tetragonal W_5Si_3 structure type phases

Investigations have been carried out on the phase diagrams of the Nb-Sn-Si and Ti-Sn-Si systems by Sun et al. [71] and Bulanova et al. [86], respectively. In both cases the existence of a ternary W_5Si_3 type compound has been reported, being Nb_5Sn_2Si and Ti_5Sn_2Si for the Nb-Sn-Si and Ti-Sn-Si systems, respectively. The stability of the latter compound was confirmed by Colinet and Tedenac using ab initio calculations [87]. The first experimental work on the Nb_5Sn_2Si compound was done by Horyn and

Lukaszewicz [73]. Pietzka and Schuster [75] prepared several ternary alloys with the T : M : Al ratio 5 : 2 :1 where T = Ti, Zr, Hf, V, Nb, Ta, Cr, Mo, W and M = Si, Ge, Sn, Pb. The Nb_5Sn_2Al and Ti_5Sn_2Al phases were amongst the compounds they found and they had the same structure as the Nb_5Sn_2Si. The T atoms (T=Nb, Ti) occupy the 4b and 16k Wyckoff positions, the Al and Si atoms the 4a positions and the Sn atoms the 8h positions [73, 75, 87].

2.8 Ab initio (Density Functional Theory)

2.8.1 Introduction

If the Nb silicide based alloys were to qualify as materials for next-generation gas-turbine components a balance between mechanical and environmental properties must be achieved. This requires optimising alloying additions in the alloys and thus renders it essential that the alloy systems of participating elements are studied thoroughly and fully understood. To achieve this goal a consistent and robust description of each system must be obtained. In that way a set of stable phases and their thermodynamic properties in regions without experimental results can be reliably predicted. As a method is faster and easier than the experiment in many cases, especial when it comes to high temperature refractory materials. Density Functional Theory (DFT) is a modern day tool that can help the researchers accomplish the above. It is a modelling method based on quantum mechanics and applied in physics and chemistry in order to determine the electronic structure (in principal the ground state) of many body systems such as atoms, molecules as well as condensed phases [88, 89]. Functionals, which are functions of another function and more specifically of electron density are used in order to describe the properties of a many electron system, hence the name of the theory. While it is not possible to solve the full time-dependent N-electron Schrödinger equation:

$$\left(-\frac{\hbar^2}{2m_e}\nabla^2 + V\left(\boldsymbol{r}, t\right)\right)\Psi\left(\boldsymbol{r}, t\right) = \varepsilon(\boldsymbol{r}, t) \qquad (2.7)$$

as it is a function of time and the position of every particle. Density functional theory gives a method to investigate the ground state electronic structure of a given system. A set of approximations and theorems is applied to the time-dependent Schrödinger equation in order to simplify it and make it reasonably feasible to be calculated. Those approximations are analysed extensively below.

While DFT had been popular in the 1970's, calculations using this method were not accurate enough until the 1990's when the models used for the exchange and correlation interactions were significantly refined. It can be said that today, in a growing number of cases, the calculations especially for solid-state systems are in quite good agreement with experimental data. As the computer power sees an ongoing increase and the computational cost decreases, DFT proves to be a valuable tool in the hands of researchers. Especially regarding the DFT modelling of metals, in the last years it is commonly accepted that it can be very accurate in terms of enthalpy of formation and elastic properties calculations [23, 87, 90], whereas in terms of vibrational properties calculations, the limitations posed from the inherent anharmonicity of the available methods can be surpassed by analytical methods that only lately became available for metals [91, 92]. Also, the cost for deriving the enthalpy of formation and the elastic and vibrational properties is undoubtedly smaller with the help of DFT than with the corresponding experimental methods, both in terms of time and work load.

2.8.2 Approximations

2.8.2.1 Born-Oppenheimer approximation

The Born-Oppenheimer approximation [93] was first proposed in 1927, in the early days of quantum mechanics, by Born and Oppenheimer and is still indispensable in quantum chemistry. It consists of two steps. In the first step, the kinetic energy of the nuclei is neglected, as a result of the assumption that nuclei are massive and slow when compared to electrons. Thus the corresponding operator (T_n) is subtracted from the total molecular Hamiltonian. In the remaining electronic Hamiltonian (H_e) the nuclear positions enter as parameters. The interactions between the nuclei and the electrons are not removed and the electrons continue to “sense” the nuclei Coulomb potential clamped at certain spatial positions. This derives from the assumption that the electrons

react so quickly to the nuclear motion that it may as well be instant. This first step is often referred to as the clamped nuclei approximation. A quasi-separable approach is of the form:

$$\psi(r,R)=\varphi(\boldsymbol{r}\ ,\ \boldsymbol{R})\ \chi\ (\boldsymbol{R}) \qquad (2.8)$$

where χ is the nuclear wave function and φ the electronic wave function that depends parametrically on the nuclear positions. The electronic Schrödinger equation is solved. The quantities r and R stand for electronic and nuclei coordinates, respectively. The electronic energy depends on the chosen positions R of the nuclei. If small step variations of these positions R take place and the electronic Schrödinger equation is repeatedly solved, E_e as a function of R can be obtained. This is the Potential Energy Surface (PES). As this procedure resembles to the conditions of the adiabatic theorem, this way of calculating PES is often called adiabatic approximation and the PES, adiabatic surface. In the second step of the Born-Oppenheimer approximation the nuclear kinetic energy T_n is reintroduced into the Schrödinger equation:

$$[T_n + E_e(R)]\ \varphi(R) = E\ \varphi(R) \qquad (2.9)$$

which then is solved. In this second step of the BO approximation, separation of vibrational, translational and rotational motions is involved:

$$E_{TOTAL} = E_{electronic} + E_{vibrational} + E_{rotational} + E_{nuclear} \qquad (2.10)$$

The nuclear spin energy is so small that it is normally omitted.

2.8.2.2 Hohenberg - Kohn and Kohn-Sham Theorems

After applying the Born-Oppenheimer approximation, the quantum-mechanical problem is narrowed down to electrons and their time-independent Schrödinger equation. Even though DFT has its roots in the Thomas-Fermi model, it has been theoretically reinforced by the Hohenberg-Kohn and Kohn-Sham theorems.

The Hohenberg-Kohn [88] and the Kohn-Sham [89] papers show that the ground state energy and charge density of interacting electrons in the potential from nuclei are exactly the same as those of non-interacting electrons in a potential from nuclei plus some extra potential. The Coulomb potential is now treated as a static external potential in which electrons are moving. Within the framework of the Kohn-Sham scheme, the fairly difficult many-body problem of interacting electrons in a static external potential is reduced to a solvable problem of non-interacting electrons moving in an effective potential:

$$E_{kin} + E_{e-e} = E_{kin}^{non-int} + E_{e-e}^{non-int}[\rho] + E_{xc}[\rho] \qquad (2.11)$$

On the right hand side, the $E_{kin}^{non-int}$, the $E_{e-e}^{non-int}$ and the extra term, are the non interacting kinetic energy, the non interacting electron energy and a functional of the electron density ρ(**r**) that is called the exchange correlation functional. The electron density is now vital in order for the Schrödinger equation to be solved and can be calculated from the wavefunctions ψ_m:

$$\rho(\boldsymbol{r}) = \sum_m |\psi_m(\boldsymbol{r})|^2 \qquad (2.12)$$

The Schrödinger equation becomes:

$$\hat{H}[\rho]\,\psi_m(\boldsymbol{r}) = E_m\psi_m(\boldsymbol{r}) \qquad (2.13)$$

in which the Hamiltonian operator is:

$$\hat{H}[\rho] = -\frac{\hbar^2}{2m_e}\nabla^2 + \hat{V}_{e-e}^{non-int}[\rho] + \hat{V}_{e-n}[\rho] + \hat{V}_{xc}[\rho] \qquad (2.14)$$

where $\hat{V}_{e-e}^{non-int}$ is the non interacting electron potential, the $\hat{V}_{e-n}[\rho]$ is the electron-nucleus potential and the $\hat{V}_{xc}[\rho]$ is the exchange correlation potential. Every term of the equation can be calculated precisely, except for the $\hat{V}_{xc}[\rho]$, as the exact functionals for exchange and correlation are not known except for the free electron gas. However several approximations exist, that allow the calculation of different physical quantities with accuracy.

2.8.2.3 Exchange Correlation Approximations

The major exchange correlation functionals are the Local Density Approximation (LDA) and the Generalised Gradient Approximation (GGA). The former, which is the older, is a pretty good approximation to the energy and depends only on the density at the coordinate where the functional is evaluated:

$$E_{xc}^{LDA}[n] = \int f(n) d^3 r \quad (2.15)$$

The Local Spin-Density Approximation (LSDA) is a generalisation of the LDA to take electron spin into account:

$$E_{xc}^{LSDA}[n_\uparrow, n_\downarrow] = \int f(n_\uparrow, n_\downarrow)\, d^3 r \quad (2.16)$$

The Generalised Gradient Approximation is still local but includes the gradient of the density at the same coordinate:

$$E_{xc}^{GGA}[n_\uparrow, n_\downarrow] = \int f(n_\uparrow, n_\downarrow, \boldsymbol{\nabla} n_\uparrow, \boldsymbol{\nabla} n_\downarrow)\, d^3 r \quad (2.17)$$

Using the latter (GGA) very good results for various physical quantities and geometries have been achieved. The PW91 [94] and PBE [95] GGA functionals have been extensively used until now and are considered equivalent.

To summarise, what started as a time-dependent, many-nuclei, many-electron quantum mechanics problem, transformed to a static, single particle quantum mechanics problem. The researcher must always bear in mind though that the Exchange-Correlation is coarsely approximated and that even "perfect" DFT is only exact for the ground state of the system.

2.8.2.4 Bloch's Theorem

The starting quantum problem has been simplified in a way that only a single particle equation needs to be solved, but it needs to be solved for enough states for every electron. Considering that even a few grams of material has 10^{23} electrons, this could mean that a large number of states are needed. One property of most of the solid state materials that can be taken advantage of is periodicity.

If the nuclei are arranged in periodically repeating pattern, their potential acting on the electrons must be periodic as well:

$$V(\boldsymbol{r} + \boldsymbol{L}) = V(\boldsymbol{r}) \quad (2.18)$$

where L is any lattice vector. This leads to the conclusion that the electron density is periodic as well:

$$\rho(\boldsymbol{r} + \boldsymbol{L}) = \rho(\boldsymbol{r}) \quad (2.19)$$

and the magnitude of the wavefunction will be periodic as well:

$$\rho(\boldsymbol{r}) = |\psi(\boldsymbol{r})|^2 \quad (2.20)$$

According to Bloch's Theorem, in a periodic potential the density has the same periodicity so the possible wavefunctions are:

$$\psi_k(\boldsymbol{r}) = e^{ik\boldsymbol{r}}\, u_k(\boldsymbol{r}) \qquad (2.21)$$

where $u_k(\mathbf{r}+\mathbf{L})=u_k(\mathbf{r})$ is a periodic function with the same periodicity as the crystal and e^{ikr} is an arbitrary phase factor. This means that :

$$\psi_k(\boldsymbol{r}+\boldsymbol{L}) = e^{ikL}\, \psi_k(\boldsymbol{r}) \qquad (2.22)$$

2.8.2.5 k-point sampling, Pseudopotentials, Cutoff Energy

There is a set of parameters that can affect the accuracy of any calculation the major of which are the k-point sampling, the pseudopotentials used and the Energy Cutoff.

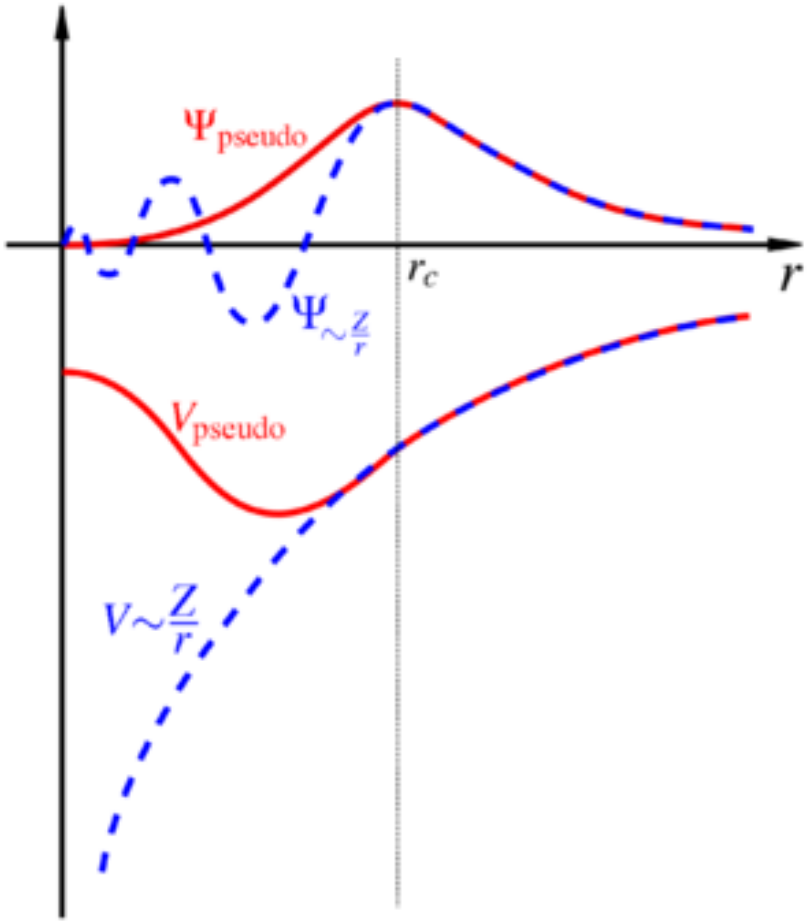

Fig. 2.9. Real potential of nucleus (blue), compared to the pseudopotential (red) (image taken from Google images)

For many materials' properties integrals over the Brillouin Zone (BZ) are necessary. In order to optimise the calculations it is always preferable to compute the functions that are to be integrated at a specific set of points over the Brillouin Zone. This is crucial in calculations where the computational effort for each BZ point is substantial. Only a finite number of k-points is used to sample the BZ. The Monkhorst-Pack (MP) [96]

scheme is implemented in most cases as it is an unbiased method of choosing a set of k-points for sampling. In fractional coordinates it is a rectangular grid of points of dimensions $M_x x M_y x M_z$, spaced evenly throughout the Brillouin Zone. The larger the dimensions of the grid the finer and more accurate will be the sampling.

Another important part of the calculation preparation is the selection of the pseudopotentials. The wavefunctions near the nuclei are not of interest as they do not affect the chemical, mechanical or electronic properties significantly. Hence, the Coulomb potential near each nucleus can be replaced with a weaker, modified potential, called pseudopotential. Due to the fact that the core electrons are all the time near the nucleus, they repel the outer electrons, so the latter "feel" a weaker potential from the nucleus. This phenomenon is known as screening. If this screening effect is taken into account in the pseudopotentials, the core electrons can be ignored by considering each atom's nucleus and core electrons as an ion and producing a pseudopotential that has the same effect on the outer electrons. As can be seen in Fig. 2.9, after a certain radius the real and the pseudo wavefunction and potentials match. Two major kinds of pseudopotentials exist; norm-conserving and ultrasoft. The methodology of norm-conserving pseudopotentials is that the pseudowavefunction matches the all electron wavefunction beyond a cutoff radius that represents the region of the core. Within that region the wavefunction has no nodes and is related to the electron wavefunction by the norm-conserving condition which states that both of these wave functions will have the same charge. These types of pseudopotentials can be highly accurate with a high energy cutoff. On the other hand, the relaxation of the norm conserving condition can be used to produce much softer pseudopotentials. In this scheme, the pseudowavefunctions are as soft as possible within the core, allowing that way the cutoff energy to be reduced. This is done by a generalised orthonormality condition. Thus the ultrasoft pseudopotentials are produced [97].

Finally, the cutoff energy parameter, which defines the basis set (set of functions that are combined in linear combinations to create molecular orbitals), is one of the most important parameters that determine the accuracy and the computational cost of a calculation. It affects the energies of the plane waves that will be included in a calculation. The basis set of the wavefunctions at each k-point can be expanded in terms of a discrete plane wave basis set. In principle an infinite plane wave basis set would be needed for the expansion of those wavefunctions. However in practice the plane waves with lower kinetic energy are more important than those with higher kinetic

energy. This means that the plane wave basis set can be reduced to include plane waves with kinetic energy less than a specified cutoff energy. As with the MP grid, the higher the Cut-off energy, the more accurate the results.

2.8.3 Density Functional Perturbation Theory (DFPT)

Linear response, or Density Functional Perturbation Theory (DFPT) is one of the most popular methods of lattice dynamics [98]. Its applicability extends further from the study of vibrational properties, as it provides an analytical way of calculating the second derivative of the total energy with respect to a given perturbation. Various properties can be computed, depending on the nature of the perturbation. When ionic positions are perturbed, the dynamical matrix and phonon frequencies are obtained, whereas when the unit cell vectors are perturbed, one can derive the elastic constants. Magnetic and electric field perturbations yield NMR and dielectric response respectively.

The force constants matrix can be calculated by differentiating the Hellman-Feynman forces on atoms, with respect to ionic coordinates. The force constants matrix depends on the ground state electron charge density and on its linear response to a distortion of atomic positions. The second order change in energy depends on the first order change of the electron density.

Density Functional Theory states that the total energy is a functional of the electron density, so by solving the DFT equations, the total energy can be minimised. In a similar way in DFPT the first order changes in density, potential and wavefunctions can be obtained by minimising the second order perturbation in total energy [99, 100].

With the help of DFPT, phonon spectra can be used to calculate energy, entropy, free energy and lattice heat capacity as a function of temperature, using the quasi-harmonic approximation [98]:

$$E(T) = E_{tot} + E_{zp} + \int \frac{\hbar\omega}{exp\left(\frac{\hbar\omega}{kT}\right)-1} f(\omega)d\omega \quad (2.23)$$

$$S(T) = k\{\int \frac{\frac{\hbar\omega}{kT}}{exp\left(\frac{\hbar\omega}{kT}\right)-1} f(\omega)d\omega - \int f(\omega)\left[1 - exp\left(-\frac{\hbar\omega}{kT}\right)\right]d\omega\} \quad (2.24)$$

$$F(T) = E_{tot} + E_{zp} + kT\int f(\omega)\ln\left[1 - exp\left(-\frac{\hbar\omega}{kT}\right)\right]d\omega \quad (2.25)$$

$$C_v(T) = k\int \frac{\left(\frac{\hbar\omega}{kT}\right)^2 exp\left(\frac{\hbar\omega}{kT}\right)}{\left[exp\left(\frac{\hbar\omega}{kT}\right)-1\right]^2} f(\omega)d\omega \quad (2.26)$$

$$C_v(T) = 9Nk(\frac{T}{\Theta_D})^3 \int_0^{\frac{T}{\Theta_D}} \frac{\chi^4 e^x}{(e^x-1)^2} dx \quad (2.27)$$

where $E_{zp} = \frac{1}{2}\int F(\omega)\hbar\omega d\omega$, is the zero point vibrational energy and $f(\omega)$ is the phonon density of states. The E_{tot} term is the total energy at 0 K, k is Boltzmann's constant, $\hbar$ is the reduced Planck's constant, $S(T)$ is the entropy versus temperature, $F(T)$ is the free energy versus temperature, $C_v(T)$ is the heat capacity at constant volume versus temperature and Θ_D is the Debye temperature. It must be noted here that the appearance of any imaginary frequency in the calculated phonon spectrum can be used as a signal of mechanically unstable crystal structure.

2.8.4 Elastic constants and equation of state

Generally the calculations regarding mainly phonons and elastic properties require optimising the structures in order to calculate each ground state. The elastic constants of a material describe its response to an applied stress, or the stress required to maintain a distortion. Both stress and strain have three tensile and three shear components, giving six in total. The linear elastic constants form a 6 x 6 matrix such that $\sigma_i=C_{ij}\varepsilon_j$ for small stresses σ and strain ε. The method to determine elastic constants in CASTEP (see below) is applying a given strain and calculating the resulting stress, since the unit cell is fixed and does not require optimisation. After acquiring the elastic constants matrix the Voigt-Reuss-Hill approximation [101, 102] can be used in order to obtain bulk (B), shear (G) modulus, Poisson's ratio (v) for polycrystalline crystal, as well as the Debye temperature [103], using the following equations:

$$B = \frac{(B_V+B_R)}{2} \quad (2.28)$$

$$G = \frac{(G_V+G_R)}{2} \quad (2.29)$$

$$E = \frac{9GB}{(3B+G)} \quad (2.30)$$

$$v = \frac{E}{2G} - 1 \quad (2.31)$$

$$\theta_D = \frac{h}{k}[\frac{3n}{4\pi}\left(\frac{N_A\rho}{M}\right)]^{1/3} u_m \quad (2.32)$$

$$u_m = [\frac{1}{3}(\frac{2}{u_t^3} + \frac{1}{u_l^3})]^{-1/3} \quad (2.33)$$

$$u_t = \sqrt{\frac{G}{\rho}} \quad (2.34)$$

$$u_l = \sqrt{\frac{B+\frac{4G}{3}}{\rho}} \quad (2.35)$$

where B, G and E are bulk, shear and elastic modulus, v is the Poisson's ratio, Θ_D is the Debye temperature, M is the molecular weight, N_A is the Avogadro's number, n is the number of atoms per formula unit, ρ is the density and u_t and u_l are the traverse and longitudinal elastic wave velocities of the polycrystalline material, respectively. Additionally, ductile or brittle behavior of a material can be deduced by taking into account Cauchy pressure and Pugh's [104] index of ductility of shear modulus over bulk modulus ratio (G/B) and Poisson's ratio (v).

Furthermore, the relation between pressure and volume, and internal energy and volume can be investigated by obtaining the Birch-Murnaghan equation of state:

$$E(V) = E_0 + \frac{9V_0B_0}{16}\left\{\left[\left(\frac{V_0}{V}\right)^{\frac{2}{3}} - 1\right]^3 B_0' + \left[\left(\frac{V_0}{V}\right)^{\frac{2}{3}} - 1\right]^2 \left[6 - 4\left(\frac{V_0}{V}\right)^{\frac{2}{3}}\right]\right\} \quad (2.36)$$

where $B_0 = -V(\frac{\partial P}{\partial V})_{P=0}$ (2.37)

is the bulk modulus

and $B_0' = (\frac{\partial B}{\partial P})_{P=0}$ (2.38)

is the pressure derivative of the bulk modulus.

Finally, the mechanical stability of a phase can be determined as any negative elastic constant in the elastic properties calculations can lead to the conclusion that the phase examined is mechanically unstable.

2.8.5 CAmbridge Serial Total Energy Package (CASTEP)

Cambridge Serial Total Energy Package (CASTEP) [91, 105] is a first principles plane wave simulation code that takes advantage of all the above in order to predict properties of materials. It provides an implementation of DFT which is based on pseudopotential description (norm-conserving and ultrasoft schemes available), extensive use of fast Fourier transform (FFT) for evaluation of the terms of the Hamiltonian, and implementation of the most popular DFT expressions for the exchange-correlation functional. As the code makes use of iterative schemes for the self-consistent minimisation in order to find the ground state, it offers a choice of methods to achieve electronic relaxation. The default and most efficient method is based on the density mixing. In this scheme the sum of electronic eigenvalues is minimised in the fixed potential. At the end of each step the new charge is mixed with the initial density until convergence is achieved. A number of options are available; linear, Kerker and Pulay mixing.

3

Methods

3.1 Experimental details

The actual compositions of the twelve Nb-based alloys studied in the current work are presented in Table 3.1. IP1 was selected in order to further understand the effect of Sn and Ti on the microstructure of Nb-18Si by submitting it to other heat treatment temperatures than the ones examined by Vellios and Tsakiropoulos [19] while the motivation for the IP2 and IP3 alloys was to study the stability and properties of the Nb_5Sn_2Si phase [71, 73]. The motivation for the IP4, IP5 and IP6 alloys was to gain experimental data for the Nb-Sn-Al ternary system and investigate the presence and stability of the Nb_5Sn_2Al. Furthermore, the incentive for the IP7, IP8, IP9, IP10 and IP11 and IP12 alloys was the investigation of the Nb-Ti-Sn and Nb-Cr-Sn systems, respectively.

Niobium (99.99 wt. %), Si (99.999 wt. %), Ti (99.99 wt. %), Cr (99.99 wt. %) and Sn (99.99 wt. %) were used as the starting materials for the IP1, IP2, IP3, IP7, IP8, IP9, IP10, IP11 and IP12 alloys. The preparation process of the alloy IP1 can be seen in the work of Vellios and Tsakiropoulos as it was the same alloy as the NV6 as-cast [19]. For the preparation of the IP4, IP5 and IP6 alloys, two series of master-alloys instead of pure elements were used. The first was Nb_3Al produced using Nb (99.99 wt. %) and Al (99.99 wt. %) available in ribbon form. The second was produced by melting Sn (99.99 wt. %) with Al (99.99 wt. %) in a tube furnace under Ar-atmosphere. This was done in order to minimise the evaporation of Sn and Al during arc melting due to the large difference of the melting points of Nb (2477 °C (2750 K)) and Sn (231 °C (504 K)) or Al (660 °C (933 K)).

All the alloys were produced by arc-melting (Fig. 3.1) under high purity Ar-atmosphere using a non-consumable tungsten electrode and a water-cooled copper crucible. They were remelted at least three times each to ensure homogeneity. Cubic specimens for heat treatment were cut and afterwards wrapped in tantalum foil, placed in an alumina boat and annealed in a tube furnace in Ar atmosphere. The IP1 alloy was annealed at 1000 ^{0}C, 1100 ^{0}C and 1300 ^{0}C for 100 hours, the IP2 at 900 ^{0}C for 100 hours and at 1200 ^{0}C for 300 hours and the IP3 at 900 ^{0}C for 100 and 200 hours. The IP4 alloy was annealed at 900 °C for 100 and 200 and at 1200 °C for 100 hours, the IP5 at 900 °C for 100 and 300 hours and at 1200 °C for 100 hours and the IP6 at 900 °C for

100 and 200 hours and at 1200 °C for 100 hours. The IP7 alloy was annealed at 900 °C for 200 and 300 and at 1200 °C for 100 and 300 hours, the IP8 at 900 °C for 100 and

Fig. 3.1. The arc-melter used in the current study.

300 hours and at 1200 °C for 100 and 300 hours, the IP9 at 900 °C for 100 and 200 hours and at 1200 °C for 100 and 200 hours and the IP10 for 100 and 200 hours and at 1200 °C for 200 hours. The IP11 alloy was annealed at 900 °C for 200 and at 1200 °C for 100 and 200 hours, and the IP12 at 900 °C for 100, 300 and 400 hours and at 1200 °C for 100 and 300 hours. The heat treatments of the alloys are summarised in Table 3.2. Titanium sponge was used as an oxygen getter and was placed at the entrance of the argon flow in the furnace. All samples were furnace cooled. The aim of the annealing was to ensure that equilibrium conditions were met.

X-ray diffraction (XRD) was used to identify the phases present in the alloys. A Siemens D-5000 diffractometer (Fig. 3.2) with monochromatic Cu Kα (λ=1.5418 Å) radiation along with JCPDS Cards (Appendix B) were used, except for the Nb_5Sn_2Al

phase for which no data existed, thus the reflection angles were calculated from the lattice constants in [75] (Appendix B). In the experiments the Cu Kα radiation source was excited by an accelerating voltage of 40 kV and a current of 30 mA, and a step of 0.06 degrees per second. The observing of the microstructures of the samples and the chemical analyses of the constituent phases and the actual compositions of the alloys were done by scanning electron microscopy (SEM), using JEOL JSM 6400 (Fig. 3.3) and FEI Inspect-F (Fig. 3.4) electron microscopes with EDS analysis facilities. Quantitative analyses were done in the former SEM which was equipped with the standards of the elements used in the alloys of this research.

The texture investigation was done using the FEI-Sirion (Fig. 3.5) microscope, equipped with an EBSD detector containing a phosphor screen. All the specimens were flat and parallelepiped and were placed at a 70º from horizontal tilted angle towards the detector. The step size was 0.15 μm/s for all specimens in the current study, that allowed for high indexing (above 85%, reaching 98.2% in some cases), as some features were found to be particularly small (~1 μm).

Fig. 3.2. The Siemens D-5000 diffractometer.

Fig. 3.3. The JEOL JSM 6400 used in the current study.

Fig. 3.4. The FEI Inspect-F used in the current study.

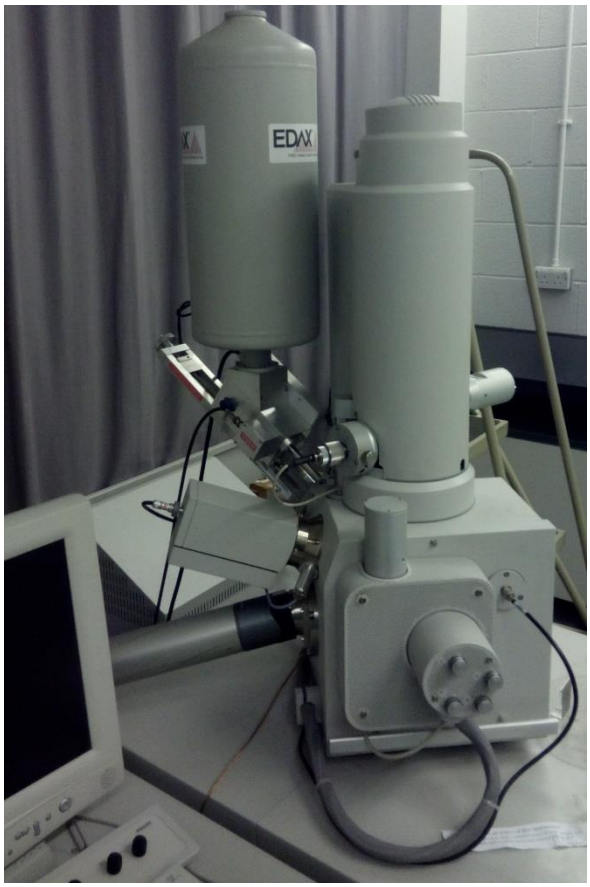

Fig. 3.5. The FEI Sirion used in the current study.

Table 3.1.

Actual compositions of the alloys in the current study.

Alloy	Nb (at. %)	Ti (at. %)	Si (at. %)	Al (at. %)	Cr (at. %)	Sn (at. %)
IP1	53	24	18			5
IP2	71		16			13
IP3	65		18			17
IP4	66			17		17
IP5	54			33		13
IP6	64			16		20
IP7	72	10				18
IP8	84	13				3
IP9	37	40				23
IP10	21	39				40
IP11	74				15	11
IP12	17				65	18

Table 3.2.

Heat treatment conditions of the alloys in the current study.

Alloy	900 °C	1000 °C	1100 °C	1200 °C	1300 °C
IP1		100 h	100 h		100 h
IP2	100 h			300 h	
IP3	100 h, 200 h				
IP4	100 h, 200 h			100 h	
IP5	100 h, 300 h			100 h	
IP6	100 h, 200 h			100 h	
IP7	200 h, 300 h			100 h, 300 h	
IP8	100 h, 300 h			100 h, 300 h	
IP9	100 h, 200 h			100 h, 200 h	
IP10	100 h, 200 h			200 h	
IP11	200 h			100 h, 200 h	
IP12	100 h, 300 h, 400 h			100 h, 300 h	

3.2. Computational details

3.2.1 Methodology

In this section the approach of calculations is described. The relevant equations are given in the Appendix A. All the calculations were performed using the CASTEP (Cambridge Serial Total Energy Package) code [91]. The density functional theory and the Kohn–Sham approach were used to calculate the fundamental eigenvalues [89] (see section 2.8.2.2). The interaction between valence electrons and core electrons was treated under the pseudopotential approximation and the plane-wave approach [106] (see section 2.8.2.5). The exchange-correlation energy was estimated by the Perdew–Wang functional (PW91) approach [94] (see section 2.8.2.3). A finite basis set correction and the Pulay scheme of density mixing were applied for the evaluation of energy and stress, while the electronic energy tolerance for the SCF solver was 1×10^{-10} eV. All geometry optimisations of the structures were performed within the Broyden-Fletcher-Goldfarb-Shanno (BFGS) minimization scheme [105], with the following thresholds for converged structures: energy change per atom, maximum residual force, maximum atomic displacement and maximum stress less than 1×10^{-7} eV, 1×10^{-4} eV/Å, 1×10^{-4} Å and 0.001 GPa, respectively.

The values of the cutoff energy and the Monkhorst-Pack grid for the integration over the Brillouin zone according to the Monkhorst–Pack scheme [96] (see section 2.8.2.5) were selected after careful convergence tests so as they would be sufficient to reduce the error in the total energy to less than 1 meV/atom. A well converged k-point set is required for high quality thermodynamics calculation, thus separate convergence tests were carried out to confirm that the error in the phonon frequencies was less than 10^{-3} cm^{-1}. The details concerning the basis set of plane wave functions, the pseudopotentials and the valences for atomic configurations, as well as the k-point grid and smearing width may vary in different systems depending on the convergence tests, thus they are described separately in each chapter.

3.2.2 Elastic properties

The elastic constants of a material describe its response to an applied stress, or the stress required to maintain a distortion. To determine elastic constants a given strain was applied and the stress was calculated. Since the unit cell was kept fixed only the internal coordinates were optimised. Both stress and strain have three tensile and three shear components, giving six in total. The linear elastic constants form a 6 x 6 matrix such that $\sigma_i = C_{ij}\varepsilon_j$ (see section 2.8.4) for small stress σ and strain ε. This matrix can be reduced as the strain patterns (sets of distortions) are based on the crystal structure of each phase by taking advantage of the linear combinations of the second order elastic constants. Thus, the maximum number of patterns required for a monoclinic structure is six and one for cubic cells. Six strain steps (varying from -0.003 to 0.003) were used for each pattern to obtain a reliable linear fit of the stress-strain relationship. After acquiring the elastic constants matrix and confirming that the mechanical stability criteria [107] are satisfied, the bulk (B), Young's (E), shear (G) moduli and Poisson's ratio (v) were obtained by using the Voigt- Reuss- Hill approximation (VRH) [101, 102] (equations 1 to 18 in Appendix). Furthermore the Debye temperature at low temperatures can be determined from elastic constants using the formulas (equations 19 to 22 in Appendix) [103] since at low temperatures the vibrational excitations arise solely from acoustic modes, i.e. when the Debye temperature is associated with lattice vibrations. In order to confirm the values of the bulk moduli, a fit of the energies versus

the volumes of the strained structures in the third order Birch-Murnaghan equation of state (B-M EOS) [108] (equation 19 in the Appendix) was carried out.

3.2.3 Finite Displacement (Supercell) method

The entropic contributions play a predominant role in the structural stability of intermetallic phases. Especially in the case of strongly ordered compounds the main contribution comes from the vibrational entropy, as the electronic and configurationally entropies are considered to be relatively small [109]. The method of finite displacements was implemented, a technique which is based on calculating the forces on atoms when slightly perturbing the ionic positions [110]. A large enough supercell is required in order to contain the sphere for which the force constant matrix comprises of non-zero elements. That sphere is described by the real space cutoff radius, after which it is assumed that no atomic interactions exist. The larger the supercell, the more accurate, but also more expensive a calculation is. Thus convergence tests of the free energy with respect to the cutoff radius took place, until the error was 1 meV/atom.

In accordance to these convergence tests, different sized supercells were used for each phase and are described in each section separately. By using the obtained phonon DOS and the formulae in [98] (see section 2.8.3), the vibrational contributions to the enthalpy, entropy, free energy and heat capacity versus temperature as well as the Debye temperature were obtained using the quasiharmonic approximation (equations 24 to 27 in Appendix). Apart from the intermetallic compounds that are under study, the phonon DOS of each element separately were calculated as well in order to obtain the finite temperature enthalpy of formation. The heat of formation per atom at 0 K was obtained from equation 28 (see Appendix) whereas using the same equation the finite temperature heat of formation per atom is defined as in equations 28 to 30 in the Appendix.

3.2.4 Linear Response method

Density Functional Perturbation Theory (DFPT) or Linear Response is one of the most popular methods of lattice dynamics [92, 98], was used in order to obtain the vibrational density of states. When ionic positions are perturbed, the dynamical matrix

and phonon frequencies can be obtained. In order for the calculations to be successful in the current study it was first ensured that every system was in the ground state, i.e., the geometry optimisation was fully converged as any underconverged structure could yield imaginary phonon frequency eigenvalues which is indicative of mechanical instability. After directly computing the phonon frequencies on Monkhorst-Pack q-vector grid of 0.05 $Å^{-1}$ separation, the results were interpolated onto a very dense q-point set, thus the phonon density of states (DOS) was obtained for each phase under investigation. By using the phonon DOS and the data in [98], the vibrational contributions to the enthalpy, entropy, free energy and heat capacity versus temperature as well as the Debye temperature were obtained using the quasiharmonic approximation (see equations 24 to 27 in the Appendix and section 2.8.3). Apart from the intermetallics that are under study, the phonon DOS of each element separately were also calculated as well in order to obtain the finite temperature enthalpy of formation. The heat of formation per atom at 0 K was obtained from equation 28 in the Appendix and the finite temperature heat of formation per atom was calculated using the equations 28 to 30 in the Appendix.

3.2.5 Quasistatic approximation

The method to calculate the elastic constants at finite temperatures is to compute the second derivatives of the free energy with respect to the strain. This is not a small task however, as apart from the static part of the free energy (free energy at 0 K), the free energy at finite temperatures is needed, which means many phonon calculations for different strains. Phonon calculations can be tremendously costly from the point of view of computational resources, especially if the reduced symmetry of the structures under study due to the application of inhomogeneous strains is taken into account. Hence, an alternative procedure known as quasistatic approximation has been proposed [111, 112] where the temperature dependences of the variety of thermodynamic quantities are extracted from the volume dependencies of the phonon density of states calculated at 0 K. The procedure consists of three main steps. The first is to express the 0 K elastic constants as a function of volume, using the stress strain approach described in section 2.2. The second step is to calculate the equilibrium volume V(T,P) at every given temperature using the quasiharmonic approximation by minimising the total free energy with respect to volume, thus finding the equilibrium volume at each temperature. In the

present study the investigated structures were obtained by varying the ratio V/V_0 (V_0 being the equilibrium volume) from 0.991 to 1.006 with an increment of 0.003. In all the structures the internal freedoms within the unit cell were fully relaxed before proceeding to the phonon calculations. In the third step the computed elastic constants from the first step at the volume V(T,P) were approximated as the corresponding values at finite temperatures. In order for the evaluation of the elastic constants as a function of temperature to be as accurate as possible, high precision geometry optimisation calculations for different volumes and robust phonon calculations are needed to obtain accurate Phonon DOS at different volumes. Using the approximation described above, expensive free energy versus strain calculations are avoided. Furthermore, application of inhomogeneous strain is not required as this method considers volume rather than strain which is much cheaper in calculation cost terms as the symmetry of the crystal is retained.

In the above procedure the assumption was made that any change of elastic constants was solely due to the thermal expansion which is in accordance with reports [113] for cubic symmetry.

4

Ab initio study of the intermetallics in the Nb-Si binary system

4.1. Introduction

The development of Nb-silicide based alloys requires the Nb-Si system to be fully understood, as it is the base upon which any further research can be built. A first principles study of the Nb-Si binary system, excluding the $NbSi_2$ silicide has been reported in [23]. The motivation for the research described here was to use Density Functional Theory (DFT) to calculate the enthalpy of formation and the elastic properties of the αNb_5Si_3, the βNb_5Si_3, the $NbSi_2$ and the Nb_3Si intermetallics at T=0 K and to compute the temperature dependence of their enthalpies of formation and to reevaluate the transformation temperature for $\beta Nb_5Si_3 \rightarrow \alpha Nb_5Si_3$.

4.2. Computational details

In the current study, ultrasoft pseudopotentials were implemented and the valences for the atomic configurations were Nb-$4s^2 4p^6 4d^4 5s^1$ and Si-$3s^2 3p^2$. An energy cutoff of 450 eV, a Gaussian smearing width of 0.3 eV and a Monkhorst-Pack grid of 0.03 A^{-1} separation were selected. For the finite temperature properties study, the finite displacement (supercell) method was implemented. Different size supercells were used, namely 4 × 4 × 4 for Nb, 3 × 3 × 3 for Si, 2 × 2 × 2 for αNb_5Si_3, βNb_5Si_3 and $NbSi_2$ and 1 × 1 × 2 for Nb_3Si.

4.3. Results and Discussion

4.3.1 Elastic properties

The calculated lattice parameters of the elemental and intermetallic phases in the present study are shown in Table 4.1. Compared with the literature, in this work the values were overestimated, and this has been attributed to the well-known underbinding of the GGA functional. The overall agreement is very good with the mean overestimation being less than 0.3%.

In Table 4.2 the results for the independent elastic constants (C_{ij}), bulk moduli (B) from elastic constants according to the Voigt-Reuss-Hill scheme and bulk moduli and first pressure derivatives of bulk moduli (B') from the B-M EOS for all compounds and elements under study are shown. It was confirmed that the mechanical stability criteria [107] were met for all phases. The elastic constants were in good agreement with the

experimental data [49, 114] for the pure elements and with previous theoretical studies [23, 115] for the intermetallics. Compared with the literature, it was observed that the values of C_{ij} obtained in the present study were in general smaller (except for the C_{12} and C_{13} of αNb_5Si_3 and the C_{13} of βNb_5Si_3) with the largest deviations observed for the $NbSi_2$ and Nb_3Si phases. This is attributed to the use of different pseudopotentials. The calculated bulk moduli from elastic constants were in very good agreement with the available data in the literature. Furthermore, it can be seen that the values of the bulk moduli obtained from the VRH approximation agreed well with those obtained by the BM fitting, with the maximum deviation between them being ~7% (for the αNb_5Si_3 and $NbSi_2$).

Table 4.1

Lattice parameters (Å) of elemental and intermetallic phases in the present study.

		a	b	c
Nb	this work	3.309	3.309	3.309
	Experimental [49]	3.311	3.311	3.311
Si	this work	5.46	5.46	5.46
	Experimental [116]	5.431	5.431	5.431
αNb_5Si_3	this work	6.599		11.917
	Experimental [117]	6.57		11.884
βNb_5Si_3	this work	10.068		5.082
	Experimental [117]	10.018		5.077
$NbSi_2$	this work	10.255		5.203
	Experimental [117]	10.224		5.189
Nb_3Si	this work	4.811		6.614
	Experimental [118]	4.791		6.588

The calculated values of the shear (G) and Young's moduli (E) are reported in Table 4.3. The highest shear modulus value was calculated for the $NbSi_2$ phase, and the shear modulus decreased from $NbSi_2$ (138.3 GPa) to αNb_5Si_3 (116.8 GPa) to βNb_5Si_3 (106.4 GPa) to Nb_3Si (71.6 GPa), which means that the most resistant compound of the three to reversible shear deformation is the $NbSi_2$. The same trend was exhibited by their stiffness as the elastic modulus (E) values decreased from 327 GPa for $NbSi_2$ to 291 GPa for αNb_5Si_3 to 268.9 GPa for βNb_5Si_3 to 190 GPa for Nb_3Si.

Table 4.2

Elastic constants (C_{ij}) and bulk modulus (B) for the Nb, Si, Nb_3Si, αNb_5Si_3, βNb_5Si_3 and $NbSi_2$ in GPa.

	VRH approximation								B-M EOS	
	C_{11}	C_{12}	C_{13}	C_{16}	C_{33}	C_{44}	C_{66}	B (GPa)	B (GPa)	B' (GPa)
Nb	241	126.3				26.7		164.5	165.1	4
Experimental [49]	253	133				31				
Experimental [119]								170.3		
Theoretical [23]	244.5	128				31.6		166.8		
Si	151.2	57.4				73.1		88.7	91.2	4
Experimental [114]	166	64				79.6				
Experimental [120]								98		
Theoretical [23]	162.4	59.1				75		93.5		
αNb_5Si_3	362.2	103.9	118.1		312.6	121.9	109.9	190.6	204	6
Theoretical [23]	372.9	96	115.5		338.1	133.5	122.1	193.1		
βNb_5Si_3	367.2	117.2	109.6		306.1	88.1	128.7	189.6	197.9	5
Theoretical [23]	378.3	119.3	107.9		318.6	89.2	132.7	193.1		
$NbSi_2$	341.6	66.3	78		427	130.1		171.6	184.3	7.6
Experimental [115]*	380.2	75.9	88.3		468	145.3				
Experimental [115]**								191.5		
Nb_3Si	252.1	169.4	128.8	6.8		78.5	91.9	183.4	183.3	5
Theoretical [23]	290.2	150.5	117.6	9.8	306	101.5	119.4	184.1		

* at T=120 K, ** at room temperature

In order to investigate whether a material is ductile or brittle, the Cauchy pressures (C_{12} - C_{44} for cubic and C_{13}-C_{44} and C_{12}-C_{66} for tetragonal) and Pugh's [104] index of ductility (the shear modulus over bulk modulus ratio (G/B)) and the Poisson's ratio (v) are the parameters that must be taken into account. The values of the aforementioned properties are given in Table 4.3. According to Pettifor [121], for metallic bonding, a positive value of Cauchy pressure means ductile material and if negative brittle. A compound would be brittle if the G/B ratio is greater than 0.57 and the v less than 0.26. Regarding the above criteria, the αNb_5Si_3 and $NbSi_2$ intermetallics should be brittle (with the latter being the most brittle) and the βNb_5Si_3 and Nb_3Si ductile (with Nb_3Si being the most ductile).

4.3.2 Enthalpies of formation

The vibrational density of states (DOS) for the compounds and elemental phases under study can be seen in Fig. 4.1. All the eigenfrequencies were found to be real, hence it is confirmed that the compounds under investigation are mechanically stable. The vibrational contribution to free energies per atom (F^{phon} (T)) was calculated and is presented for all compounds and elemental phases in Fig. 4.2. It can be seen that the F^{phonon} decreases faster in the following order: $NbSi_2$-αNb_5Si_3-βNb_5Si_3-Nb_3Si. After taking F^{phonon} into account, the phonon contribution to the enthalpy of formation (ΔH_f^{phon} (T)) was evaluated (Fig. 4.3). The ΔH_f^{phon} (T) rises faster in the order Nb_3Si-$NbSi_2$-βNb_5Si_3-αNb_5Si_3. In Fig. 4.4 the enthalpy of formation versus temperature of all the stable intermetallic compounds of the Nb-Si system is shown. At T=0 K the heat of formation (ΔH_f^0) increases from αNb_5Si_3 (-62.231 kJ/mole) to βNb_5Si_3 (-59.338 kJ/mole) to $NbSi_2$ (-50.365 kJ/mole) to Nb_3Si (-37.34 kJ/mole). In Table 4.4 it can be seen that the above values for αNb_5Si_3, Nb_3Si and $NbSi_2$ are in good agreement with the available experimental and calculated data. As the temperature rises the ΔH_f (T) increases more steeply for the 5-3 silicides, especially for the αNb_5Si_3, which crosses the βNb_5Si_3 above 2000 K. The slopes of the Nb_3Si and $NbSi_2$ are similar and rise slower than those for the 5:3 stoichiometry phases.

Table 4.3

Calculated shear (G) and elastic (E) moduli in GPa, Poisson's ratio (v), Cauchy pressures in GPa, G/B ratio and Debye temperature (Θ_D) from elastic constants and Phonon DOS for Nb, Si, Nb_3Si, αNb_5Si_3, βNb_5Si_3 and $NbSi_2$.

	G	E						Θ_D (K)		
	VRH	VRH	v	C_{12}-C_{44}	C_{13}-C_{44}	C_{12}-C_{66}	G/B	Phonon DOS	Elastic constants	Literature
Nb	36.5	101.9	0.396	99.6			0.228	277	268	
Experimental [119]	37.5	104.9	0.397							275
Experimental [115]										267
Theoretical [23]	36.6									266
Si	61.2	149.2	0.216	-17.4			0.701	647	628	
Experimental [122]	64.1	155.8	0.215							645
Experimental [115]										646
Theoretical [23]	58.2									608
αNb_5Si_3	116.8	291	0.246		-3.8	-6	0.613	512	532	
Theoretical [23]	127.9									555
βNb_5Si_3	106.4	269	0.264		21.5	-11.5	0.561	489	508	
Theoretical [23]	109.8									515
$NbSi_2$	138.3	327	0.182		-52.1		0.806	632	664	
Experimental [115]*	153.2	362.8	0.183							688
Nb_3Si	71.6	190.1	0.327		50.3	77.5	0.39	407	401	
Theoretical [23]	96.4									462
Experimental [123]										430

*at room temperature

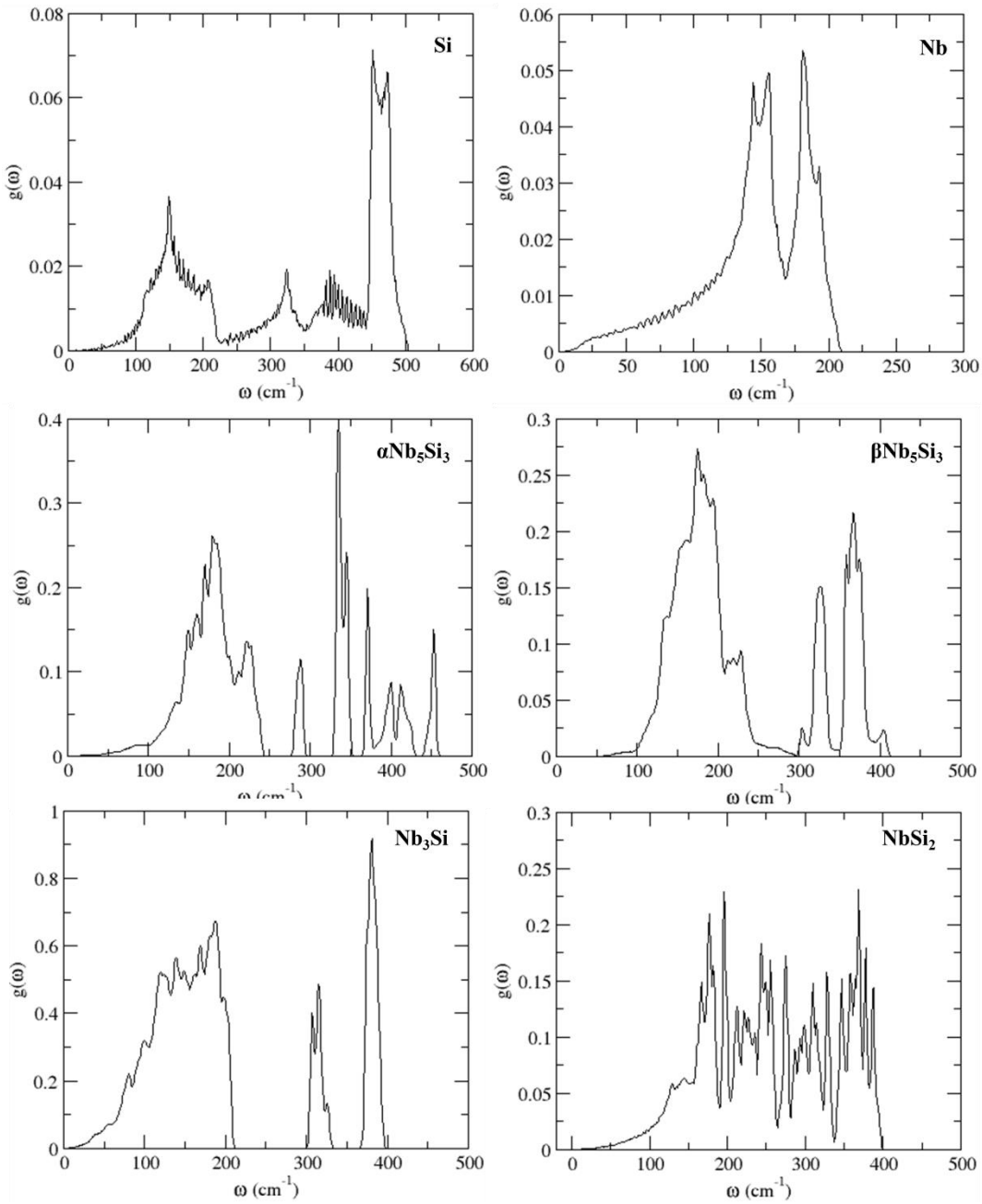

Fig. 4.1. Phonon density of states for the Nb, Si, Nb_3Si, αNb_5Si_3, βNb_5Si_3 and $NbSi_2$.

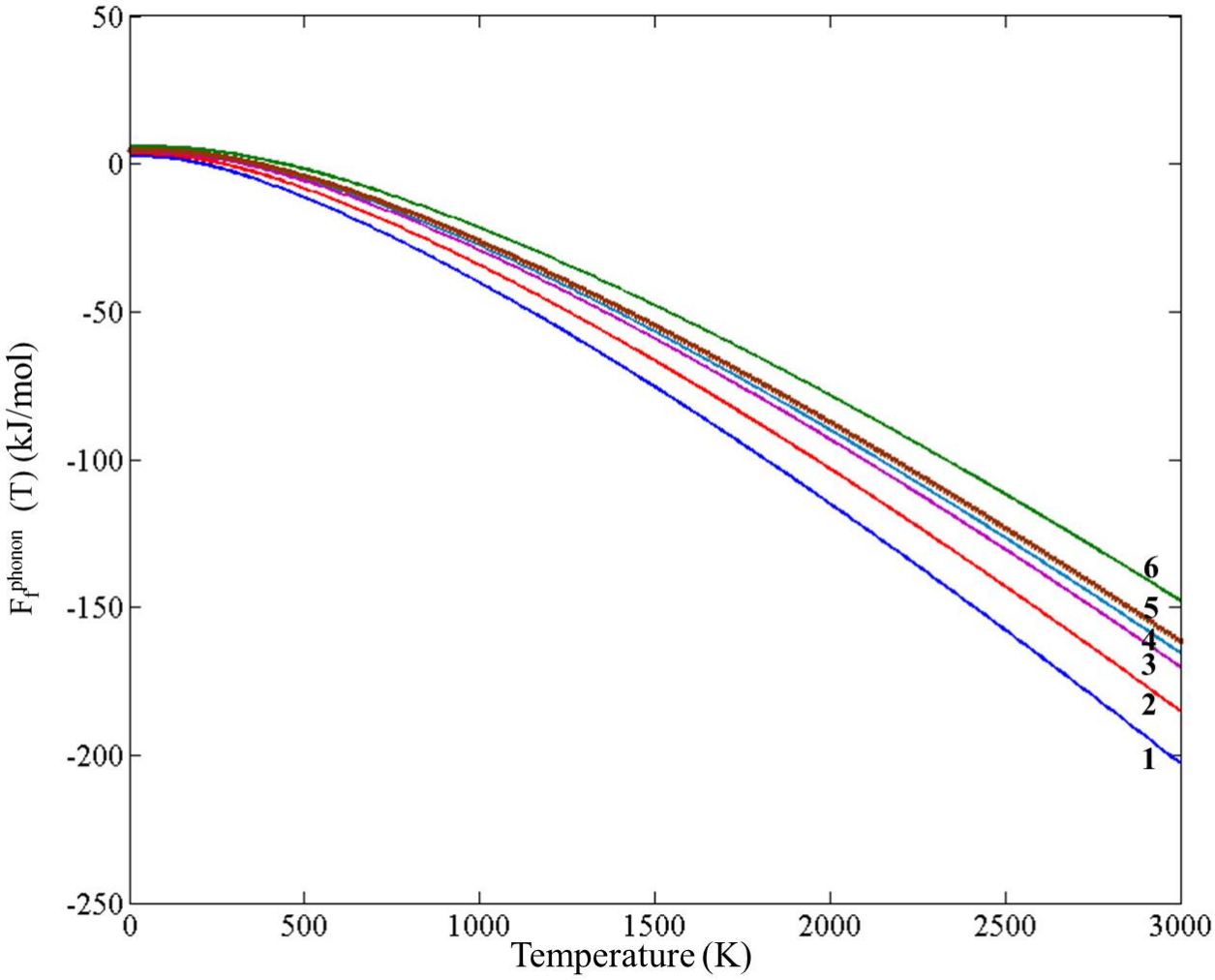

Fig. 4.2. Phonon contribution to free energies calculated for the Nb (1), Nb_3Si (2), βNb_5Si_3 (3), αNb_5Si_3 (4), $NbSi_2$ (5) and Si (6).

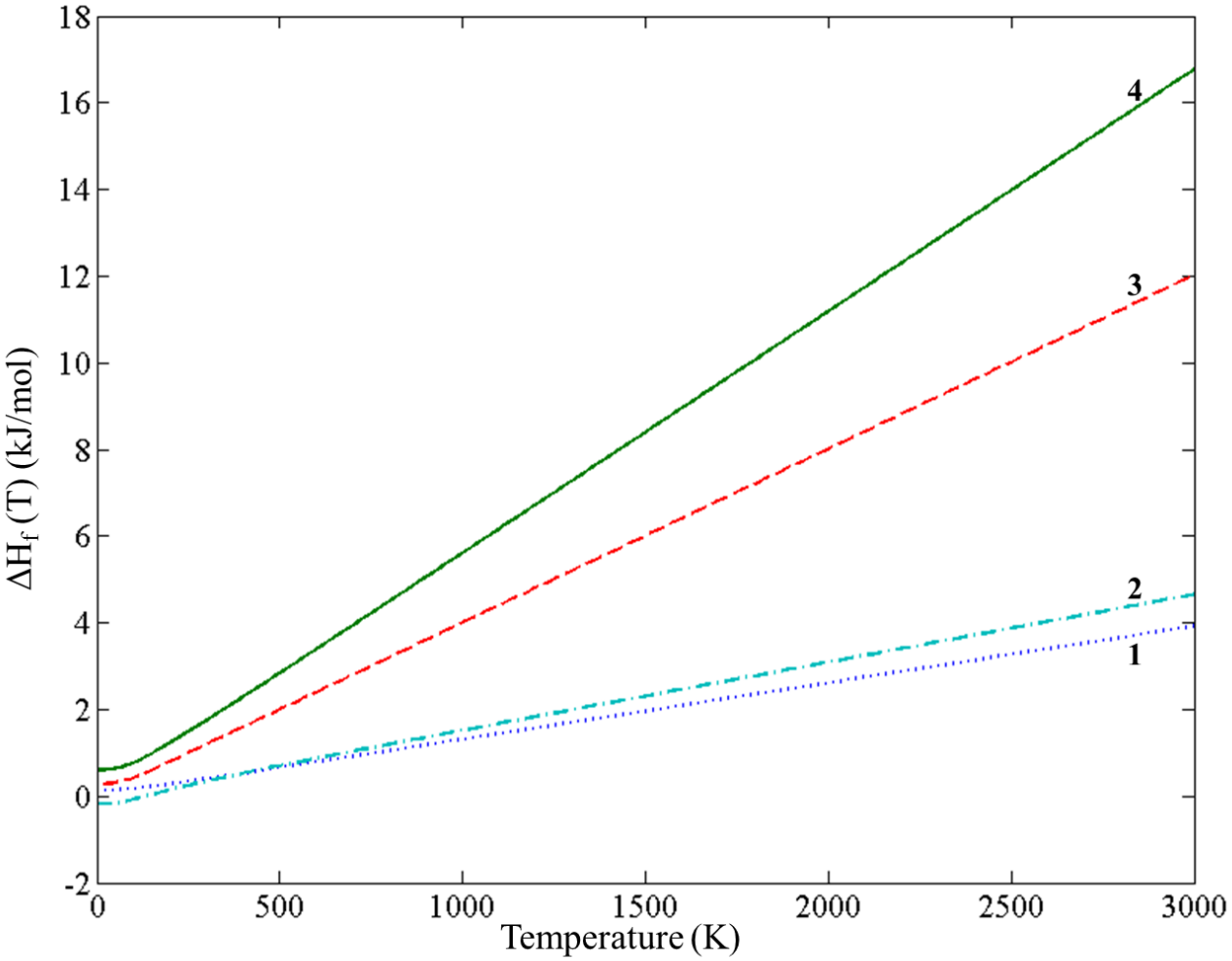

Fig. 4.3. Phonon contribution to enthalpies of formation calculated for the Nb_3Si (1), $NbSi_2$ (2), βNb_5Si_3 (3) and αNb_5Si_3 (4).

Table 4.4

Enthalpies of formation (kJ/mol) for Nb, Si, Nb_3Si, αNb_5Si_3, βNb_5Si_3 and $NbSi_2$.

		Enthalpy of formation	
Intermetallic	Temperature (K)	Current study	Literature
αNb_5Si_3	298	-61.2	-64.6 ±2.4 [124]
	298	-61.2	-47.7 to -64.7* [53]
	298	-61.2	-52 to -65.3* [13]
βNb_5Si_3	298	-58.5	
NbSi2	298	-49.9	-53.7±1.6 [124]
	298	-49.9	-46 to -59.4* [53]
Nb_3Si	298	-37	-29.6 to -35.9* [53]
	0	-37.3	-40.5 [23]

*CALPHAD assessments

4.3.3 Phase transitions

After acquiring the ΔH_f (T) for all the phases, the phase equilibria at finite temperatures can be investigated. In the Nb-Si phase diagram [14] below 2038 K the Nb_3Si transforms via a eutectoid reaction to Nb and αNb_5Si_3. As it was mentioned above, both the Nb_3Si and αNb_5Si_3 heats of formation increase owing to the phonon contribution. However, the heat of formation of the latter phase increases much faster, resulting to the Nb_3Si lying below the tie line between Nb and αNb_5Si_3 at about 1704 K, so that it becomes stable above that temperature, as it can be seen in Fig. 4.5. The difference between the phase diagram [14] and the value of the current study is about 16 % and reduces to 12 % when the lowest reported [15] transformation temperature is considered. These differences are satisfactory considering the use of the quasi harmonic approximation.

Another phase transition takes place for the 5:3 stoichiometry phases. According to the phase diagram [14], the lower and upper transition temperatures where the αNb_5Si_3 transforms to βNb_5Si_3 are 1918 K and 2208 K, respectively. As it can be seen in Fig. 4.4, the αNb_5Si_3 phase is stable until 2085 K where its heat of formation curve crosses that of the βNb_5Si_3, which becomes stable above that temperature. This transition temperature becomes clearer in Fig. 4.5 where the difference between the enthalpies of formation of the competing phases is shown. Comparing the calculated transition temperature with those reported in the literature [14, 16], it is clear that the agreement is very good. Also, comparing with the value from the work of Chen et al. (3000 K) [23], the value from the present work is significantly closer to the literature [14, 16]. For the 1:2 stoichiometry it can be seen in Fig. 4.6 that the $NbSi_2$ phase is stable all the way down to room temperature as it lies below the tie line between αNb_5Si_3 and Si through the whole range of temperatures. This is in agreement with the Nb-Si phase diagram.

4.3.4 Debye temperatures

The resultant phonon DOS was used to calculate the Debye temperature. It should be noted that it is considered more difficult to obtain accurate values in this way than through the elastic constants (see above) because as a low temperature property the Debye temperature is determined by low energy phonons i.e. the acoustic phonons. The lower the temperature the smaller the part of the Brillouin Zone that contributes

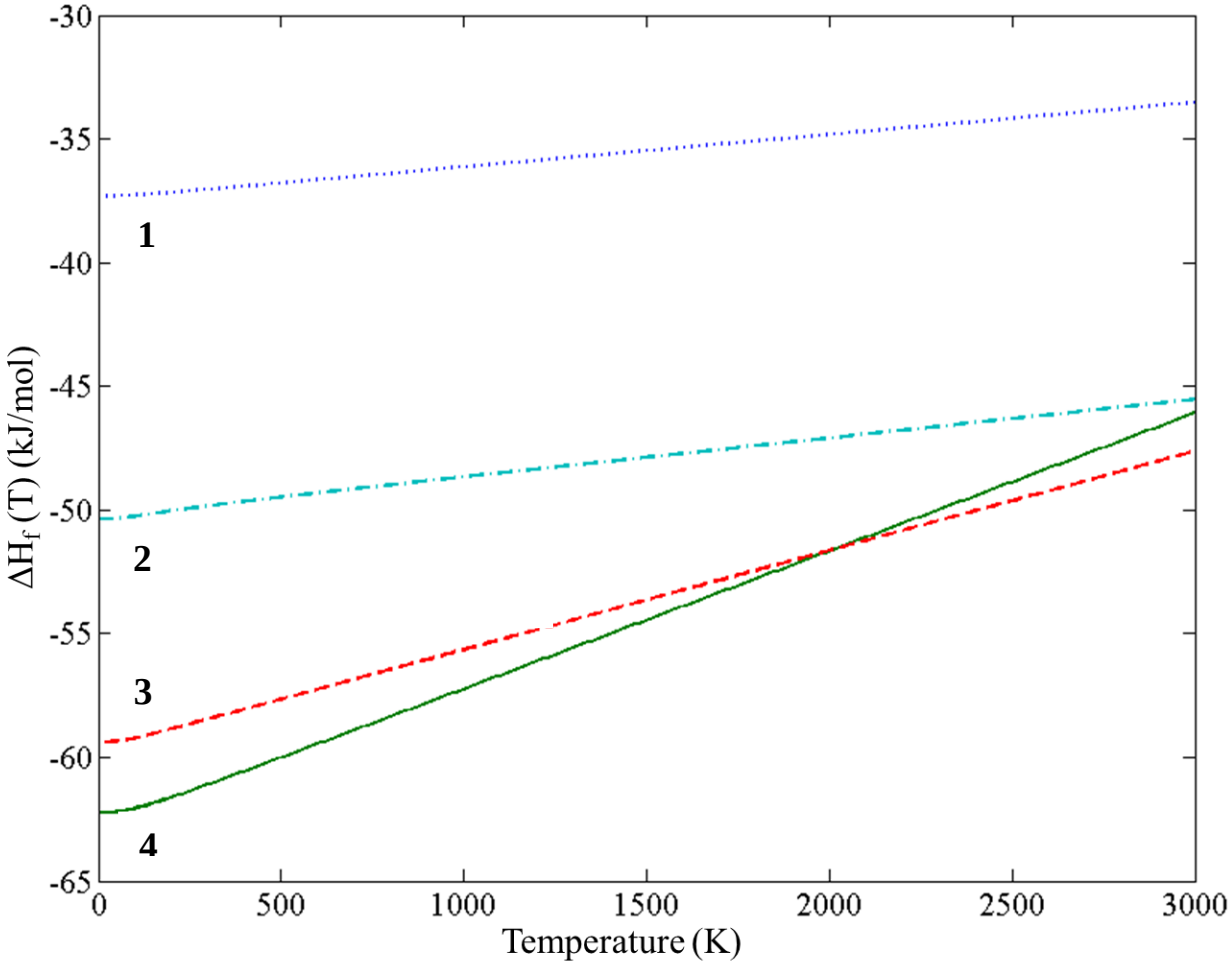

Fig. 4.4. Enthalpies of formation calculated for the Nb_3Si (1), $NbSi_2$ (2), βNb_5Si_3 (3) and αNb_5Si_3 (4).

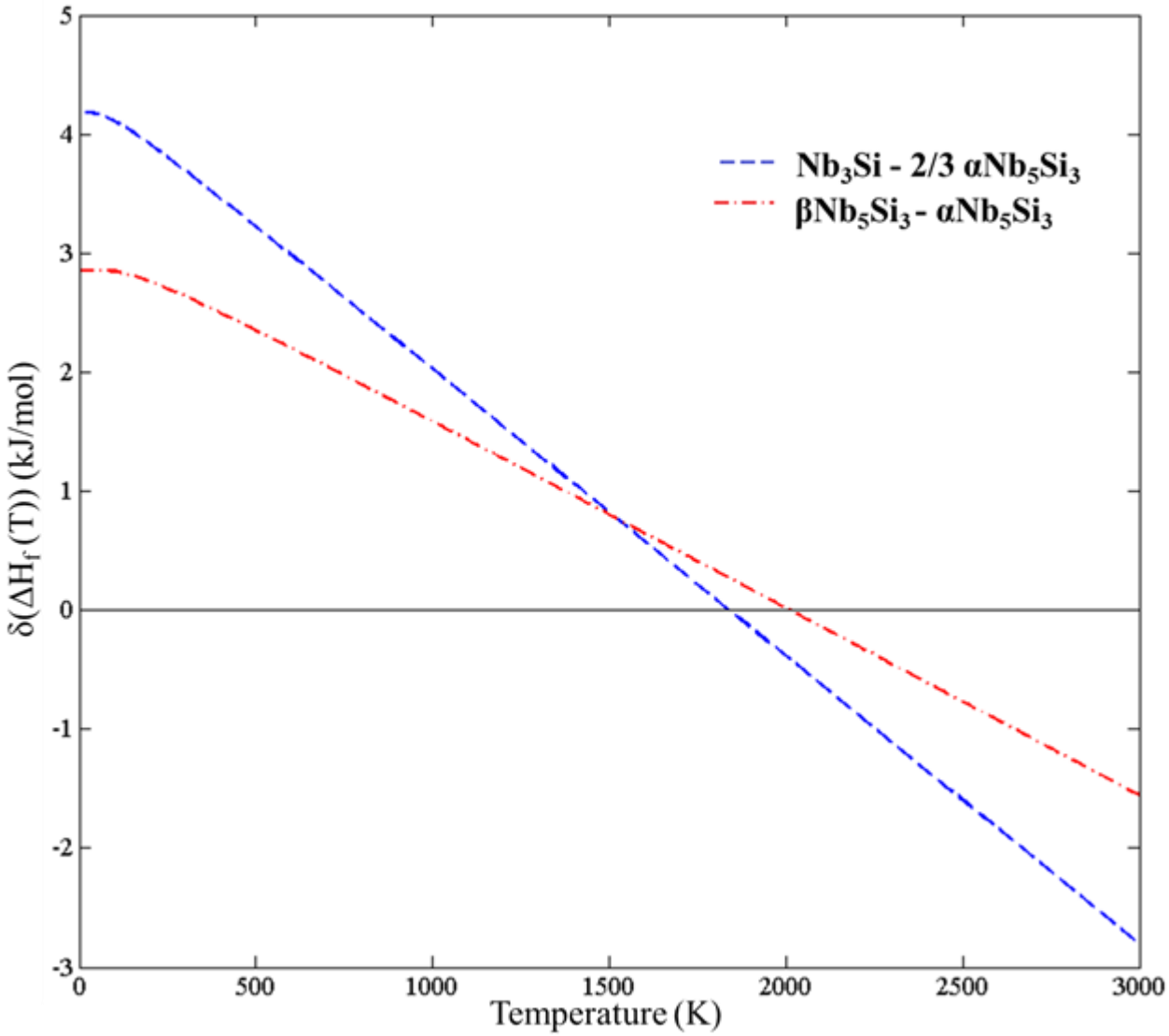

Fig. 4.5. Difference of heats of formation between competing phases αNb_5Si_3 and βNb_5Si_3 and Nb_3Si and Nb and αNb_5Si_3 with respect to the tie line between Nb and αNb_5Si_3 (solid line)

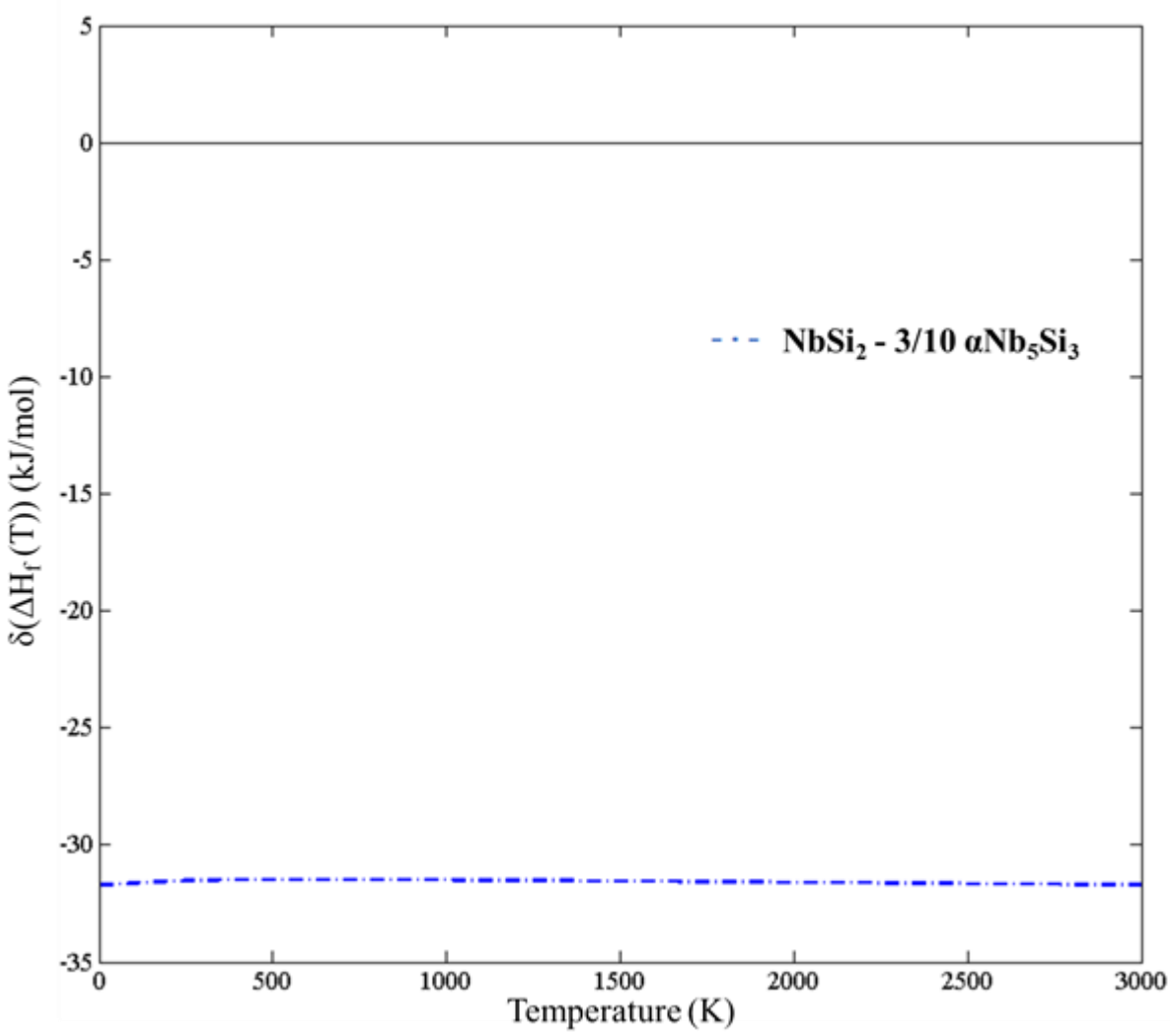

Fig. 4.6. Difference of heats of formation between competing phases of $NbSi_2$ and αNb_5Si_3 with respect to the tie line between αNb_5Si_3 and Si.

to thermodynamics. Despite this fact, the calculated values given in Table 4.2 are in good agreement with [23, 122] and the values calculated in the present study from the elastic constants. For the elemental phases both the results from the phonon DOS and the elastic constants are in good agreement with the literature. Regarding the intermetallics studied, the Debye temperatures calculated from both methods are also in good agreement with the available data in the literature, with the phonon DOS calculated values being lower than those calculated using the elastic constants, with the exception of Nb_3Si.

4.4. Conclusions

First principles calculations were carried out for the Nb_3Si, αNb_5Si_3, βNb_5Si_3 and $NbSi_2$ intermetallic compounds and their constituent elements. Elastic constants, bulk, shear and Young's modulus, Poisson's ratio and Debye temperature were calculated. According to the calculations the high temperature phases (βNb_5Si_3 and Nb_3Si) should be "ductile" with Nb_3Si being the most ductile and the αNb_5Si_3 and $NbSi_2$ are brittle (with the latter being the most brittle). The enthalpies of formation with regard to temperature were calculated for all the intermetallic compounds, which enabled the investigation of the transition temperatures of Nb_3Si to Nb, αNb_5Si_3 and βNb_5Si_3 to αNb_5Si_3, and the stability of the $NbSi_2$ at low and elevated temperatures. There was a good agreement between the results of the present study and the phase diagram. Despite the fact that the quasi harmonic approximation was used in the phonon calculations, this work is another demonstration of the usefulness of the ab initio calculations for phase equilibria studies.

5

Ab initio study of the intermetallics in the Nb-Sn binary system

5.1. Introduction

Advancing our understanding of how alloying with Sn affects the microstructure and properties of Nb-silicide based alloys and improving alloy design require better understanding of the properties of the phases in the Nb-Sn binary system.

The motivation for the present study was to investigate the elastic and thermodynamic properties of the Nb-Sn compounds. The chapter focuses on the calculation of the elastic constants and phonon properties to produce a complete set of data for the aforementioned compounds. This data will be used to support the design of Nb silicide based alloys.

5.2. Computational details

To reduce the basis set of plane wave functions used to describe the real electronic functions norm conserving pseudopotentials [125] were implemented and the valences for the atomic configurations were Sn-5$s^2$5p^2 and Nb-4$d^4$5s^1. An energy cutoff of 500 eV, a Gaussian smearing of 0.7 eV and a Monkhorst–Pack k-point grid separation of 0.03 $Å^{-1}$ were employed. For the phonon calculations the linear response method (see section 3.2.4) was used, while for the calculation of the linear expansion coefficients and elastic properties versus temperature of the cubic Nb and Nb_3Sn phases the quasistatic approximation (see section 3.2.5) was implemented.

5.3. Results and discussion

5.3.1 Elastic properties at 0 K

The calculated lattice constants of Nb, Sn, Nb_3Sn, Nb_6Sn_5 and $NbSn_2$ are given in Table 5.1. The values obtained in the present work are in good agreement with those reported in the literature. The highest deviation (about 2.5 %) is for the c lattice parameter of Sn. Table 5.2 gives the results for the independent elastic constants (C_{ij}), bulk moduli (B) calculated from elastic constants according to the Voigt-Reuss-Hill (VRH) approximation, and the bulk moduli and first pressure derivatives of bulk moduli (B') from the Birch-Murnaghan equation of state for all compounds and elements at 0 K. The mechanical stability criteria [126] were satisfied for all phases. The elastic constants and bulk moduli were in good agreement with the experimental data [49, 51] for the pure elements and with a previous theoretical study [48] for the Nb_3Sn.

Furthermore, the bulk moduli obtained by the B-M EOS fitting were in very good agreement with those calculated using the VRH approximation, with the biggest deviation (~3.5 %) for the Nb_6Sn_5. The Nb_3Sn had the highest bulk modulus (166.5 GPa) that decreased to 141.3 GPa for the Nb_6Sn_5 and to 106.7GPa for the $NbSn_2$. Thus, among the three intermetallics the Nb_3Sn phase is the most resistant to uniform compression.

The calculated values of the shear (G) and Young's (E) moduli are given in Table 5.3. The Nb_3Sn has the highest shear modulus that decreases in the same sequence as the bulk modulus, which means that the Nb_3Sn is the most resistant compound of the three to plastic deformation. The same is the ranking of the intermetallics in terms of their stiffness with the elastic modulus (E) values being 172.7 GPa for the Nb_3Sn, 143.7 GPa for the Nb_6Sn_5 and 132.9 GPa for the $NbSn_2$.

The values of the Cauchy pressure are also listed in Table 5.3. According to [121], for metallic bonding a higher value of Cauchy pressure means more ductile material. Thus, the Nb_3Sn can be regarded as the less brittle compared with the other two intermetallics in the Nb-Sn system.

5.3.2 Enthalpies of formation

The vibrational density of states (DOS) for the compounds and elemental phases under study can be seen in Fig. 5.1. All the eigenfrequencies were found to be real, hence it is validated that the compounds under investigation are mechanically stable. The vibrational contribution to free energy per atom (F^{phon} (T)) was calculated and is presented for the compounds and elemental phases in Fig. 5.2. The F^{phonon} of the intermetallics decreases in the following order: Nb_3Sn – Nb_6Sn_5 –$NbSn_2$ with the first two almost coinciding and the latter decreasing much faster. After taking F^{phonon} into account, the phonon contribution to the enthalpy of formation (ΔH_f^{phon} (T)) was computed (Fig. 5.3 (a)). The ΔH_f^{phon} (T) rises faster in the following order: $NbSn_2$ - Nb_6Sn_5 - Nb_3Sn. In Fig. 5.3 (b) the enthalpy of formation versus temperature of all the stable intermetallic compounds of the Nb-Sn system is shown. In Table 5.4 the enthalpies of formation of the intermetallics of the present study are compared with the available literature [127-129] and it can be seen that there is good agreement between the former and latter data.

5.3.3 Temperature dependence of elastic properties

In order to investigate the temperature dependence of the elastic properties of the cubic phases in the present study (Nb and Nb_3Sn), the quasistatic approximation was implemented. First the temperature dependence of the volume was calculated as it was discussed in section 2.4. The volume versus temperature curves of Nb and Nb_3Sn are shown in Fig. 5.4. The linear thermal expansion coefficients at 293 K of Nb and Nb_3Sn were calculated using this data and were respectively ~7.9 μm/mK and ~6.4 μm/mK and in good agreement with the literature [130, 131]. In Fig. 5.5 the elastic constants versus temperature of the cubic phases are shown. Comparing the results for

Table 5.1
Lattice constants (in Å) of Nb, Sn, Nb_3Sn, Nb_6Sn_5 and $NbSn_2$.

	Nb	Sn	Nb_3Sn	Nb_6Sn_5	$NbSn_2$
Lattice constant(s) (this work)	3.299	a=5.781 c=3.102	5.258	a=5.591 b=9.185 c=16.702	a=9.772 b=5.595 c=18.809
Lattice constant(s) from previous work	3.311 [a]	a=5.832 [b] c=3.182 [b]	5.289 [c]	a=5.656 [d] b=9.199 [d] c=16.843 [d]	a=9.874 [e] b=5.626 [e] c=19.116 [e]

[a] Ref [49], [b] Ref [52], [c] Ref [64], [d] Ref [132] [e] Ref [133]

Table 5.2

Elastic constants (C_{ij}) and bulk modulus (B) in GPa of Nb, Sn, Nb_3Sn, Nb_6Sn_5 and $NbSn_2$.

	VRH approximation									B-M EOS		
	C_{11}	C_{12}	C_{13}	C_{22}	C_{23}	C_{33}	C_{44}	C_{55}	C_{66}	B	B	B'
Nb	244	124.5					27			164.3	163.1	4.004
	253 [a]	133 [a]					31 [a]					
										170.3 [b]		
Sn	74.2	58	22.2			81.2	23.4		9.9	47.8	45.01	3.703
	83.7 [c]	48.7 [c]	28.1 [c]			96.7 [c]	17.5 [c]		7.4 [c]			
	73.5 [d]	23.4 [d]	28 [d]			87 [d]	22 [d]		22.7 [d]			
	73.5 [e]	44.2 [e]	40.7 [e]			103 [e]	38.3 [e]		42.8 [e]			
Nb_3Sn	282.4	110.1					53.8			167.6	167.5	4
										166.5 [f]		
Nb_6Sn5	266.5	83	90.4	228.2	110.6	210.4	65.5	62.9	25	141.3	146.5	4
$NbSn_2$	180.8	77.3	68.9	178.5	60.1	188.3	52.5	37.3	57.4	106.7	107.9	4

[a] Ref. [49], [b] Ref. [134] [c] Ref. [52], [d] Ref. [135], [e] Ref. [136] [f] Ref. [48]

Table 5.3

Calculated shear modulus (G), elastic modulus (E) in GPa, Poisson's ratio (v), Cauchy pressures (C_{12}-C_{44} for cubic, C_{13}-C_{44} and C_{12}-C_{66} for tetragonal and hexagonal and C_{12}-C_{66}, C_{13}-C_{55} and C_{23}-C_{44} for orthorhombic) in GPa, G/B ratio and Debye temperature (Θ_D) from elastic constants for Nb, Sn, Nb_6Sn_5, $NbSn_2$ and Nb_3Sn.

	G		E									Θ_D (K)			
	VRH		VRH		v	C_{12}-C_{44}	C_{13}-C_{44}	C_{12}-C_{66}	C_{13}-C_{55}	G/B	C_{23}-C_{44}	Phonon DOS	Elastic constants		
Nb	37.4	37.5 [a]	104.3	101.9 [a]	0.394	97.5				0.228		277	268	275 [b]	267 [c]
Sn	17.3		46.2		0.339		-1.2	48.1		0.362		181	170	202 [e]	
Nb_3Sn	65	74.9 [d]	172.7	195.3 [d]	0.328	56.3				0.388		291	336	308 [b]	282 [d]
Nb_6Sn_5	54		143.7		0.331			58	27.5	0.382	45.1	201	218		
$NbSn_2$	51.4		132.9		0.292			19.9	31.6	0.482	7.6	239	256		

[a] Ref. [134], [b] Ref. [51], [c] Ref. [115], [d] Ref [48], [e] Ref. [52]

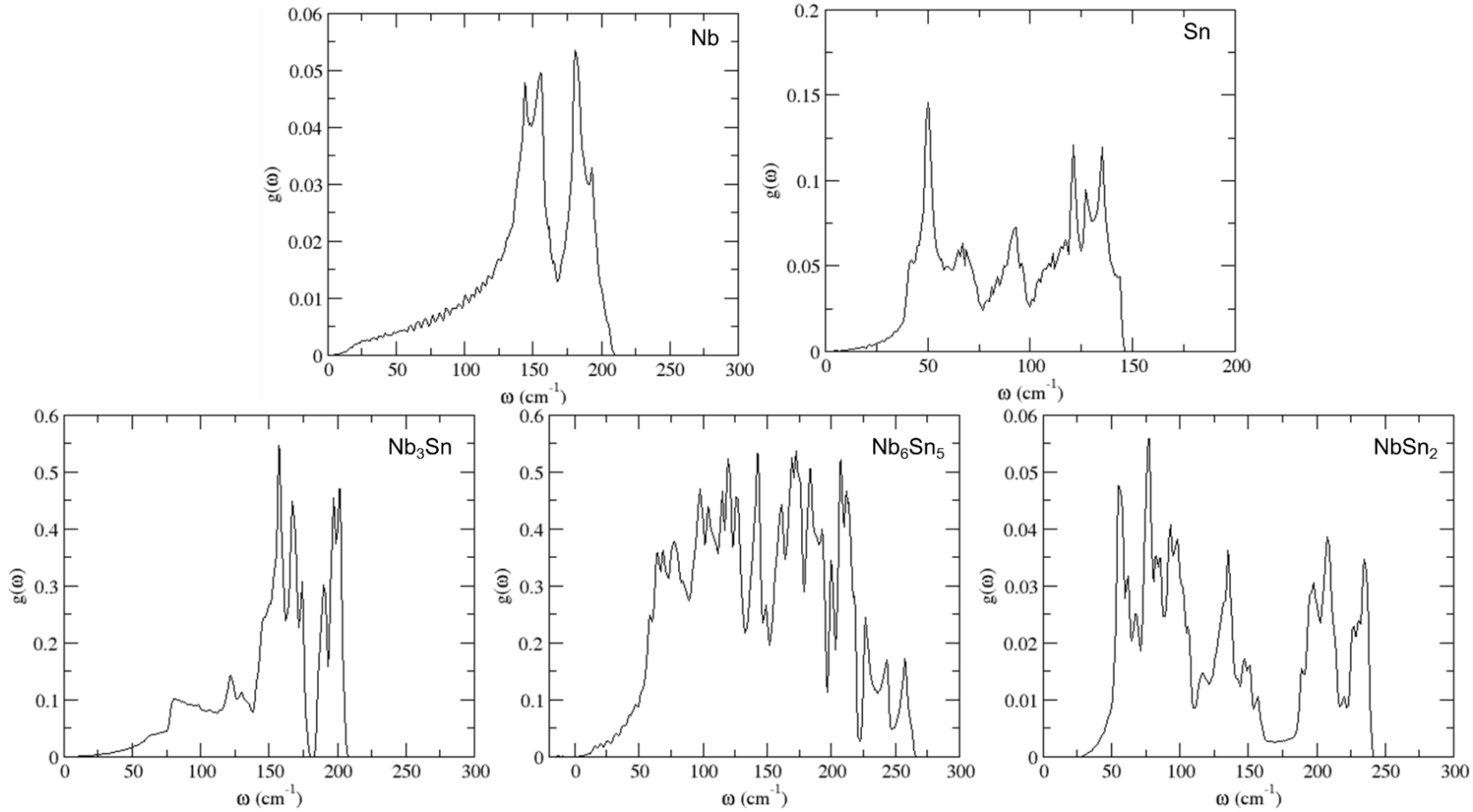

Fig. 5.1. Phonon density of states of Nb, Sn, Nb_3Sn, Nb_6Sn_5 and $NbSn_2$.

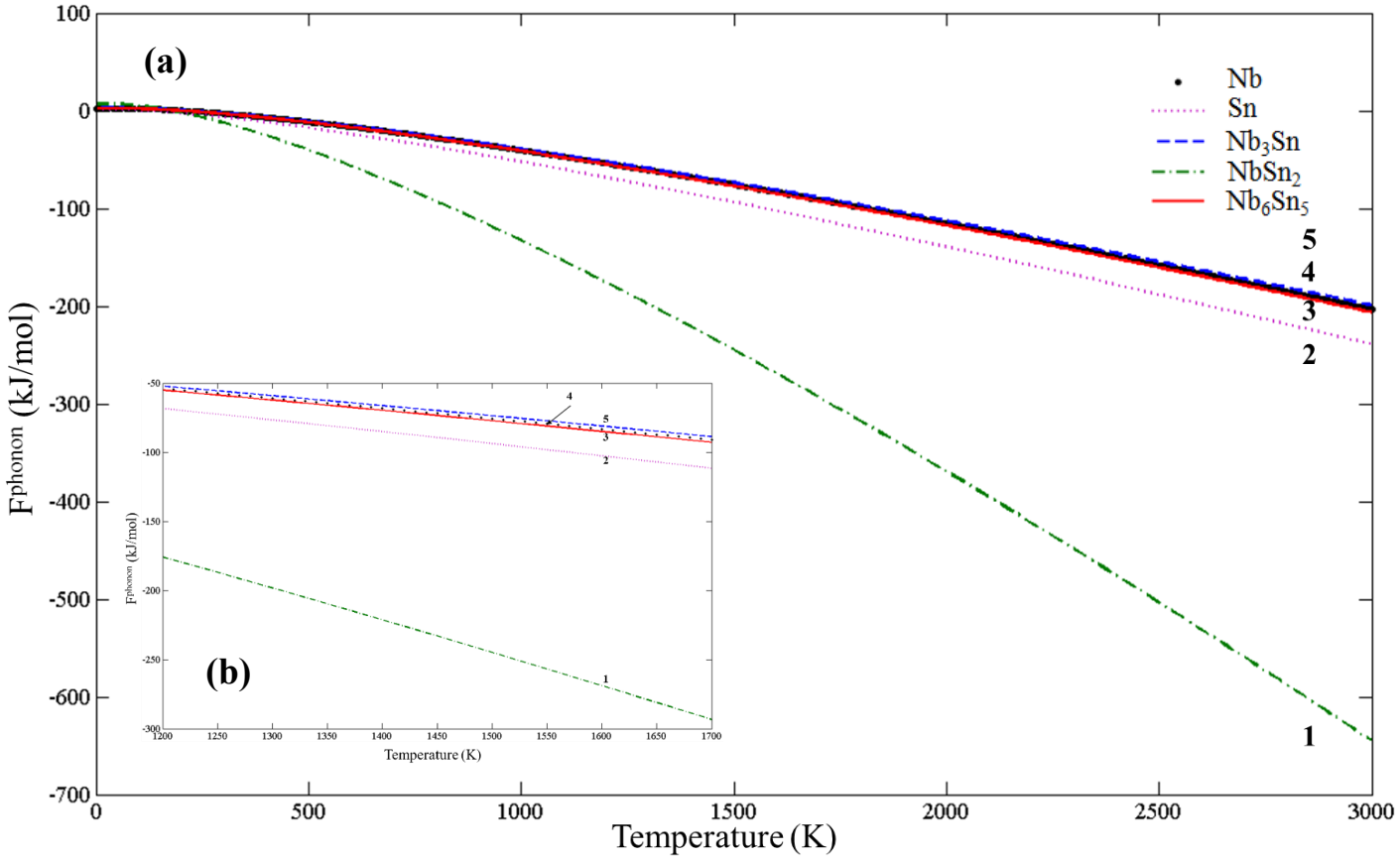

Fig. 5.2. (a) Phonon contribution to free energies calculated by the linear response method for all intermetallics and single elements. The curves of Nb_6Sn_5, Nb, Nb_3Sn (numbered 3, 4 and 5, respectively) are very close to each other. The $NbSn_2$ curve is denoted as 1 and the curve of Sn as 2. (b) The same diagram as (a), for a smaller range of temperatures (1200 to 1700 K) in order to distinguish better between the curves of Nb_6Sn_5, Nb, Nb_3Sn.

Nb with the literature [137] it can be seen that overall the agreement is very good (Table 5.5). The C_{44} constant of Nb becomes negative at 2750 K, which is its melting point. Moreover the aforementioned coefficient decreased slower than the other independent constants, and the C_{11} decreased the fastest. The results for Nb_3Sn were also in good agreement with the experimental data [138]. The curves of the C_{12} and C_{44} constants had similar slopes, with the latter decreasing slightly slower than the former, while the curve of C_{11} showed the steepest descent of all three independent elastic constants. The largest discrepancy was noticed for the C_{44} coefficient with the results of the current study and the literature being ~51 and ~40 GPa, respectively. After obtaining the elastic constants of both phases the bulk, shear and elastic moduli were computed with the VRH approximation (Fig. 5.6). All the moduli decreased with increasing temperature. The bulk and elastic moduli of the Nb and Nb_3Sn the bulk and the elastic moduli exhibited similar gradients and the shear modulus decreased slower. The bulk modulus curve of the Nb_3Sn crosses the Young's modulus curve at 2600 K where the former becomes higher. Furthermore, owing to the above behavior of the bulk and shear moduli of both phases the Poisson's ratios showed increasing slope (Fig. 5.7). In the case of Nb v was ~0.47 close to the melting point, starting from ~0.39 (see Table 5.3) at 0 K. For the Nb_3Sn on the other hand the total increase was smaller, from ~0.328 at 0 K (Table 5.3) to ~0.335 at the compound's melting point. Also it must be noted that the curve increases slower until ~2200 K, and above that temperature it rises significantly.

5.3.4 Debye temperatures

The phonon DOS was used to calculate the Debye temperatures. The values calculated using the phonon DOS (Table 5.3) were in very good agreement with [48, 51] and those calculated from the elastic constants values. For the elemental and intermetallic phases both the results for the Debye temperatures calculated from the Phonon DOS and the elastic constants were in excellent agreement with the available data in the literature (Table 5.3). The Nb_3Sn phase exhibits the highest Debye temperature of all the stable intermetallics in the Nb-Sn system.

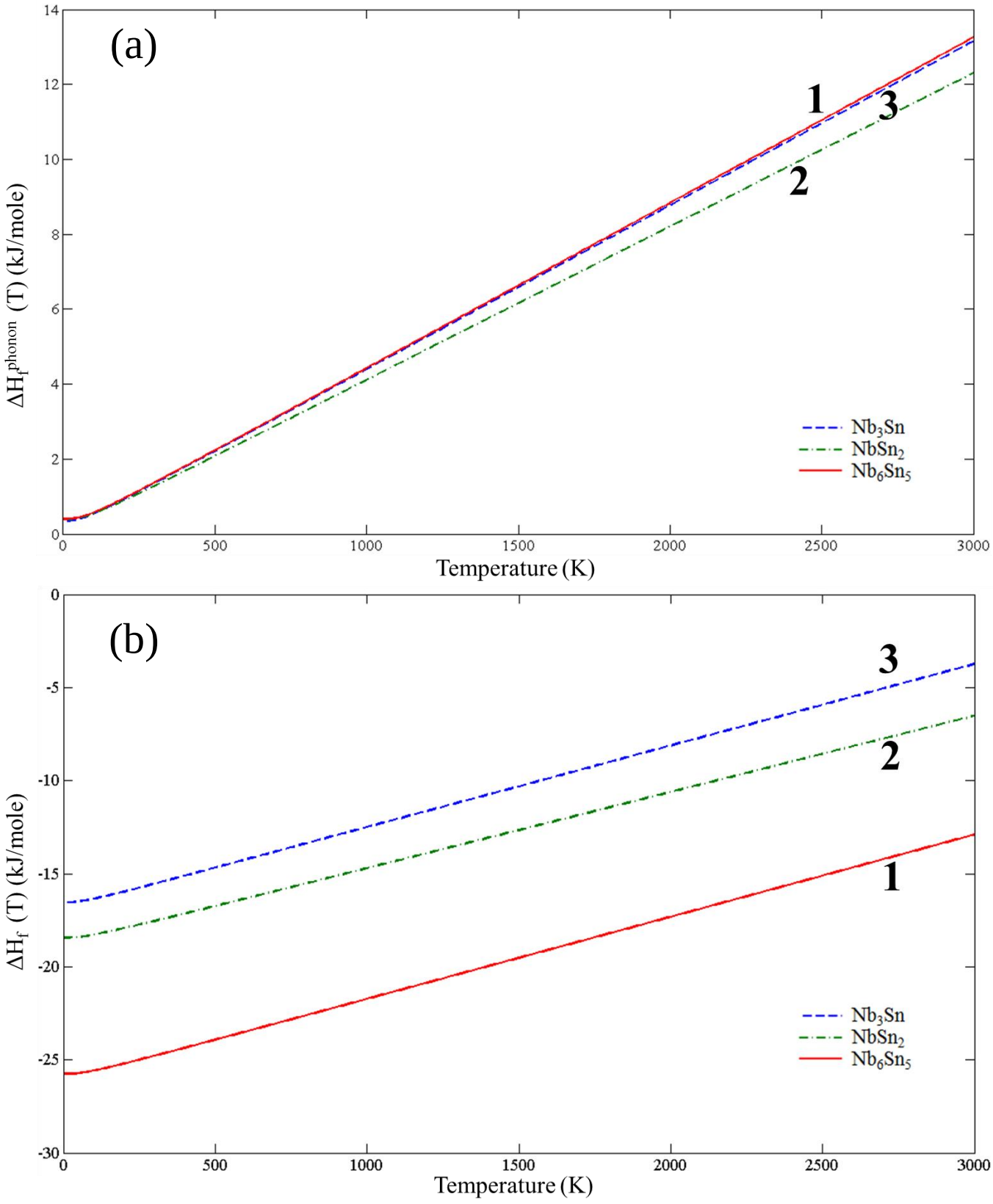

Fig. 5.3. (a) Phonon contributions to the enthalpy of formation and (b) calculated total enthalpy of formation versus temperature (b) for Nb_6Sn_5 (1), $NbSn_2$ (2) and Nb_3Sn (3).

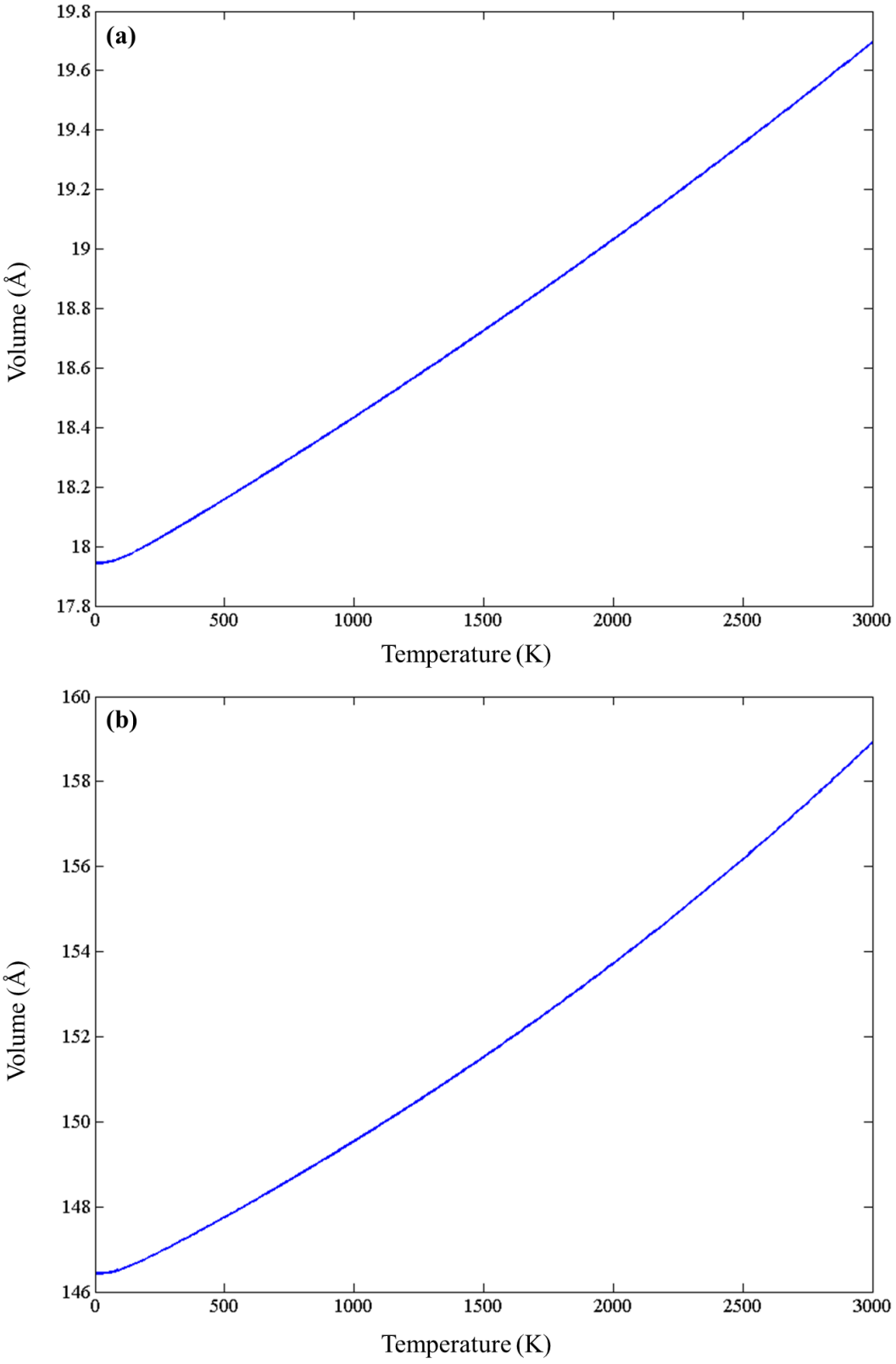

Fig. 5.4. Temperature dependence of the volume of (a) Nb and (b) Nb_3Sn

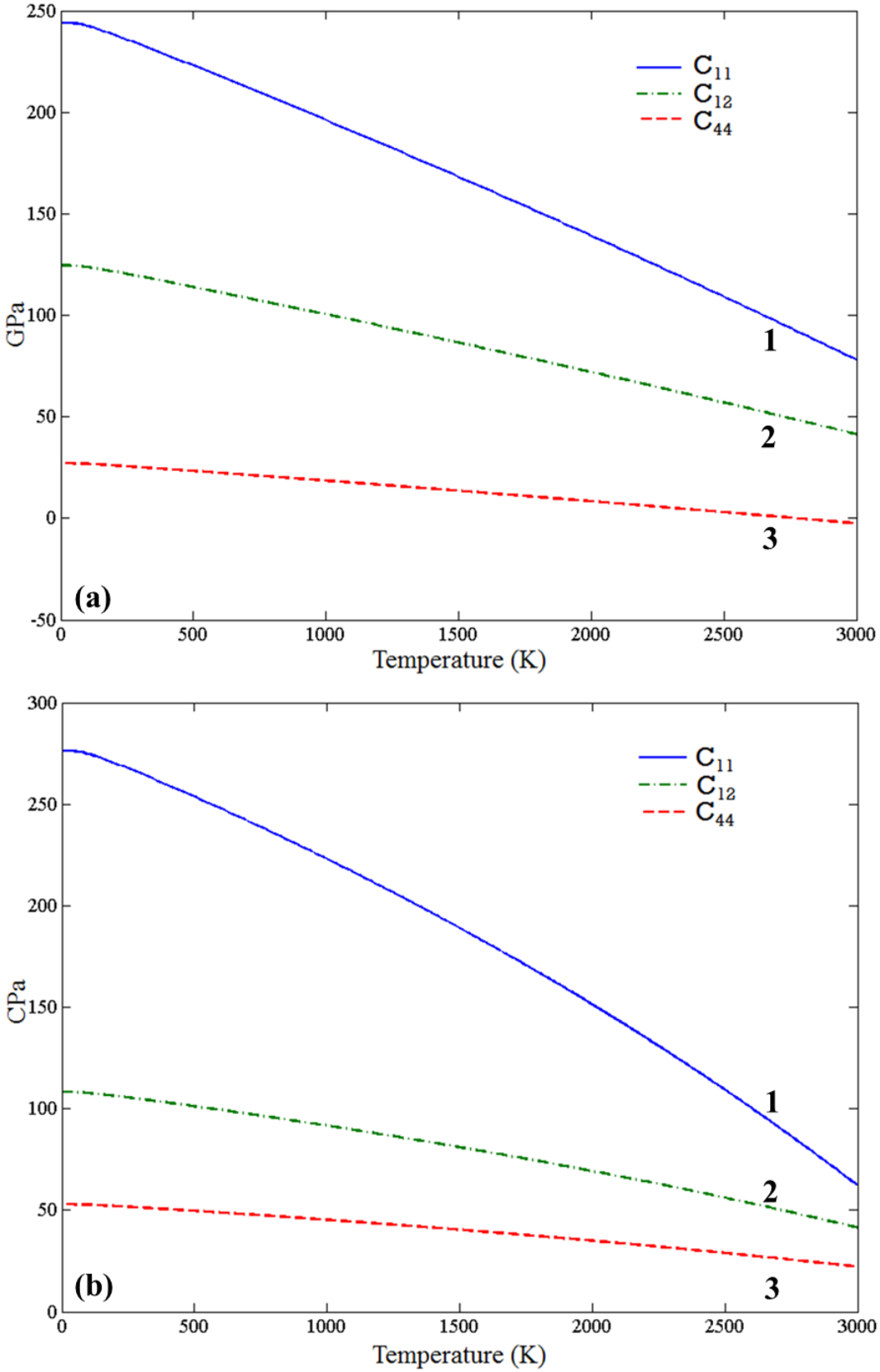

Fig. 5.5. The C_{11} (1), C_{12} (2) and C_{44} (3) elastic constants of (a) Nb and (b) Nb_3Sn versus temperature.

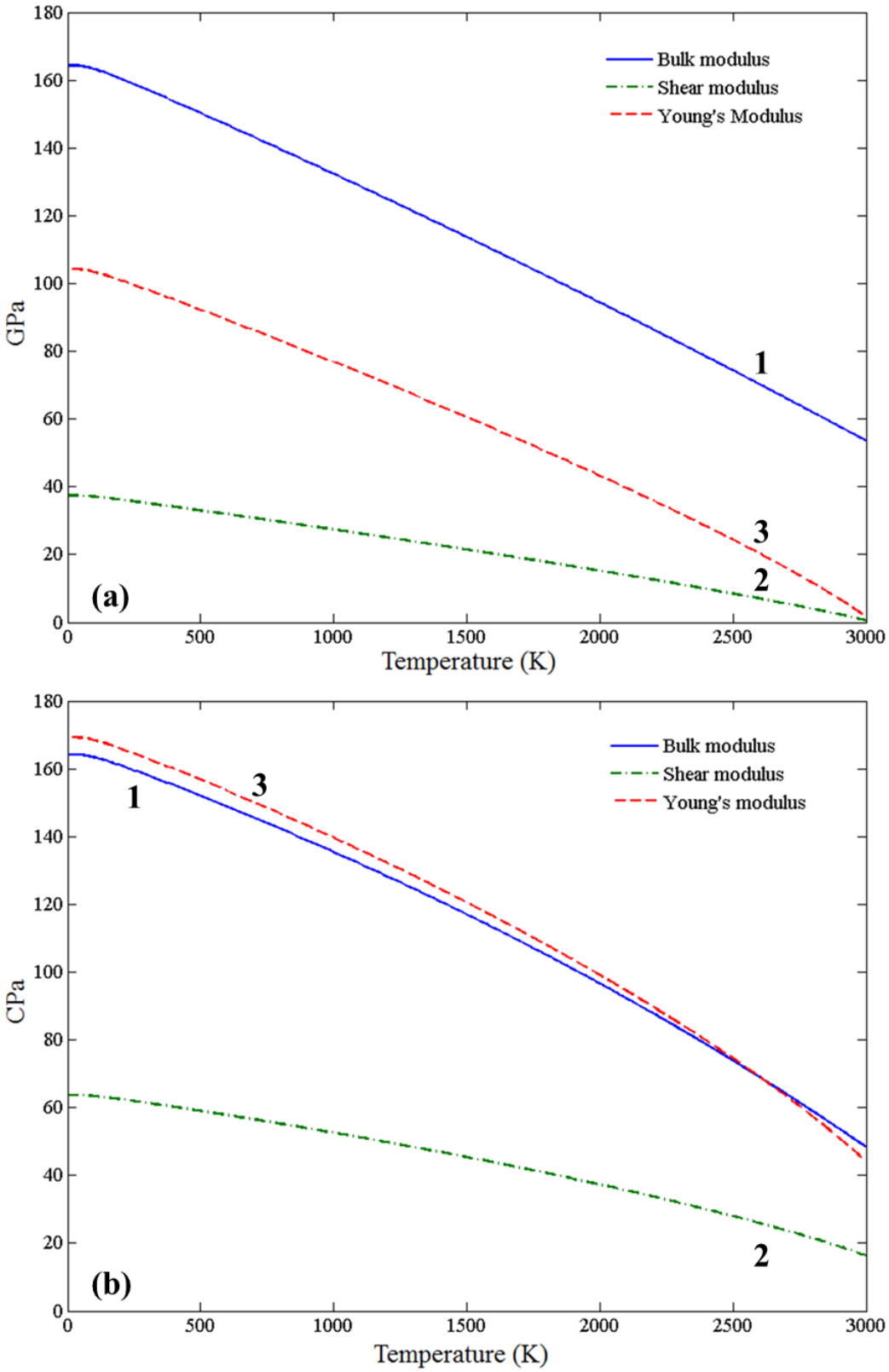

Fig. 5.6. Bulk (1), shear (2) and Young's (3) moduli of (a) Nb and (b) Nb_3Sn versus temperature.

Table 5.4

Calculated enthalpies of formation of Nb_6Sn_5, $NbSn_2$ and Nb_3Sn.

	Enthalpy of formation (kJ/mol)		
Temperature (K)	Nb_3Sn	Nb_6Sn_5	$NbSn_2$
0 (this work)	-16.542	-25.755	-18.434
298 (this work)	-15.628	-24.829	-17.583
298 (previous work)	-16.57 [c]		
298 (previous work)	-16.19 [c]		
298 (previous work)	-16.4 [b]		
298 (previous work)	-16 [a]	-22 [a]	-16 [a]

[a] Ref. [127] , [b] Ref. [128] , [c] Ref. [129]

Table 5.5

Calculated elastic constants and bulk and shear moduli in GPa of Nb and Nb_3Sn at 300 K compared with available experimental results.

	C_{11}	C_{12}	C_{44}	B	G
Nb	233.7	119.3	25.2	157.4	35.2
[137]	235	121	28.2	159	37.5
Nb_3Sn	265.4	104.8	51.3	158.3	61.4
[138] *	253.8	112.4	39.6	159.5	50.1

*(Single crystal)

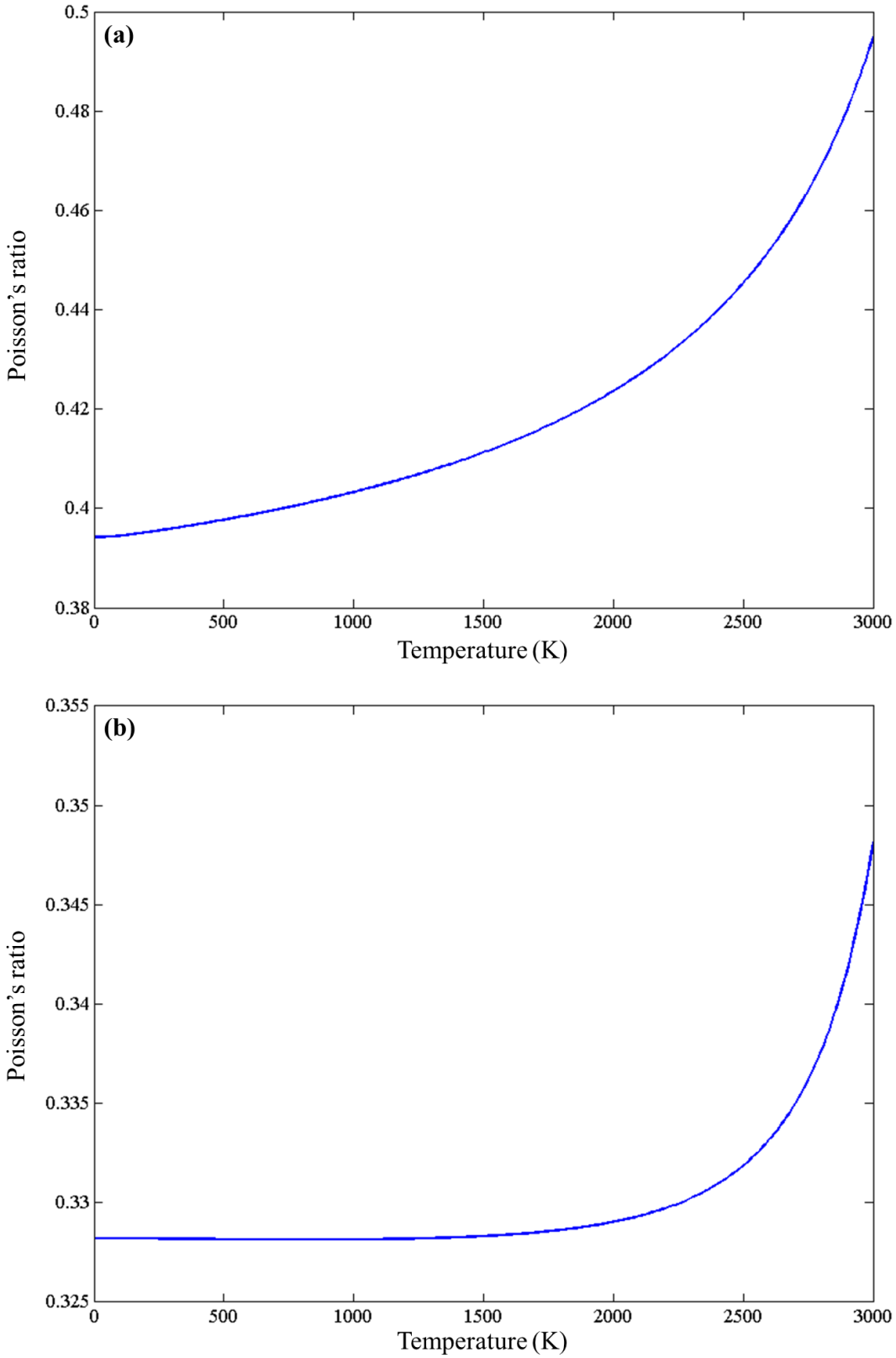

Fig. 5.7. The Poisson's ratios of (a) Nb and (b) Nb_3Sn versus temperature.

5.4. Conclusions

First principles calculations were carried out for the Nb_3Sn, Nb_6Sn_5 and $NbSn_2$ intermetallic compounds and the Nb and Sn elements. The elastic constants, bulk, shear and Young's moduli, Poisson's ratio and Debye temperatures were calculated for all the phases and were in good agreement with the available data in the literature. It is concluded that the Nb_3Sn is the less brittle of the Nb-Sn compounds. For the Nb_6Sn_5 and $NbSn_2$ phases data for elastic properties and Debye temperatures were reported for the first time. Furthermore, the enthalpies of formation versus temperature were calculated for all the intermetallic compounds. Combining the quasiharmonic with the quasistatic approximation the temperature dependence of the bulk, shear and elastic moduli and Poisson's ratios of the Nb and Nb_3Sn were calculated and were in good agreement with the available data in the literature. The thermal expansion coefficient of Nb was in very good agreement with the literature, while the thermal expansion coefficient of Nb_3Sn was reported for the first time.

6

Ab initio study of the intermetallics in the Nb-Al binary system

6.1. Introduction

Due to their very good high temperature properties the transition metal-Aluminium compounds are being subjected to extensive research. In order to understand fully the alloy behaviour and fully investigate the binary and ternary phase diagrams, information on the intermetallic compounds is of great importance. The motivation for the present study was to investigate the elastic and thermodynamic properties of the Nb-Al compounds. This work focuses on the calculation of the elastic constants and phonon properties to produce a complete set of data for the $NbAl_3$, the Nb_2Al and Nb_3Al compounds. This data will be used to support the design of Nb based intermetallics alloys.

6.2. Computational details

To reduce the basis set of plane wave functions used to describe the real electronic functions norm conserving pseudopotentials were implemented and the valences for the atomic configurations were Al-$3s^2$ $3p^1$ and Nb-$4d^4 5s^1$. A Monkhorst–Pack k-point grid separation of 0.03 $Å^{-1}$, an energy cutoff of 700 eV and a Gaussian smearing of 0.7 eV were used. The phonon calculations were conducted using the linear response method (section 3.2.4), while for the calculation of the linear expansion coefficients and elastic properties versus temperature of the Nb_3Al phase the quasistatic approximation (section 3.2.5) was implemented.

6.3. Results and discussion

6.3.1 Elastic properties at 0 K

The calculated lattice parameters of Nb, Al, Si, Nb_3Al, Nb_2Al and $NbAl_3$ are compared with the experimental lattice constants in Table 6.1. It can be seen that the lattice parameters for the elemental phases are slightly underestimated whereas for $NbAl_3$ they are somewhat overestimated but are overall in good agreement with the values from previous work, with the c lattice constant of $NbAl_3$ showing the largest error of about 0.7%. In Table 6.2 the results for the independent elastic constants (C_{ij}), bulk moduli (B) from elastic constants according to the Voigt-Reuss-Hill (VRH)

scheme and bulk moduli and first pressure derivatives of bulk moduli ($B^{'}$) from the Birch-Murnaghan equation of state (B-M EOS) are shown for all phases. It is established that the mechanical stability criteria [107] are met for all phases.

Comparing the value of bulk modulus of $NbAl_3$ with [65] it is clear that they are in good agreement and their consistency is validated by the results of the B-M EOS fitting. Of all the intermetallics the Nb_3Al has the highest bulk modulus of 162.2 GPa, with the value for Nb_2Al being quite close (161.5 GPa). The corresponding value for $NbAl_3$ was found to be 132.5 GPa. It is thus suggested that the most resistant to applied pressure of the Nb-Al intermetallics is the Nb_3Al.

In Table 6.3 the calculated values of shear modulus (G), Young's modulus (E) and Debye temperature (Θ_D) are reported. The shear modulus decreases from $NbAl_3$ (106.5 GPa), to Nb_2Al (72.3 GPa) to Nb_3Al (61.6 GPa), which means that the most resistant compound of the three to reversible deformation upon shear strain is the $NbAl_3$. The same ranking applies for the stiffness of the compounds as the Young's modulus (E) values were 252 GPa for $NbAl_3$, 188.7 GPa for Nb_2Al and 164 GPa for Nb_3Al. It can be seen that the highest to the lowest sequence for the elastic and shear moduli was reverse compared with the corresponding sequence for the Bulk modulus. Ductile or brittle behavior of a material can be deduced by taking into account Cauchy pressure and Pugh's [104] index of ductility of shear modulus over bulk modulus ratio (G/B) and Poisson's ratio (v). The values of the aforementioned properties are listed in Table 6.3. According to [121], for metallic bonding, a positive value of Cauchy pressure means ductile behavior and brittle if negative. The other two conditions point to brittle behavior when the G/B ratio is greater than 0.57 and the v is less than 0.26.

Table 6.1

Lattice constants for Nb, Al, $NbAl_3$, Nb_2Al and Nb_3Al.

	Nb	Al	$NbAl_3$	Nb_2Al	Nb_3Al
Lattice constant(s) (this work) (Å)	3.299	4.022	a=3.803 c=8.602	a=9.945 c=5.119	5.171
Lattice constant(s) from previous work (Å)	3.311[a]	4.098[b]	a=3.801[c] c=8.538	a=9.942 [d] c=5.16	5.187 [e]

[a] Ref [49], [b] Ref [114], [c] Ref [65], [d] Ref [139], [e] Ref [140]

The data in Table 6.3 would thus suggest that the $NbAl_3$ is the most brittle compound. Hence, the sequence from the less to most ductile intermetallic is $NbAl_3$ to Nb_2Al to Nb_3Al.

6.3.2 Enthalpies of formation

The vibrational density of states (DOS) for the elements and compounds under study can be seen in Fig. 6.1. All the eigenfrequencies were found to be real, thus the mechanical stability of the compounds under study is confirmed. The vibrational contribution to free energies per atom (F^{phon} (T)) was calculated and is presented in Fig. 6.2. It can be seen that the F^{phonon} decreases faster in the order $NbAl_3$, Nb_2Al, Nb_3Al. After taking F^{phon} into account, the phonon contribution to the enthalpy of formation (ΔH_f^{phon} (T)) was obtained. It rises faster for $NbAl_3$ while for Nb_3Al it exhibits the smallest slope of the three curves. The curve of Nb_2Al has about half the slope of the corresponding value of $NbAl_3$. By taking into consideration the total internal energies of the constituent elements and the compounds, the enthalpies of formation versus temperature (ΔHf (T)) were obtained and they are shown in Fig. 6.3. At 0 K the heat of formation (ΔH_f^0) increases from $NbAl_3$ (-47.374 kJ/mol) to Nb_2Al (-28.753 kJ/mol) to Nb_3Al (-22.481 kJ/mol). The $NbAl_3$ compound has the lowest ΔH_f in the whole range of temperatures, while Nb_3Al has the highest corresponding value until approximately 2930 K, in which temperature the ΔH_f of Nb_2Al rises higher. The enthalpies of formation agree well with the experimental data as it can be seen in Table 6.4.

Table 6.2

Elastic constants (C_{ij}) and bulk modulus (B) of Nb, Al, $NbAl_3$, Nb_2Al and Nb_3Al in GPa.

	VRH approximation							Birch-Murnaghan EOS	
	C_{11}	C_{12}	C_{13}	C_{33}	C_{44}	C_{66}	B	B	B'
Nb	244	124.5			27		164.3	163.1	4.004
	253 [a]	133 [a]			31 [a]		173 [*]		
Al	107.4	57.6			30.3		74.2	76.47	4.037
	107 [b]	61 [b]			28 [b]		74.3 [*]		
$NbAl_3$	255.6	101.4	51.2	274.8	104	140.5	132.5	136	4
	260.2 [c]	96.7 [c]	46.5 [c]	280.3 [c]	109.9 [c]	142.5 [c]	131 [c]		
Nb_2Al	264.2	109.9	105.8	282	66.1	68.3	161.5	159.9	4
Nb_3Al	272.8	106.9			50.5		162.2	162.1	4

[a] Ref. [49], [b] Ref. [141], [c] Ref. [65], [*] calculated from data in Ref [49] and [141] for Nb and Al, respectively.

Table 6.3

Calculated shear (G) and elastic moduli (E) in GPa, Poisson's ratio (v), Cauchy pressure (C_{12} - C_{44} for cubic, C_{13}-C_{44} and C_{12}-C_{66} for tetragonal), G/B ratio and Debye temperature (Θ_D) from elastic constants for Nb, Al, $NbAl_3$, Nb_2Al and Nb_3Al.

	G	E						Θ_D (K)		
	VRH	VRH	v	C_{12}-C_{44}	C_{13}-C_{44}	C_{12}-C_{66}	G/B	Phonon DOS	Elastic constants	
Nb	37.4	104.3	0.394	97.5			0.228	277	268	275[b]
	37.5[a]	104.9[a]	0.397[a]							
Al	28	74.7	0.334	27.3			0.377	394	420	428[b]
	26.2[a]	70.6[a]	0.345[a]							
$NbAl_3$	106.5	252	0.183		-52.8	-39.1	0.804	744	793	753
Nb_2Al	72.3	188.7	0.305		39.7	41.6	0.448	243	269	
Nb_3Al	61.6	164	0.331	56.4			0.38	353	374	370[b]
	74.2[c]	193.5[c]								

[a] Ref [119], [b] Ref [122], [c] Ref [48], [d] Ref [65]

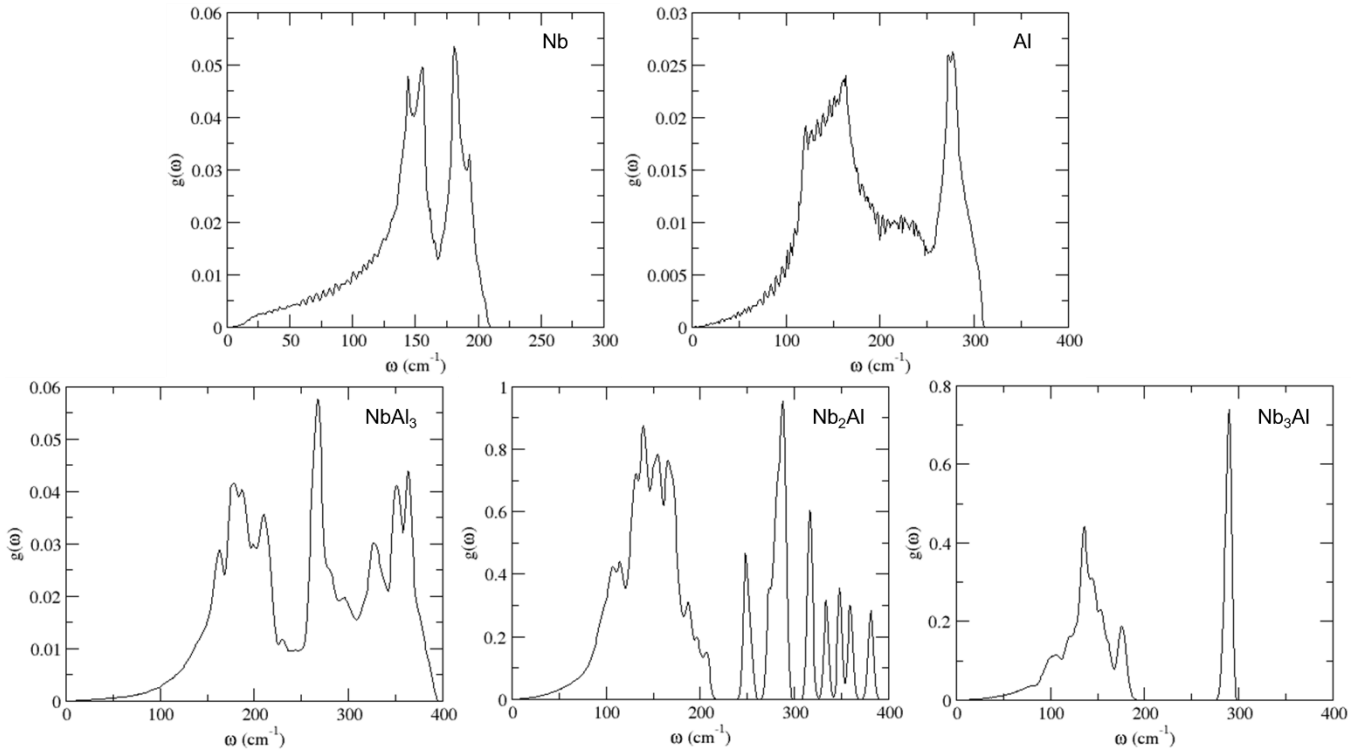

Fig. 6.1. Phonon density of states for Nb, Al, $NbAl_3$, Nb_2Al and Nb_3Al.

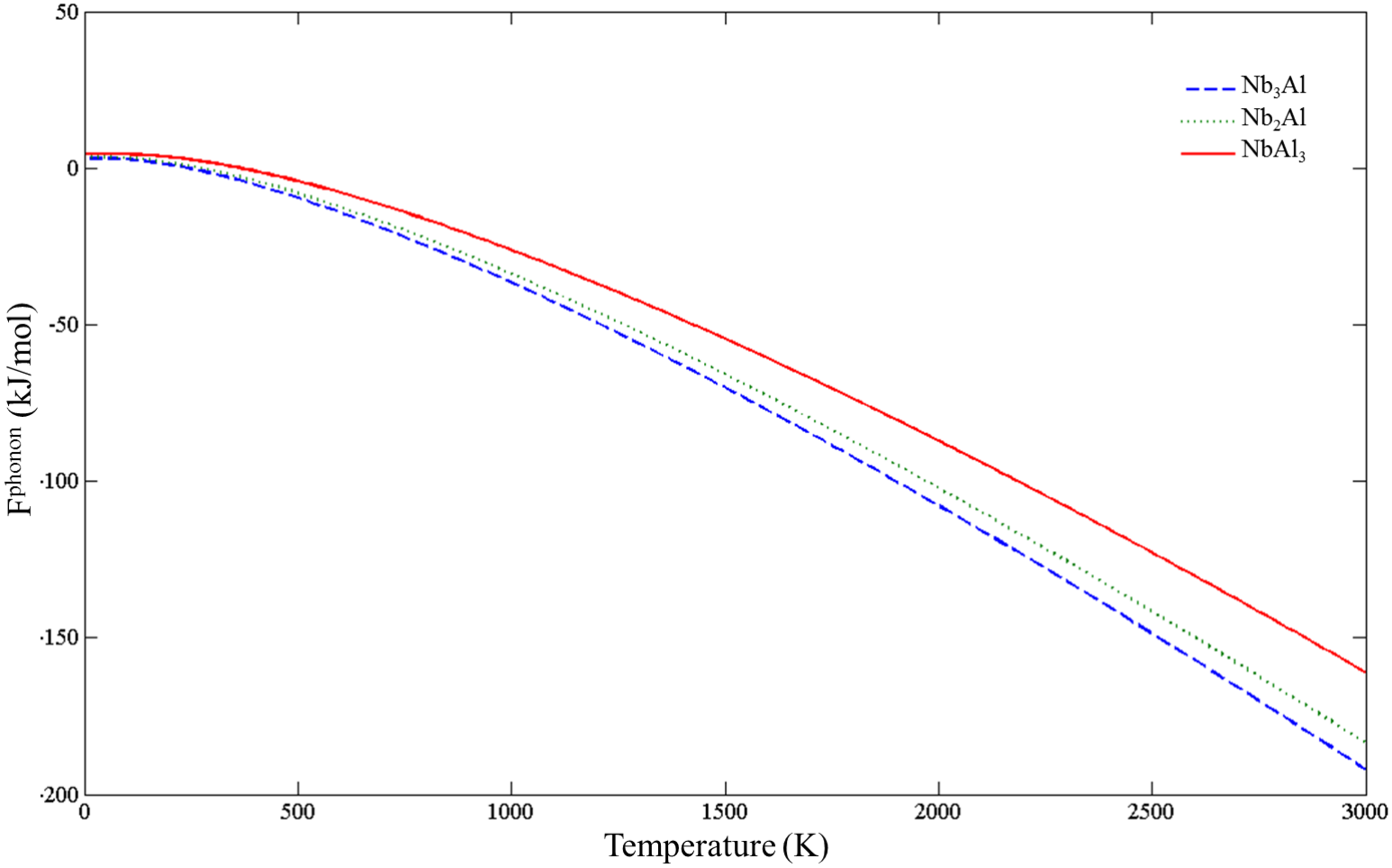

Fig. 6.2. Phonon contribution to free energies calculated by the linear response method for all intermetallics.

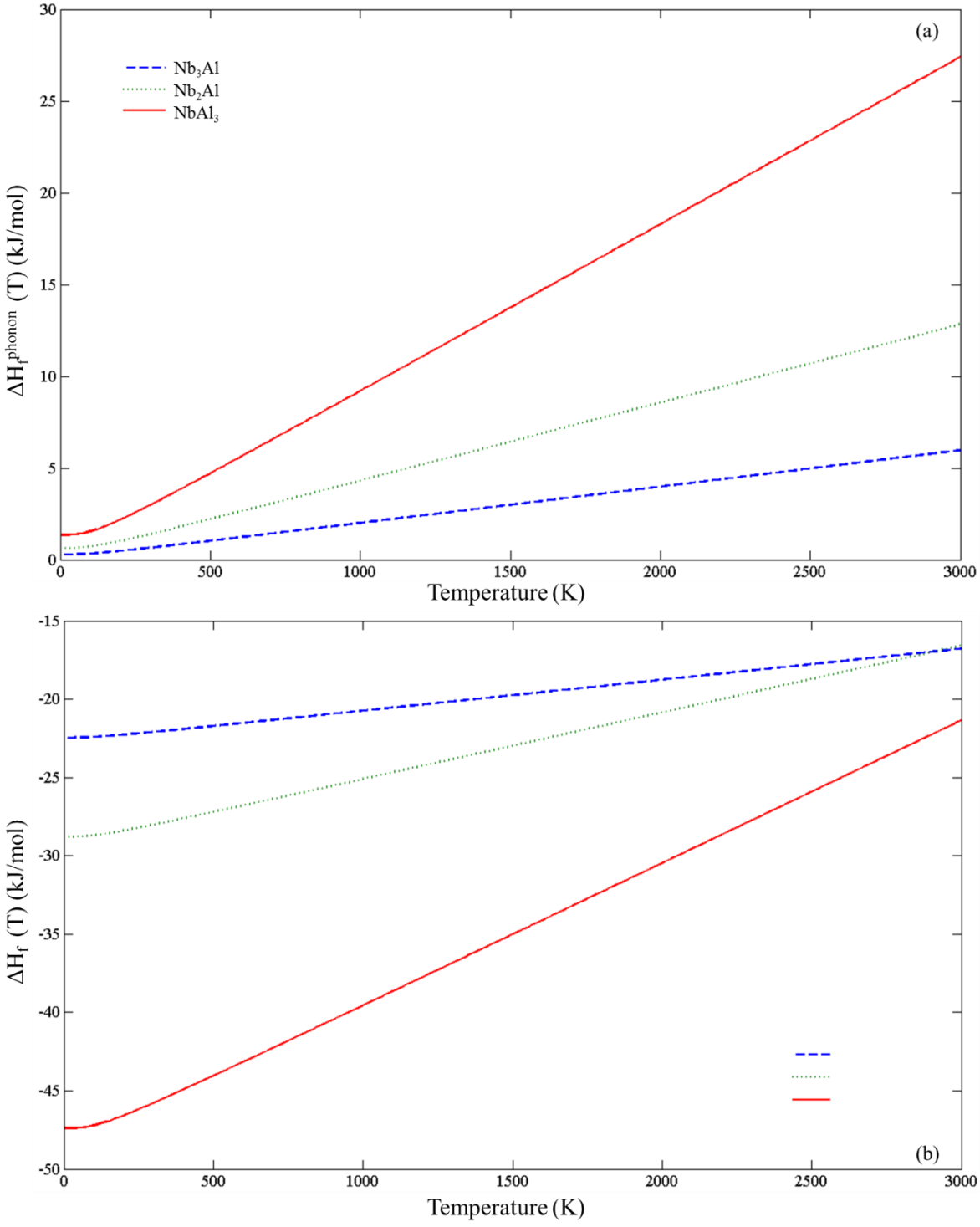

Fig. 6.3. Phonon contributions to the enthalpy of formation (a) and calculated total enthalpy of formation versus temperature (b) for $NbAl_3$, Nb_2Al and Nb_3Al.

Table 6.4

Enthalpy of formation at 298 K of $NbAl_3$, Nb_2Al and Nb_3Al.

Enthalpy of formation at 298 K (kJ/mol)		
Intermetallic	Current study	Experiment
$NbAl_3$	-45.85	-40.62 [a]
Nb_2Al	-28.048	-25.086 [b]
Nb_3Al	-22.114	-19.297 [b]

[a] Ref [62], [b] Ref [63]

6.3.3 Temperature dependence of the elastic properties of Nb_3Al

In order to investigate the temperature dependence of the elastic properties of the Nb_3Al, the quasistatic approximation was implemented. First the temperature dependence of the volume was calculated using the method discussed in section 2.4. The volume versus temperature curves are shown in Fig. 6.4. The linear thermal expansion coefficient at 293 K was calculated using this data and was 6.992 μm/mK. In Fig. 6.5 the elastic constants versus temperature are shown. The curves of the C_{12} and C_{44} constants had similar slopes, while the curve of C_{11} showed the steepest descent of all three independent elastic constants. After obtaining the elastic constants of both phases the bulk, shear and elastic moduli were computed with the VRH approximation (Fig. 6.6). All the moduli decreased with increasing temperature. The elastic modulus exhibited the fastest decrease and the shear modulus the slowest. Furthermore, owing to the above behavior of the bulk and shear moduli of both phases the Poisson's ratios showed increasing slope (Fig. 6.7). Close to the melting point of the Nb_3Al the Poisson's ratio was ~0.364 starting from ~0.333. Unfortunately, to the author's knowledge no experimental data of the above properties exist in the literature to be used for comparison.

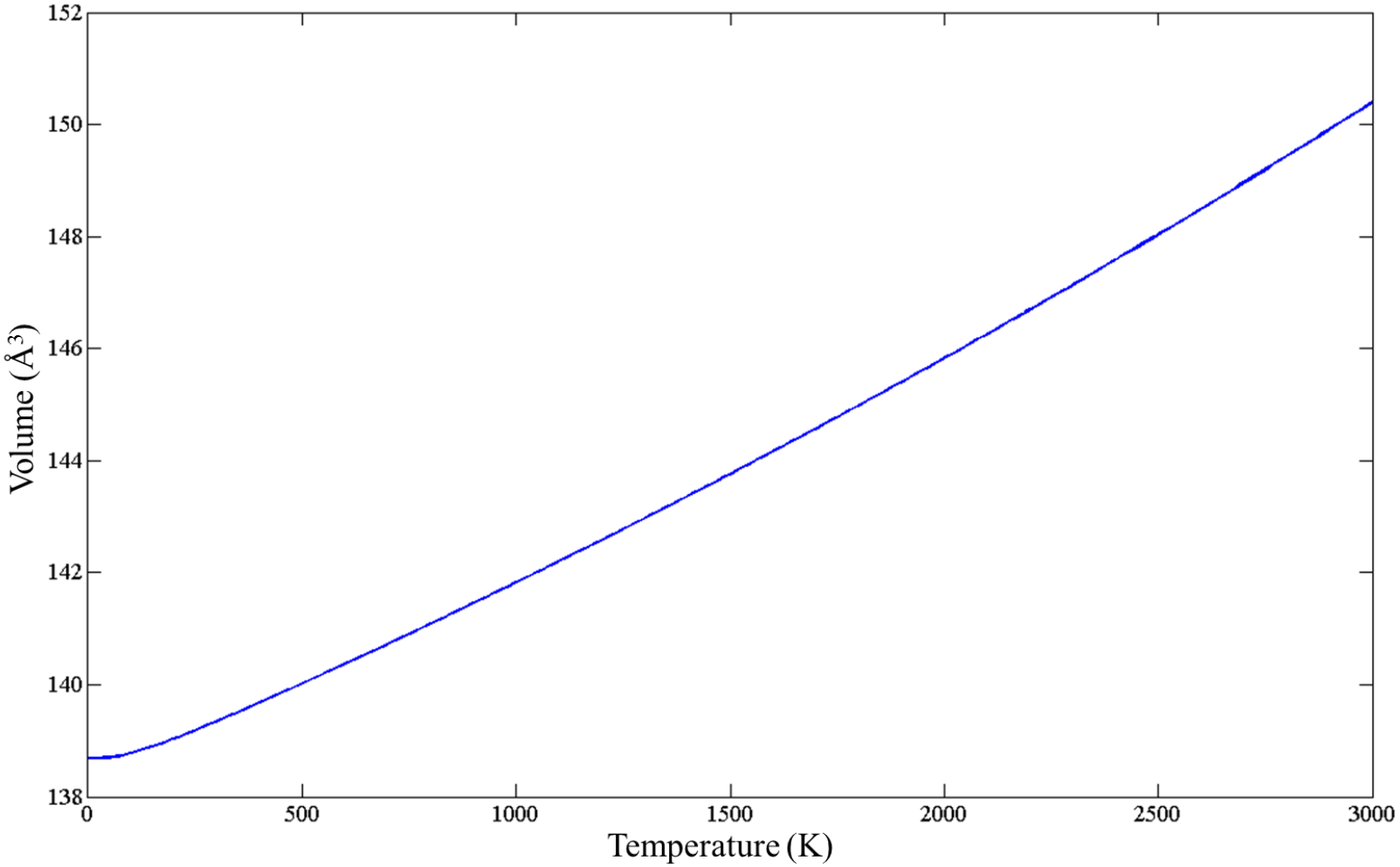

Fig. 6.4. Temperature dependence of the volume of Nb_3Al.

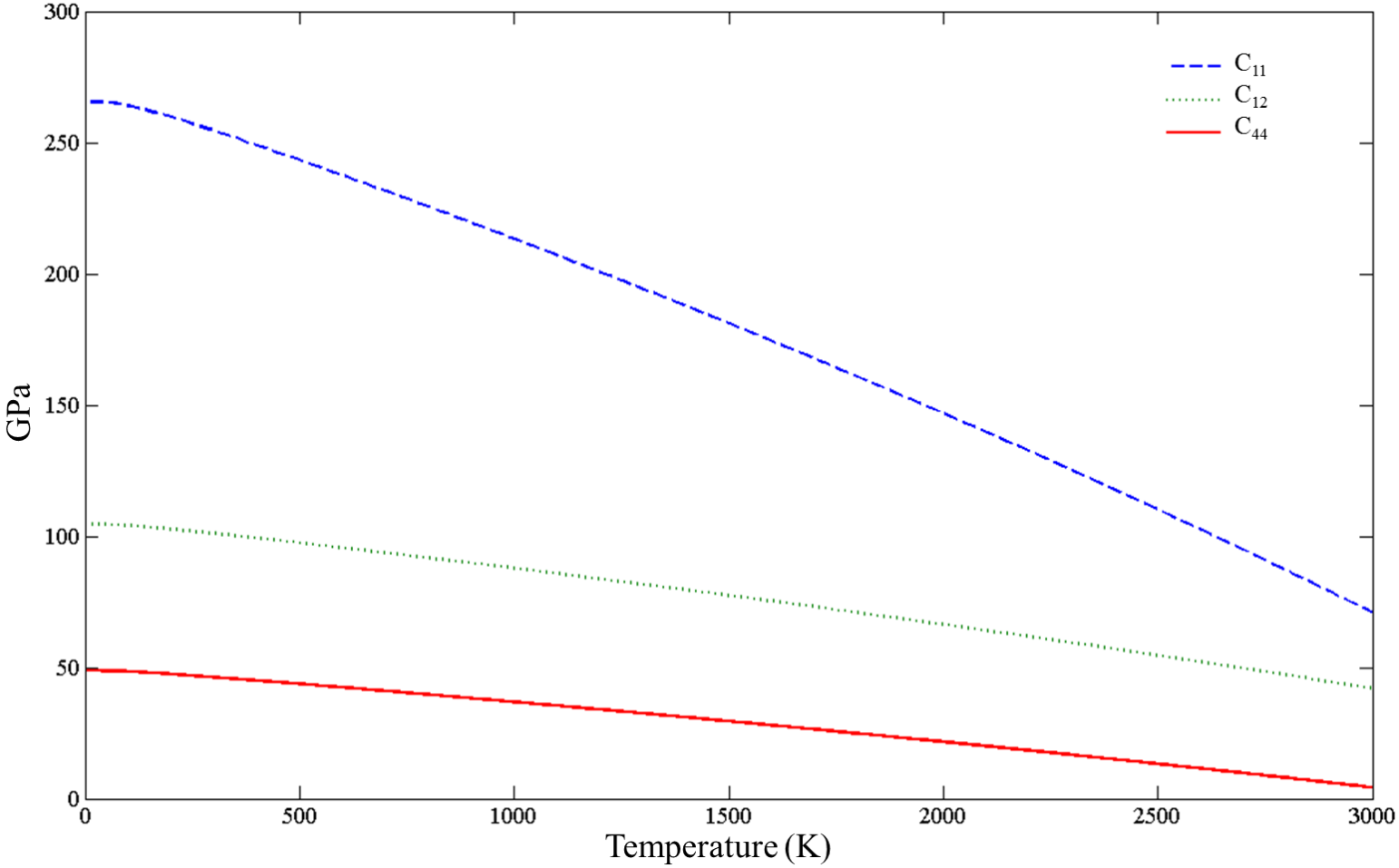

Fig. 6.5. The C_{11}, C_{12} and C_{44} elastic constants of Nb_3Al versus temperature.

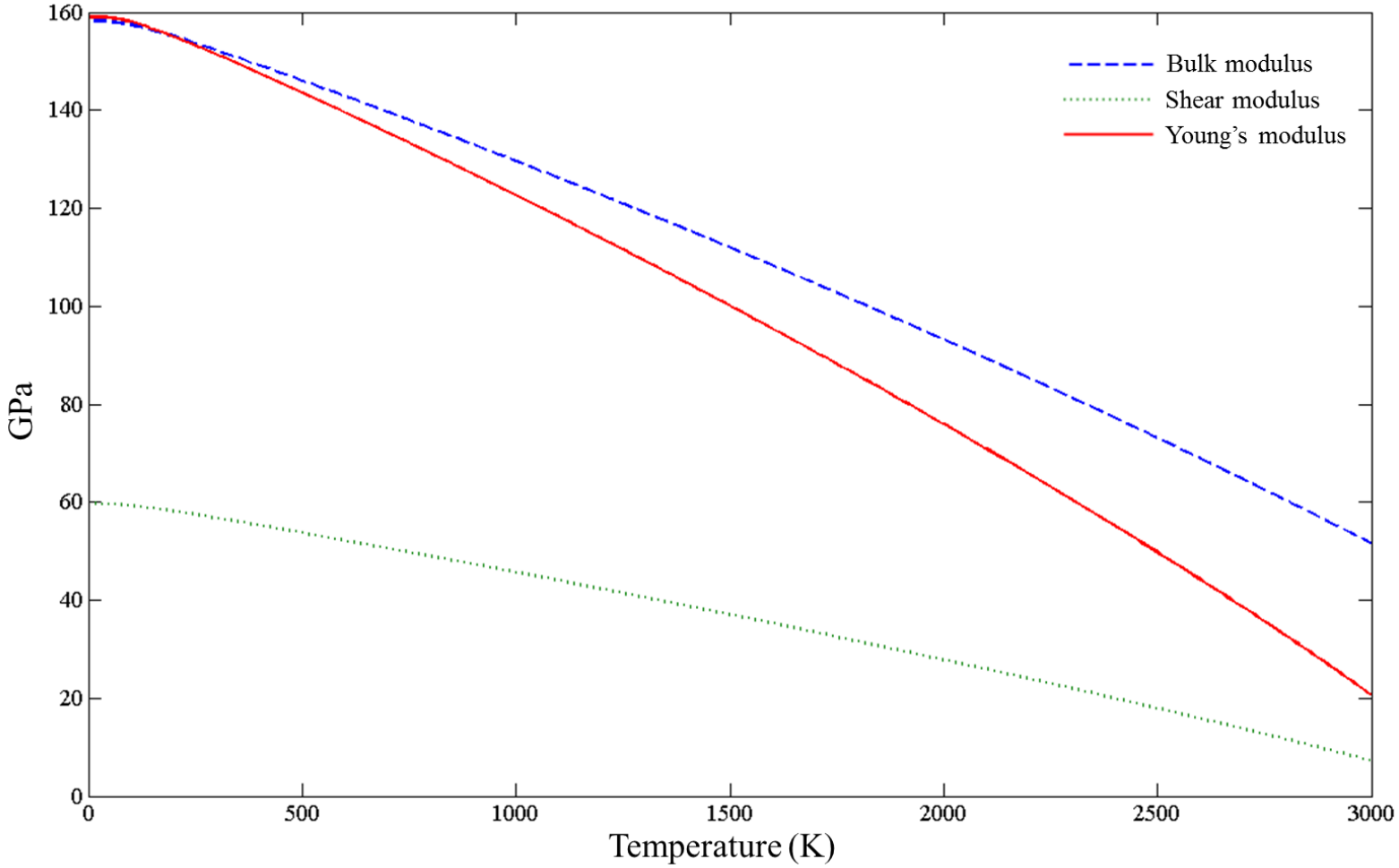

Fig. 6.6. Bulk, shear and Young's moduli of Nb_3Al versus temperature.

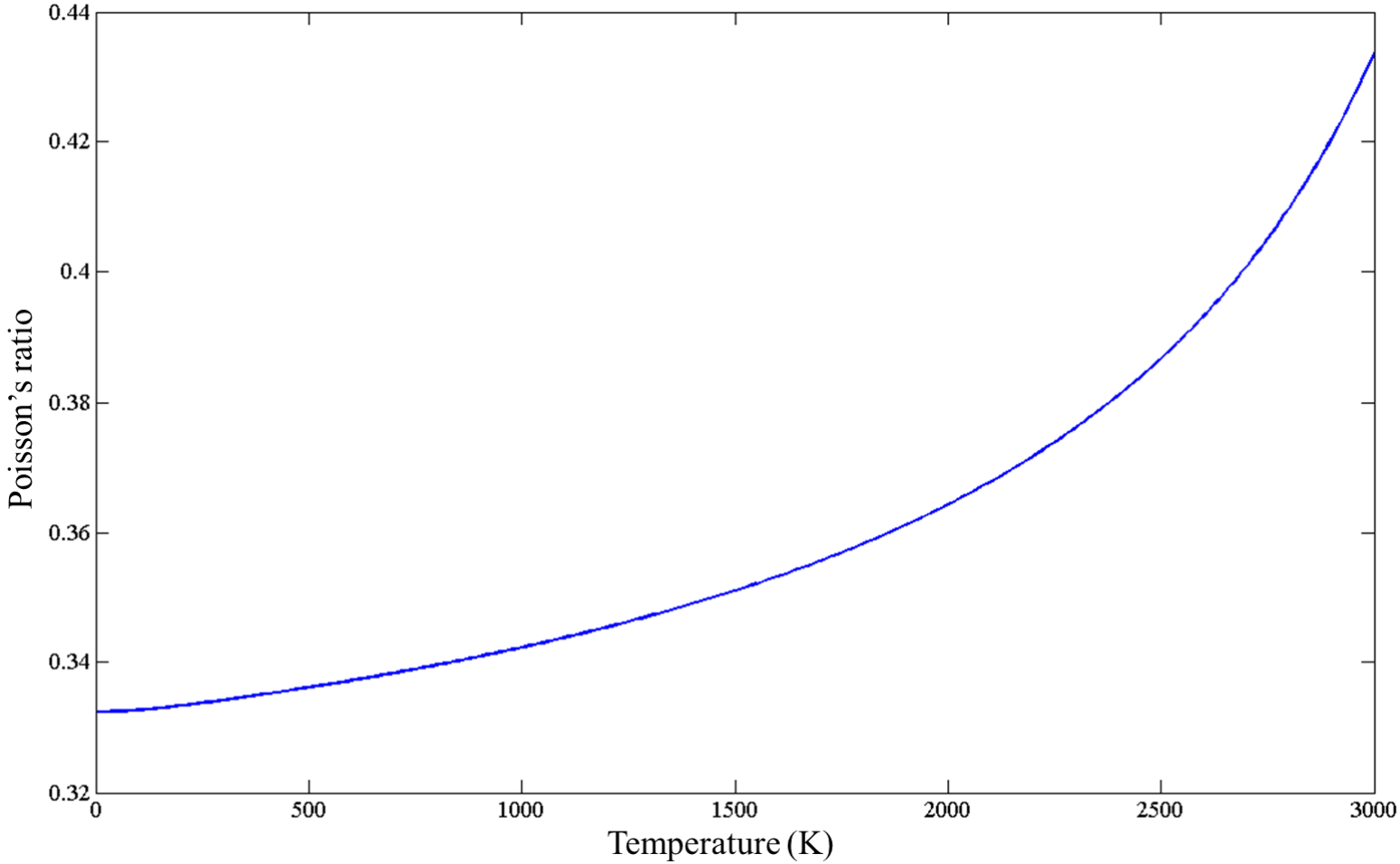

Fig. 6.7. The Poisson's ratio of Nb_3Al versus temperature.

6.3.4 Debye temperatures

The Debye temperature values calculated from the elastic constants decrease from $NbAl_3$ (520 °C (793 K)) to Nb_3Al (100 °C (374 K)) to Nb_2Al (-4 °C (269 K)). The Θ_D of Nb_3Al in the present study is in good agreement with the available results from the literature. The largest deviation was for $NbAl_3$ when comparing the Θ_D value with the value in [65] and was about 5 %. It should be noted that the latter value was not calculated from elastic constants, but was derived from the phonon DOS. The resultant phonon DOS from the calculations in section 3.2 were also used to calculate the Debye temperatures. The calculated Θ_D values (Table 6.3) were in good agreement with both the data from previous work and the results of the present study that were calculated from the elastic constants.

6.4. Conclusions

First principles calculations were carried out for the $NbAl_3$, Nb_3Al, Nb_2Al and their constituent elements. Elastic constants, bulk, shear and Young's modulus, Poisson's ratio and Debye temperature were calculated. Specifically for the Nb_2Al, most of the data were obtained for the first time. The temperature dependence of the free energy and enthalpy of formation regarding the intermetallic phases is reported for the first time. Comparison with available experimental and theoretical data shows good agreement with this work. It is concluded that Nb_3Al has the highest bulk, modulus value, while $NbAl_3$ is the stiffest and most brittle of the Nb-Al intermetallics. The Θ_D value of $NbAl_3$ is the highest amongst the Nb-Al compounds. Finally, the linear thermal expansion coefficient and temperature dependence of the elastic properties of the Nb_3Al were calculated and reported for the first time.

7

Ab initio study of binary and ternary $Nb_3(X,Y)$ A15 intermetallic phases (X,Y= Sn, Al, Si, Ge)

7.1. Introduction

The motivation for the present study was to investigate the elastic and thermodynamic properties of binary and ternary A15 Nb based intermetallics and to compare their stability with the *tP*32 competing structure. Calculations of the elastic constants and phonon properties are used to produce a complete set of data for the Nb_3Sn, Nb_3Al, Nb_3Ge, Nb_3Si, Nb_6SnAl, Nb_6AlSi, Nb_6SnSi, Nb_6SnGe, Nb_6AlGe and Nb_6SiGe intermetallics. It must be noted that the Nb_6XY phases (denoted also as $Nb_3(X,Y)$) are ternary A15 structures with equi-atomic occupancies in the non-Nb sub-lattice. There is experimental and theoretical data for the vibrational and elastic properties of Nb, Si, Sn, Ge and Al [119, 120] and their Debye temperatures [122]. There is also experimental data for the linear thermal expansion coefficients of Nb, Al and Nb_3Ge [12, 119, 142].

7.2. Computational details

To reduce the basis set of plane wave functions used to describe the real electronic functions norm conserving pseudopotentials were implemented and the valences for the atomic configurations were Al-$3s^2 3p^1$, Sn-$5s^2 5p^2$, Nb-$4d^4 5s^1$, Ge-$4s^2 5p^2$ and Si-$3s^2 3p^2$. A Monkhorst–Pack k-point grid separation of 0.03 $Å^{-1}$, an energy cutoff of 1200 eV and a Gaussian smearing of 0.7 eV were used. The phonon calculations were conducted using the linear response method (section 3.2.4).

7.3. Results and discussion

The calculated lattice constants of the pure elements and the binary and ternary A15 phases are compared with the experimental ones in Table 7.1. It can be seen that in the present calculations and with the exception of Si the lattice constants are slightly underestimated but overall are in good agreement with the experimental values, with the lattice constant of Al showing the largest difference of 1.85 %. Table 7.2 gives the results for the independent elastic constants (C_{ij}) and bulk moduli (B) for all elements and compounds under study. In this table the bulk moduli were calculated from elastic constants according to the Voigt-Reuss-Hill (VRH) scheme and values are also given for bulk moduli and first pressure derivatives of bulk moduli (B') from the Birch-Murnaghan equation of state (B-M EOS). It was confirmed that the mechanical stability criteria [107] are met for all phases. For the pure elements it can be seen that the elastic

constants are in good agreement with the experimental data. The values of the bulk moduli of the Nb_3Sn and Nb_3Al are in good agreement with other theoretical [48, 64] results and the consistency of the calculation is validated by the results of the B-M EOS fitting. The current results show that the Nb_3Si has the highest bulk modulus of 181.5 GPa and that the bulk moduli of the Nb_3Sn and Nb_3Al are close to each, other being 167.6 GPa and 162.2 GPa, respectively, while the corresponding value for Nb_3Ge is 174.2 GPa. This means that the most resistant to applied pressure of the four binary intermetallics of this study is the Nb_3Si. From the bulk modulus values of the ternary A15 phases it can be seen that Si and Ge tend to increase bulk modulus, while Sn and Al have the opposite effect.

The calculated values of shear modulus (G), Young's modulus (E) and Debye temperature (Θ_D) are given in Table 7.3. The Nb_3Si phase has the highest shear modulus value and the shear modulus decreases from Nb_3Si (80.3 GPa) to Nb_3Ge (73.5 GPa), to Nb_3Sn (65 GPa) to Nb_3Al (61.6 GPa), which means that the most resistant binary compound to reversible deformation upon shear strain is the Nb_3Si. The same ranking applies for the stiffness of the compounds as the elastic modulus (E) values as they are 210 GPa for Nb_3Si, 193.3 GPa for Nb_3Ge, 172.7 GPa for Nb_3Sn and 164 GPa for Nb_3Al. Judging from the values of the aforementioned moduli for the ternary phases, it is suggested that Si and Ge additions increase them, while Sn and Al decrease them.

Ductile or brittle behavior of a material can be deduced by taking into account the Cauchy pressure and Pugh's [104] index of ductility of shear modulus over bulk modulus ratio (G/B) and Poisson's ratio (v). The values of the aforementioned properties are listed in Table 7.3.

According to [121], for metallic bonding, a positive value of Cauchy pressure means ductile behavior and brittle if negative. The other two conditions point to brittle behavior when the G/B ratio is greater than 0.57 and the v is less than 0.26. Bearing that in mind, it can be seen from Table 7.3 that the Nb_3Si and Nb_3Al are the most and least brittle binary compounds, respectively and that Sn and Al additions improve ductility, while Si and Ge have the opposite effect.

Comparing the shear moduli, Young's moduli and Debye temperature values of the Nb_3Sn and Nb_3Al of this study with data in [48], it can be seen that there is disagreement, which in the case of Nb_3Al is 17%, 15% and 18% in G, E and Θ_D,

Table 7.1

Lattice constants pure elements and binary and ternary A15 phases.

Phase	this work (Å)	literature (Å)	deviation (%)
Nb	3.299	3.311 [a]	0.36
Sn	a=5.741 c=3.102	a=5.832 [b] c=3.182 [b]	Δa/a=1.56 Δc/c=1.37
Al	4.022	4.098 [c]	1.85
Si	5.469	5.431 [d]	0.70
Ge	5.738	5.658 [d]	1.41
Nb_3Sn	5.258	5.289 [e]	0.59
Nb_3Al	5.171	5.187 [e]	0.31
Nb_3Ge	5.151	5.168 [e]	0.33
Nb_3Si	5.101	5.155 [f]	1.05
Nb_6SnAl	5.221	5.255 [g]	0.65
Nb_6AlSi	5.136	5.173 [h]	0.72
Nb_6SnSi	5.186	5.216 [i]	0.58
Nb_6SnGe	5.21	5.217 [j]	0.13
Nb_6AlGe	5.161	5.175 [k]	0.27
Nb_6SiGe	5.126	5.173 [h]	0.91

[a] Ref [49], [b] Ref [52], [c] Ref [114], [d] Ref [143], [e] Ref [64], [f] Ref [144], [g] Ref [76], [h] Ref [21], [I] Ref [145], [j] Ref [146], [k] Ref [147]

Table 7.2
Elastic constants (C_{ij}) and bulk moduli (B) of pure elements and binary and ternary A15 phases in GPa.

	VRH approximation							B-M EOS	
Phase	C_{11}	C_{12}	C_{13}	C_{33}	C_{44}	C_{66}	B	B	B'
Nb	244	124.5			27		164.3	163.1	4.004
	253[a]	133[a]			31[a]		170.3[a]		
Sn	74.2	58	22.2	81.2	23.4	9.9	51.8	53.2	3.703
	72.3[b]	59.4[b]	35.8[b]	88.4[b]	22[b]	22.5[b]	58 [b]		
Al	107.4	57.6			30.3		74.2	76.47	4.037
							75.2[a]		
Si	152.1	56.7			74.1		88.5	90.22	4.019
							98[c]		
Ge	113.9	40.5			55.2		65	67.5	4.035
	128.5[c]	48.3[c]			66.8[c]		75[c]		
Nb_3Sn	282.4	110.1			53.8		167.6	167.5	4
							160.5[d]		
							166.5[e]		
Nb_3Al	272.8	106.9			50.5		162.2	162.1	4
							156.3[d]		
							165.5[e]		
Nb_3Ge	298.3	112.2			62.8		174.2	174	4
Nb_3Si	314.8	114.9			69.3		181.5	181.2	4
Nb_6SnAl	276.7	107.7			52		164	163.8	4
Nb_6AlSi	293.3	110.1			59.4		171.1	170.6	4
Nb_6SnSi	296.6	111.7			62		173.3	173	4
Nb_6SnGe	288.9	111.1			58.6		170.3	170	4
Nb_6AlGe	284.9	109.4			56.8		167.9	167.2	4
Nb_6SiGe	305.9	113.5			66.4		177.6	177	4

[a] Ref. [119] , [b] Ref [52], [c] Ref. [120], [d] Ref. [64], [e] Ref. [48]

Table 7.3

Calculated shear (G) and elastic moduli (E) in GPa, Poisson's ratio (v), Cauchy pressure in GPa, G/B ratio and Debye temperature (Θ_D) from elastic constants for pure elements and binary and ternary A15 phases.

	G	E						Θ_D (K)			
Phase	VRH	VRH	v	C_{12}-C_{44}	C_{13}-C_{44}	C_{12}-C_{66}	G/B	Phonon DOS	Elastic constants		
Nb	37.4	104.3	0.394	97.5			0.228	277	268	275 [b]	
	37.5 [c]	104.9 [c]	0.397 [c]								
Sn	16.3	44.3	0.357	54.1	-1.2	48.1	0.315	254	217	230 [b]	
	17.7 [c]	48 [c]	0.355 [c]								
Al	28	74.7	0.334	27.3			0.377	394	420	428 [b]	
	26.2 [c]	70.6 [c]	0.345 [c]								
Si	62.1	151	0.216	-17.4			0.701	647	628	645 [b]	
	64.1 [d]	155.8 [d]	0.215 [d]								
Ge	46.9	113.4	0.209	-14.7			0.722	393	386	360 [b]	
	41 [d]	104 [d]									
Nb_3Sn	65	172.7	0.328	56.3			0.388	291	336	308 [b]	282 [a]
	74.9 [a]	195.3 [a]									
Nb_3Al	61.6	164	0.331	56.4			0.380	353	374	370 [b]	316 [a]
	74.2 [a]	193.5 [a]									
Nb_3Ge	73.5	193.3	0.315	49.4			0.422	344	376		
Nb_3Si	80.3	210	0.307	45.6			0.442	383	420		
Nb_6SnAl	63.2	168	0.329	55.7			0.385	332	355		
Nb_6AlSi	70.7	186.4	0.318	50.7			0.413	386	398		
Nb_6SnSi	72.8	191.6	0.316	49.7			0.420	360	378		
Nb_6SnGe	69.3	183.1	0.321	52.5			0.407	342	359		
Nb_6AlGe	67.6	178.8	0.323	52.6			0.403	350	377		
Nb_6SiGe	77	201.8	0.311	47.1			0.434	378	400		

[a] Ref. [48], [b] Ref. [122] [c] Ref. [52], [d] Ref [120].

Table 7.4

Calculated enthalpies of formation of binary and ternary A15 phases (unless denoted otherwise) compared with the literature.

Phase	Temperature (K)	ΔH_f from the present study (kJ/mol)	Literature (kJ/mol)
Nb_3Sn	298	-15.583	-16.7 to -16 [a]
	1273	-11.36	13.232 [a]
Nb_3Al	298	-22.101	-19.297 [b]
	298	-20.376	-19.7 [c]
Nb_3Si	0	-34.73	-32.8 [d]
Nb_3Ge	0	-33.288	
Nb_6SnAl	0	-16.646	
Nb_6AlSi	0	-26.062	
Nb_6SnSi	0	-23.321	
Nb_6SnGe	0	-32.029	
Nb_6AlGe	0	-29.633	
Nb_6SiGe	0	-35.629	
Nb_3Si *tP*32	0	-37.3	-40.5 [e]
	298	-37	-29.6 to -35.9 [f]
Nb_6SiSn *tP*32	0	-15.985	
Nb_6SiAl *tP*32	0	-22.497	
Nb_6SiGe *tP*32	0	-36.021	

[a] Ref [28], [b] Ref [63], [c] Ref [148], [d] Ref [23], [e] Ref [41], [f] Ref [92]

respectively. The Debye temperature of Nb_3Al calculated from the elastic constants in the present study is in very good agreement with the literature. The Θ_D value decreases as one moves from Nb_3Si (147 °C (420 K)) to Nb_3Ge (103 °C (376 K)), to Nb_3Al (101 °C (374 K)) to Nb_3Sn (63 °C (336 K)). When Si or Ge are added to the A15 structure the Debye temperature tends to increase. The aforementioned property tends to decrease in the presence of Sn and Al.

The vibrational density of states (DOS) for the elemental phases and compounds under study were computed and all the eigenfrequencies were found to be real, hence it was confirmed that the compounds under investigation are mechanically stable (Fig. 7.1). The phonon contribution to free energies per atom ($F^{phon}(T)$) was calculated and is presented for all elemental phases and binary compounds in Fig. 7.2. It can be seen that the F^{phonon} decreases faster in the order Nb_3Si, Nb_3Al, Nb_3Ge, Nb_3Sn. In Fig. 7.3 the phonon contribution to the free energy of the ternary compounds is shown. It can be seen that it decreases faster in the order Nb_6AlSi, Nb_6GeSi, Nb_6SiSn, Nb_6GeAl, Nb_6AlSn, Nb_6GeSn. After taking F^{phon} into account, the phonon contribution to the enthalpy of formation ($\Delta H_f^{phon}(T)$) was evaluated. The $\Delta H_f^{phon}(T)$ rises faster for Nb_3Sn, owing to the steep descent of the vibrational contribution to the free energy of Sn compared with the other elements, as it can be seen in Fig. 7.4. The $\Delta H_f^{phon}(T)$ of Nb_3Si on the other hand exhibits the smallest slope of the four curves, which is attributed to the behaviour of the $F^{phon}(T)$ of Si, while the curves of Nb_3Al and Nb_3Ge are close to each other and have about half the slope of the corresponding value of Nb_3Sn. Regarding the ternary phases, the $\Delta H_f^{phon}(T)$ increases faster in the order Nb_6AlSi, Nb_6GeSn, Nb_6GeAl, Nb_6SiSn, Nb_6AlSn, Nb_6GeSn. The enthalpies of formation versus temperature ($\Delta H_f(T)$) were obtained and are shown in Figs 7.5 and 7.6. At 0 K the heat of formation (ΔH_f^0) increases from Nb_3Si (-34.734 kJ/mol) to Nb_3Ge (-33.288 kJ/mol), to Nb_3Al (-22.467 kJ/mol) to Nb_3Sn (-16.54 kJ/mole). In Table 7.4 the good agreement between the present study and previous experimental results regarding the enthalpies of formation of the intermetallics is shown. The Nb_3Si phase has the lowest $\Delta H_f(T)$ of the binary A15

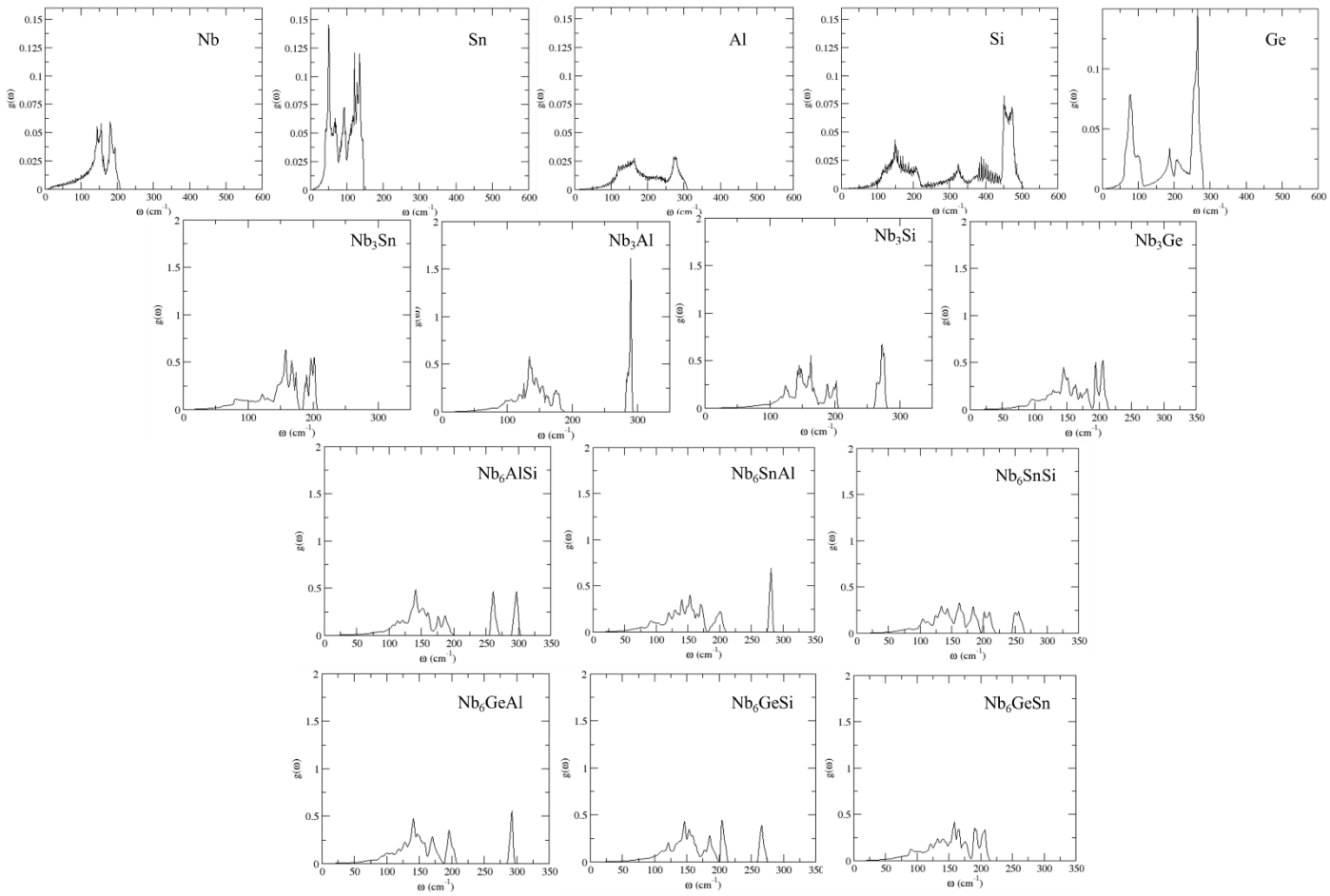

Fig. 7.1. Phonon DOS of the pure elements and binary and ternary A15 intermetallics of the present study.

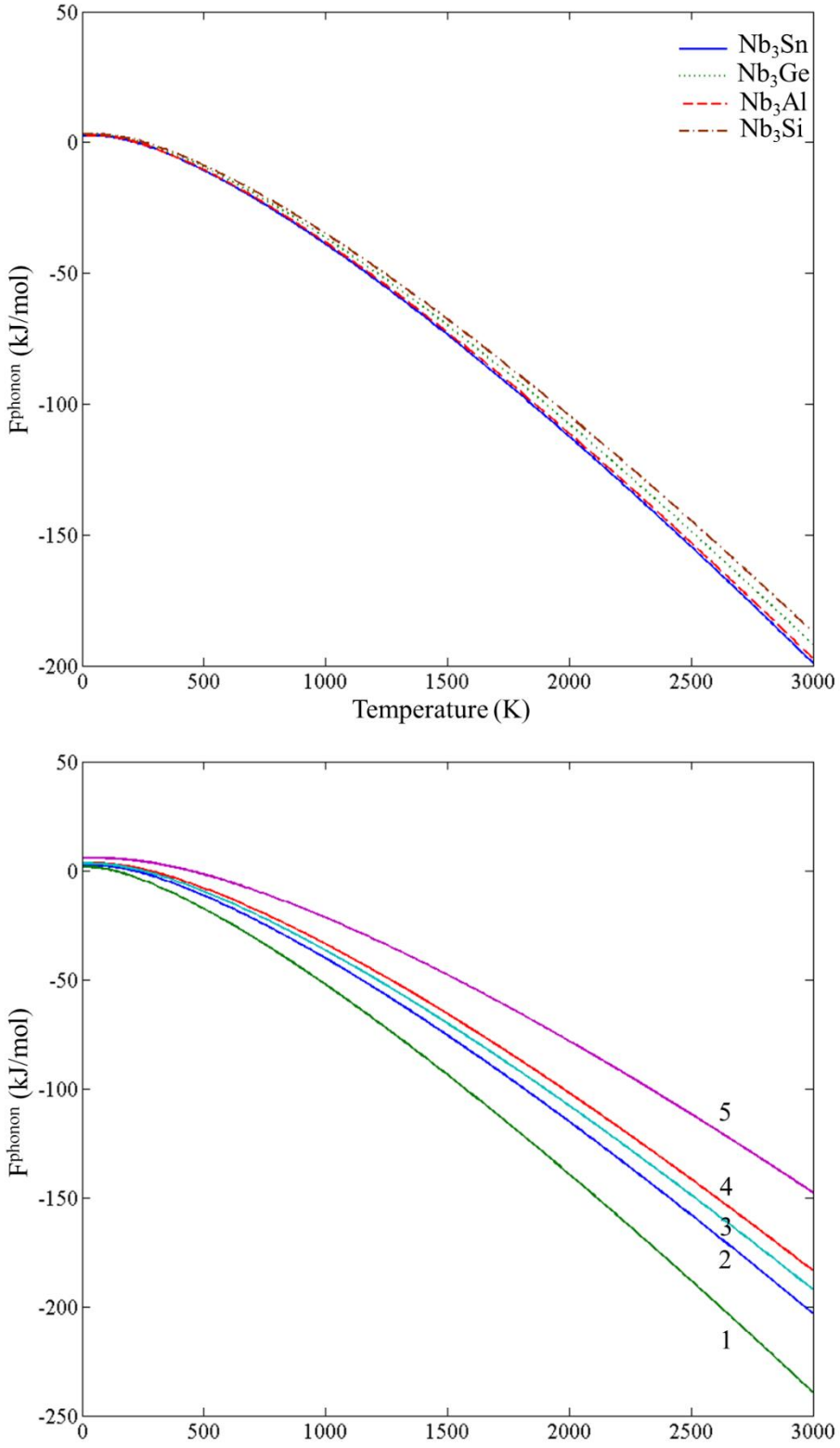

Fig. 7.2. Phonon contribution to free energies of the (a) binary A15 phases and (b) Sn (1), Nb (2), Ge (3), Al (4) and (5) Si.

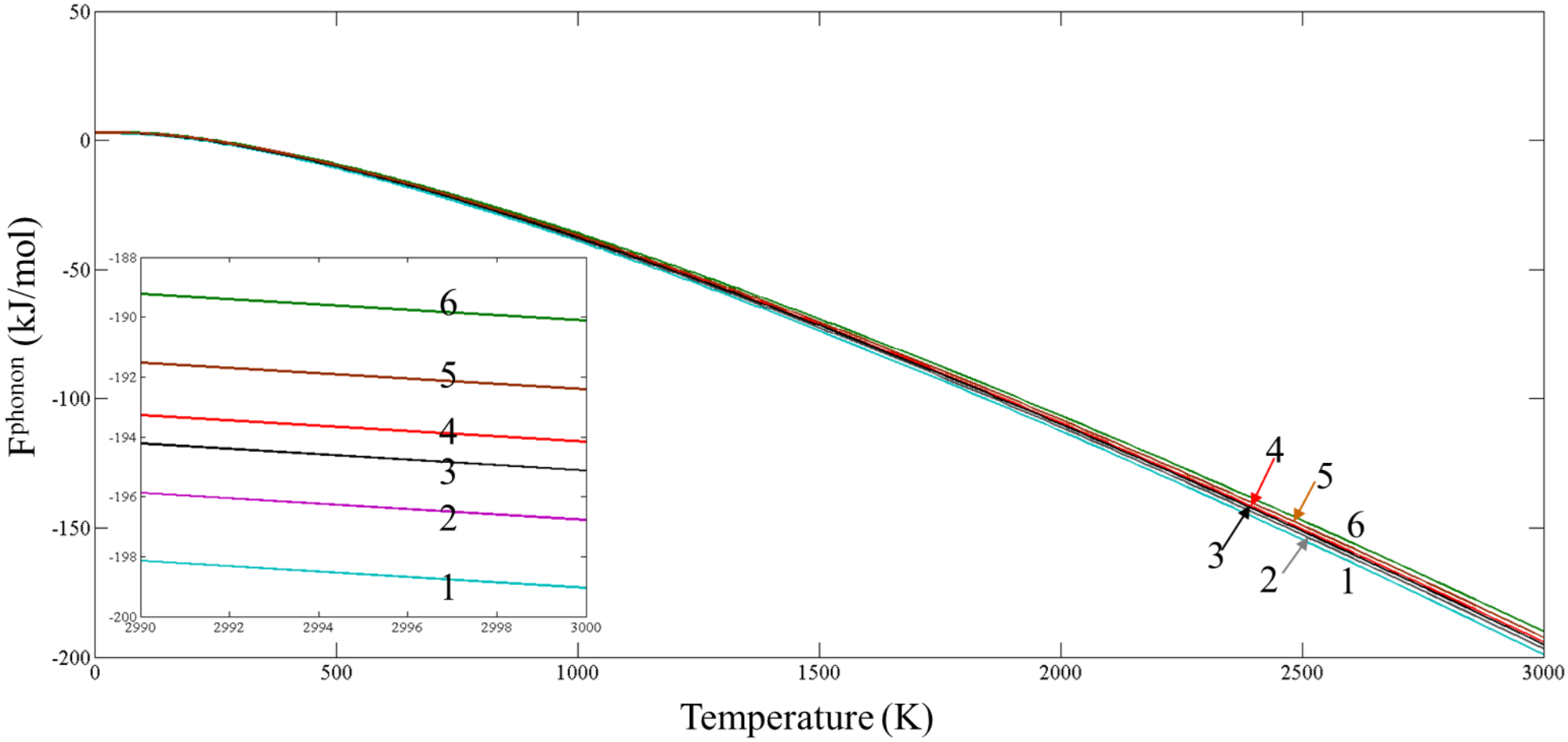

Fig. 7.3. Phonon contribution to free energies of the ternary A15 phases; Nb_6GeSn (1), Nb_6AlSn (2), Nb_6GeAl (3), Nb_6SiSn (4), Nb_6GeSi (5) and Nb_6AlSi (6).

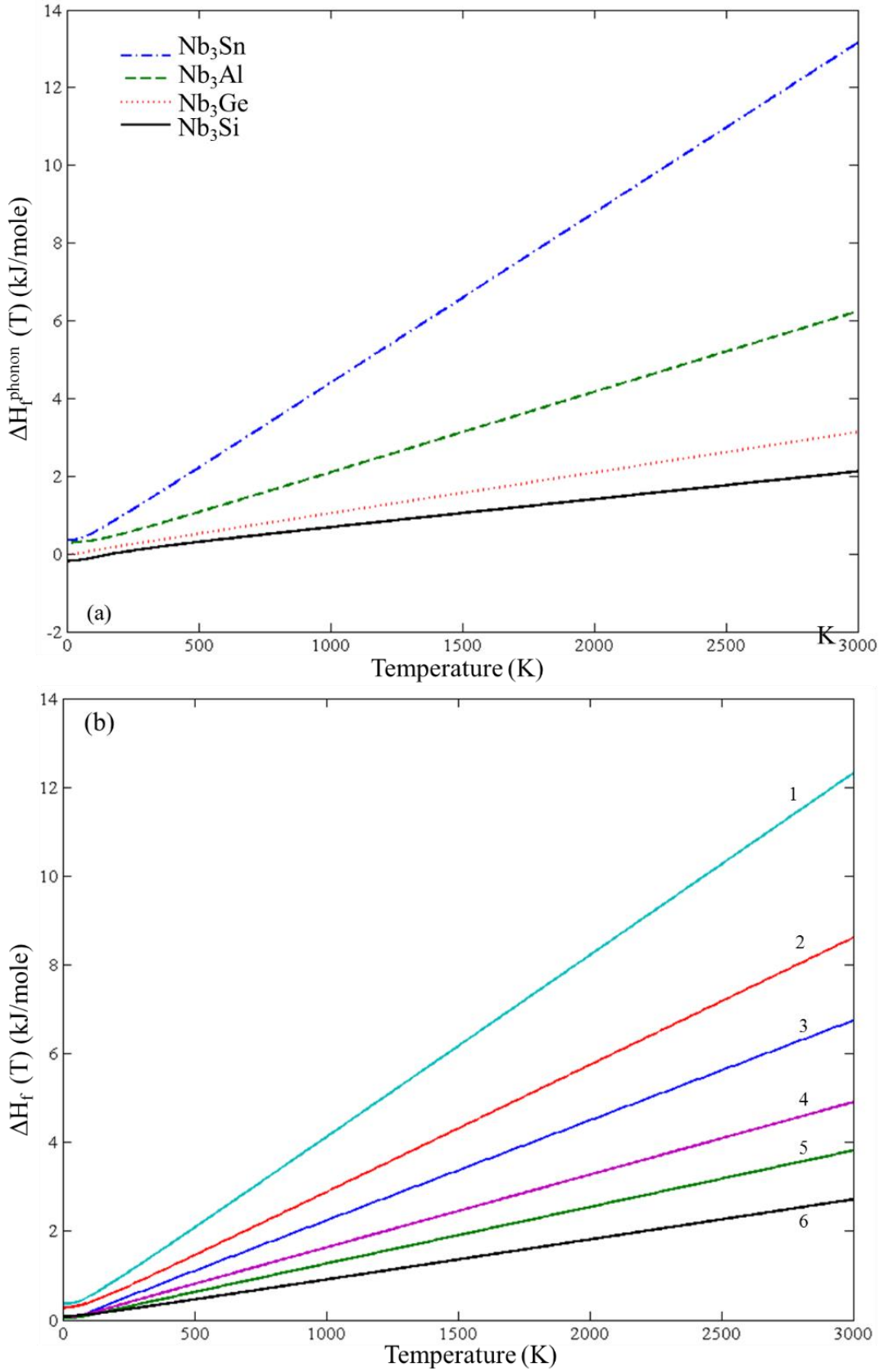

Fig. 7.4. Phonon contributions to the enthalpy of formation of (a) the binary and (b) the ternary (Nb_6GeSn (1), Nb_6AlSn (2), Nb_6SiSn (3), Nb_6GeSi (4), Nb_6AlSi (5) and Nb_6GeAl (6)) A15 phases.

Table 7.5

Linear thermal expansion coefficients of Nb, Al, Nb_3Sn, Nb_3Al, Nb_3Ge and Nb_3Si (μm/mK).

Phase	this work	literature
Nb *	7.9	7.3 [a]
Al *	22.5	23.1 [b]
Nb_3Sn	6.4	
Nb_3Al	7	
Nb_3Ge	7.6	7.7 [c]
Nb_3Si	8.1	

* At room temperature, [a] Ref [130], [b] Ref [149] , [c] Ref [150]

intermetallics, while the Nb_3Sn is the phase with the highest value in the whole range of temperatures. The $\Delta H_f(T)$ of the *tP*32 Nb_3Si [22] is also shown in Fig. 7.6 and Table 7.4. It is confirmed that the tetragonal Nb_3Si is more stable than the cubic Nb_3Si. Even though the phonon contribution in the enthalpy of formation of the *tP*32 Nb_3Si exhibits a steeper ascent than that of the A15 Nb_3Si, in the whole range of temperatures the enthalpy of formation of the former structure is always lower than that of the latter, owing mostly to the considerably lower enthalpy of formation at 0 K. Regarding the ternary intermetallics containing Si and Sn, Al or Ge the enthalpy of formation at 0 K was calculated, separately for A15 and *tP*32 structure and the values are given in Table 7.4. It is suggested that Sn and Al additions stabilise the A15 structure and Ge addition stabilises the *tP*32 structure.

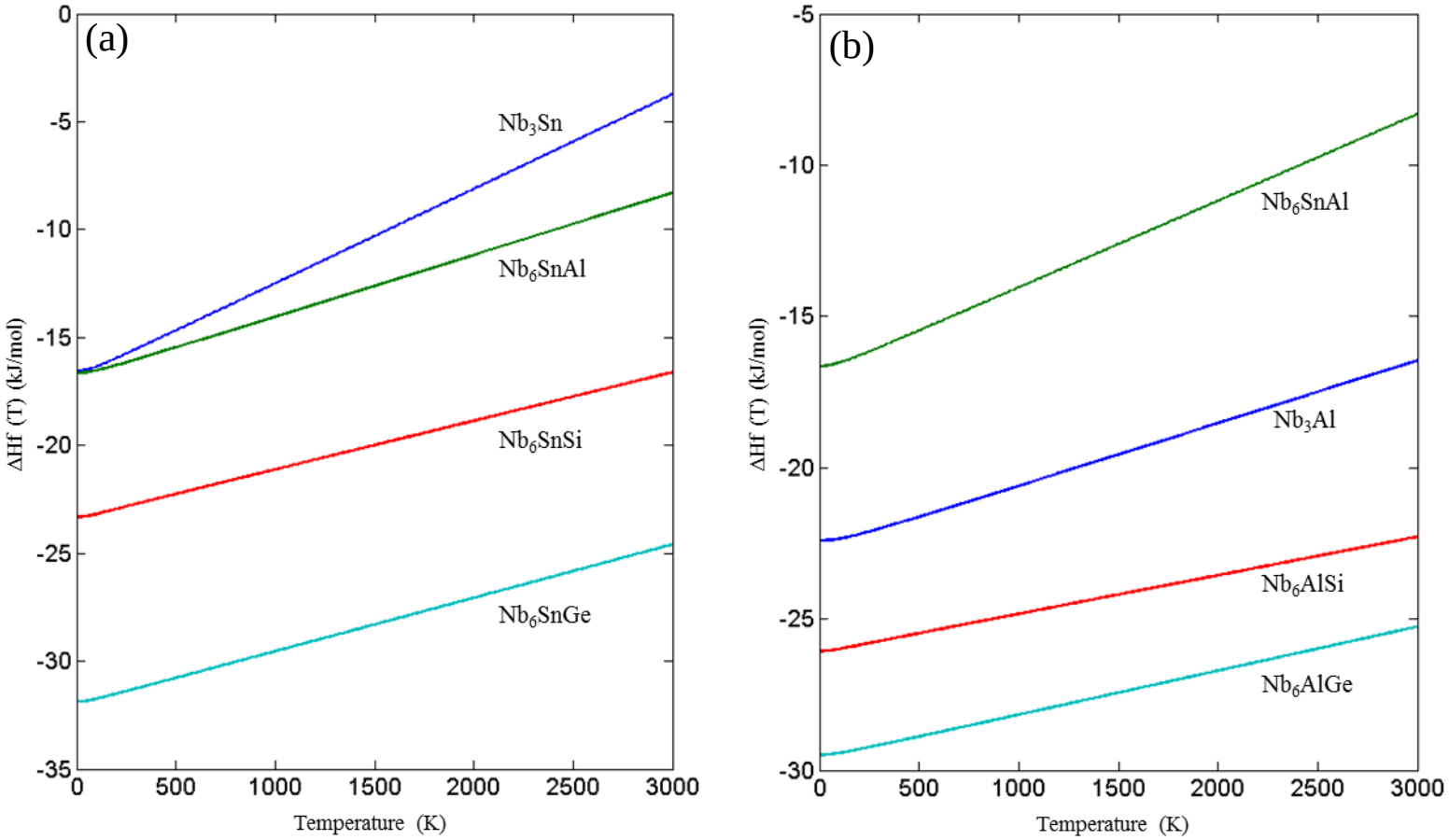

Fig. 7.5. Enthalpy of formation curves showing the influence of each element under study in the (a) Nb_3Sn and (b) Nb_3Al intermetallics.

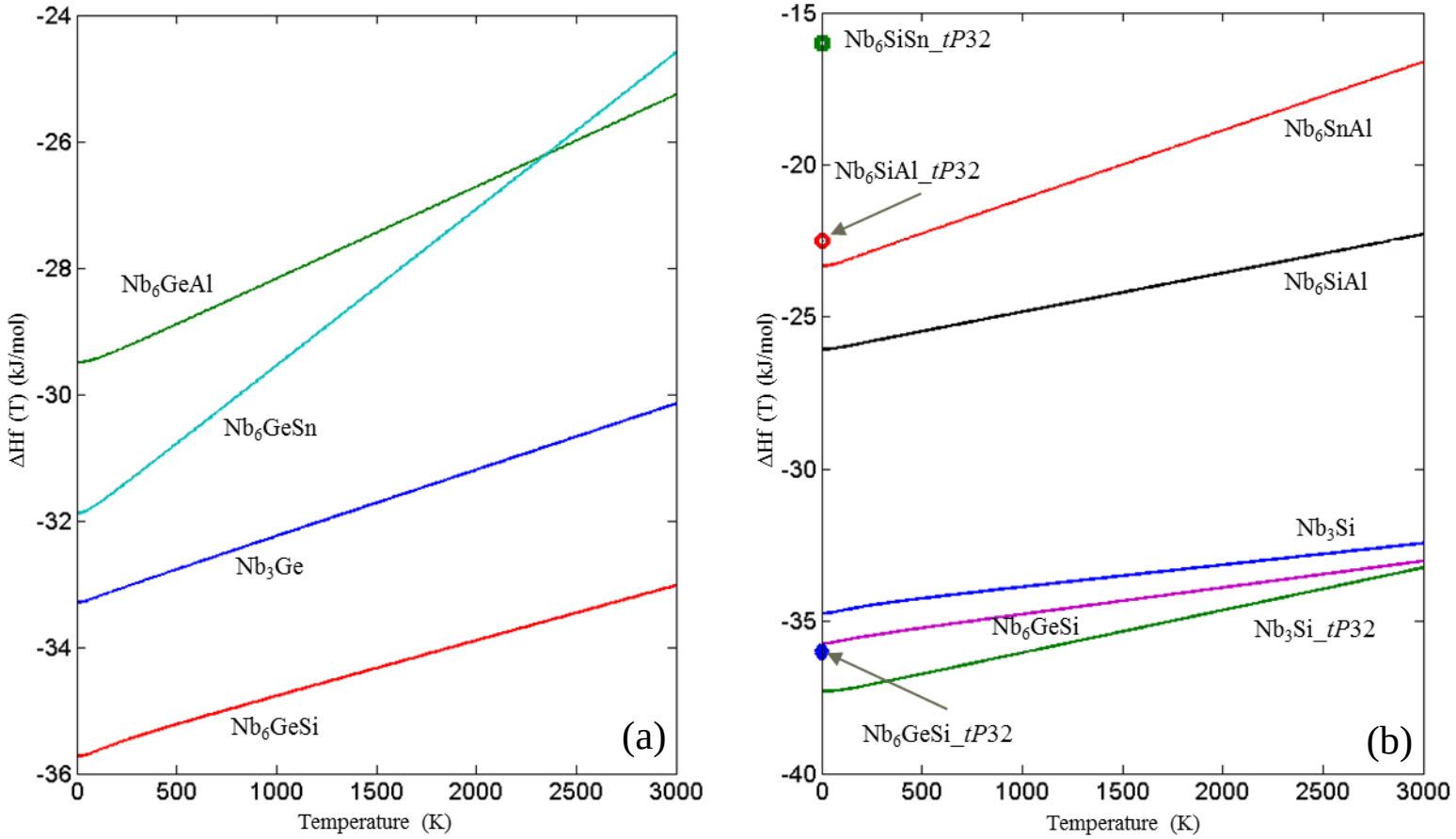

Fig. 7.6. Enthalpy of formation curves showing the influence of each element under study in the (a) Nb_3Ge and (b) Nb_3Si intermetallics. All phases are of A15 structure unless denoted otherwise.

The linear thermal expansion coefficients of Nb, Al, Nb_3Sn, Nb_3Al, Nb_3Ge and Nb_3Si (A15) phases are shown in Table 7.5. The agreement with the available experimental data is excellent, a fact that demonstrates the power and usefulness of the linear response method. Regarding the A15 phases the aforementioned property tends to decrease in the order Nb_3Si (8.1 μm/mK), Nb_3Ge (7.6 μm/mK), Nb_3Al (7 μm/mK), Nb_3Sn (6.4 μm/mK).

The resultant phonon DOS from the calculations was also used to calculate the Debye temperature. The calculated Θ_D values (Table 7.3) were in good agreement with both the experimental data [122] and the results of the present study that were calculated from elastic constants values. For the elemental phases the results were in good agreement with the literature. The overall correlation validates the quality of the calculations.

7.4. Conclusions

First principles calculations were carried out for binary and ternary A15 intermetallic compounds and their constituent elements. Elastic constants, bulk, shear and Young's modulus, Poisson's ratio and Debye temperature were calculated. In the case of the Nb_3Si (A15), most of the data were obtained for the first time. The temperature dependence of the enthalpy of formation regarding the intermetallic phases is reported for the first time. The linear thermal expansion coefficients of Nb, Al, Nb_3Sn, Nb_3Al, Nb_3Ge and Nb_3Si (A15) are reported as well. Comparison with available experimental and other theoretical data shows good agreement with this work. It is concluded that the Nb_3Si has the highest bulk, shear and Young's modulus values and that it is the stiffest and less ductile of the four binary intermetallics of the present study. The Nb_3Si has the highest Debye temperature of all the A15 compounds in the present study. It is also concluded that Al and Sn additions improve ductility and Ge and Si additions increase the Debye temperature. Finally the enthalpy of formation results suggest that the Sn and Al additions in the Nb_3Si stabilise the A15 structure over the competing *tP*32, while the Ge addition has the opposite effect.

8

Ab initio study of the ternary W_5Si_3 type TM_5Sn_2X compounds (TM=Nb, Ti and X=Al,Si)

8.1. Introduction

This chapter presents the results of a study that used Density Functional Theory to evaluate the stability and the electronic, vibrational and elastic properties of the $TMSn_2X$ (TM=Nb, Ti and X=Al,Si) ternary phases. The results will be useful for the construction and/or optimisation of the Nb-Si-Sn, Nb-Al-Sn, Ti-Si-Sn and Ti-Al-Sn systems (see also sections 2.5.2 and 2.5.3).

8.2. Computational details

To reduce the basis set of plane wave functions used to describe the real electronic functions norm conserving pseudopotentials were implemented and the valences for the atomic configurations were Nb-$4s^2 4p^6 4d^4 5s^1$, Ti-$3s^2 3p^6 3d^2 4s^2$, Sn-$5s^2 5p^2$, Al-$3s^2 3p^1$ and Si-$3s^2 3p^2$. A 9×9×9 Monkhorst–Pack k-point grid, an energy cutoff of 550 eV and a Gaussian smearing of 0.3 eV were used. The phonon calculations were conducted using the supercell method as discussed in section 3.2.3. The size of the supercells that were used was 2×2×2 for the ternary phases, 4×4×4 for Nb and Al and 3×3×3 for Ti, Si and Sn.

8.3. Results and Discussion

8.3.1 Elastic properties

The calculated lattice parameters are shown in Table 8.1 where they are compared with the values reported in the literature. It can be seen that there is good agreement as the mean deviation of all the lattice parameters is ~0.6 %. The results for the independent elastic constants (C_{ij}), bulk moduli (B) from elastic constants according to the Voigt-Reuss-Hill scheme and bulk moduli and first pressure derivatives of bulk moduli ($B^{'}$) from the B-M EOS for all intermetallic phases and elements of this study are shown in Table 8.2. In Table 8.3 the calculated values of the shear modulus (G) and Young's modulus (E) are reported. It was confirmed that the mechanical stability criteria [107] are met for all compounds. The elastic constants were in good agreement with the experimental data for the pure elements [49, 114]. To the authors' knowledge no data exists for the ternary intermetallics. Comparing the bulk moduli obtained from the VRH approximation and the B-M EOS fitting of all the phases, it can be seen that they were in excellent agreement, with the maximum deviation between them being ~7% for the Ti_5Sn_2Al phase.

Table 8.1

Lattice parameters of Nb, Si, Al, Sn, Nb_5Sn_2Si, Ti_5Sn_2Si, Nb_5Sn_2Al and Ti_5Sn_2Al in Å.

	a	c
Nb	3.309	3.309
	3.311[a]	3.311[a]
Si	5.46	5.46
	5.431[b]	5.431[b]
Al	4.103	4.103
	4.098[c]	4.098[c]
Sn	5.798	3.144
	5.832[d]	3.182[d]
Nb_5Sn_2Si	10.683	5.145
	10.541[e]	5.138[e]
Ti_5Sn_2Si	10.582	5.05
	10.558[f]	5.03[f]
Nb_5Sn_2Al	10.735	5.203
	10.629[g]	5.216[g]
Ti_5Sn_2Al	10.612	5.184
	10.549[g]	5.242[g]

[a] Ref [49], [b] Ref [116], [c] Ref [114], [d] Ref [52], [e] Ref [73], [f] Ref [87], [g] Ref [75]

Table 8.2

Elastic constants (C_{ij}) and bulk modulus (B) for Nb, Si, Al, Sn, Nb_5Sn_2Si, Ti_5Sn_2Si, Nb_5Sn_2Al and Ti_5Sn_2Al in GPa.

	VRH approximation							B-M EOS	
	C_{11}	C_{12}	C_{13}	C_{33}	C_{44}	C_{66}	B	B	B'
Nb	241	126.3			26.7		164.5	165.1	4.005
	253[a]	133[a]			31[a]				
Si	151.2	57.4			73.1		88.7	91.2	4.009
	166[b]	64[b]			79.6[b]				
Al	107.4	57.6			30.3		74.2	76.47	4.037
	107[b]	61[b]			28[b]				
Sn	74.2	58	22.2	81.2	23.4	9.9	51.8	52.01	3.703
	72.3[c]	59.4[c]	35.8[c]	88.4[c]	22[c]	22.5[c]	54.9[c]		
Nb_5Sn_2Si	303.5	104.4	98.9	313.4	74.4	98.7	169.4	168.8	5
Ti_5Sn_2Si	214.8	73.6	71.1	189.6	51.6	75.3	116.6	119.7	5
Nb_5Sn_2Al	286.5	97	95.7	269.6	62.5	81.7	157.6	158.6	5
Ti_5Sn_2Al	211.5	75.1	63.3	178.6	47.3	69.8	111.1	118.9	5

[a] Ref. [32], [b] Ref. [31], [c] Ref [37]

Table 8.3

Calculated shear modulus (G) and elastic modulus (E) in GPa, Poisson's ratio (v), Cauchy pressures in GPa, G/B ratio and Debye temperature (Θ_D) from elastic constants and Phonon DOS (PDOS) for Nb, Si, Al, Sn, Nb_5Sn_2Si, Ti_5Sn_2Si, Nb_5Sn_2Al and Ti_5Sn_2Al.

	G	E						Θ_D (K)		
	VRH	VRH	v	C_{12}-C_{44}	C_{13}-C_{44}	C_{12}-C_{66}	G/B	PDOS	Elastic constants	Literature
Nb	36.5	101.9	0.396	99.6			0.228	277	268	275[a]
	37.5[b]	104.9[b]	0.397[b]							
Si	61.2	149.2	0.216	-17.4			0.701	647	628	645[a]
	64.1[c]	155.8[c]	0.215[c]							
Al	28	74.7	0.334	27.3			0.377	394	420	428[a]
	26.2[b]	70.6[b]	0.345[b]							
Sn	16.3	44.3	0.357		-1.2	48.1	0.315	254	217	230[a]
	17.7[d]	48[b]	0.355[d]							
Nb_5Sn_2Si	89.7	228.7	0.275		24.5	5.7	0.53	311	327	
Ti_5Sn_2Si	61.8	157.6	0.275		19.5	-1.7	0.53	305	326	
Nb_5Sn_2Al	77.1	198.9	0.29		33.2	15.3	0.489	298	305	
Ti_5Sn_2Al	58.6	149.5	0.276		16	5.3	0.527	300	320	

[a] Ref [122], [b] Ref [119], [c] Ref [120], [d] Calculated from Ref [52].

The Nb_5Sn_2Si phase had the highest values of bulk, shear and Young's moduli of all the intermetallics, while the Ti_5Sn_2Al had the lowest. All these properties decreased from Nb_5Sn_2Si, to Nb_5Sn_2Al, to Ti_5Sn_2Si, to Ti_5Sn_2Al. It can be seen that all the moduli were significantly higher when Nb was the transition metal in the ternary phase. Furthermore the Si-containing phases had slightly higher values of bulk, shear and elastic moduli than those that contained Al.

To determine whether a material is ductile or brittle, Cauchy pressures (C_{12} - C_{44} for cubic and C_{13}-C_{44} and C_{12}-C_{66} for tetragonal), Pugh's [104] index of ductility (shear modulus over bulk modulus ratio (G/B)) and Poisson's ratio (v) are taken into account. The values of the aforementioned properties are listed in Table 8.3. According to [121], for metallic bonding, a positive value of Cauchy pressure means ductile material whereas if negative brittle. The other two conditions for a compound to be brittle are the G/B ratio to be greater than 0.57 and the v less than 0.26. Regarding all the aforementioned criteria the data in Table 8.3 indicates that the Nb_5Sn_2Al and Ti_5Sn_2Si are the most and less ductile phases, respectively, in the present study.

8.3.2 Enthalpies of formation

The phonon density of states (DOS) for the compounds and elemental phases under study can be seen in Fig. 8.1. All the eigenfrequencies were found to be real, hence it was confirmed that the compounds under investigation are mechanically stable. After obtaining the computed phonon DOS the vibrational contribution to free energies per atom (F^{phon} (T)) was calculated and is presented for all compounds and elemental phases in Fig. 8.2. It can be seen that the F^{phonon} decreases faster in the order; Nb_5Sn_2Al- Ti_5Sn_2Si- Ti_5Sn_2Al- Nb_5Sn_2Si. After taking F^{phonon} into account, the phonon contribution to the enthalpy of formation (ΔH_f^{phon} (T)) was evaluated (Fig. 8.3). The ΔH_f^{phon} (T) rises faster for Nb_5Sn_2Al, while for the other three intermetallics the corresponding curves show very small differences between them. In Fig. 8.4 the enthalpy of formation versus temperature of all the ternary intermetallic compounds is shown. In Table 8.4 it is shown that at T=0 K the heat of formation (ΔH_f^0) increases from Ti_5Sn_2Si (-50.655 kJ/mol) to Ti_5Sn_2Al (-36.471 kJ/mol) to Nb_5Sn_2Si (-30.296 kJ/mol) to Nb_5Sn_2Al (-21.516 kJ/mol). The above values are in good agreement with the available experimental data. As the temperature rises the ΔH_f (T) increases more steeply for the Nb_5Sn_2Al, while the curves of the other three phases show approximately the same slope.

8.3.3 Debye temperatures

The resultant phonon DOS were also used to calculate the Debye temperature. It should be noted that it is considered more difficult to obtain accurate values using this approach than through the elastic constants (see above) because as a low temperature property the Debye temperature is determined by low energy phonons i.e. the acoustic phonons. The lower the temperature the smaller the part of Brillouin Zone that contributes to thermodynamics. The calculated values (Table 8.3) were in very good agreement with [23, 122] and the values calculated from elastic constants in the present study. For the elemental phases both the results from the phonon DOS and the elastic

constants were in excellent agreement with the literature. The Nb_5Sn_2Si and Nb_5Sn_2Al had the highest and lowest Debye temperatures, respectively.

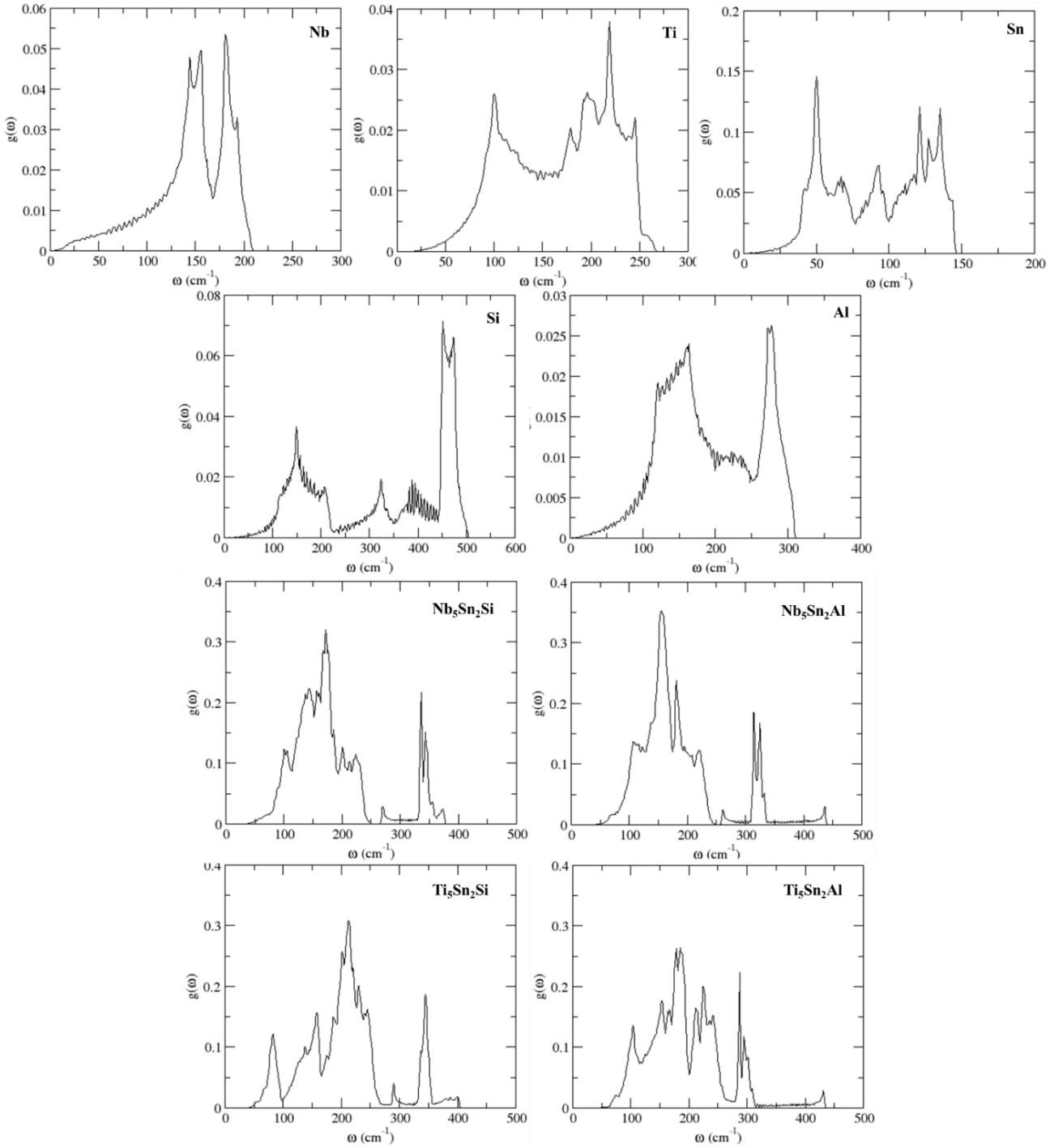

Fig. 8.1. Phonon density of states of Nb, Si, Al, Sn, Nb_5Sn_2Si, Ti_5Sn_2Si, Nb_5Sn_2Al and Ti_5Sn_2Al.

Table 8.4

Enthalpies of formation (kJ/mol) at T=0 K for Nb_5Sn_2Si, Ti_5Sn_2Si, Nb_5Sn_2Al and Ti_5Sn_2Al.

	Enthalpy of formation	
Intermetallic	Current study	Literature
Nb_5Sn_2Si	-30.296	
Ti_5Sn_2Si	-50.655	-50.751 *
Nb_5Sn_2Al	-21.516	
Ti_5Sn_2Al	-36.471	

* Ref [87]

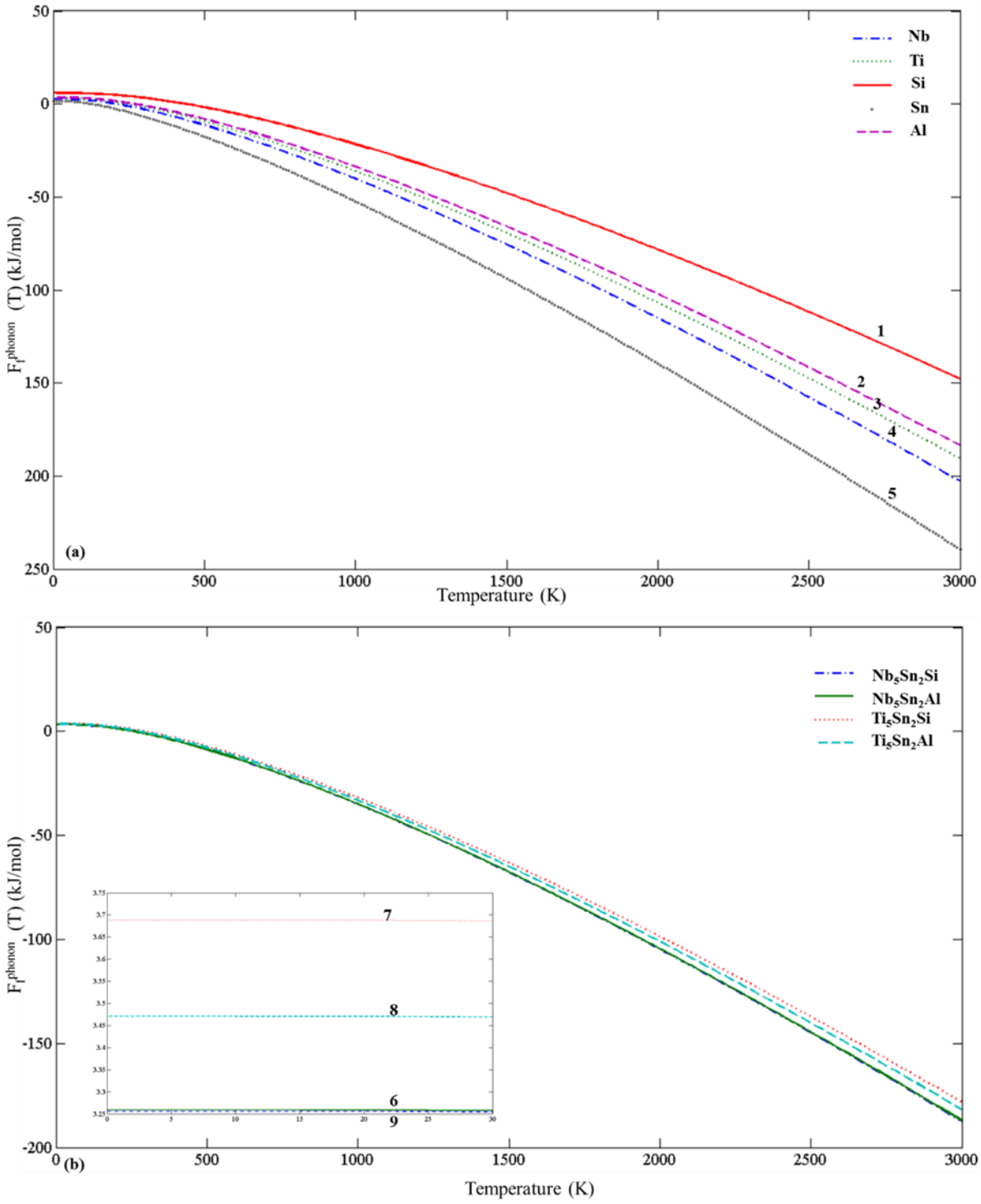

Fig. 8.2. Phonon contribution to free energies for (1) Si, (2) Al, (3) Ti, (4) Nb, (5) Sn, (6) Nb_5Sn_2Al, (7) Ti_5Sn_2Si, (8) Ti_5Sn_2Al and (9) Nb_5Sn_2Si

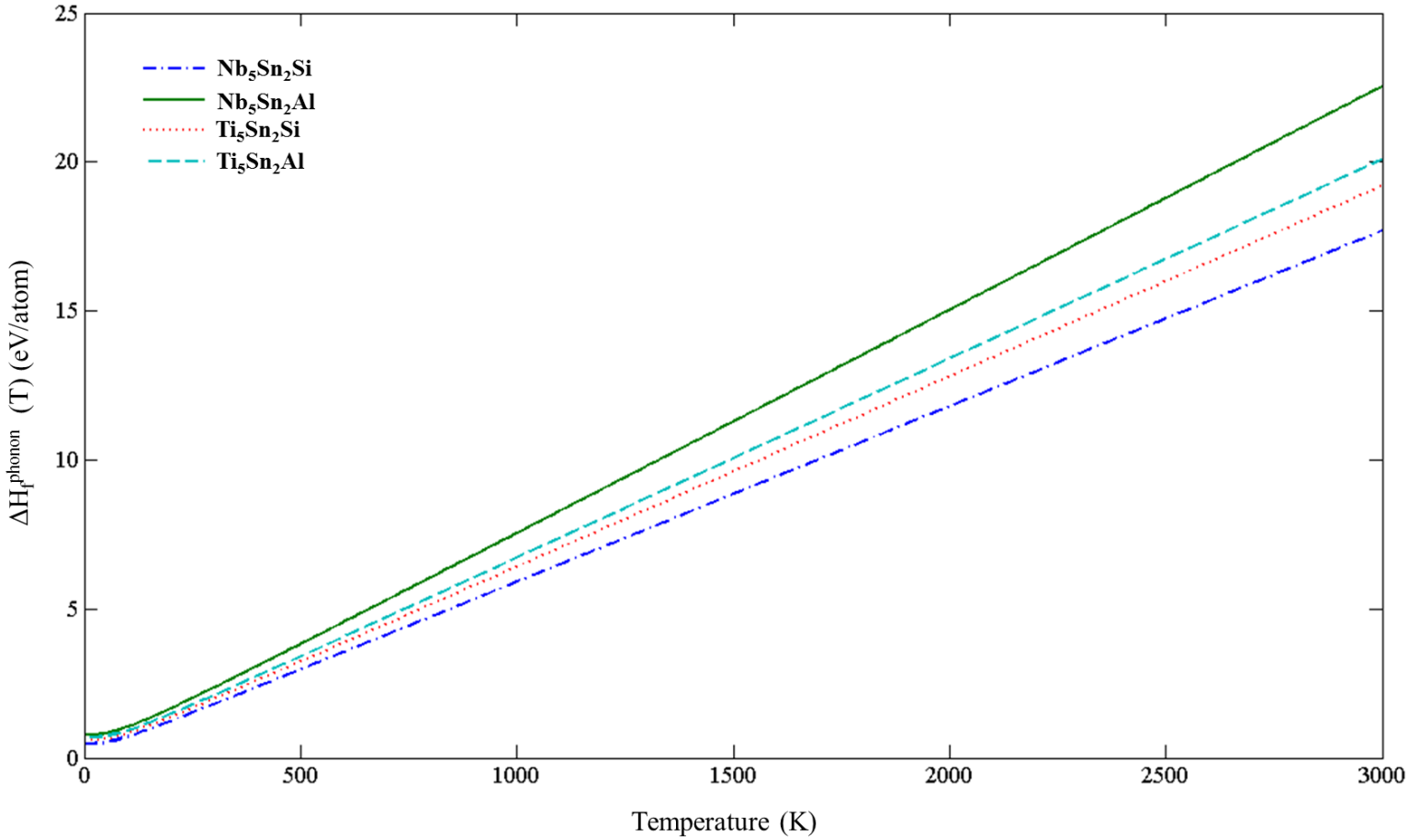

Fig. 8.3. Phonon contribution to enthalpies of formation of Nb_5Sn_2Si, Ti_5Sn_2Si, Nb_5Sn_2Al and Ti_5Sn_2Al.

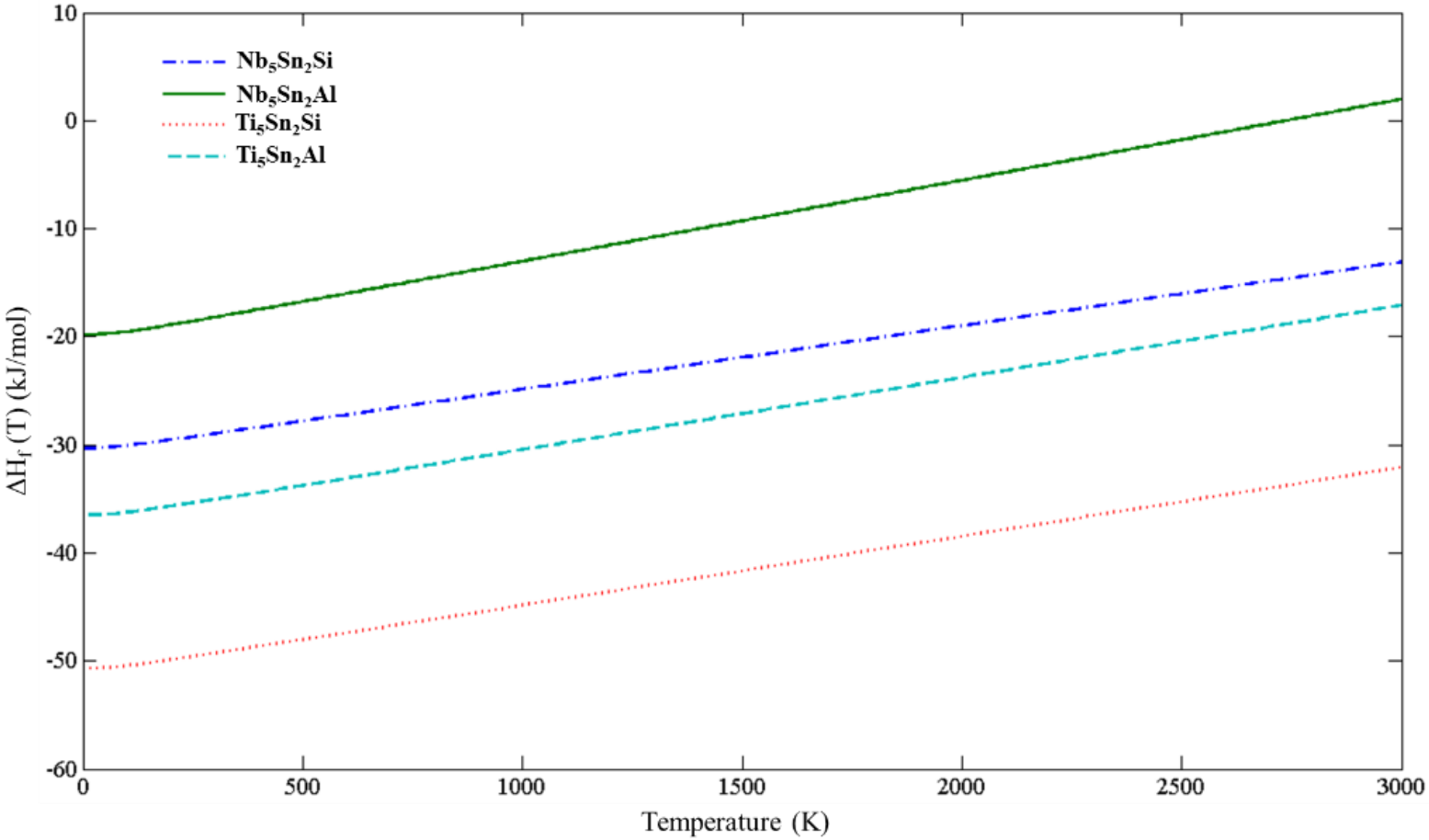

Fig. 8.4. Enthalpies of formation of Nb_5Sn_2Si, Ti_5Sn_2Si, Nb_5Sn_2Al and Ti_5Sn_2Al.

8.4. Conclusions

First principles calculations were carried out for the Nb_5Sn_2Al, Ti_5Sn_2Si, Ti_5Sn_2Al and Nb_5Sn_2Si intermetallic compounds and their constituent elements. Elastic constants, bulk, shear and Young's moduli, Poisson's ratio and Debye temperature were calculated for the first time. The temperature dependence of free energy and enthalpy of formation of the intermetallic phases is reported for the first time. The Nb_5Sn_2Al and Ti_5Sn_2Si are the most and less ductile phases, respectively. The Nb_5Sn_2Si phase is the stiffest and most resistant to uniform compression and to reversible deformation upon shear strain.

9

Phase equilibria in Nb-Si-Sn ternary alloys at 900 °C and 1200 °C

9.1 Introduction

According to Sun et al. [71] in the Nb-Si-Sn ternary system there are eight stable intermetallics. Three of those are in the Nb-Sn system and are Nb_3Sn, Nb_6Sn_5 and $NbSn_2$. The ab initio study of these phases was presented in chapter 5. The Nb_3Sn (Pm3n, cP8, Cr_3Si) has a primitive cell of 8 atoms. The phase melts at 2647 K and has a wide compositional range for Sn. Nb_6Sn_5 has a D2H-25 orthorhombic structure (I*mmm*, oI48, αTi_5Si_3) with a primitive cell of 22 atoms and a melting temperature of 1180 K. $NbSn_2$ is D2H-24 orthorhombic (F*ddd*, *oI*48, $CuMg_2$) with its primitive cell containing 12 atoms and melting temperature at 1100 K. The other four phases exist in the Nb-Si binary system and are the Nb_3Si (*tP*32, P42/n, Ti_3P), which is stable above 2038 K, the αNb_5Si_3 (*tI*32, $D8_1$, Cr_5B_3), which transforms to βNb_5Si_3 (*tI*32, $D8_m$, W_5Si_3), with upper and lower transformation temperatures of 2208 and 1918 K, respectively, and the $NbSi_2$ (*hP*9, C40, $CrSi_2$) which is stable below 2208 K. The ab initio study of the intermetallics of this system was presented in chapter 4. The final stable intermetallic is a ternary phase, Nb_5SiSn_2 (I4/*mcm*, D8m,W_5Si_3). This phase was studied in the previous chapter together with other TM_5Sn_2X compounds (TM=Nb, Ti and X=Al,Si)

Sun et al. introduced a thermodynamic description of the Nb-Si-Sn system based on previous experimental work by Waterstrat and Muller [72], Vellios and Tsakiropoulos [19] and Horyn et al. [73]. The 900 °C Nb-rich isothermal section of the system [71] can be seen in Fig. 2.4. The Nb_5Sn_2Si is a ternary compound which Sun et al. [71] treated as stoichiometric and was modelled to be stable up to and 900 °C (1473 K), which agreed with the experimental findings of Horyn and Lukaszewicz [73]. No comprehensive experimental evidence about the temperature range of the stability of this compound exist.

The alloys IP2 (Nb-16Si-13Sn) and IP3 (Nb-18Si-17Sn) in this research were manufactured to verify the stable phases (in particular the Nb_5Sn_2Si intermetallic) and the phase equilibria in the Nb-Si-Sn ternary system.

9.2. Results

9.2.1. Alloy Nb-16Si-13Sn (IP2)

As cast. According to the XRD data (Fig. 9.1) and the SEM (Fig. 9.2 (a-b)) the microstructure of IP2-AC consists of Nb_5Si_3, $Nb_3(Sn,Si)$ and Sn solid solution. The XRD data suggests that both the βNb_5Si_3 and the αNb_5Si_3 were present in the as cast alloy. Macrosegregation of Sn was evident throughout the ingot (Fig. 9.2 (a)), while a fine lamellar eutectic between the Nb_3Sn and Nb_5Si_3 was formed (Fig. 9.2 (b)). The compositions of the constituent phases in the IP2-AC are shown in Table 9.1. Tin content in Nb_5Si_3 was ~1.2 at. %. The Si/Sn ratio in $Nb_3(Sn,Si)$ was ~1.1 with the Si+Sn content being 26.1 at. %.

Heat treated. The alloy was given two separate heat treatments, at 900 ^{0}C for 100 h (IP2-HT-900 ^{0}C/100h) and at 1200 ^{0}C for 300 h (IP2-HT-1200 ^{0}C/300h). After the heat treatment at 900 ^{0}C for 100 hours the aforementioned phases were present together with the Nb_5Sn_2Si and Nb_6Sn_5 intermetallics (Fig. 9.3). This was confirmed by XRD (Fig. 9.1). According to the XRD data the number of peaks corresponding to βNb_5Si_3 was significantly reduced compared with the as cast alloy. According to the chemical analysis (Table 9.1) the Sn content in the Nb_5Si_3 and Nb_6Sn_5 was ~1.6 and ~44.4 at. %, respectively. The Si/Sn ratio in $Nb_3(Sn,Si)$ was ~1 with the Si+Sn content being 27.4 at. %. The chemical analysis of Nb_5Sn_2Si showed that it deviated slightly from its stoichiometric composition, namely 60.7 at. % Nb- 25.8 at. % Sn- 13.5 at. % Si instead of 62.5 at. % Nb- 25 at. % Sn-12.5 at. % Si.

The ternary Nb_5Sn_2Si phase always formed next to large areas of solid solution of Sn (Fig. 9.3). A boundary separating the areas containing $Nb_3(Sn,Si)$ and Nb_5Sn_2Si formed, as can be seen in the X-ray line scan in Fig. 9.4 and the X-ray element maps in Fig. 9.5. The concentration of Sn drops when moving across the boundary from the Nb_5SiSn_2 region to the $Nb_3(Si,Sn)$ region. Nb_6Sn_5 formed in areas where Sn_{ss} was in the as cast alloy, as it can be seen in Fig. 9.3. Finally, the fine lamellar eutectic observed in IP2-AC was still evident in the microsctructure.

To investigate the temperature range of the Nb_5Sn_2Si phase, the IP2 alloy was annealed at 1200 ^{0}C. The alloy was heat treated for 300 hours in order to ensure that the composition was closest to the phase equilibrium. After heat treatment, the large

area analysis showed that the average overall Sn content was ~12 at. %, confirming that significant Sn was not volatilised and that the alloy remained in the same compositional range. The typical microstructure of the IP2-HT-1200 ^{0}C /300h alloy is shown in Fig. 9.6. The XRD (Fig. 9.1) and EDS (Table 9.1) data confirm that the present phases were the Nb_3Sn and Nb_5Si_3. The XRD also suggested that only the αNb_5Si_3 phase was present. Regarding the Nb_5Sn_2Si, it can be deduced from the EDS and the XRD results that it was not stable at 1200 ºC at this composition. In the BSE images (Fig. 9.6) and the X-Ray element maps (Fig. 9.7) it can be seen that no Sn_{ss} remained, while the fine eutectic between the αNb_5Si_3 and the Nb_3Sn was still evident. The Si/Sn ratio in $Nb_3(Sn,Si)$ was ~0.4 while the Si+Sn content was ~23 at. %.

Due to the presence of Sn that melts at low temperatures, it is difficult to obtain homogeneity in these alloys using the arc melting technique. In order to investigate the equilibria between different phases and the stability of the phase fields, large area analyses were performed and compared with the calculated phase diagram of Sun et al. [71]. The areas analysed in IP2-HT-900 ^{0}C/100h are shown in Figure 9.8 (a). Taking into account the segregation of Sn, especially for areas 2, 3 and 4 it can be seen that the experimental results regarding the phase fields are in good accordance with the phase diagram given by Sun et al [71], and as such although the sample shows segregation it can be used to verify equilibrium phase fields.

Table 9.1.

Data from EDS analysis for the composition of the phases in IP2-AC, IP2-HT-900 ^{0}C/100h, IP2-HT-1200 ^{0}C/300h, IP3-AC, IP3-HT-900 ^{0}C/100h and IP3-HT-900 ^{0}C/200h.

	Nb (at. %)	Si (at. %)	Sn (at. %)
IP2-AC			
$Nb_3(Sn,Si)$	73.9 ± 0.3	13.5 ± 0.2	12.6 ± 0.1
Nb_5Si_3	63.9 ± 0.2	34.9 ± 0.1	1.2 ± 0.1
IP2-HT-900 ^{0}C/100h			
$Nb_3(Sn,Si)$	72.6 ± 0.1	13.6 ± 0.1	13.8 ± 0.1
Nb_5Sn_2Si	60.7 ± 0.2	13.6 ± 0.2	25.8 ± 0.1
Nb_5Si_3	62.3 ± 0.2	36.1 ± 0.1	1.6 ± 0.1
Nb_6Sn_5	54.3 ± 0.1	1.3 ± 0.1	44.4 ± 0.1
IP2-HT-1200 ^{0}C/300h			
$Nb_3(Sn,Si)$	77.1 ± 0.1	6.1 ± 0.1	16.8 ± 0.2
Nb_5Si_3	63.3 ± 0.3	33.3 ± 0.3	3.5 ± 0.2
IP3-AC			
$Nb_3(Sn,Si)$	73.1 ± 0.1	13.9 ± 0.4	13.0 ± 0.2
Nb_5Si_3	62.8 ± 0.6	35.4 ± 0.2	1.8 ± 0.2
Nb_5Sn_2Si	60.2 ± 0.3	13.4 ± 0.1	26.4 ± 0.3
IP3-HT-900 ^{0}C/100h			
$Nb_3(Sn,Si)$	74.9 ± 0.2	12.6 ± 0.3	12.5 ± 0.1
Nb_5Sn_2Si	61.5 ± 0.4	13.2 ± 0.1	25.3 ± 0.2
Nb_5Si_3	62.5 ± 0.4	35.7 ± 0.5	1.8 ± 0.2
Nb_6Sn_5	55.4 ± 0.1	0.6 ± 0.1	44.0 ± 0.1
IP3-HT-900 ^{0}C/200h			
$Nb_3(Sn,Si)$	74.8 ± 0.3	12.7 ± 0.1	12.5 ± 0.2
Nb_5Sn_2Si	62.3 ± 0.2	12.7 ± 0.2	25.0 ± 0.5
Nb_5Si_3	63.5 ± 0.5	35.0 ± 0.5	1.4 ± 0.2
Nb_6Sn_5	53.7 ± 0.3	0.5 ± 0.2	45.8 ± 0.1

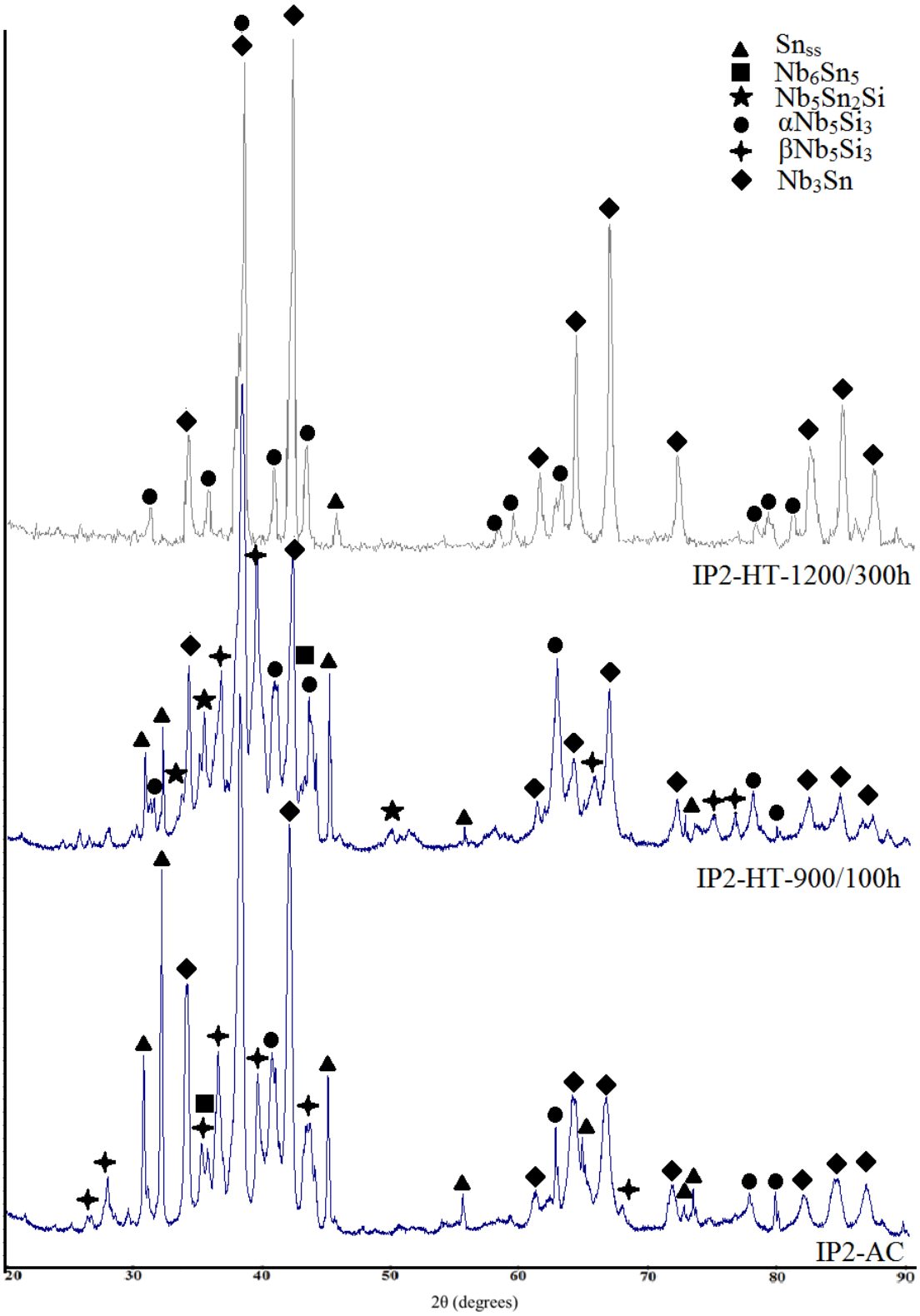

Fig. 9.1. XRD diffractograms of IP2-AC, IP2-HT-900 ^{0}C /100h and IP2-HT-1200 ^{0}C /300h

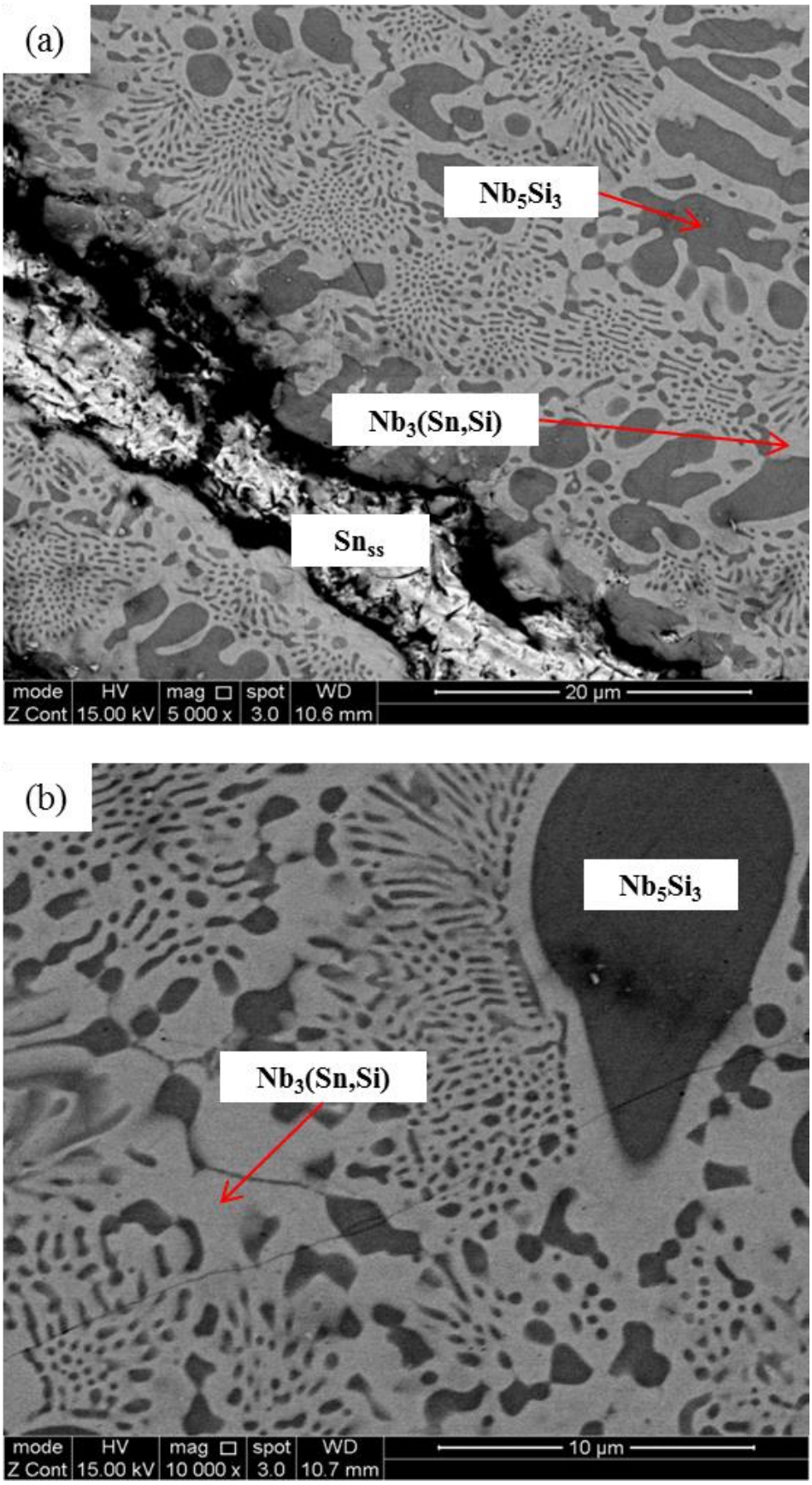

Fig. 9.2. BSE images of IP2-AC showing the macrosegregation of Sn (a) and the fine lamellar eutectic between Nb_5Si_3 and Nb_3Sn (a and b).

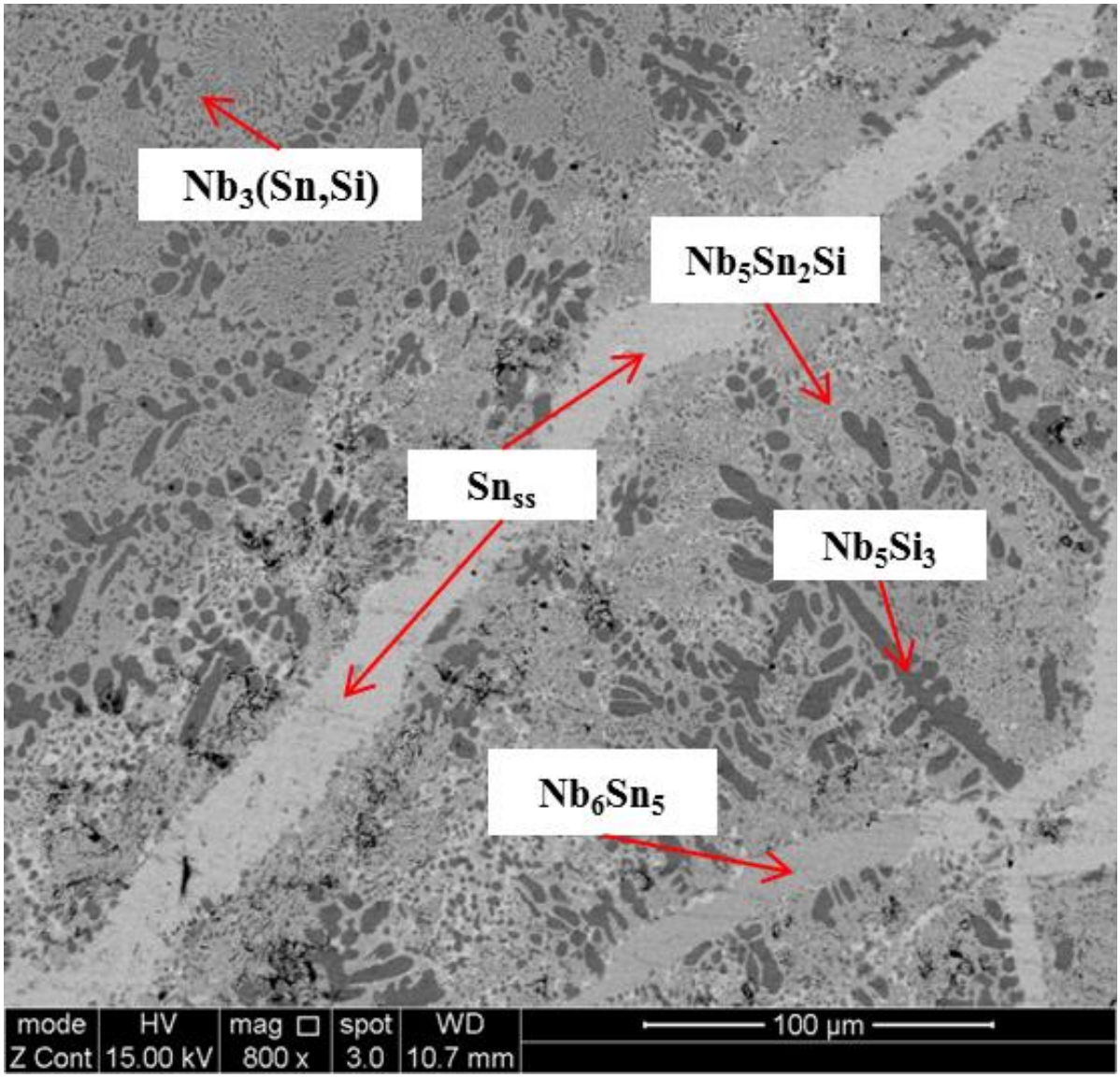

Fig. 9.3. BSE image of IP2-HT-900 ^{0}C/100h.

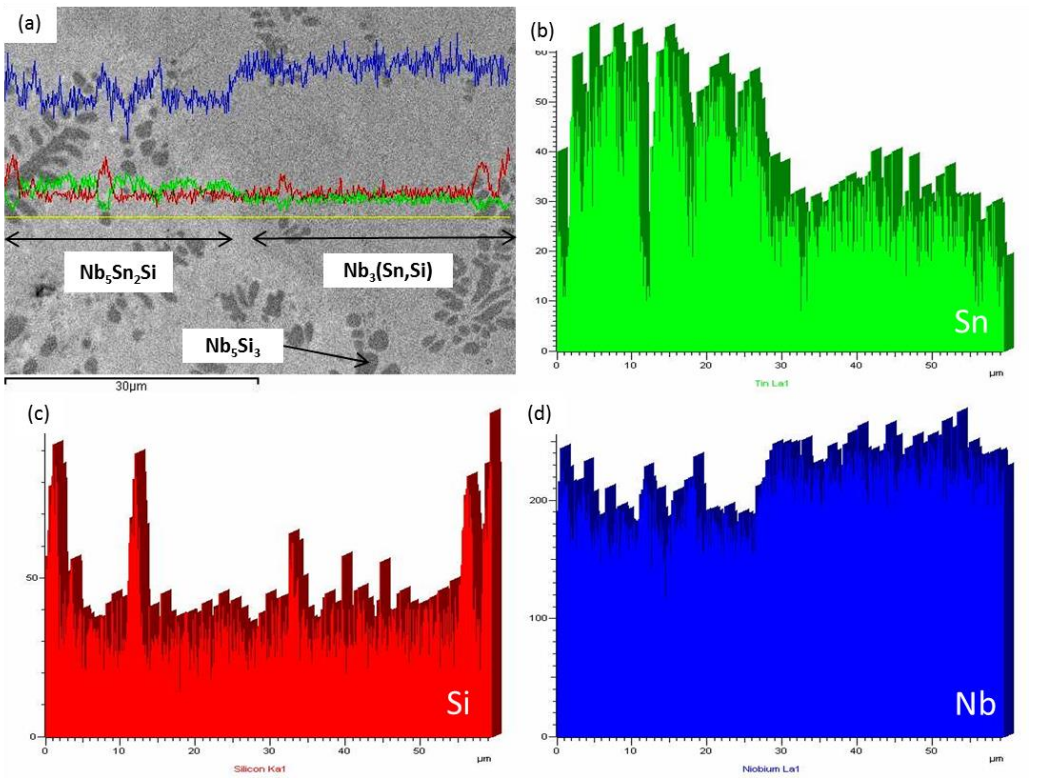

Fig. 9.4. (a) BSE image of IP2-HT 900 ^{0}C/100h and (b), (c), (d) X-ray line scan of Sn, Si, and Nb, respectively.

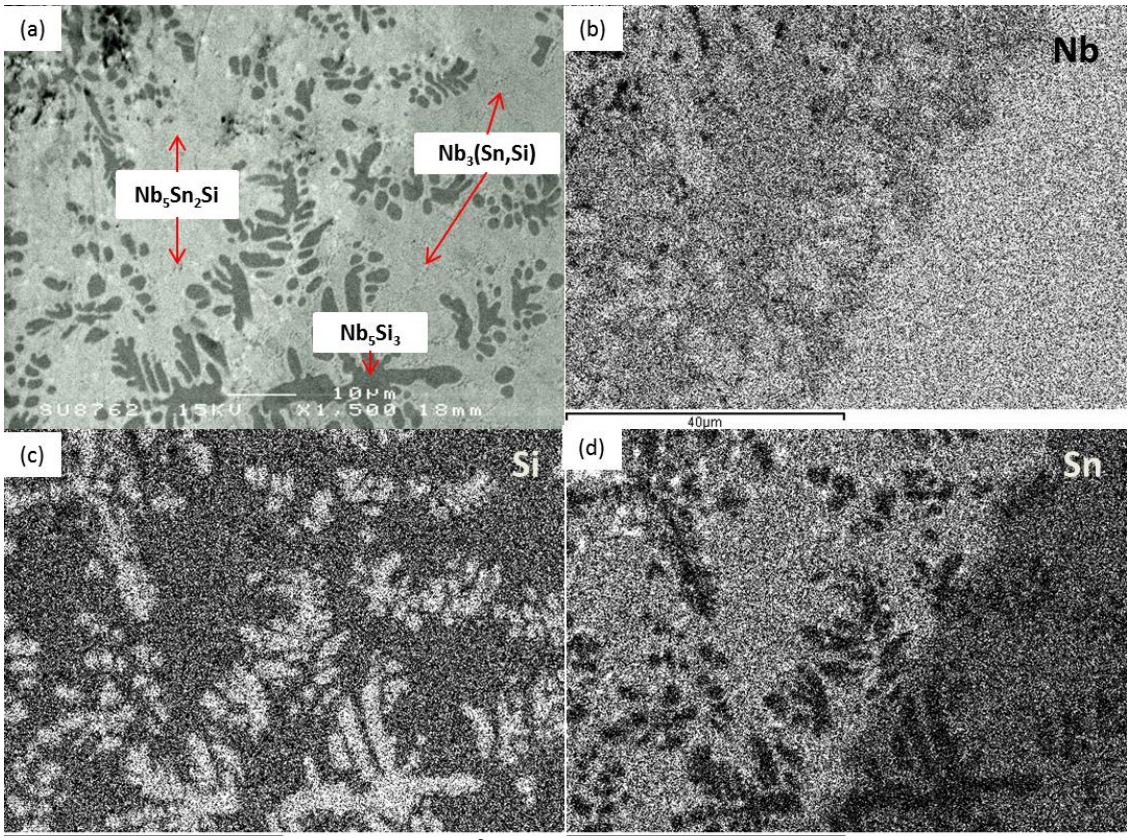

Fig. 9.5. (a) BSE image of IP2-HT-900 ^{0}C/100h and (b), (c), (d) X-ray element map of Nb, Si, and Sn respectively. The interface between Nb_5Sn_2Si and $Nb_3(Sn,Si)$ is clear in Nb (b) and Sn (d) maps.

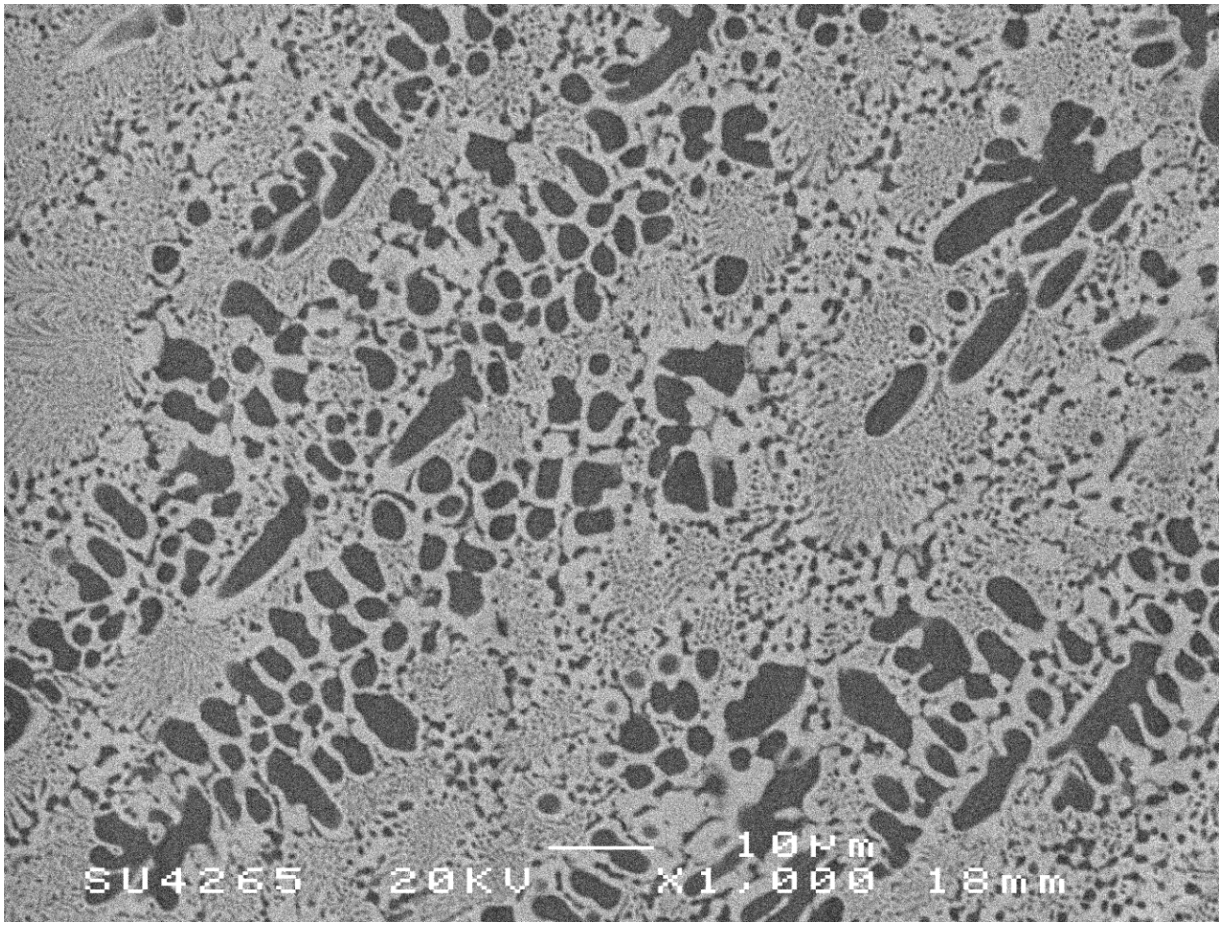

Fig. 9.6. BSE image showing the typical microstructure of IP2-HT-1200 ^{0}C /300h.

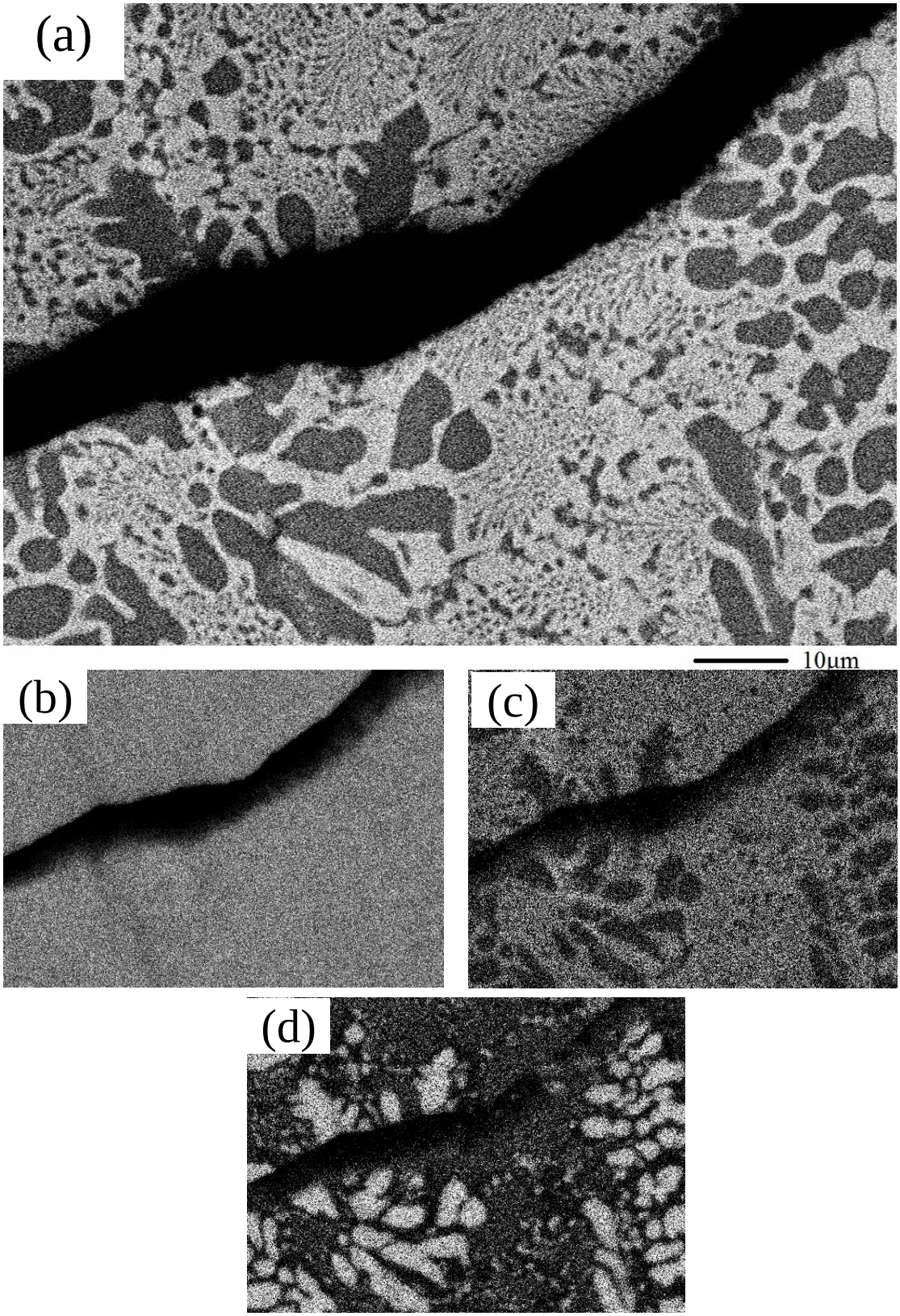

Fig. 9.7. (a) BSE image of IP2-HT-1200 ^{0}C /300h and (b), (c), (d) X-ray element map of Nb, Sn, and Si, respectively. The dark area in (a) is the area that Sn occupied in the as cast alloy.

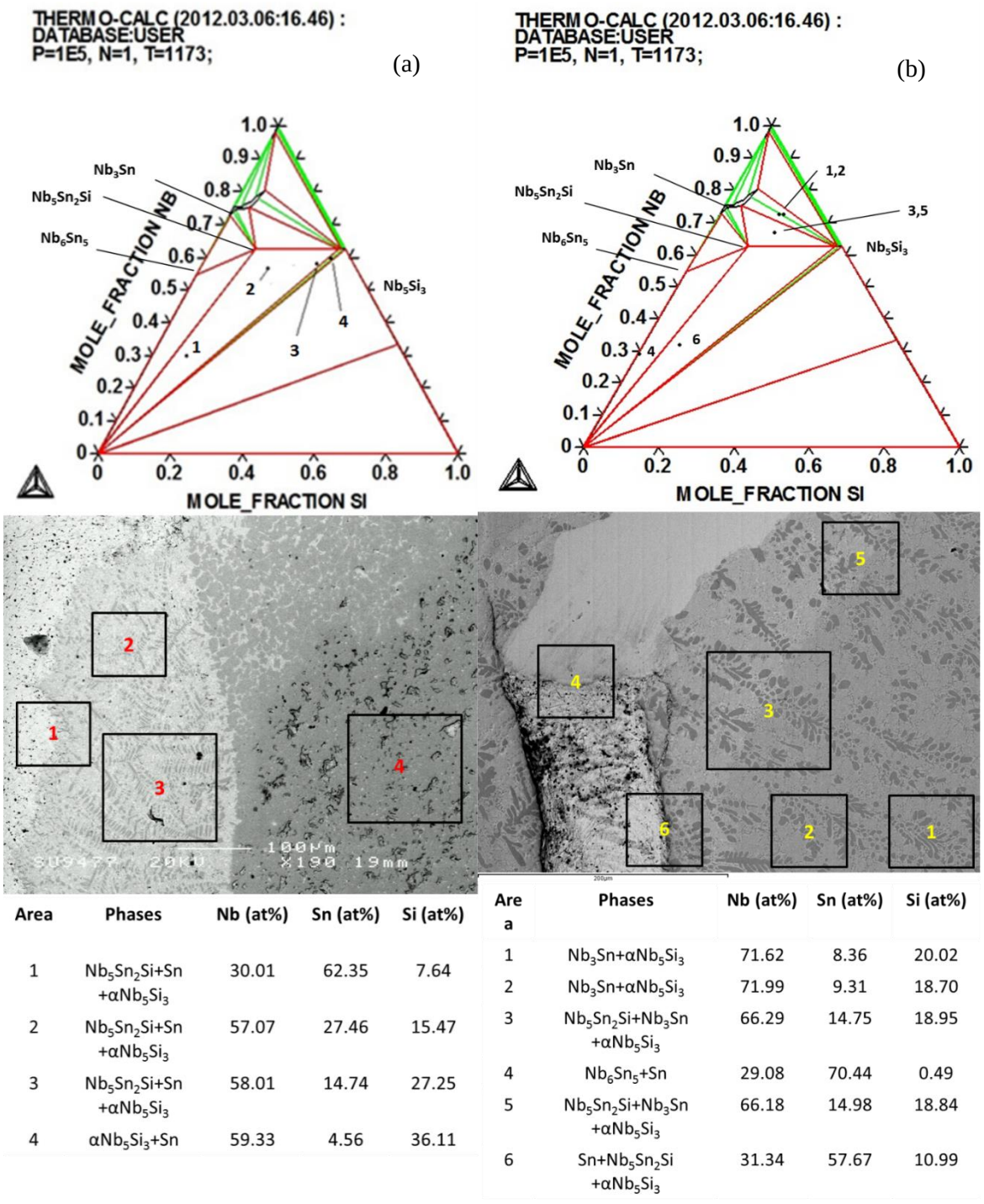

Area	Phases	Nb (at%)	Sn (at%)	Si (at%)
1	Nb_5Sn_2Si+Sn +αNb_5Si_3	30.01	62.35	7.64
2	Nb_5Sn_2Si+Sn +αNb_5Si_3	57.07	27.46	15.47
3	Nb_5Sn_2Si+Sn +αNb_5Si_3	58.01	14.74	27.25
4	αNb_5Si_3+Sn	59.33	4.56	36.11

Area	Phases	Nb (at%)	Sn (at%)	Si (at%)
1	Nb_3Sn+αNb_5Si_3	71.62	8.36	20.02
2	Nb_3Sn+αNb_5Si_3	71.99	9.31	18.70
3	Nb_5Sn_2Si+Nb_3Sn +αNb_5Si_3	66.29	14.75	18.95
4	Nb_6Sn_5+Sn	29.08	70.44	0.49
5	Nb_5Sn_2Si+Nb_3Sn +αNb_5Si_3	66.18	14.98	18.84
6	Sn+Nb_5Sn_2Si +αNb_5Si_3	31.34	57.67	10.99

Fig. 9.8. Area analyses of (a) IP2-HT-900 ^{0}C/100h and (b) IP3-HT-900 ^{0}C/200h. Due to the presence of Sn that has low melting point, bulk equilibrium was difficult to achieve, but the local equilibria were in good agreement with Sun et al. [71].

9.2.2. Alloy Nb-18Si-17Sn (IP3)

As cast. From XRD (Fig. 9.9) and EDS data (Table 9.1) it can be seen that in IP3-AC the phases that were present were Sn_{ss}, $Nb_3(Sn,Si)$, βNb_5Si_3 and Nb_5Sn_2Si. According to the XRD (Fig. 9.9) both the αNb_5Si_3 and βNb_5Si_3 were present in the as cast alloy. Macrosegregation of Sn (Fig. 9.10 (a)) and a fine eutectic structure consisting of $Nb_3(Sn,Si)$ and Nb_5Si_3 were again observed (Fig. 9.10 (b)). The Nb_5Sn_2Si phase formed a zone between the solid solution of Sn and the $Nb_3(Sn,Si)$ phase (Fig. 9.10 (a)). The compositions of the constituent phases in the IP3-AC are shown in Table 9.1. The Si/Sn ratio in $Nb_3(Sn,Si)$ was ~1.1 while the Si+Sn content was ~26.9 at. %. The Sn content in Nb_5Si_3 was 1.8 at. %. Sn and Si contents were slightly higher than the stoichiometry in Nb_5Sn_2Si phase (26.4 at. % Sn-13.4 at. % Si).

Heat treated. The alloy was given 2 separate heat treatments; IP3 was heat treated at 900 ^{0}C for 100 h (IP3-HT-900 ^{0}C/100h) and subsequently for an extra 100 h to achieve conditions closer to equilibrium (IP3-HT-900 ^{0}C/200h). In IP3-HT-900 ^{0}C/100h, XRD (Fig. 9.9) indicates that all phases were still present, including both the αNb_5Si_3 and βNb_5Si_3. In addition, Nb_6Sn_5 formed in some areas next to the Sn solid solution and the volume fraction of the Nb_5Sn_2Si phase increased, as shown in Fig. 9.11. Microscopy showed the fine eutectic between $Nb_3(Sn,Si)$ and Nb_5Si_3 was still evident. The compositions of the constituent phases in IP3- 900 ^{0}C/100h can be found in Table 9.1. The Sn content in Nb_5Si_3 was 1.8 at. %. In the $Nb_3(Sn,Si)$ phase the ratio Si/Sn was approximately 1 and Si+Sn was 25.1 at. %. The Si content in Nb_6Sn_5 was ~ 0.6 at. %. In Nb_5Sn_2Si the Sn and Si contents were 25.3 and 13.2 at. %, respectively.

Following additional 100 h heat treatment at 900^{0}C (IP3-HT-900 ^{0}C/200h) the Sn_{ss} and Nb_6Sn_5 fractions were significantly reduced and in many areas of the specimen only traces were observed. In contrast the fraction of Nb_5Sn_2Si increased (Fig. 9.12 and 9.13). The fine eutectic lamellar structure between $Nb_3(Si,Sn)$ and Nb_5Si_3 was again still evident but according to XRD only the αNb_5Si_3 phase remained. The composition of phases is shown in Table 9.1. The Sn concentration in Nb_5Si_3 was ~ 1.4 at. %. The Si content of remaining Nb_6Sn_5 was ~ 0.5 at. %. The Nb_5Sn_2Si phase was close to its stoichiometric composition (62.3 at. % Nb- 25 at. % Sn-12.7 at. % Si).

Again, due to the partitioning of Sn (shown in the Sn X-ray element maps in Fig. 9.12 (b),(f)), area analyses of the IP3-HT-900 ^{0}C/100h were conducted in order to confirm the phase equilibria in the ternary system from the local equilibria (Fig. 9.8 (b)). It can be seen that all the experimental data (presented as points in the 900 ^{0}C Nb-Si-Sn isotherm) are in good agreement with the calculated diagram by Sun et al. [71].

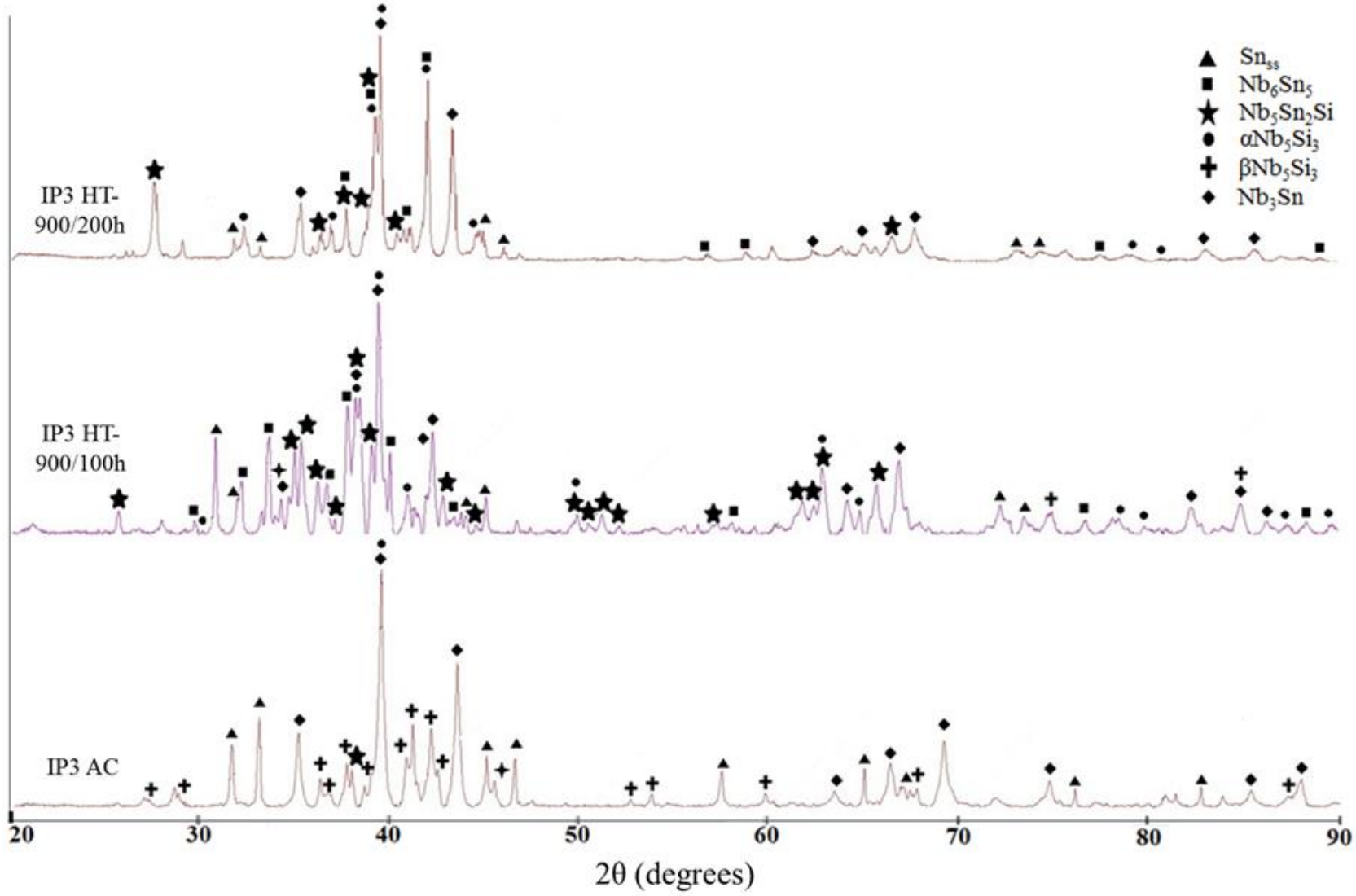

Fig. 9.9. XRD diffractograms of the IP3 alloys in the as cast and heat treated conditions.

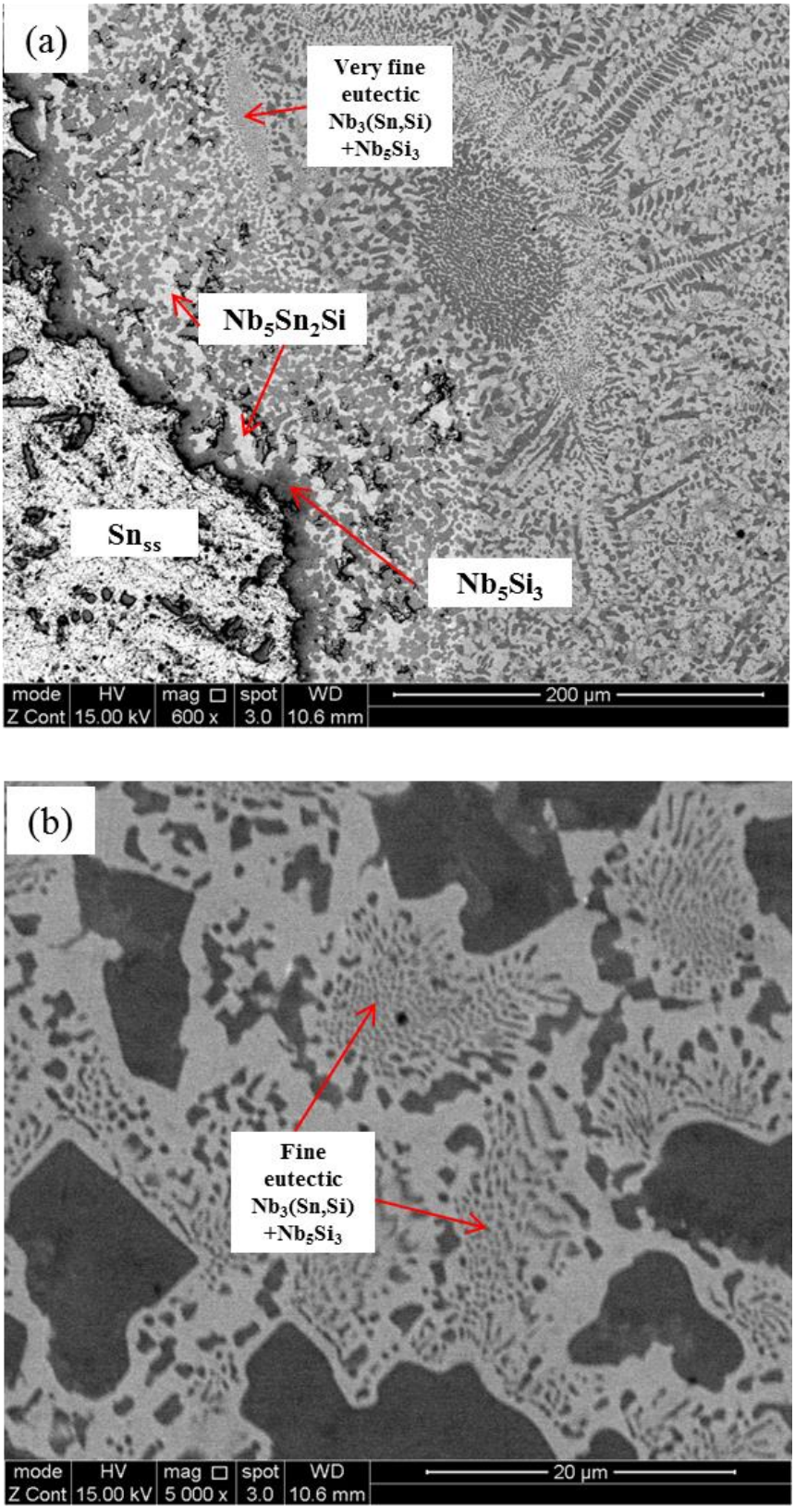

Fig. 9.10. BSE images showing the microstructure close to the area of Sn_{ss} (a) and the fine eutectic (a and b) in the IP3-AC.

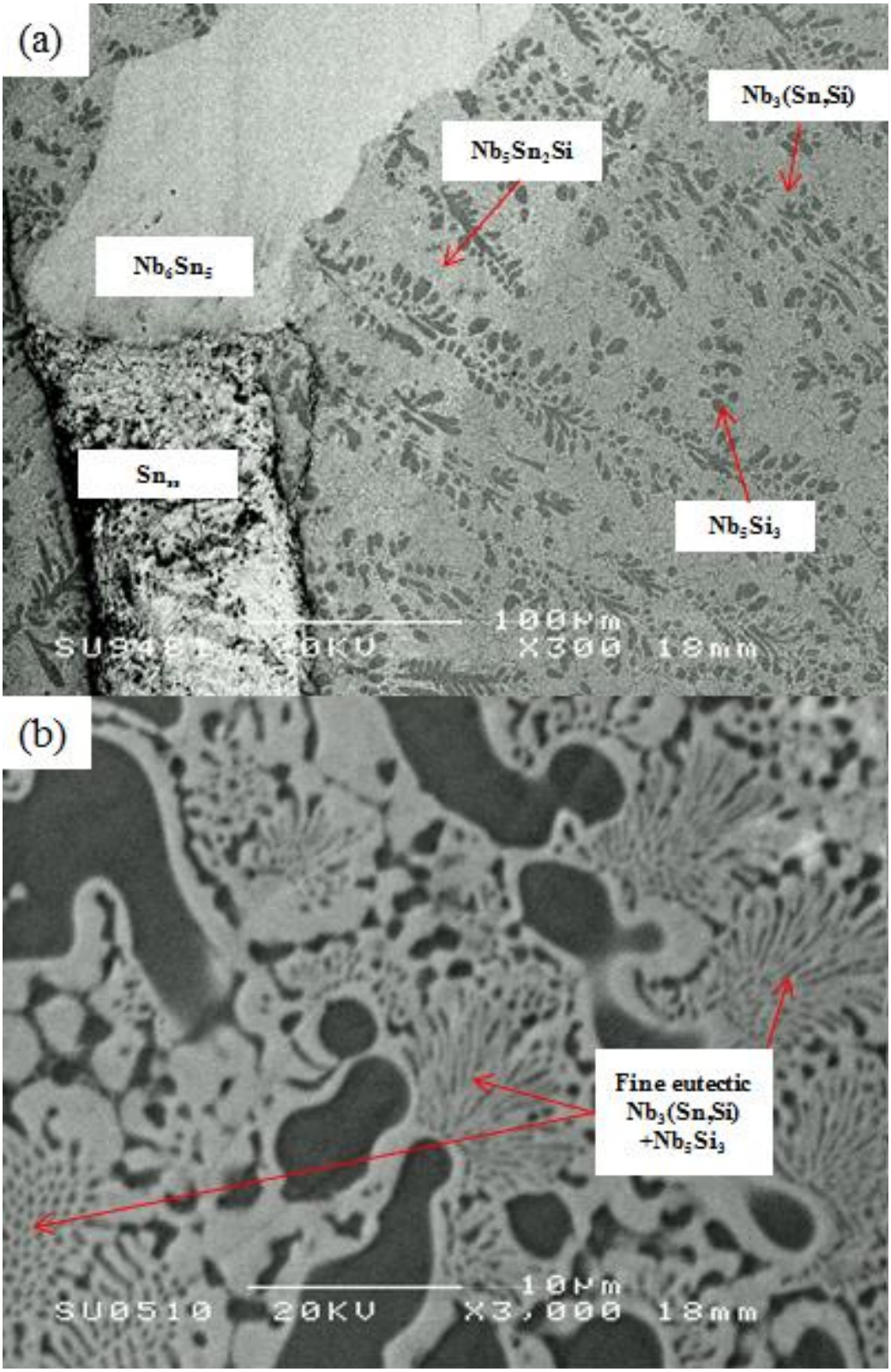

Fig. 9.11. BSE images of IP3-HT-900 ^{0}C/100h microstructure

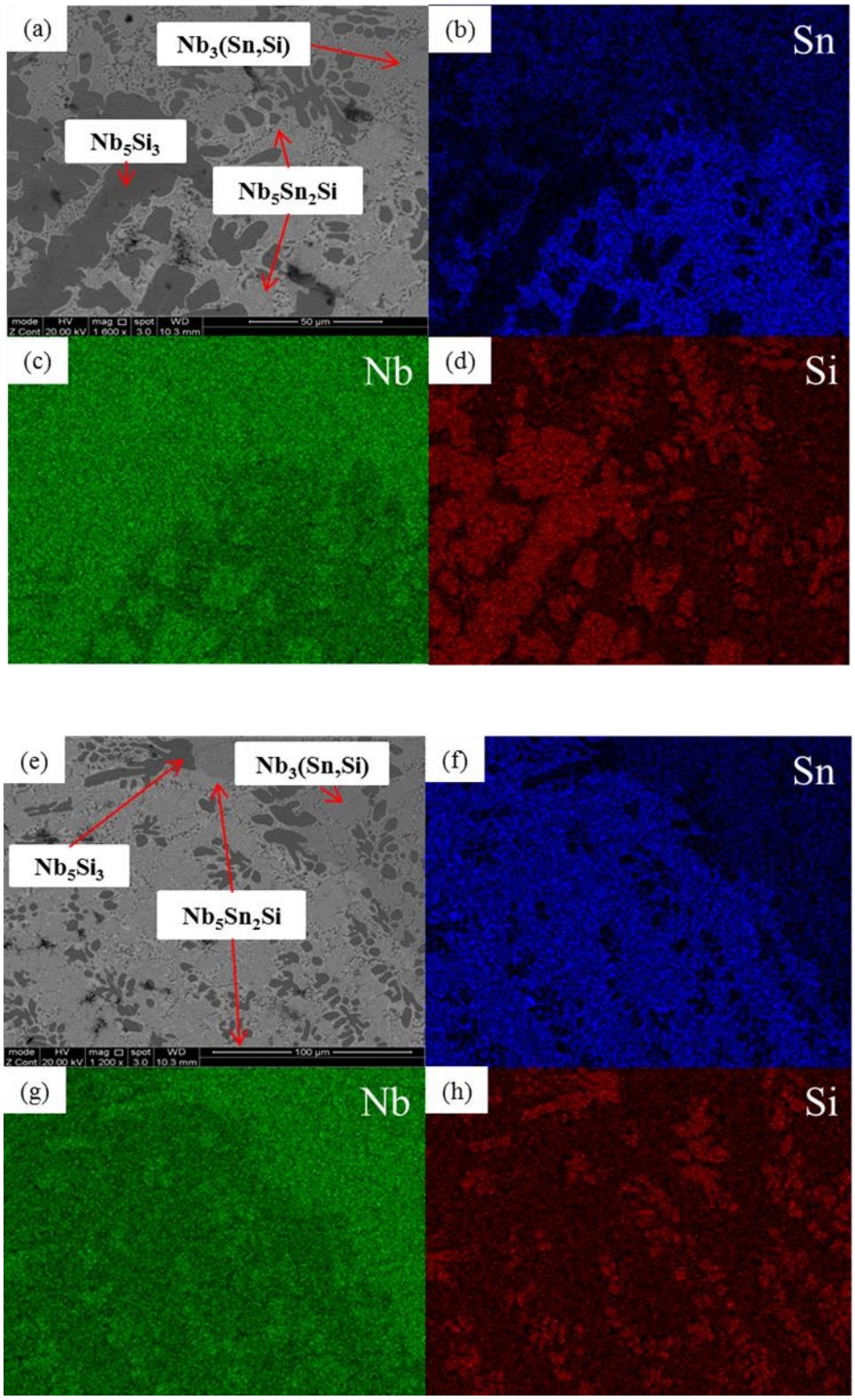

Fig. 9.12. (a),(e) BSE images of IP3-HT-900 ^{0}C/200h, (b),(f) element maps of Sn, (c),(g) element maps of Nb and (d),(h) element maps of Si.

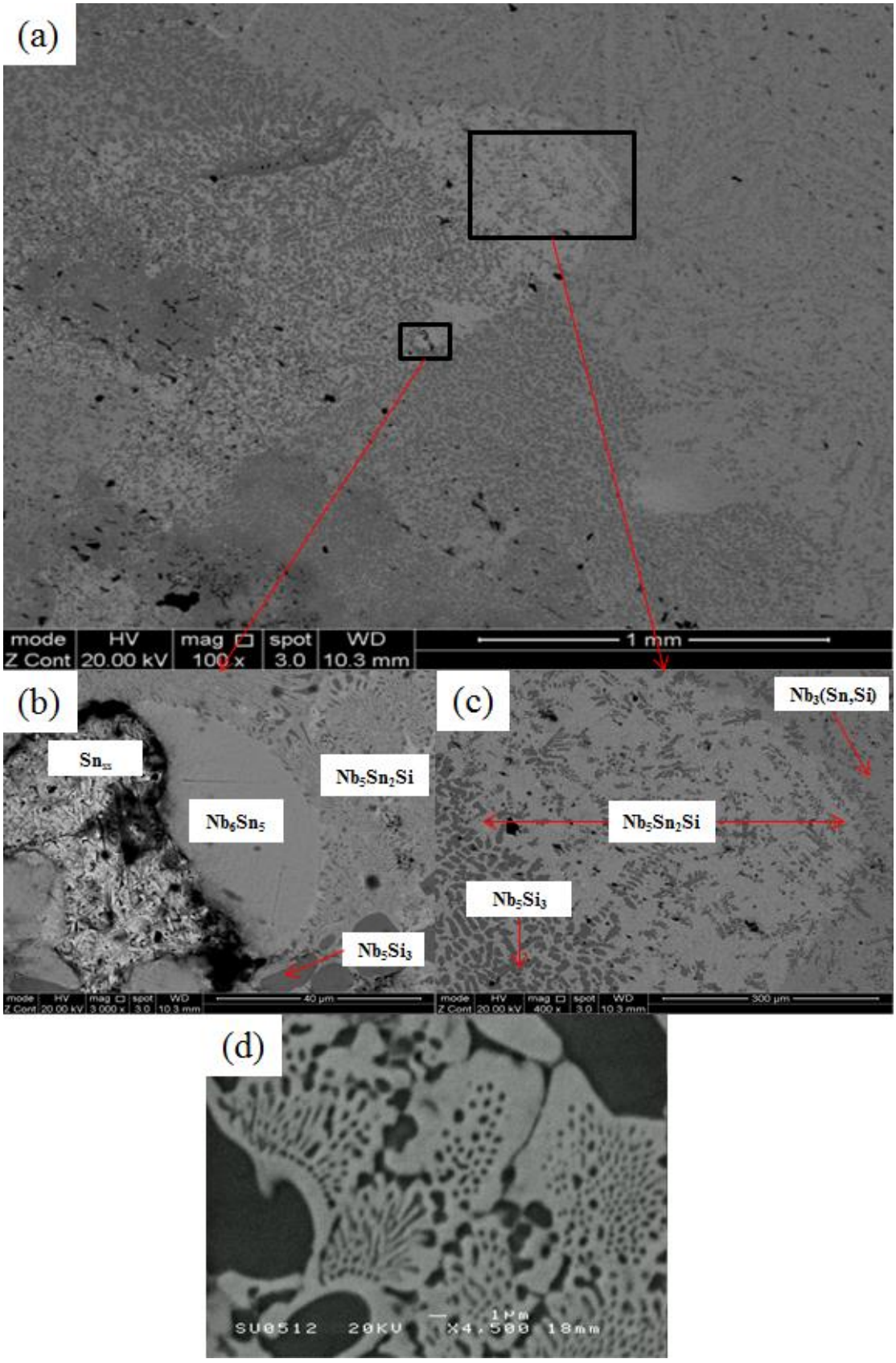

Fig. 9.13. BSE images of IP3-HT-900 ^{0}C/200h microstructure. Only traces of Sn_{ss} and Nb_6Sn_5 are evident in the microstructure

9.3 Discussion

The ternary compound, Nb_5Sn_2Si, was observed in IP2 and IP3 heat treated at 900°C and IP3 AC. In IP2-AC the ternary phase was not observed. A possible explanation for this is the lower content of Sn in the IP2 alloy (~ 13 at. %) compared with the IP3 alloy (~ 17 at. %). Thus, alloy IP3 is lower in the tie-triangle and closer to the Nb_5Sn_2Si phase, and as such will contain a greater amount of the phase. Microscopy showed that Nb_5Sn_2Si primarily formed next to regions of Sn_{ss}, forming a layer between Sn_{ss} and Nb_3Sn. After heat treatment the volume fraction of Nb_5Sn_2Si increased. The interface between Nb_3Sn and Nb_5Sn_2Si was seen to advance in the direction of Nb_3Sn, indicating the diffusion of Sn to react with Nb_3Sn. This, along with the simultaneous significant reduction of the volume fraction of the solid solution of Sn, indicates the Sn reacting with $Nb_3(Sn,Si)$ to form the Nb_5Sn_2Si phase. It is suggested that the reaction L(Sn) + $Nb_3(Sn,Si)$ → Nb_5Sn_2Si occurs.

At 1200 ºC the ternary Nb_5Sn_2Si was absent which agrees somewhat with the modelling of Sun et al. [71]. However, the exact decomposition temperature of this phase below 1200 °C was not established. The lack of the ternary phase at 1200 °C disagrees with the results of Geng et al. [36] and Knittel et al. [151] who reported the presence of this phase during oxidation at 1200 °C. This could be because the O stabilises the ternary phase at higher temperatures. At 1200 °C, the Sn content in the $Nb_3(Sn,Si)$ and Nb_5Si_3 phases was increased compared with the corresponding content in the as-cast alloy, which is in line with the decomposition of the Sn solid solution, the absence of the Nb_5Sn_2Si ternary compound and the fact that no significant volatilization of Sn occurred. The Si/Sn in the $Nb_3(Sn,Si)$ ratio in the IP2 alloy was significantly reduced to about 0.4 while the Sn solubility in Nb_5Si_3 increased compared with the as-cast as the Sn content rose from 1.2 to 3.5 at. %. The above indicate that the alloy entered the two phase region between Nb_3Sn and Nb_5Si_3 [71].

According to the XRD data the αNb_5Si_3 co-exists with βNb_5Si_3 in the as cast IP2 and IP3, while in the 100 hours heat treated alloys βNb_5Si_3 peaks were significantly decreased. In the IP3-HT-900 ^{0}C/200h no trace of βNb_5Si_3 was observed, only αNb_5Si_3 was seen. In IP2-HT-1200 ^{0}C/300h the βNb_5Si_3 was also fully transformed to αNb_5Si_3. This indicates that βNb_5Si_3 is the primary phase that forms during solidification, however αNb_5Si_3 is the equilibrium phase at 900 and 1200 °C.

The Nb_6Sn_5 phase was formed after the heat treatment adjacent to regions of Sn_{ss} in all the samples (except IP3-HT-900 ºC/200 h). It showed negligible solubility of Si. According to Toffolon et al. [28] it forms from the reaction L(Sn) + Nb_3Sn → Nb_6Sn_5 which occurs at 911 ^{0}C. This suggests that it is a metastable phase that forms from a reaction between the areas of unreacted Sn and equilibrium Nb_3Sn. Based on the equilibrium phase diagram modelled by Sun et al. [71], the equilibrium phases in IP2 at 900 ºC should be Nb_3Sn, αNb_5Si_3 and Nb_5Sn_2Si. The presence of Sn and Nb_6Sn_5 indicate non-equilibrium conditions owing to the difficulties of forming homogenous alloys using the arc melting technique, with elements with widely differing melting temperatures. Despite the fact that bulk equilibrium was difficult to achieve, the local equilibria were in good agreement with Sun et al. [71] (Fig. 9.8). In the case of IP3-900 ºC/300 h, heat treated for the longest period, the microstructure was closest to equilibrium conditions, and as such only traces of Sn and Nb_6Sn_5 were present.

According to the phase diagram of Nb-Si-Sn by Sun et al. [71] the solubility of Si in the Nb_3Sn phase at 900 ^{0}C is up to ~ 6 at. %. In contrast, in the present study silicon solubility was measured to be up to ~ 13 at. %. Results from the present work agree with Galasso et al. [145] and Vellios and Tsakiropoulos [19]. The Si/Sn ratio in the $Nb_3(Sn,Si)$ phase in IP2 and IP3 (as cast and heat treated alloys) was approximately 1.

The suggested solidification path of IP2-AC based on the observed microstructure is L → L + βNb_5Si_3 → L + βNb_5Si_3 + $Nb_3(Sn,Si)$)→ L + βNb_5Si_3 + $Nb_3(Sn,Si)$ + (Nb_5Si_3 + $Nb_3(Sn,Si)$)$_{eutectic}$ → Sn + βNb_5Si_3 + $Nb_3(Sn,Si)$ + (Nb_5Si_3 + $Nb_3(Sn,Si)$)$_{eutectic}$ with βNb_5Si_3 as the primary phase and some βNb_5Si_3 → αNb_5Si_3 transformation taking place during cooling as both αNb_5Si_3 and βNb_5Si_3 were observed in the as cast alloy . The corresponding path for IP3-AC is suggested to be L → L + βNb_5Si_3 → L + βNb_5Si_3 + $Nb_3(Sn,Si)$ → L + βNb_5Si_3 + $Nb_3(Sn,Si)$ + (Nb_5Si_3 + $Nb_3(Sn,Si)$)$_{eutectic}$ → L + βNb_5Si_3 + $Nb_3(Sn,Si)$ + (Nb_5Si_3 + $Nb_3(Sn,Si)$)$_{eutectic}$ + Nb_5Sn_2Si→ Sn + βNb_5Si_3 + $Nb_3(Sn,Si)$ + (Nb_5Si_3 + $Nb_3(Sn,Si)$)$_{eutectic}$ + Nb_5Sn_2Si with some βNb_5Si_3 → αNb_5Si_3 transformation, as in IP2-AC.

The solidification path for IP2 and IP3 was calculated using the Scheil solidification [152] model which is integrated in Thermo-Calc [153], using data from [71]. The resulting path for both alloys was L → L + βNb_5Si_3 → L + βNb_5Si_3 + αNb_5Si_3 → L + αNb_5Si_3 + Nb_3Sn → L + Nb_3Sn→L + Nb_3Sn + Nb_5Sn_2Si→ Sn + Nb_3Sn + Nb_5Sn_2Si which is inconsistent with experimental data mainly regarding the absence of the 5-3 silicide in the final constitution of the as cast. This demonstrates the need to reoptimise

the thermodynamic database according to the experimental data obtained in the present work.

9.4 Conclusions

The as cast and heat treated alloys Nb-16Si-13Sn (IP2) and Nb-18Si-17Sn (IP3) were investigated. The conclusions of this study are as follows:

- The microstructure of IP2-AC consisted of $Nb_3(Sn,Si)$, Nb_5Si_3 and Sn. After the heat treatment at 900°C, $Nb_3(Sn,Si)$, Nb_5Si_3, Sn, Nb_6Sn_5 and Nb_5Sn_2Si were present. The equilibrium phases are considered to be $Nb_3(Si,Sn)$, αNb_5Si_3 and Nb_5Sn_2Si (Sn and Nb_6Sn_5 are metastable). After the heat treatment at 1200°C, $Nb_3(Sn,Si)$ and αNb_5Si_3 were present. The equilibrium phases are considered to be $Nb_3(Si,Sn)$ and αNb_5Si_3.
- The microstructure of IP3-AC consisted of $Nb_3(Sn,Si)$, Nb_5Sn_2Si, Nb_5Si_3 and Sn, while after the heat treatments $Nb_3(Sn,Si)$, Nb_5Si_3, Sn, Nb_6Sn_5 and Nb_5Sn_2Si were evident. The equilibrium phases are considered to be the same as in IP2 at 900 °C.
- The $\alpha(Nb,Ti)_5Si_3$ co-existed with $\beta(Nb,Ti)_5Si_3$ in the IP2-AC as well as in the IP3-AC, while after the heat treatment for 100 hours the transformation $(Nb,Ti)_5Si_3 \rightarrow \alpha(Nb,Ti)_5Si_3$ took place, with traces of $\beta(Nb,Ti)_5Si_3$ being left. In the IP3-HT-900 ^{0}C/200h only the $\alpha(Nb,Ti)_5Si_3$ was present which suggests that in 200 hours all the $\beta(Nb,Ti)_5Si_3$ transformed to $\alpha(Nb,Ti)_5Si_3$.
- A fine eutectic structure between $Nb_3(Sn,Si)$ and Nb_5Si_3 was evident in the IP2 and IP3 as cast as well as the heat treated alloys.
- The Nb_5Sn_2Si phase was present at 900 ºC and absent at 1200 ºC, indicating that the phase decomposes below 1200 ºC.

10

Phase equilibria in Nb-Al-Sn ternary alloys at 900 °C and 1200 °C

10.1. Introduction

To date the binary phase diagrams of the constituent elements have been thoroughly investigated experimentally and to the author's knowledge there is no data on ternary equilibria. As discussed in section 2.5.3, the Nb-Al system contains the phases $NbAl_3$, Nb_3Al and Nb_2Al [79]. The ab initio study of those intermetallics was presented in chapters 6 and 7. The Nb-Sn system consists of $NbSn_2$, Nb_6Sn_5 and Nb_3Sn [28] intermetallics. The ab initio study of this system was presented in chapter 5. The Sn-Si system has no intermetallic phases. Nb_3Al and Nb_3Sn are isomorphous (same A15 structure) and show complete solid solubility ($Nb_3Al_xSn_{1-x}$) [76]. Furthermore, the existence of a ternary compound with the stoichiometry Nb_5Sn_2Al has been reported by [75], but no comprehensive experimental data exist, especially regarding equilibrium data and temperature range of stability. Similarly to the Nb_5Sn_2Si phase discussed in Chapter 9, the Nb_5Sn_2Al intermetallic is reported to have the W_5Si_3 structure type which belongs to a wide range of ternary intermetallics (see chapter 8). It must be noted that as no data exists for the Nb_5Sn_2Al phase, the reflections in XRD were calculated from the lattice constants in [75] (Table B.2 in Appendix B).

The alloys IP4 (Nb-17Al -17Sn), IP5 (Nb-33Al-13Sn) and IP6 (Nb-16Al-20Sn) were manufactured for the current study. The aim was to verify the stable phases (in particular the Nb_5Sn_2Al compound) and establish the phase equilibria in the Nb-Al-Sn ternary system.

10.2. Results

10.2.1. Alloy Nb-17Al -17Sn (IP4)

As cast. The microstructure of the Nb-17Al-17Sn as cast alloy (IP4-AC) can be seen in Fig. 10.1 (a-b) and the compositions of the constituent phases are shown in Table 10.1. Primarily, large areas of Nb_3Sn were observed, while in the grain boundaries three other phases were formed; namely $NbSn_2$, $NbAl_3$ and Nb_2Al (Fig. 10.1 (a-b)). XRD confirmed the presence of these 4 phases (Fig. 10.2). The content of Al in Nb_3Sn was ~10 at. % while in $NbSn_2$ is ~7 at. %. The Sn content in $NbAl_3$ and Nb_2Al was about 4

at. % and 10 at. %, respectively. Areas of Sn-rich Nb_2Al were evident (Fig. 10.1b) with a Sn content of ~17 at. %. The Al/Sn ratio and Al+Sn sum in Nb_3Sn were 0.66 and 25.51 at. % respectively.

Heat treated. The alloy was given 3 separate heat treatments; 100 h at 900 °C, 200 h at 900 °C and 100 h at 1200 °C. In Fig. 10.1 (c-d) the microstructure after 100 hours at 900 ^{0}C is shown (IP4-HT-900 ^{0}C/ 100h). Similarly to the as cast sample, bulk areas of Nb_3Sn were evident, while at the grain boundaries $NbAl_3$ and Nb_2Al were present in addition to the Nb_5Sn_2Al ternary compound. $NbSn_2$ was not observed. XRD (10.2) confirmed the presence of these phases.

EDS maps of the microstructure of IP4-HT-900 ^{0}C/ 100h are shown in Fig. 10.3. Evidence of the ternary phase is clear in the Sn maps, where areas of high Sn concentrations are observed. The ternary phase was close to its stoichiometric formula 61.5 at% Nb - 13.6 at% Al -25 at% Sn. The Al concentration in Nb_3Sn was similar to the as cast. The Al/Sn ratio and Al+Sn sum in Nb_3Sn was 0.72 and 26.65 at. %, respectively. In Nb_2Al the Al concentration decreased by less than 4 at. %. Areas of Sn-rich Nb_2Al were again observed, with the Sn and Al contents being about 17 and 19 at. %, respectively. The $NbAl_3$ phase became poorer in Sn and was always surrounded by areas containing Nb_5Sn_2Al (Figures 10.1 (d), 10.3).

IP4 was heat treated for a further 100 hours at 900 ^{0}C to see if equilibrium could be achieved. The same constituent phases were present in the alloy IP4-HT-900 ^{0}C/ 200h (Fig. 10.1 (e-f)). No significant changes occurred in the compositions of the phases (Table 10.1). The Al/Sn ratio (0.75) and Al+Sn sum (26.72 at. %) for Nb_3Sn was also unchanged. However some features of the grain boundaries were altered. At the grain boundaries only remnants of $NbAl_3$ were evident. Pores were observed where $NbAl_3$ previously existed (10.1 (f)). Comparing XRD patterns it appears that $NbAl_3$ peaks are less intense after heat treatment while those attributed to Nb_3Sn and Nb_2Al are more intense (Fig 10.2).

IP4 was also heat treated at 1200 ^{0}C for 100 hours. The microstructure consisted primarily of two phases, Nb_2Al and Nb_3Sn. Areas of Sn-rich and very Sn-rich Nb_2Al phase were evident throughout the alloy, as can be seen in Fig. 10.1 (g-h). Sn content varied between ~2-6 at. % and ~18 at. %. The Al content in Nb_3Sn was ~9.5 at. %, which was slightly less than in the as cast and the heat treated alloys at 900 ^{0}C. The

ratio of Al/Sn was 0.61 and the Al+Sn sum 24.98 at. % in Nb_3Sn, which was again slightly less than measured in the as cast and 900 °C heat treated alloy.

Table 10.1
Data from EDS analysis for the composition of the phases in IP4-AC, IP4-HT-900 ^{0}C/100h, IP4-HT-900 ^{0}C/200h and IP4-HT-1200 ^{0}C/100h.

	Nb (at. %)	Al (at. %)	Sn (at. %)
IP4-AC			
Nb_3Sn	74.5 ± 0.6	10.2 ± 0.6	15.4 ± 0.3
$NbAl_3$	25.9 ± 0.4	70.4 ± 0.3	3.7 ± 0.2
Nb_2Al	59.5 ± 0.3	30.7 ± 0.3	9.8 ± 0.4
$NbSn_2$	34.9 ± 0.3	6.5 ± 0.5	58.6 ± 05
Sn-rich Nb_2Al	64.9 ± 0.2	18.0 ± 0.3	17.1 ± 0.3
IP4-HT-900 ^{0}C/100h			
Nb_3Sn	73.4 ± 0.5	11.2 ± 0.4	15.4 ± 0.3
Nb_5Sn_2Al	61.5 ± 0.4	13.6 ± 0.5	24.9 ± 0.3
$NbAl_3$	27.0 ± 0.2	72.3 ± 0.4	0.7 ± 0.1
Nb_2Al	65.9 ± 0.2	25.1 ± 0.3	9.0 ± 0.2
Sn-rich Nb_2Al	63.2 ± 0.5	19.4 ± 0.3	17.3 ± 0.3
IP4-HT-900 ^{0}C/200h			
Nb_3Sn	73.3 ± 0.5	11.5 ± 0.2	15.3 ± 0.2
Nb_5Sn2Al	62.5 ± 0.5	13.0 ± 0.1	24.5 ± 0.3
$NbAl_3$	26.4 ± 0.2	72.1 ± 0.3	1.4 ± 0.1
Nb_2Al	65.8 ± 0.6	25.4 ± 0.2	8.8 ± 0.1
Sn-rich Nb_2Al	62.7 ± 0.6	20.3 ± 0.3	17.0 ± 0.2
IP4-HT-1200 ^{0}C/100h			
Nb_3Sn	75.0 ± 0.6	9.6 ± 0.1	15.4 ± 0.2
Nb_2Al	62.4 ± 0.6	35.6 ± 0.3	2.0 ± 0.1
Sn-rich Nb_2Al	65.2 ± 0.5	28.8 ± 0.3	6.1 ± 0.2
Very Sn-rich Nb_2Al	63.1 ± 0.2	19.1 ± 0.1	17.8 ± 0.1

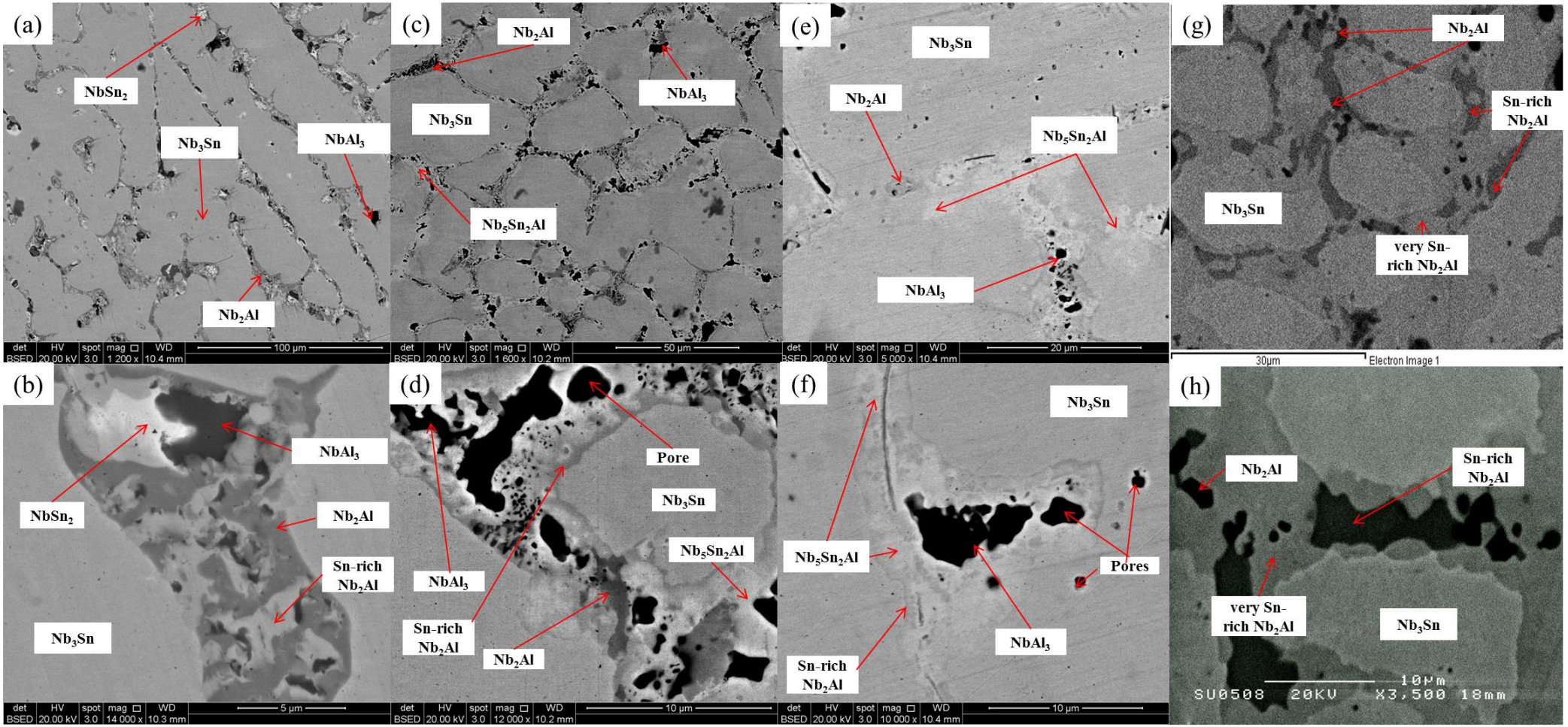

Fig. 10.1. BSE images of IP4-AC (a-b), IP4-HT-900 ^{0}C /100h (c-d), IP4-HT-900 ^{0}C /200h (e-f) and IP4-HT-1200 ^{0}C /100h (g-h).

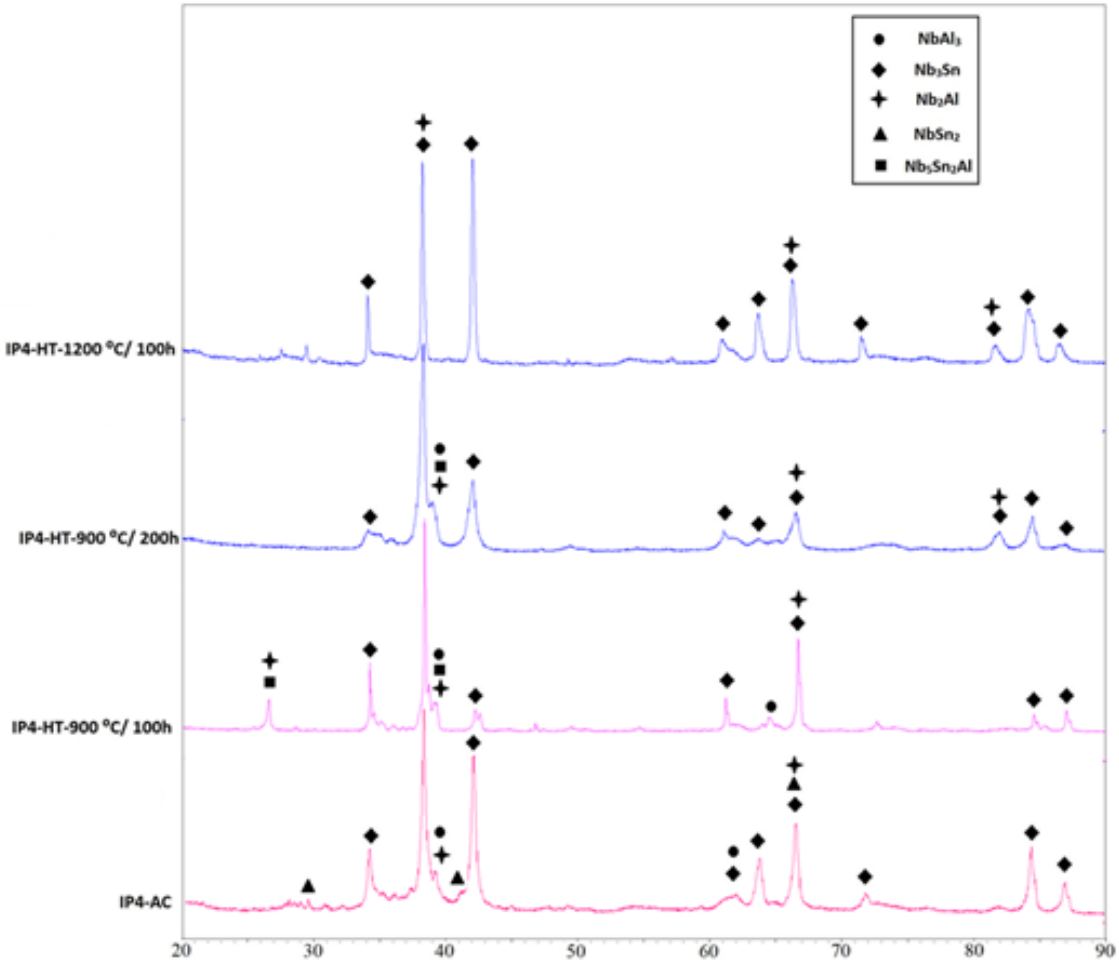

Fig. 10.2. XRD diffractograms of IP4-AC, IP4-HT-900 ^{0}C /100h, IP4-HT-900 ^{0}C /200h and IP4-HT-1200 ^{0}C /100h

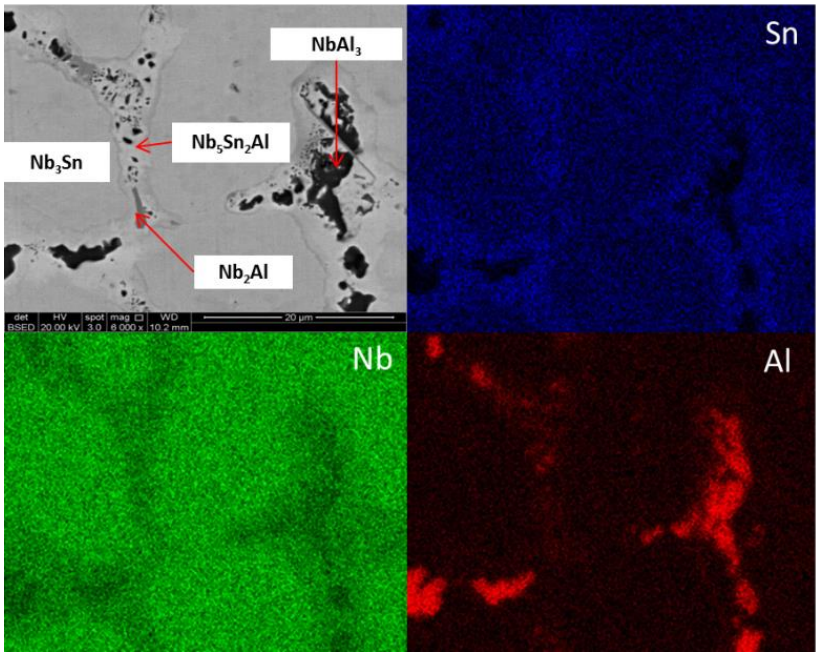

Fig. 10.3. X-ray element maps of IP4-HT-900 ^{0}C/100h

10.2.2. Alloy Nb-33Al-13Sn (IP5)

As cast. The microstructure and the compositions of the phases present in the Nb-35Al-11Sn as cast alloy (IP5-AC) can be seen in Fig. 10.4 (a-b) and Table 10.2, respectively. The SEM images along with XRD (Fig. 10.5) confirm that four phases were formed; namely Nb_3Al, $NbAl_3$, $NbSn_2$ and Nb_2Al, with Nb_3Al having the largest volume fraction. In the Nb_3Al phase the Sn content was ~12 at. %, while in Nb_2Al was ~7 at. %. Of all the aluminides, Sn showed the least solubility in $NbAl_3$ of less than 2 at. %. The Sn/Al ratio in the Nb_3Al phase was ~0.7 while the sum of Al+Sn was ~29 at. %.

Heat treated. IP5-AC was given 3 separate heat treatments; 100 h at 900 °C, 300 h at 900 °C and 100 h at 1200 °C. In Fig. 10.4 (c-d) the microstructure of the alloy after heat treatment at 900 ^{0}C for 100 hours (IP5-HT-900 ^{0}C/ 100h) can be seen. Large areas of Nb_3Al were again evident, as in the as-cast alloy, with the Sn/Al ratio increasing to about 0.75 and Al+Sn to ~29 at. %. The Nb_5Sn_2Al ternary compound was formed along with $NbAl_3$ and Nb_2Al. The $NbSn_2$ intermetallic was again no longer present. The composition of Nb_5Sn_2Al again was close to stoichiometry (61.9 Nb - 13.2Al -24.9Sn at. %). The concentration of Sn in Nb_3Al, Nb_2Al and $NbAl_3$ was similar to the as cast. Al content was also similar, except for the Nb_2Al where Al concentration was decreased by ~4 at. %. Some areas of Sn-rich Nb_2Al were again observed. The Sn and Al content were more than 20 and 19 at. % respectively.

IP5 was heat treated for a further 200 hours at 900 ^{0}C (IP5-HT-900 ^{0}C/ 300h) to achieve an equilibrium microstructure. Although a significant change in the microstructure was seen (volume fraction of phases), no major change in compositions was observed. Nb_2Al became the dominant phase, whereas only traces of the Nb_3Al phases were found (Fig. 10.4 (e)). XRD showed less intense peaks for Nb_3Al, confirming the SEM results (Fig. 10.5). At the grain boundaries $NbAl_3$, Nb_5Sn_2Al and Sn-rich Nb_2Al were present (Fig. 10.4 (f)).

The IP5-AC alloy was also heat treated at 1200 ^{0}C for 100 hours. Two phases were present in the microstructure; $NbAl_3$ and Nb_2Al. Areas of Sn-rich Nb_2Al were evident throughout the alloy, with larger volume fraction than the Nb_2Al with lower Sn content observed in the previous samples (Fig. 10.4 (g-h)). Compared with the as cast sample, the $NbAl_3$ intermetallic had approximately the same composition, while Nb_2Al was

poorer in Sn by ~2.5 at. % (Table 10.2). The Sn content in the Sn-rich Nb_2Al phase decreased by ~3 at. % to ~17 at. % compared with the 900 ^{0}C heat treated alloys. Neither $NbSn_2$ or the ternary phase, Nb_5Sn_2Al, were observed. This suggests that Nb_5Sn_2Al does not form at 1200 ^{0}C and therefore has a decomposition temperature between 900-1200 °C, which is similar to the ternary phase Nb_5Sn_2Si, in the Nb-Si-Sn system (Chapter 9).

Table 10.2

Data from EDS analysis for the composition of the phases in IP5-AC, IP5-HT-900 ^{0}C/100h, IP5-HT-900 ^{0}C/300h and IP5-HT-1200 ^{0}C/100h.

	Nb (at %)	Al (at %)	Sn (at %)
IP5-AC			
Nb_3Al	70.8 ± 0.6	17.1 ± 0.4	12.1 ± 0.3
$NbAl_3$	26.3 ± 0.4	72.0 ± 0.6	1.7 ± 0.1
Nb_2Al	58.2 ± 0.4	34.4 ± 0.3	7.4 ± 0.2
$NbSn_2$	31.5 ± 1.5	4.8 ± 0.4	63.7 ± 1.4
IP5-HT-900 ^{0}C/100h			
Nb_3Al	71.3 ± 0.6	16.4 ± 0.4	12.3 ± 0.2
Nb_5Sn_2Al	61.9 ± 0.4	13.2 ± 0.1	24.9 ± 0.4
$NbAl_3$	26.9 ± 0.4	72.4 ± 0.6	0.7 ± 0.1
Nb_2Al	62.3 ± 0.6	30.9 ± 0.2	6.8 ± 0.1
Sn-rich Nb_2Al	60.2 ± 0.6	19.5 ± 0.2	20.3 ± 0.4
IP5-HT-900 ^{0}C/300h			
Nb_3Al	71.4 ± 0.5	16.7 ± 0.4	11.9 ± 0.2
Nb_5Sn_2Al	62.7 ± 0.4	13.0 ± 0.3	24.3 ± 0.5
$NbAl_3$	26.6 ± 0.2	73.2 ± 0.4	0.3 ± 0.1
Nb_2Al	61.1 ± 0.3	33.6 ± 0.2	5.3 ± 0.1
Sn-rich Nb_2Al	61.2 ± 0.5	18.1 ± 0.2	20.7 ± 0.2
IP5-HT-1200 ^{0}C/100h			
$NbAl_3$	26.9 ± 0.4	72.4 ± 0.4	0.7 ± 0.1
Nb_2Al	62.8 ± 0.4	32.4 ± 0.5	4.7 ± 0.1
Sn-rich Nb_2Al	62.6 ± 0.5	20.1 ± 0.4	17.3 ± 0.3

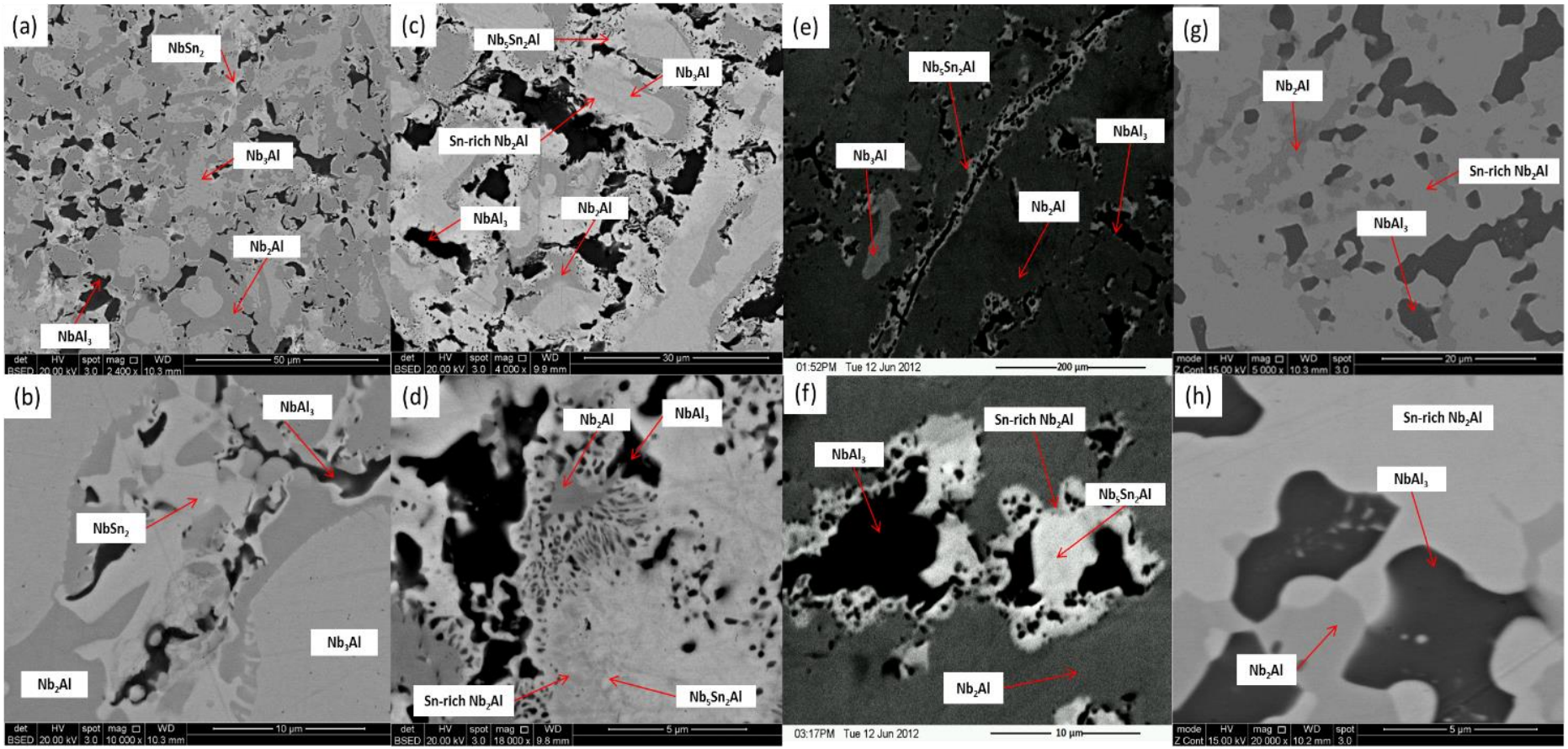

Fig. 10.4. BSE images of IP5-AC (a-b), IP5-HT-900 ^{0}C /100h (c-d), IP5-HT-900 ^{0}C /300h (e-f) and IP5-HT-1200 ^{0}C /100h (g-h)

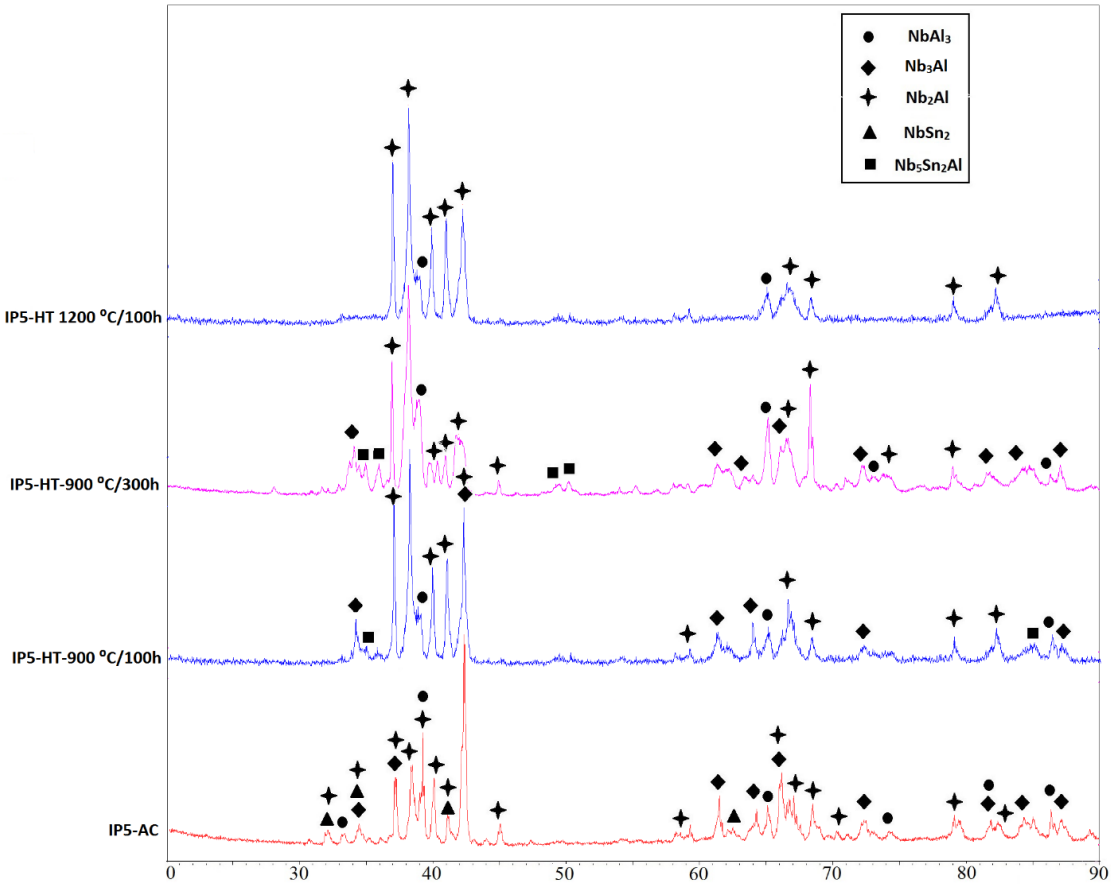

Fig. 10.5. XRD diffractograms of IP5-AC, IP5-HT-900 ^{0}C /100h, IP5-HT-900 ^{0}C /300h and IP5-HT-1200 ^{0}C /100h

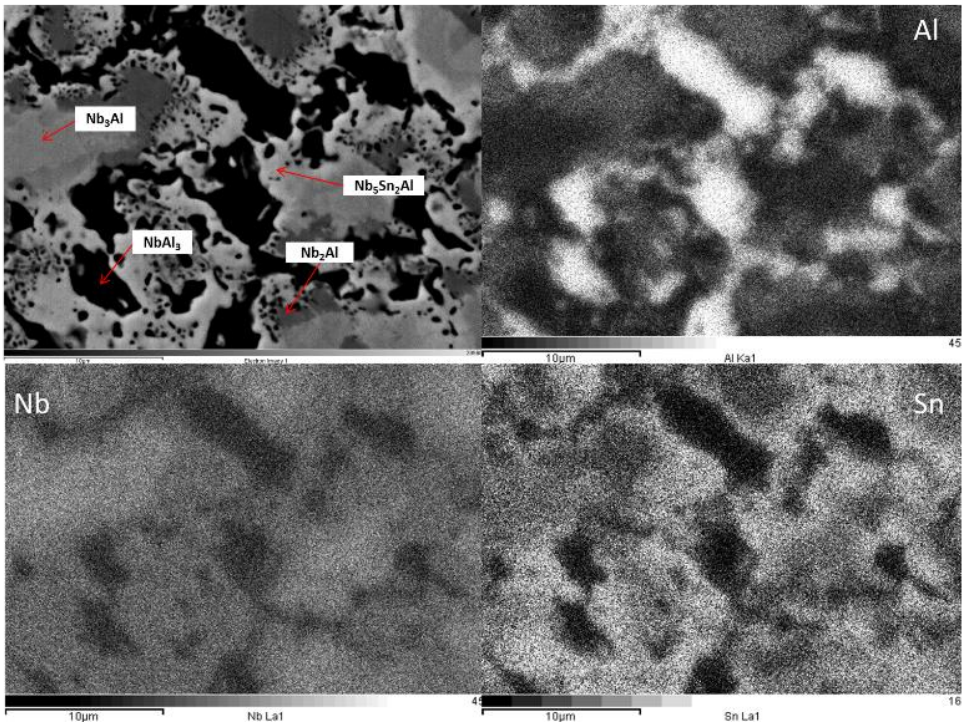

Fig. 10.6. X-ray element maps of IP5-HT-900 ^{0}C/100h

10.2.3. Alloy Nb-16Al-20Sn (IP6)

As cast. In Fig. 10.7 (a-b) BSE images of the Nb-16Al-20Sn as cast alloy (IP6-AC) are shown. Again, four intermetallics were identified in the microstructure; Nb_3Sn, Nb_2Al, $NbSn_2$ and $NbAl_3$. The predominant phase was Nb_3Sn. The other phases were accumulated at the grain boundaries. In these area Sn-rich Nb_2Al was also observed (Fig. 10.7 (b)). Phase analysis was confirmed using XRD (Table 10.8). The compositions of the aforementioned phases are given in Table 10.3. The concentration of Al in Nb_3Sn was ~9 at. %, while the Al/Sn ratio was ~0.5 and the Al+Sn sum less than 26 at. %. The $NbSn_2$ phase contained ~6.8 at. % Al. $NbAl_3$, Nb_2Al and the Sn-rich Nb_2Al contained ~1.6, ~7.7 and ~17 at. % Sn respectively.

Heat treated. The alloy was given 3 separate heat treatments; 100 h at 900 °C, 200 h at 900 °C and 100 h at 1200 °C. After 100 hours at 900 ^{0}C (IP6-HT-900 ^{0}C/ 100h), Nb_3Sn, Nb_2Al and $NbAl_3$ were still present along with newly formed Nb_5Sn_2Al (Fig. 10.8 and Fig. 10.7c-d). The $NbSn_2$ was no longer observed. The Nb_3Sn was again the matrix phase, while the other phases were present at the phase boundaries (Fig. 10.7 (c-d)). The Al content in Nb_3Sn increased by about 1 at. % with the Al/Sn ratio increasing to 0.55 and the Al+Sn sum less than 27 at. %. The Nb_5Sn_2Al was formed with its formula being close to stoichiometry (Table 10.3). The bright areas in the X-ray element map of Sn in Fig. 10.9 depict the areas where the ternary compound is present. Sn concentration in Nb_2Al decreased slightly, whereas in Sn-rich Nb_2Al it increased, in both cases by about 2 at. %. The $NbAl_3$ intermetallic had a similar composition to the phase in the as cast alloy.

The XRD pattern (Fig. 10.8) along with the EDS analysis (Table 10.3) confirmed that after a further hundred hours at 900 ^{0}C (IP6-HT-900 ^{0}C/ 200h) the composition of the constituent phases did not undergo any notable changes compared with IP6-HT-900 ^{0}C/ 100h. The same did not apply to the microstructure as a significant alteration took place. The volume fraction of $NbAl_3$ decreased considerably (Fig. 10.7 (e-f)). Nb_3Sn continued to be the matrix phase, whereas the rest of the phases again accumulated at the grain boundaries.

The IP6-AC alloy was also heat treated at 1200 ^{0}C for 100 hours (IP6-HT-1200 ^{0}C/ 100h). The microstructure was significantly altered after the heat treatment compared

with the as cast. In the heat treated sample, only Nb_3Sn (matrix) and Nb_2Al were observed. The $NbSn_2$ and $NbAl_3$ were no longer present, while the dark areas were pores (Fig. 10.7 (g-h)). Results were confirmed by XRD (Fig. 10.8). Nb_2Al again formed Sn-rich areas with larger volume fraction than the Nb_2Al with low Sn content. As it can be seen in Table 10.3, the composition of Nb_3Sn was approximately the same compared with the IP6-AC, with the Al/Sn ratio being 0.51 and Al+Sn concentration sum being 26.6 at. %. Sn content in Nb_2Al decreased by ~3 at. % to 4.6 at%, while in Sn-rich Nb_2Al Sn increased by ~4 at. % to ~21 at%.

Table 10.3

Data from EDS analysis for the composition of the phases in IP6-AC, IP6-HT-900 ^{0}C/100h, IP6-HT-900 ^{0}C/200h and IP6-HT-1200 ^{0}C/100h.

	Nb (at. %)	Al (at. %)	Sn (at. %)
IP6-AC			
Nb_3Sn	74.1 ± 0.5	8.6 ± 0.3	17.3 ± 0.3
$NbAl_3$	27.0 ± 0.4	71.4 ± 0.5	1.6 ± 0.2
Nb_2Al	60.2 ± 0.6	32.1 ± 0.4	7.7 ± 0.2
$NbSn_2$	30.2 ± 0.9	6.8 ± 0.2	63.0 ± 1.3
Sn-rich Nb_2Al	65.7 ± 0.6	17.1 ± 0.3	17.2 ± 0.3
IP6-HT-900 ^{0}C/100h			
Nb_3Sn	73.1 ± 0.6	9.6 ± 0.3	17.3 ± 0.3
Nb_5Sn_2Al	62.5 ± 0.6	11.9 ± 0.3	25.6 ± 0.4
$NbAl_3$	27.8 ± 0.5	71.0 ± 0.5	1.2 ± 0.1
Nb_2Al	60.5 ± 0.4	34.1 ± 0.4	5.3 ± 0.2
Sn-rich Nb_2Al	64.3 ± 0.5	16.2 ± 0.3	19.5 ± 0.2
IP6-HT-900 ^{0}C/200h			
Nb_3Sn	73.4 ± 0.4	9.4 ± 0.2	17.3 ± 0.3
Nb_5Sn_2Al	62.8 ± 0.4	12.3 ± 0.2	24.9 ± 0.3
$NbAl_3$	26.8 ± 0.3	72.3 ± 0.3	0.9 ± 0.1
Nb_2Al	61.7 ± 0.5	32.9 ± 0.4	5.4 ± 0.1
Sn-rich Nb_2Al	64.2 ± 0.5	17.1 ± 0.3	18.7 ± 0.2
IP6-HT-1200 ^{0}C/100h			
Nb_3Sn	74.0 ± 0.6	8.5 ± 0.3	17.5 ± 0.3
Nb_2Al	60.3 ± 0.4	35.1 ± 0.3	4.6 ± 0.2
Sn-rich Nb_2Al	62.5 ± 0.4	16.2 ± 0.3	21.3 ± 0.3

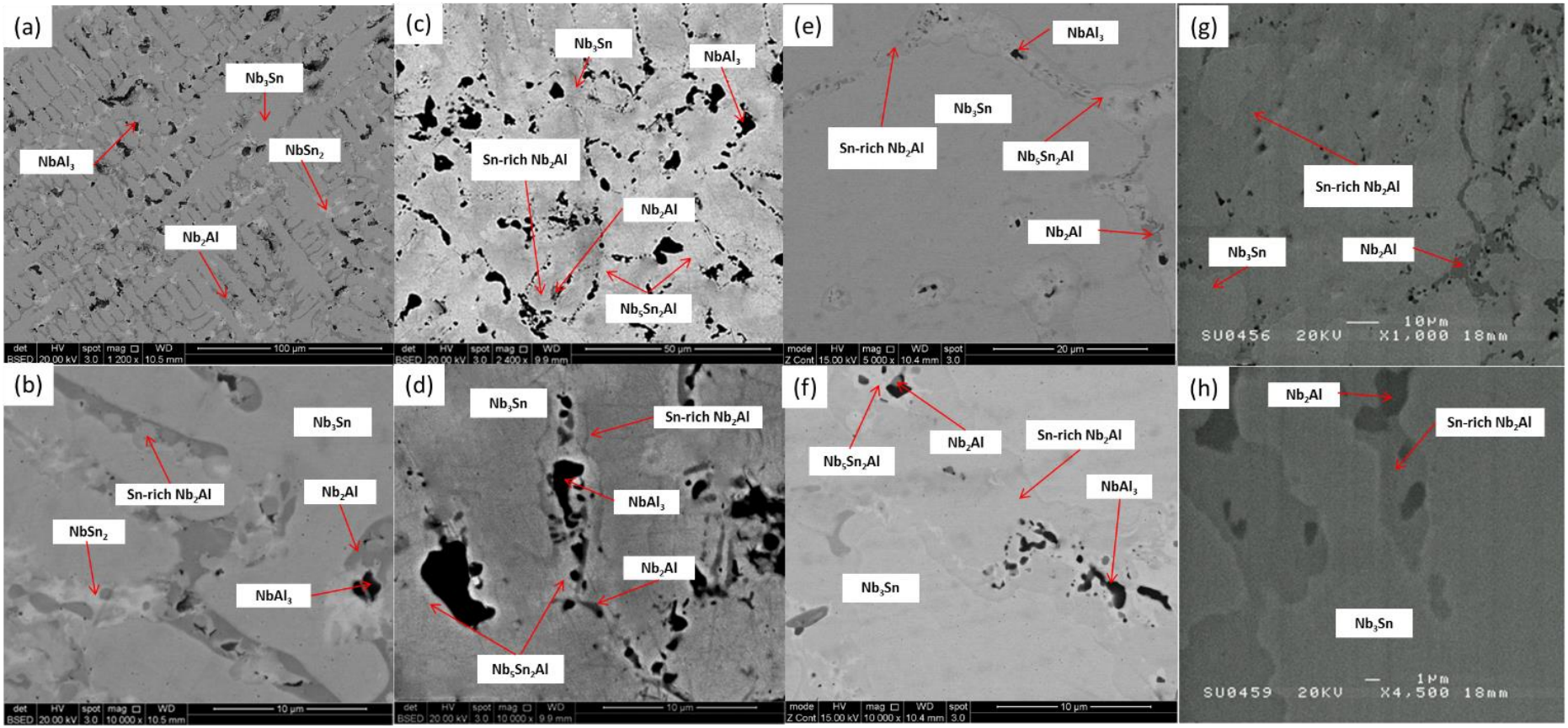

Fig. 10.7. BSE images of IP6-AC (a-b), IP6-HT-900 ^{0}C /100h(c-d), IP6-HT-900 ^{0}C /200h (e-f) and IP6-HT-1200 ^{0}C /100h (g-h)

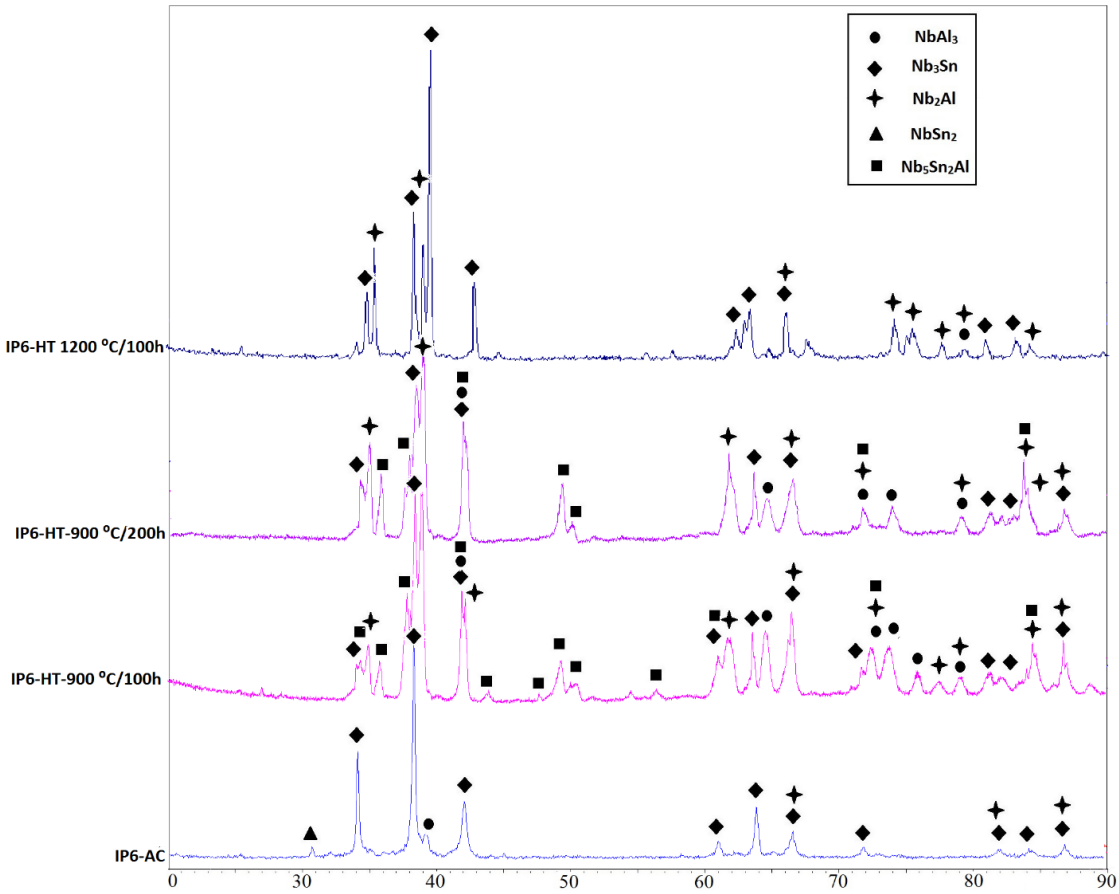

Fig. 10.8. XRD diffractograms of IP6-AC, IP6-HT-900 ^{0}C /100h, IP6-HT-900 ^{0}C /200h and IP6-HT-1200 ^{0}C /100h

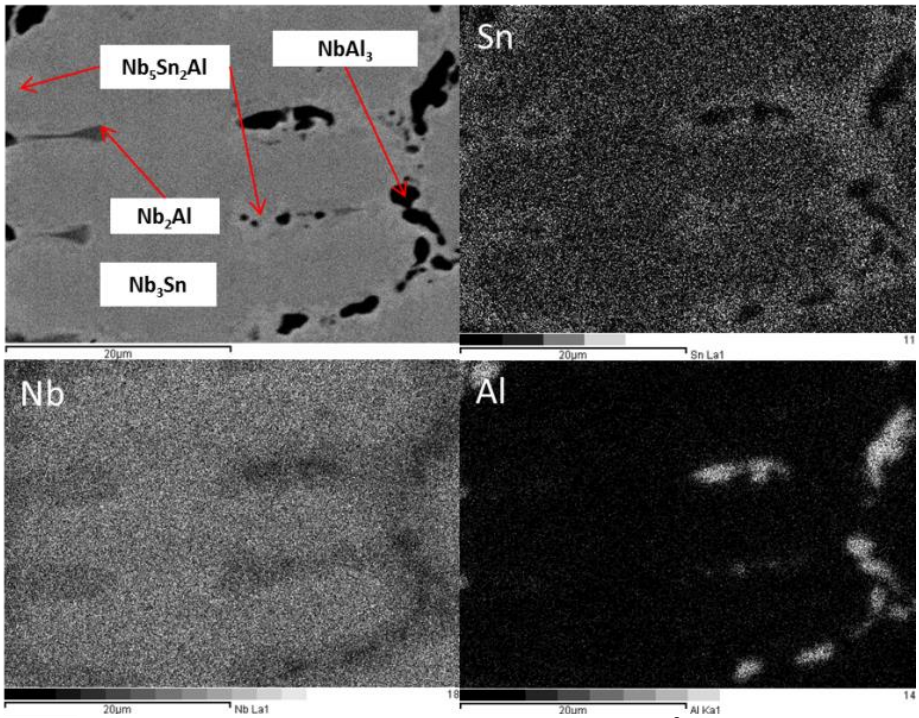

Fig. 10.9. X-ray element maps of IP6-HT-900 ^{0}C/100h

10.3. Discussion

All the as-cast alloys in the present study contained $NbSn_2$, $NbAl_3$, Nb_2Al and Nb_3Sn (IP4, IP6) or Nb_3Al (IP5). The $NbSn_2$ phase was formed to be metastable, disappearing after heat treatment at 900 and 1200 °C. For the alloys IP4 and IP6 after heat treatment at 900°C for 200 hours the fraction of $NbAl_3$ diminished significantly, thus it is concluded that this phase was also metastable at the given compositions. For the IP5 alloy, only remnants of Nb_3Al were present after 300 hours of annealing at 900°C, indicating that it was not an equilibrium phase. The solubility of Al in the $NbSn_2$ ranged from 4.8 at. % (IP5) to 6.8 at. % (IP6). In $NbAl_3$ and Nb_2Al the solubility of Sn was found to be up to 3.65 at. % (IP4) and 9.77at. % (IP4) respectively. In IP4 and IP6 Sn-rich areas of Nb_2Al were observed with Sn solubility up to about 18 at. % (IP4), whereas in IP5 no such areas were noticed. In both IP4 and IP6 the Al/Sn ratio in Nb_3Sn increased after the heat treatment at 900 ^{0}C, whereas it remained constant after the heat treatment at 1200 ^{0}C, compared with the as-cast alloys. In IP5 there was no significant change in the Sn/Al ratio in Nb_3Al after the heat treatment at 900 ^{0}C. The Sn+Al sum in A15 phases (Nb_3Sn and Nb_3Al) in IP4 and IP6 was ~25-26 at. %, while in IP5 it was ~29 at. %.

It is clear that the Nb_5Sn_2Al compound was present in all the heat treated specimens at 900 ^{0}C. It primarily formed in the grain boundaries, co-existing in most cases with $NbAl_3$ and Nb_2Al. The ternary compound was however not formed at 1200 ^{0}C. This suggest that the phase is stable up to a temperature between 900 and 1200 ^{0}C. Its stability appears to be similar to the ternary phase Nb_5Sn_2Si (Chapter 9). Its composition was found to be close to stoichiometry, which suggests that it behaves as a line compound, similarly to the Nb_5Sn_2Si phase.

The solidification paths have been deduced based on the as cast microstructure. In the as cast IP4 and IP6 alloys, as the primary Nb_3Sn solidified from the melt, the remaining liquid became leaner in Sn but richer in Al near Nb_3Sn. Thus Nb_2Al was formed at the grain boundaries, along with Sn-rich areas between Nb_2Al and Nb_3Sn. After that and as the melt was still rich in Al the $NbAl_3$ phase was formed again in the grain boundaries, whereas the last phase to solidify was $NbSn_2$ as the melt became leaner in Al and richer in Sn. It is suggested that the solidification path of IP4 and IP6 was $L \rightarrow L+Nb_3Sn \rightarrow L+Nb_3Sn+Nb_2Al \rightarrow L+Nb_3Sn+Nb_2Al+NbAl_3 \rightarrow Nb_3Sn+Nb_2Al+NbAl_3+NbSn_2$. On the other hand, in the as cast IP5 alloy the Nb_3Al solidified first and closely after that the Nb_2Al. At that point the melt was still rich enough in Al to produce $NbAl_3$

whereas after that it became leaner in Al and richer in Sn, thus allowing the formation of the $NbSn_2$. The suggested solidification path of IP5 was $L \rightarrow L+Nb_3Al \rightarrow L+Nb_3Al+Nb_2Al \rightarrow L+Nb_3Al+Nb_2Al+NbAl_3 \rightarrow Nb_3Al+Nb_2Al+NbAl_3+NbSn_2$

10.4. Conclusions

The as cast and heat treated alloys Nb-17Al-17Sn (IP4), Nb-33Al-13Sn (IP5) and Nb-16Al-20Sn (IP6) were investigated. The conclusions of this study are as follows:

- The equilibrium phases in IP4 and IP6 at 900 ^{0}C are Nb_3Sn, Nb_5Sn_2Al and Nb_2Al. The primary phase is Nb_3Sn. The Nb_5Sn_2Al and Nb_2Al form at the grain boundaries.
- The equilibrium phases in IP4 and IP6 at 1200 ^{0}C are Nb_3Sn and Nb_2Al. The primary phase is Nb_3Sn. The Nb_2Al forms at the grain boundaries.
- The equilibrium phases in IP5 at 900 ^{0}C are Nb_2Al, Nb_5Sn_2Al and $NbAl_3$. The primary phase is Nb_2Al. The Nb_5Sn_2Al and $NbAl_3$ form at the grain boundaries.
- The equilibrium phases in IP5 at 1200 ^{0}C are Nb_2Al and $NbAl_3$. The primary phase is Nb_2Al. The $NbAl_3$ forms at the grain boundaries.
- The Nb_2Al shows a high solubility for Sn, reaching up to 21 at. % in the Sn-rich areas. Based on EDS analysis it is concluded that Sn substitutes for Al atoms.
- Tin and Al substitute for each other in the A15 phase (Nb_3Al and Nb_3Sn)
- Tin shows limited solubility in $NbAl_3$, not exceeding ~3.6 at. %. Similarly to Nb_2Al, Sn substitutes for Al atoms.
- The solubility of Al in $NbSn_2$ varies from ~4.8 to ~6.8 at. %.
- The Nb_5Sn_2Al is a ternary intermetallic which decomposes somewhere between ~900 and ~1200 ^{0}C and it can be treated as a line compound.
- The solidification path for all the alloys was: $L \rightarrow L+A15 \rightarrow L+A15+Nb_2Al \rightarrow L+A15+Nb_2Al+NbAl_3 \rightarrow A15+Nb_2Al+NbAl_3+NbSn_2$.

11

Phase equilibria in Nb-Ti-Sn ternary alloys at 900 °C and 1200 °C

11.1. Introduction

To date the binary phase diagrams of the constituent elements have been thoroughly investigated experimentally. The Nb-Sn system consists of $NbSn_2$, Nb_6Sn_5 and Nb_3Sn intermetallics [28]. The ab initio study of these phases was presented in chapter 5. The intermetallic phases in the Ti-Sn system are Ti_3Sn, Ti_2Sn, Ti_5Sn_3, Ti_6Sn_5 and Ti_2Sn_3 [77]. No binary phases exist in the Nb-Ti system [70]. Limited ternary data exists which reports that Ti substitutes for Nb atoms in Nb_3Sn at 700 °C [154], 1200 °C [19, 30] and 1600 °C [155]. A single pseudo binary at 1600 °C between Nb_3Sn and Ti_3Sn has been published [155]. Changes in phases and lattice parameters as Nb is replaced by Ti are given [155]. Holeck et al. report that the solubility limit of Ti in Nb_3Sn is 45 at. %. Above this a two phase mixture of Nb_3Sn and Ti_3Sn was observed [155].

The alloys IP7 (Nb-10Ti-18Sn), IP8 (Nb-13Ti-3Sn), IP9 (Nb-40Ti-23Sn) and IP10 (Nb-39Ti-40Sn) were manufactured in the current research. The motivation of this work was to verify the stable phases and the phase equilibria in the Nb-Ti-Sn ternary system.

11.2. Results

11.2.1. Alloy Nb-10Ti -18Sn (IP7)

As cast. The microstructure of the Nb-10Ti -18Sn as cast alloy (IP7-AC) can be seen in Fig. 11.1 (a-b), while the compositions of the constituent phases are shown in Table 11.1. Primarily, large areas of Nb_3Sn were observed (bright areas). Within Nb_3Sn, Nb solid solution (Nb_{ss}, grey areas) was formed along with Ti-rich regions (dark areas) at the grain boundaries. EDS and XRD were not conclusive owing to the low volume fraction of the phase. The content of Ti and Sn in Nb_3Sn was 9.2 and 18.4 at. % respectively. In the Nb_{ss} the amount of Ti and Sn substitution was 9.3 and 10 at. %, respectively, making the Ti/Sn ratio ~1.

Heat treated. The alloy was given 4 separate heat treatments; 200 h at 900 °C, 300 h at 900 °C and 200 h at 1200 °C and 300 h at 1200 °C. In Fig. 11.1 (c-d) the microstructure of the alloy after 200 hours at 900 ^{0}C is shown (IP7-HT-900 ^{0}C/ 200h). There was no significant change in the

microstructure. Bulk areas of Nb_3Sn remained. The Nb_{ss} was again present and some precipitation of Ti (dark spots) at the grain boundaries was seen. As it can be seen in Table 11.1 the composition of Nb_3Sn was approximately the same as in the as cast alloy. In Nb_{ss} the Ti content increased to 11.4 at. % whereas the Sn content reduced slightly. The Ti/Sn ratio for Nb_{ss} reached ~1.2. The similarity of the heat treated alloy to the as cast was confirmed by XRD (Fig. 11.2).

Due to the low volume fraction of the areas of dark phase, EDS could not be used. Thus the IP7-HT-900 ^{0}C/ 200h was heat treated for a further 100 h at 900 ^{0}C. This was also done to ensure that equilibrium conditions were met. In Fig. 11.3 X-ray element maps of the IP7-HT-900 ^{0}C/ 300h alloy are shown. Titanium and Sn maps indicate that the dark contrast phase formed at the grain boundaries contains more Ti and Sn and less Nb than the other phases. After the heat treatment the dark contrast phase coarsened and as such the composition could be measured using EDS. EDS analysis confirmed that the phase was Ti_3Sn (Table 11.1). The Nb content in the Ti_3Sn was 19.5 at. % and the Sn content was close to stoichiometry at just over 24 at. %. The composition of Nb_3Sn was similar to that measured in IP7-HT-900 ^{0}C/ 200h. The Nb_{ss} in contrast was poorer in Ti (8.6 at. %) and richer in Sn (11 at. %). The Ti/Sn ratio was approximately 0.8. Images of the microstructure of the IP7-HT-900 ^{0}C/ 300h are shown in Fig. 11.1 (e-f).

The IP7-AC was heat treated at 1200 ^{0}C for 100 hours. The microstructure consisted of Nb_{ss}, Nb_3Sn and Ti_{ss} (Fig. 11.1 (g-h)). Morphologically there was a notable difference in the areas of the Ti_{ss} in the grain boundaries between Nb_3Sn and the solid solution as the dark spots (Ti_{ss}) were evidently coarsened compared with the corresponding areas of the as cast and heat treated at 900 °C samples. Niobium and Sn contents in Ti_{ss} were 19.4 and 5 at. %, respectively. The Ti content in Nb_3Sn was ~8.8 at. %, while the Sn concentration was 18.7 at. %. The composition of Nb_{ss} changed dramatically. The Sn content decreased to 3.1 at. % and the Ti content to 6.1 at. %. The resulting Ti/Sn ratio was ~2.

To ensure the alloy was at equilibrium, the IP7-HT-1200 ^{0}C/ 100h alloy was heat treated for a further 200 hours. In Fig. 11.1 (i-j) it can be seen that again Nb_3Sn makes up the matrix. Nb_{ss} and Ti_{ss} also formed. Ti_{ss} was confirmed by XRD (Fig. 11.2). In the Nb_{ss} there was precipitation of Ti to the grain boundaries. The Ti_{ss} and Nb_{ss} areas are evident in the Ti and Nb maps respectively (Fig. 11.4). Titanium and Sn contents in Nb_3Sn were 9.4 and 18.6 at. % respectively, while in Nb_{ss} the corresponding values were 7.1 and 2.7 respectively with the Ti/Sn ratio being ~2.6. Lastly, in

Ti_{ss} the Nb and Sn concentrations were about 19.6 and 5.5 at. % respectively. In Fig. 11.4 the X-ray element maps of the IP7-HT-1200 ^{0}C/ 300h alloy are shown. The dark areas in the BSE image (Ti_{ss}) were richer in Ti and poorer in Nb and Sn than the other phases. Compositions of these areas from EDS are given in Table 11.1 and confirm this result.

Table 11.1.

Data from EDS analysis for the composition of the phases in IP7-AC, IP7-HT 900 ^{0}C/200h, IP7-HT-900 ^{0}C/300h, IP7-HT-1200 ^{0}C/100h and IP7-HT-1200 ^{0}C/300h.

	Nb (at %)	Ti (at %)	Sn (at %)
IP7-AC			
Nb_3Sn	72.4 ± 0.2	9.2 ± 0.2	18.4 ± 0.1
Nb_{ss}	80.8 ± 0.2	9.3 ± 0.1	9.9 ± 0.1
IP7-HT-900 ^{0}C/200h			
Nb_3Sn	72.8 ± 0.2	8.9 ± 0.2	18.3 ± 0.2
Nb_{ss}	79.4 ± 0.1	11.4 ± 0.2	9.2 ± 0.1
IP7-HT-900 ^{0}C/300h			
Nb_3Sn	73.0 ± 0.2	8.6 ± 0.1	18.4 ± 0.1
Nb_{ss}	80.5 ± 0.2	8.6 ± 0.1	10.9 ± 0.1
Ti_3Sn	19.5 ± 1.6	56.4 ± 1.4	24.1 ± 1.4
IP7-HT-1200 ^{0}C/100h			
Nb_3Sn	72.5 ± 0.3	8.8 ± 0.2	18.7 ± 0.2
Nb_{ss}	90.8 ± 0.1	6.1 ± 0.2	3.1 ± 0.2
Ti_{ss}	19.4 ± 2.5	75.7 ± 2.6	5.0 ± 0.9
IP7-HT-1200 ^{0}C/300h			
Nb_3Sn	72.0 ± 0.3	9.4 ± 0.2	18.6 ± 0.2
Nb_{ss}	90.2 ± 0.3	7.1 ± 0.2	2.7 ± 0.2
Ti_{ss}	19.6 ± 1.6	75.0 ± 1.9	5.5 ± 0.6

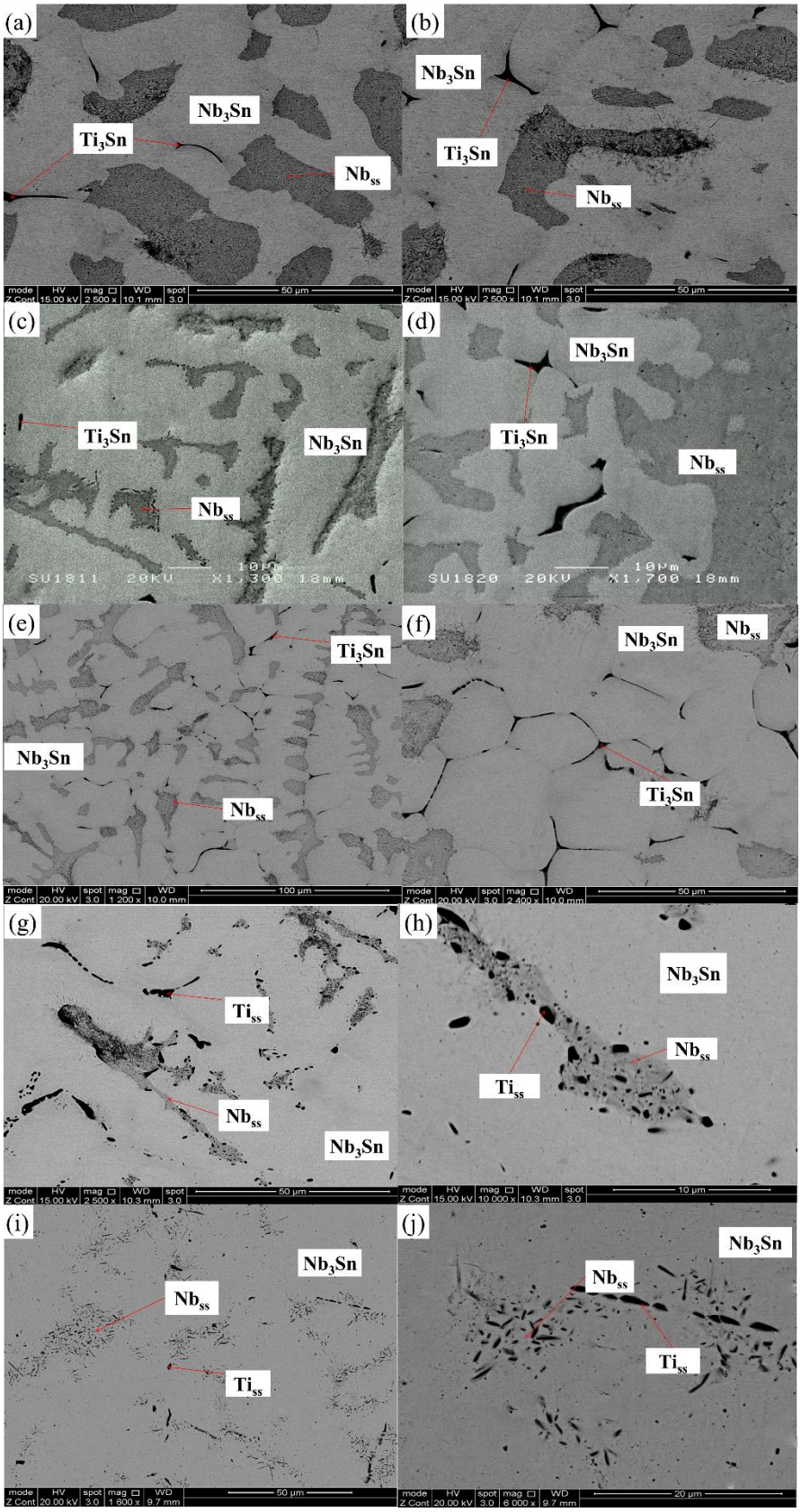

Fig. 11.1. BSE images of IP7-AC (a-b), IP7-HT-900 ^{0}C/200h (c-d), IP7-HT-900 ^{0}C/300h (e-f), IP7-HT-1200 ^{0}C/100h (g-h) and IP7-HT-1200 ^{0}C/300h (i-j)

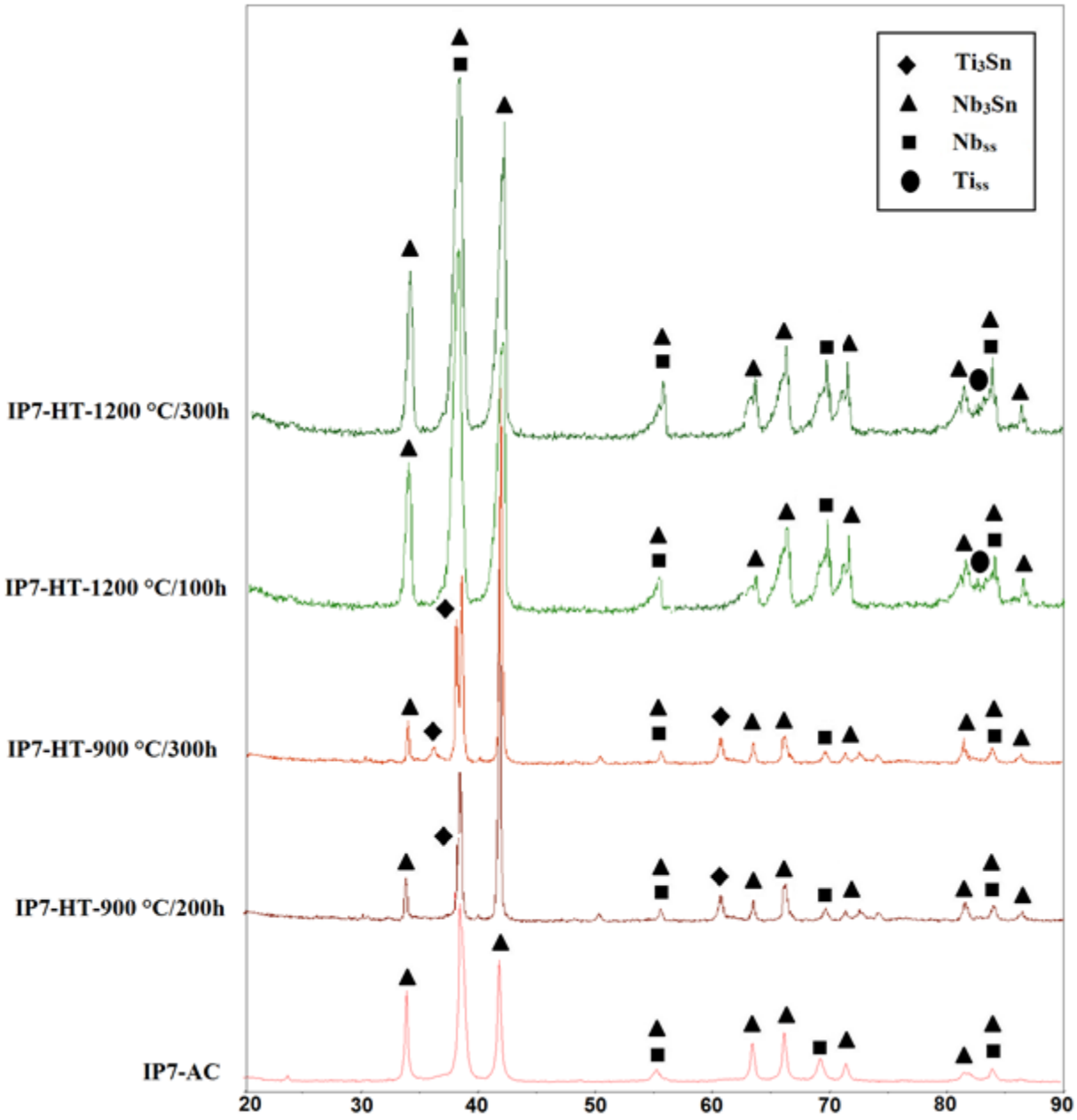

Fig. 11.2. XRD diffractograms of IP7-AC, IP7-HT-900 ^{0}C /200h, IP7-HT-900 ^{0}C /300h, IP7-HT-1200 ^{0}C /100h and IP7-HT-1200 ^{0}C /300h

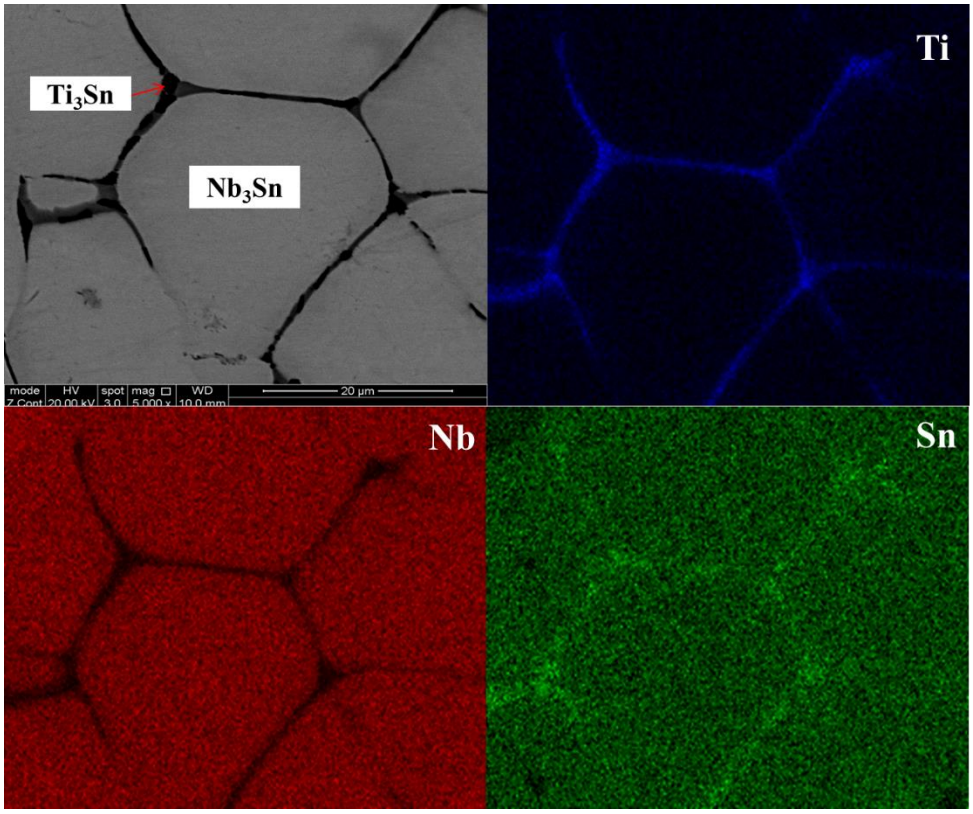

Fig. 11.3. X-ray element maps of IP7-HT-900 ^{0}C/300h

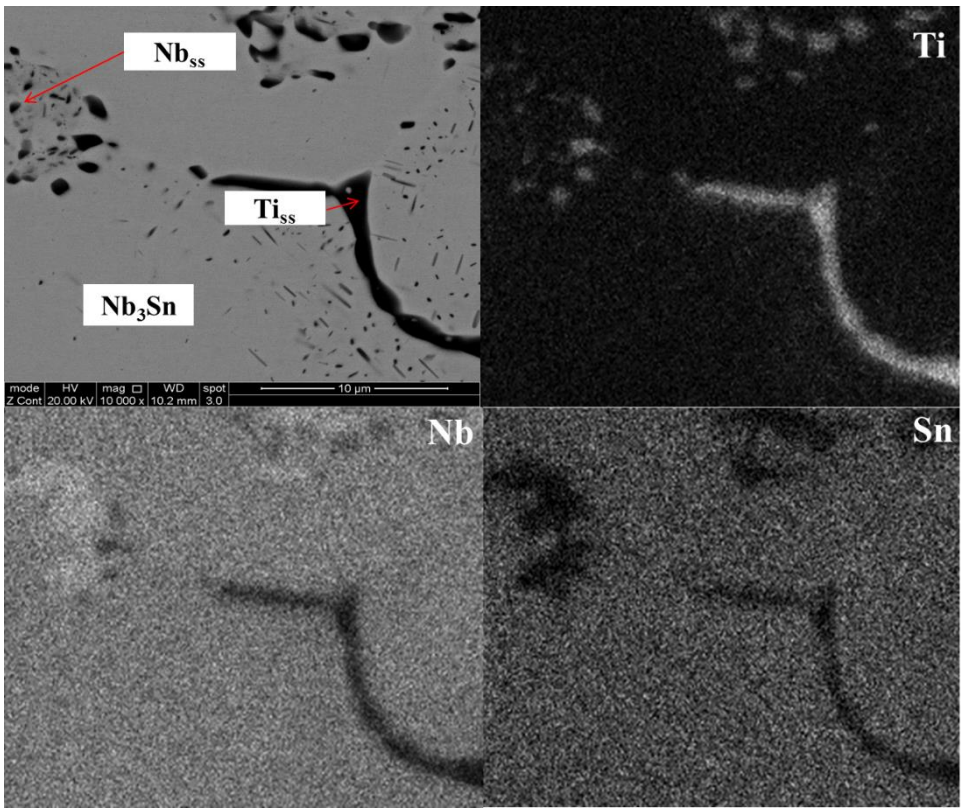

Fig. 11.4. X-ray element maps of IP7-HT-1200 ^{0}C/300h

11.2.2. Alloy Nb-13Ti -3Sn (IP8)

As cast. The microstructure of the Nb-13Ti -3Sn as cast alloy (IP8-AC) consisted of only a single phase, Nb_{ss} as it can be seen in Fig. 11.5 (a-b) and confirmed by the XRD (Fig. 11.6). In Table 11.2 the composition of the solid solution is shown which coincides with the alloy composition. The Ti and Sn contents were 13.9 and 3.2 at. %, respectively.

Heat treated. The alloy was given 4 separate heat treatments; 100 h at 900 °C, 300 h at 900 °C and 100 h at 1200 °C and 300 h at 1200 °C. The microstructure of the alloy heat treated at 900 ^{0}C for 100 hours (IP8-HT-900 ^{0}C/ 100h) in shown in Fig. 11.5 (c-d). The microstructure consisted of Nb_{ss} with some partitioning of Ti (dark areas) to the grain boundaries. The Ti content in Nb_{ss} was slightly reduced from 13.9 (as-cast) to 13.6 at. %. In order to make sure that the equilibrium state was reached as well as to be conclusive as to the composition of the dark contrast areas, IP8-HT-900 ^{0}C/ 100h was heat treated for a further 200 hours. The Ti at the grain boundaries did not undergo significant coarsening, as it can be seen in Fig. 11.5 (e-f). The Ti content in the solid solution further decreased to 13.2 at. % (Table 11.2). In the XRD patterns of the IP8-HT-900 ^{0}C/ 100h and the IP8-HT-900 ^{0}C/ 300h (Fig. 11.6) only the Nb_{ss} was evident most probably owing to the small volume fraction of Ti_{ss}.

The IP8-AC was heat treated at 1200 ^{0}C for 100 hours (IP8-HT-1200 ^{0}C/ 100h). Again bulk Nb_{ss} and Ti at the grain boundaries were observed (Fig. 11.5 (g-h) and Table 11.2). The concentration of Ti in Nb_{ss} was lower than in the as cast by more than 1 at. %. The amount of Sn was similar. The sample was heat treated for a further 200 hours. The Ti at the grain boundaries coarsened (Fig. 11.5 (i-j)) and the Ti content in the solid solution was reduced slightly (by 0.7 at. %), a fact indicative of the partitioning of Ti to the grain boundaries. The X-ray element maps of the microstructure are shown in Fig. 11.7. It is clear that the dark areas in the BSE image are Ti rich (bright areas in Ti map) and poor in Nb and Sn (dark areas in Nb and Sn maps), indicating that the phase is Ti_{ss}. The darker areas within Nb_{ss} (Fig. 11.5 (i-j)) were Nb_{ss} slightly richer in Ti (~1 at. % richer than the regular Nb_{ss}). The EDS and XRD analysis (Fig. 11.6) did not provide conclusive evidence of this phase due to its low volume fraction.

Table 11.2.

Data from EDS analysis for the composition of the phases in IP8-AC, IP8-HT-900 ^{0}C/100h, IP8-HT-900 ^{0}C/300h, IP8-HT-1200 ^{0}C/100h and IP8-HT-1200 ^{0}C/200h. Note: Ti_{ss} features were too small to analyse

	Nb (at %)	Ti (at %)	Sn (at %)
IP8-AC			
Nb_{ss}	82.9 ± 0.1	13.9 ± 0.1	3.2 ± 0.1
IP8-HT-900 ^{0}C/100h			
Nb_{ss}	83.4 ± 0.1	13.6 ± 0.2	3.0 ± 0.1
IP8-HT-900 ^{0}C/300h			
Nb_{ss}	83.6 ± 0.1	13.2 ± 0.2	3.2 ± 0.2
IP8-HT-1200 ^{0}C/100h			
Nb_{ss}	84.0 ± 0.1	12.7 ± 0.2	3.3 ± 0.1
IP8-HT-1200 ^{0}C/200h			
Nb_{ss}	84.7 ± 0.1	12.0 ± 0.2	3.2 ± 0.1

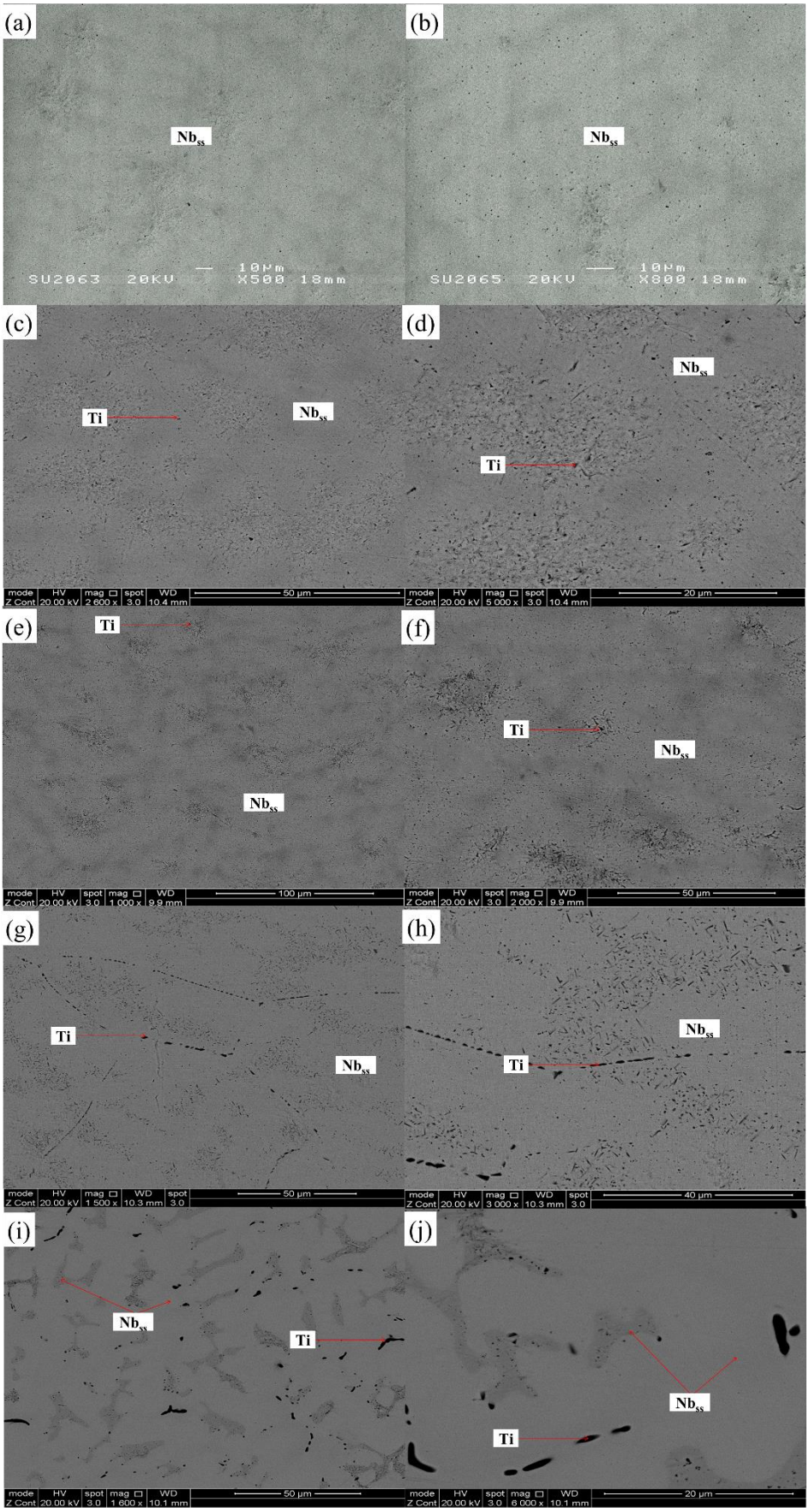

Fig. 11.5. BSE images of IP8-AC (a-b), IP8-HT-900 ^{0}C/200h (c-d), IP8-HT-900 ^{0}C/300h (e-f), IP8-HT-1200 ^{0}C/100h (g-h) and IP8-HT-1200 ^{0}C/300h (i-j)

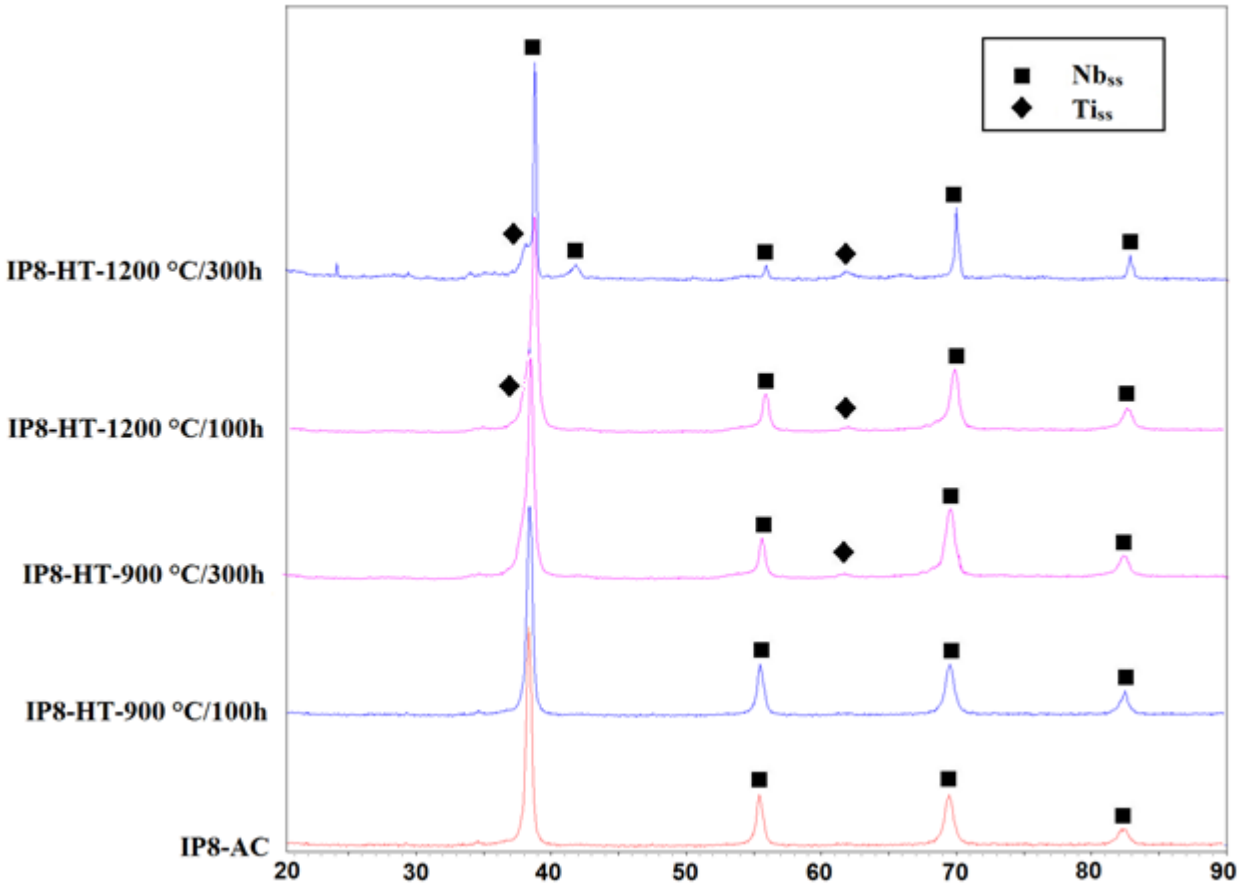

Fig. 11.6. XRD diffractograms of IP8-AC, IP8-HT-900 ^{0}C /100h, IP8-HT-900 ^{0}C /300h, IP8-HT-1200 ^{0}C /100h and IP8-HT-1200 ^{0}C /300h

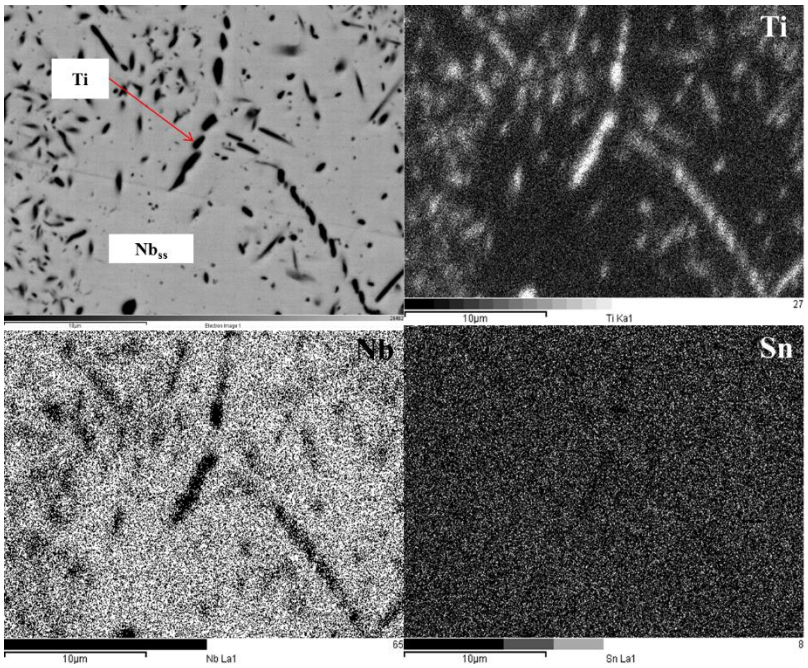

Fig. 11.7. X-ray element maps of IP8-HT-1200 ^{0}C/300h

11.2.3. Alloy Nb-40Ti -23Sn (IP9)

As cast. In Fig. 11.8 (a-b) the microstructure of the as-cast Nb-40Ti-23Sn (IP9-AC) alloy is shown. Ti_3Sn and Nb_3Sn were present, with Nb_3Sn being the primary phase (brighter areas) and Ti_3Sn formed in the grain boundaries (darker areas). These phases were confirmed by XRD (Fig. 11.9). Ti and Sn contents in Nb_3Sn were about 32.6 and 20.7 at. %, respectively, whereas Nb and Sn contents in Ti_3Sn were ~15.3 and ~25.4 at. %, respectively (Table 11.3). Between Ti_3Sn and Nb_3Sn there were always areas of Nb-rich Ti_3Sn (grey contrast areas) within which the Nb content was ~30 at. %, while the Sn concentration was approximately 24 at. %.

Heat treated. The alloy was given 4 separate heat treatments; 100 h at 900 °C, 200 h at 900 °C and 100 h at 1200 °C and 200 h at 1200 °C. After the heat treatment at 900 ^{0}C for 100 hours (IP9-HT-900 ^{0}C/ 100h), there were no noticeable differences in the phases present or morphology of the microstructure compared with the as-cast alloy (Fig. 11.8 (c-d)). The compositions of the constituent phases did not vary significantly. Niobium-rich Ti_3Sn was still present along with Nb_3Sn and Ti_3Sn. The Ti_3Sn intermetallic was poorer in Nb and richer in Ti, both by ~2.5 at. % (Table 11.3). In contrast, the concentration of Ti in Nb_3Sn was lower, and the Nb content higher, both by approximately 2 at. %. The IP9-HT-900 ^{0}C/ 100h was heat treated for an additional 100 h in order to attain equilibrium. The microstructure again consisted of the same phases (Fig. 11.8 (e-f)), confirmed by XRD (Fig. 11.9). The composition of the phases was similar to the previous sample (Table 11.3). In both the IP9-HT-900 ^{0}C/ 100h and IP9-HT-900 ^{0}C/ 200h, the borders around the Ti_3Sn intermetallic were significantly darker indicating higher Ti content (Fig. 11.8 (f)). The IP9-AC was heat treated at 1200 ^{0}C for 100 hours. There were no substantial alterations in the microstructure or phases compared with the as cast alloy, as it is shown in Fig. 11.8 (g-h)). Titanium content in Ti_3Sn increased by ~4 at. % and the Nb content decreased by the same amount. In Nb_3Sn the Ti content decreased by ~1.5 at. %, whereas Nb content was increased by about 1 at. %. The Nb-rich Ti_3Sn areas became poorer in Ti by ~1 at. % and richer in Nb by ~1.7 at. %, compared with the as cast alloy. The IP9-HT-1200 ^{0}C/100h was heat treated for a further 100 hours. Again no significant changes in the microstructure occurred (Fig. 11.8 (i-j)). EDS showed no noteworthy changes in compositions (Table 11.3). The XRD diffractograms of IP9-HT-1200 ^{0}C/100h and IP9-HT-1200 ^{0}C/200h alloys were very similar (Fig. 11.9).

Table 11.3.

Data from EDS analysis for the composition of the phases in IP9-AC, IP9-HT-900 ^{0}C/100h, IP9-HT-900 ^{0}C/200h, IP9-HT1200 ^{0}C/100h and IP9-HT-1200 ^{0}C/200h.

	Nb (at %)	Ti (at %)	Sn (at %)
IP9-AC			
Nb_3Sn	46.7 ± 0.1	32.6 ± 0.2	20.7 ± 0.2
Ti_3Sn	15.3 ± 0.4	59.2 ± 0.4	25.5 ± 0.3
Nb-rich Ti_3Sn	29.5 ± 0.4	46.8 ± 0.5	23.7 ± 0.5
IP9-HT-900 ^{0}C/100h			
Nb_3Sn	48.5 ± 0.2	30.8 ± 0.2	20.7 ± 0.1
Ti_3Sn	12.9 ± 0.2	61.6 ± 0.3	25.6 ± 0.2
Nb-rich Ti_3Sn	30.2 ± 0.3	46.2 ± 0.3	23.6 ± 0.3
IP9-HT-900 ^{0}C/200h			
Nb_3Sn	48.7 ± 0.2	30.5 ± 0.3	20.8 ± 0.2
Ti_3Sn	13.4 ± 0.4	61.4 ± 0.4	25.2 ± 0.3
Nb-rich Ti_3Sn	30.8 ± 0.5	46.1 ± 0.4	23.1 ± 0.4
IP9-HT-1200 ^{0}C/100h			
Nb_3Sn	47.6 ± 0.1	31.1 ± 0.2	21.3 ± 0.1
Ti_3Sn	11.4 ± 0.4	63.4 ± 0.3	25.2 ± 0.2
Nb-rich Ti_3Sn	31.2 ± 0.6	45.6 ± 0.5	23.2 ± 0.4
IP9-HT-1200 ^{0}C/200h			
Nb_3Sn	47.8 ± 0.1	31.4 ± 0.1	20.8 ± 0.2
Ti_3Sn	11.3 ± 0.4	63.5 ± 0.2	25.3 ± 0.2
Nb-rich Ti_3Sn	30.9 ± 0.5	45.9 ± 0.4	23.2 ± 0.4

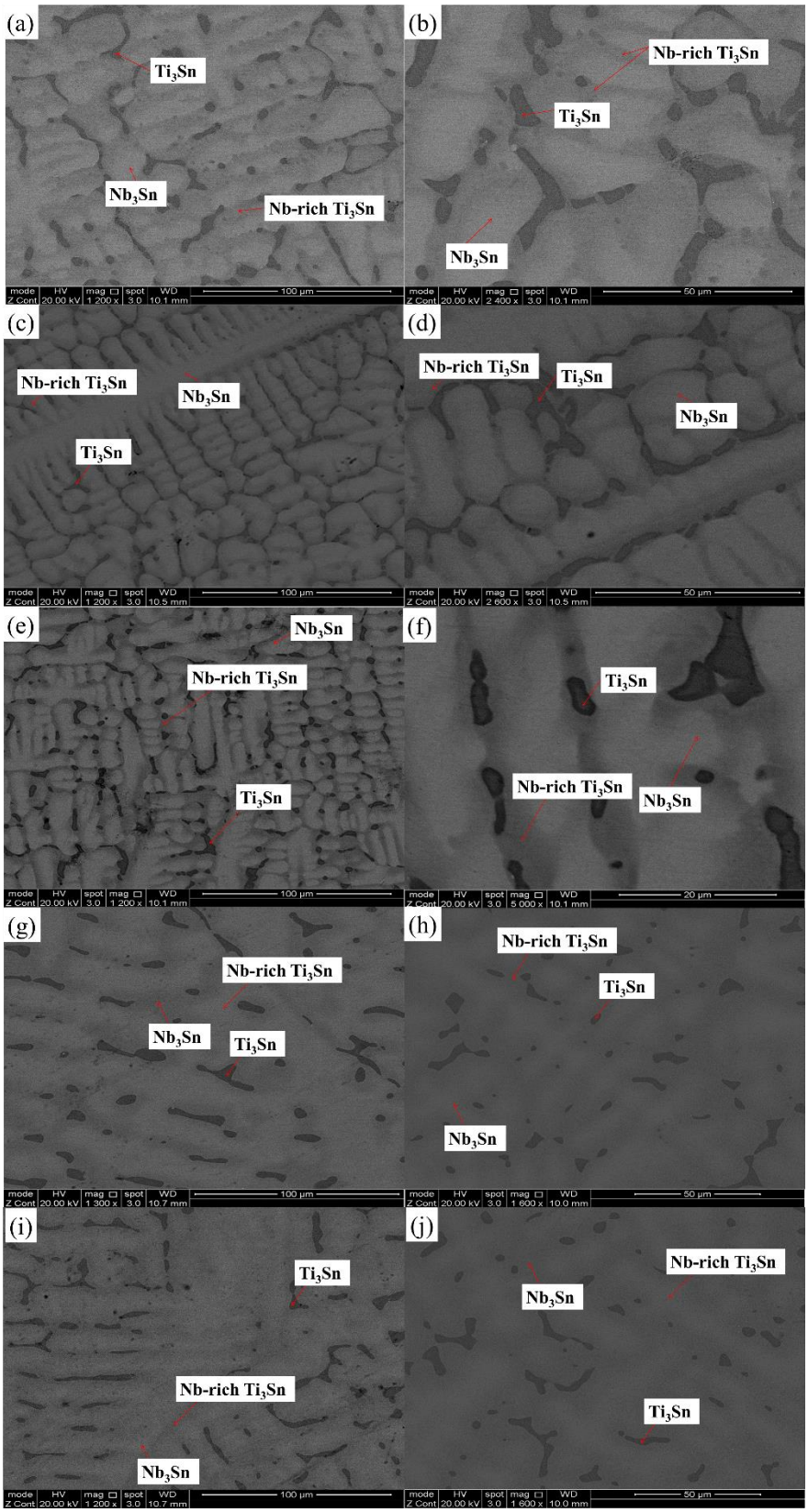

Fig. 11.8. BSE images of in in IP9-AC (a-b), IP9-HT 900 ^{0}C/100h (c-d), IP9-HT 900 ^{0}C/200h (e-f), IP9-HT 1200 ^{0}C/100h (g-h) and IP9-HT 1200 ^{0}C/200h (i-j)

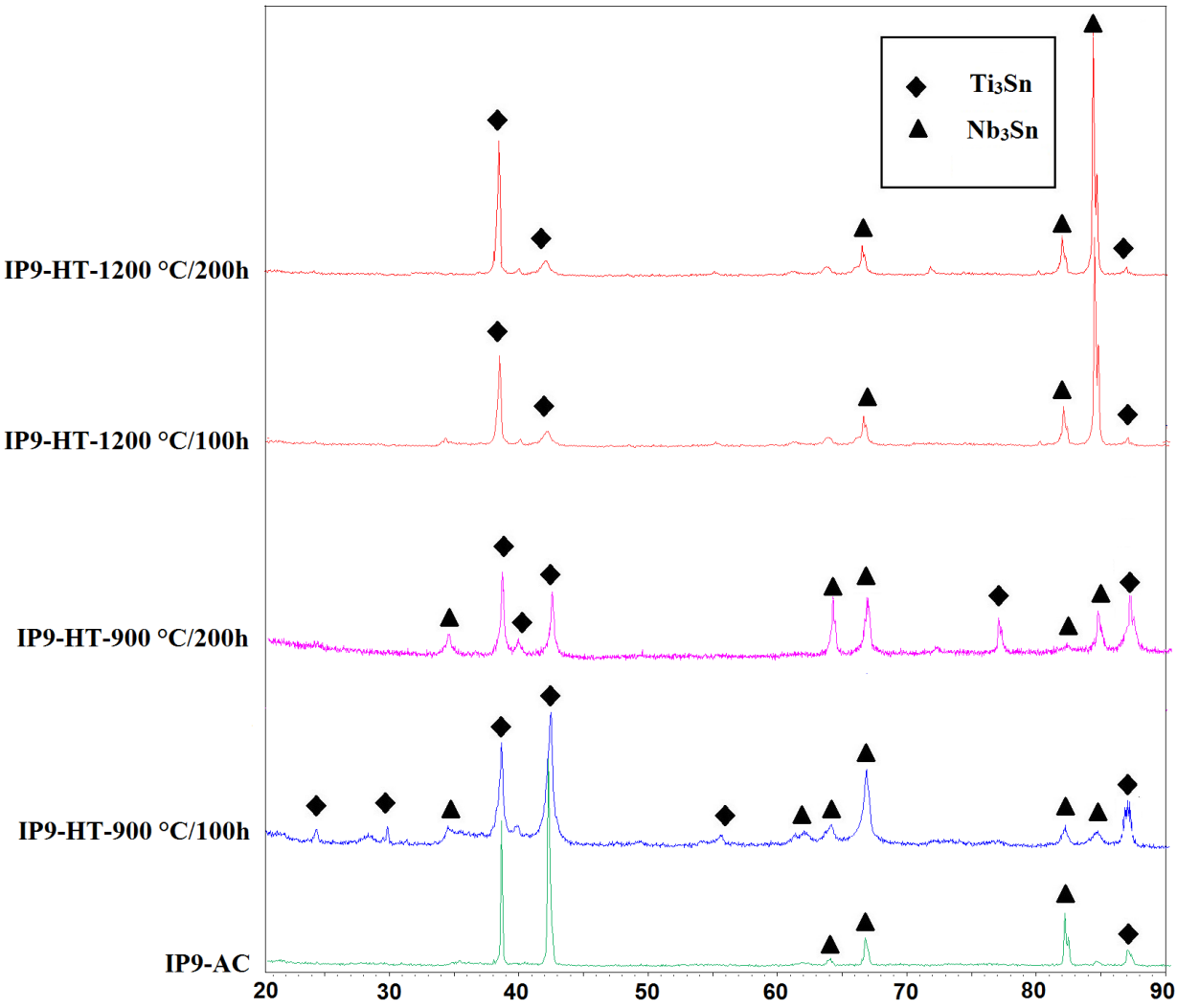

Fig. 11.9. XRD diffractograms of IP9-AC, IP9-HT-900 ^{0}C /100h, IP9-HT-900 ^{0}C /200h, IP9-HT-1200 ^{0}C /100h and IP8-HT-1200 ^{0}C /200h. The very large peak at ~85° most possibly is due to the preferential orientation due to the method used (bulk sample analysis)

11.2.4. Alloy Nb-39Ti -40Sn (IP10)

As cast. From the BSE images of IP10-AC (Fig. 11.10 (a-b)) it is evident that three phases were present. As it was confirmed by the XRD (Fig. 11.11) and EDS analysis, these were Nb_3Sn (brighter grains) and Ti_6Sn_5 (darker areas) with Nb-rich Ti_6Sn_5 areas (grey areas) having the highest volume fraction. The compositions of the phases are given in Table 11.4. The Ti content in Nb_3Sn was 28.6 at. % while the Nb content was 45.7 at. %. The Nb content varied from 9.2 in Ti_6Sn_5 to 16.7 at. % in Nb-rich Ti_6Sn_5.

Heat treated. The alloy was given 3 separate heat treatments; 100 h at 900 °C, 200 h at 900 °C and 200 h at 1200 °C. After 100 h at 900 °C there was partitioning of Ti in Nb_3Sn to the grain boundaries between Nb_3Sn and Nb-rich Ti_6Sn5 (Fig. 11.10 (c-d)). The composition of the Ti-rich areas (dark areas) could not be measured using EDS as there were too small. The XRD analysis of IP10-HT-900 ^{0}C/100h indicated that it was Ti_3Sn. After heat treatment the volume fraction of the regular Ti_6Sn_5 decreased significantly. Compared with the as-cast alloy, the composition of the Nb_3Sn and Nb-rich Ti_6Sn_5 did not undergo any considerable changes (Table 11.4), while the regular Ti_6Sn_5 became about 2.5 at. % richer in Ti and 2 at. % poorer in Sn.

IP10-HT-900 ^{0}C/100h was heat treated for an additional 100 hours at 900 °C. As it can be seen in Fig. 11.10 (e-f), the dark areas at the grain boundaries of Nb_3Sn coarsened significantly, and thus they were analysed by EDS. The EDS confirmed that the dark phase was Ti_3Sn with Nb and Ti contents of 14.5 and ~60 at. %, respectively. According to the BSE images only traces of the regular Ti_6Sn_5 were present. Compared with the IP10-HT-900 ^{0}C /100h, no significant alterations of the chemical compositions of the present phases were noted.

IP10-AC was heat treated at 1200 °C for 200 hours. The microstructure consisted of Nb-rich Ti_6Sn_5, Nb_3Sn and Ti_3Sn with remnants of regular Ti_6Sn_5, as can be seen in the BSE images in Fig. 11.10 (g-h) and XRD in Fig. 11.11. In Fig. 11.12 the X-ray element maps of the IP10-HT-1200 ^{0}C/200h are shown, which clarify the presence of the aforementioned phases. The Ti element map highlights the location of phases in the microstructure. The brightest areas are Ti_3Sn whereas the darkest areas are Nb_3Sn. The Ti_6Sn_5 and Nb-rich Ti_6Sn_5 can also be distinguished by their brightness in the Ti map (the latter being darker than Ti_6Sn_5 regions). Compared with the IP10-AC, Nb_3Sn was considerably poorer in Ti and correspondingly richer in Nb by approximately 5 at. %. Ti_6Sn_5 was poorer in Ti by ~2 at. % and richer in Nb by ~3 at. %. Regarding the Nb-rich Ti_6Sn_5, the Sn content was about 1.3 at. % higher with respect to the IP10-AC. In Ti_3Sn the Sn content was 26.1 at. %, while Ti and Nb were 58.8 and 15.1 at. %, respectively.

Table 11.4. Data from EDS analysis for the composition of the phases in IP10-AC, IP10-HT-900 ^{0}C/100h, IP10-HT-900 ^{0}C/200h and IP10-HT-1200 ^{0}C/200h.

	Nb (at %)	Ti (at %)	Sn (at %)
IP10-AC			
Nb_3Sn	45.7 ± 0.2	28.6 ± 0.3	25.7 ± 0.2
Nb-rich Ti_6Sn_5	16.7 ± 0.1	41.1 ± 0.3	42.2 ± 0.2
Ti_6Sn_5	9.2 ± 0.8	51.8 ± 1.5	39.0 ± 1.5
IP10-HT-900 ^{0}C /100h			
Nb_3Sn	45.9 ± 0.3	28.3 ± 0.2	25.8 ± 0.2
Nb-rich Ti_6Sn_5	16.5 ± 0.2	41.2 ± 0.2	42.3 ± 0.2
Ti_6Sn_5	8.8 ± 0.5	54.3 ± 1.3	36.9 ± 1.2
IP10-HT-900 ^{0}C /200h			
Nb_3Sn	46.5 ± 0.5	27.3 ± 0.5	26.2 ± 0.5
Nb-rich Ti_6Sn_5	17.1 ± 0.1	40.2 ± 0.3	42.7 ± 0.2
Ti_6Sn_5	9.0 ± 1.1	52.9 ± 1.5	38.1 ± 1.6
Ti_3Sn	14.5 ± 1.5	59.8 ± 2.2	25.7 ± 2.4
IP10-HT-1200 ^{0}C /200h			
Nb_3Sn	50.5 ± 0.3	23.8 ± 0.2	25.7 ± 0.3
Nb-rich Ti_6Sn_5	16.1 ± 0.4	40.4 ± 0.8	43.5 ± 0.9
Ti_6Sn_5	12.2 ± 0.5	50.0 ± 0.5	37.8 ± 0.5
Ti_3Sn	15.1 ± 0.7	58.8 ± 0.9	26.1 ± 0.6

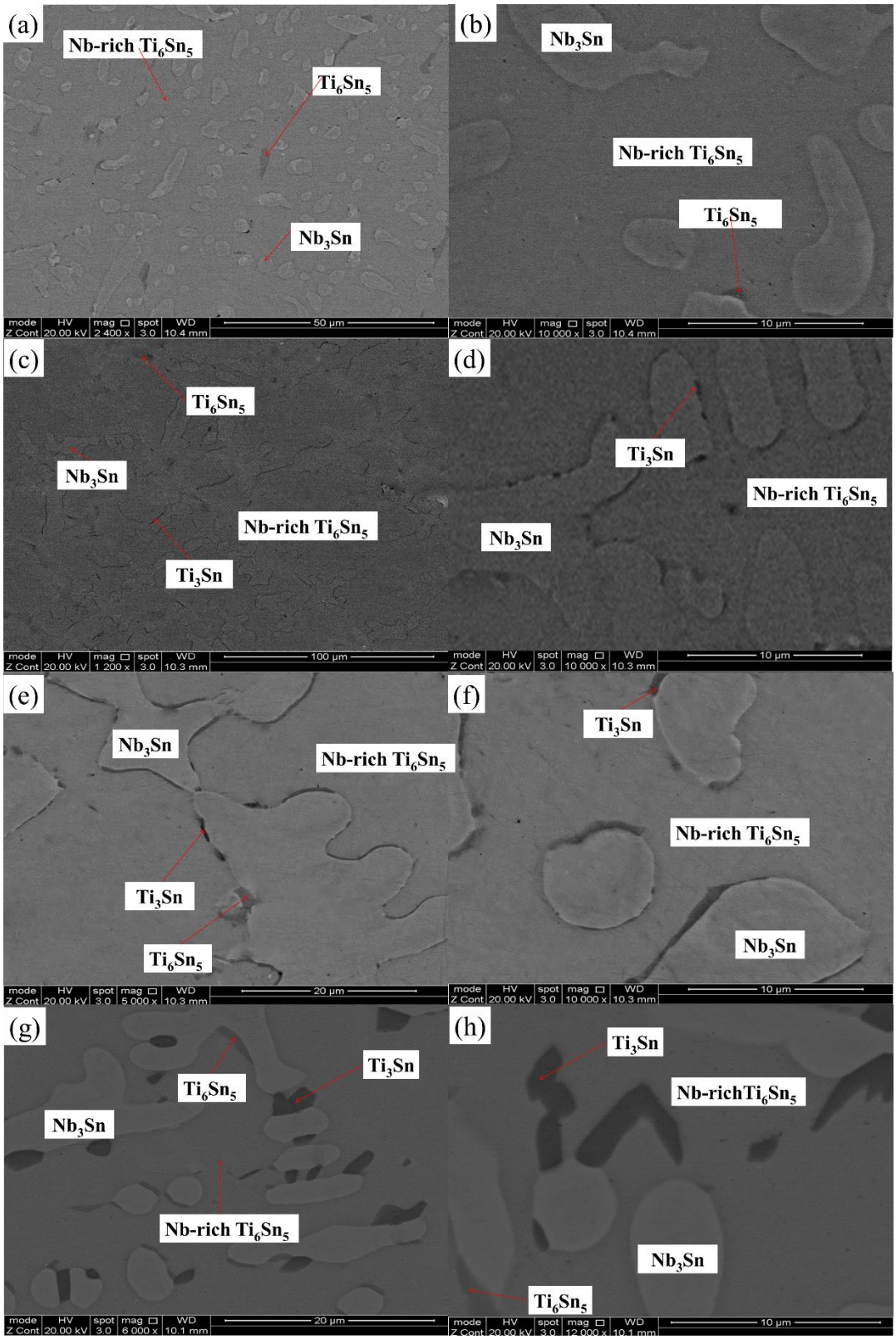

Fig. 11.10. BSE images of in in IP10-AC (a-b), IP10-HT-900 ^{0}C/100h (c-d), IP10-HT-900 ^{0}C/200h (e-f) and IP10-HT-1200 ^{0}C/200h (g-h)

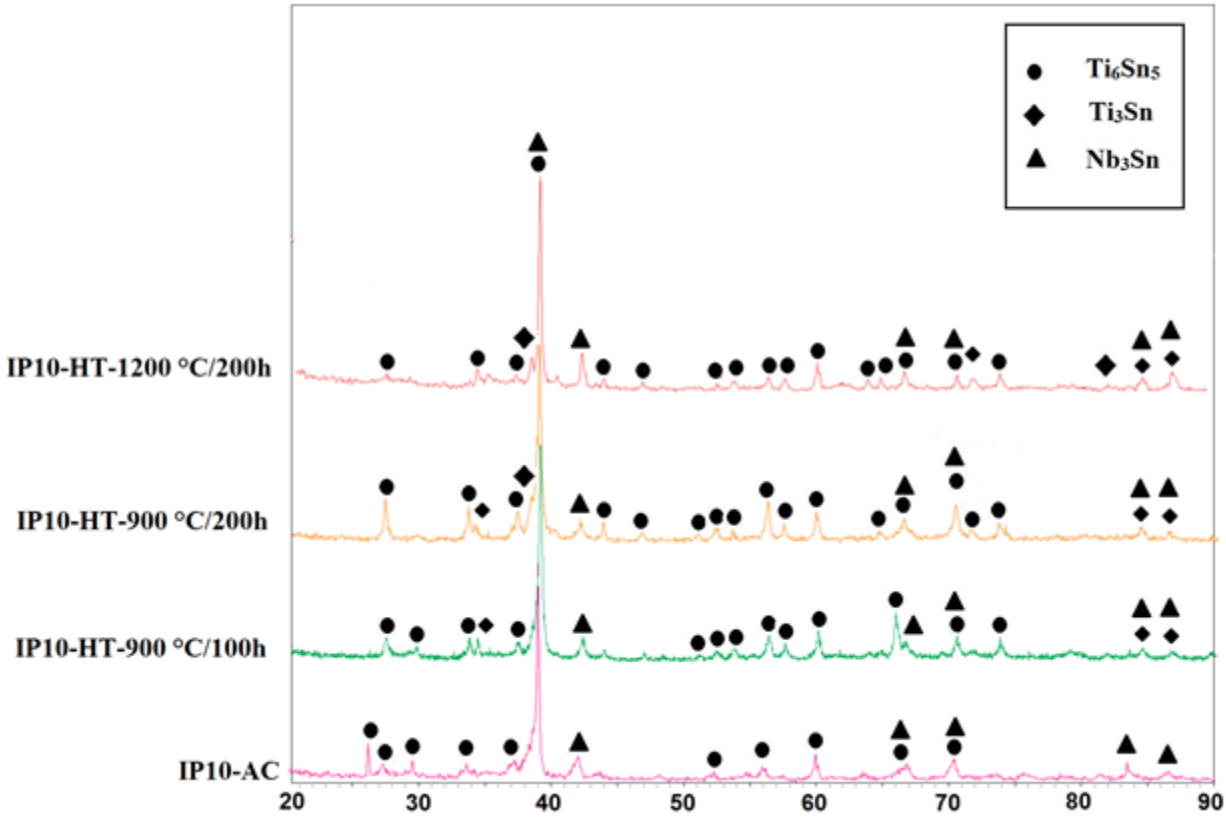

Fig. 11.11. XRD diffractograms of IP10-AC, IP10-HT-900 ^{0}C /100h, IP10-HT-900 ^{0}C /200h and IP10-HT-1200 ^{0}C /200h

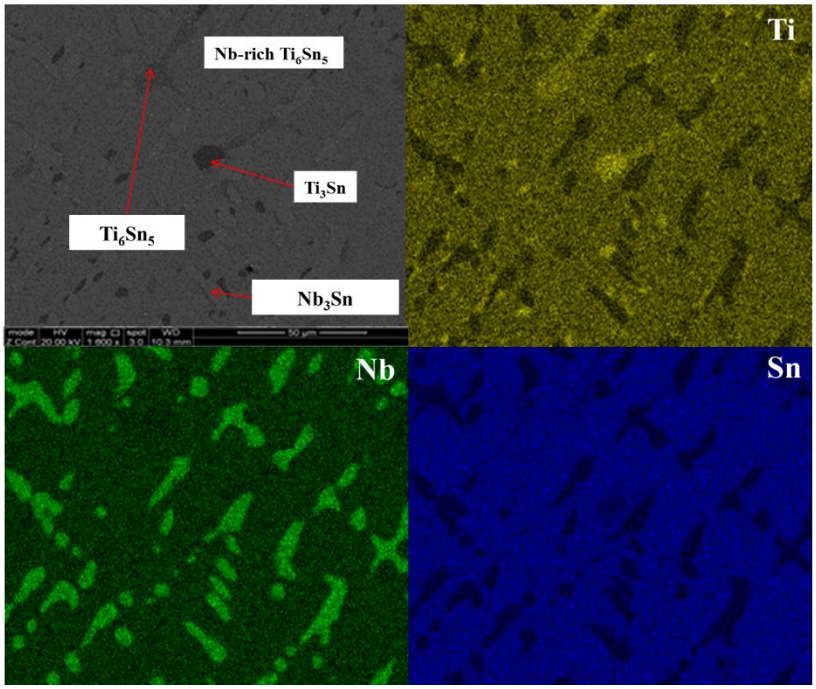

Fig. 11.12. X-ray element maps of IP10-HT-1200 ^{0}C/200h

11.3. Discussion

Regarding the IP7 alloy the suggested equilibrium at 900 °C is Nb_{ss}, Nb_3Sn and Ti_3Sn, while at 1200 °C it is Nb_{ss}, Nb_3Sn and Ti_{ss}. The Nb_{ss} shows a striking compositional variation between 900 and 1200 °C. It was considerably richer in Nb at 1200 °C by ~10 at. % compared with the 900 °C, while it was poorer in Ti and significantly poorer in Sn by about 1.5 and 8 at. %, respectively. At 900 °C the Ti/Sn ratio of Nb_{ss} decreased as the hours of heat treatment increased, mainly due to the decrease in Ti content, a fact that agrees with the precipitation of Ti to the grain boundaries to form Ti_3Sn. Also considerable coarsening of the Ti_3Sn, which was always formed in the grain boundaries, took place as the heat treatment time increased. Hence, it is suggested that Ti moves from the solid solution to form the Ti_3Sn phase at 900 °C. On the contrary, the Ti/Sn ratio of Nb_{ss} increased as the hours of heat treatment increased at 1200 °C. Furthermore, the compositions of Nb_3Sn and Ti_3Sn in all the IP7 specimens investigated indicate that it is more probable for Ti to substitute Nb as the Sn content was found constant in Nb_3Sn and Ti_3Sn at ~18 at. % and ~25 at. %, respectively which correspond well with the typical compositions of the aforementioned phases in the literature [28, 77]. In the IP7-AC alloy the primary phase formed was Nb_{ss}. After that the melt became richer in Sn, leading to the formation of Nb_3Sn. It is suggested that the solidification path was $L \rightarrow L+Nb_{ss} \rightarrow Nb_{ss}+Nb_3Sn$.

Considering the IP8 alloy, the primary phase formed was Nb_{ss} along with some Ti_{ss} evident after the heat treatments at 900 °C and 1200 °C. Compared with the as-cast alloys in both IP8-HT-900 °C/300h and IP8-HT-1200 °C/200h the Ti content decreased by ~0.7 at. % and ~2 at. % respectively. Furthermore, in both cases the Ti_{ss} volume fraction increased after the heat treatment at the grain boundaries of the solid solution. Thus, it can be suggested that Ti moves from Nb_{ss} to the grain boundaries to form Ti_{ss}. According to the Nb-Ti phase diagram [70] in the vicinity of the IP8 composition the microstructure should consist of only Nb_{ss}. These results suggest that despite its low content, Sn presence causes Ti to partition from Nb_{ss}. This suggests that in the ternary phase diagram one would expect a miscibility gap to exist between Nb_{ss} and Ti_{ss} in the presence of Sn, which may have implications for alloy design.

In the IP9 alloy the suggested equilibrium phases at 900 °C and 1200 °C are Nb_3Sn and Ti_3Sn. After heat treatment at both temperatures, the Ti_3Sn was richer in Ti (~2 at. % at 900 °C and ~4 at. % at 1200 °C) and correspondingly poorer in Nb compared with the as-cast alloy. On the other

hand, Nb_3Sn and Nb-rich Ti_3Sn areas became slightly poorer in Ti and richer in Nb. The above indicates that Ti diffuses from Nb_3Sn to Ti_3Sn during annealing. Tin content in Nb_3Sn and Ti_3Sn was ~ 21 at. % and 26 at. %, respectively, in all the samples. It is suggested that Ti mainly substitutes Nb in Nb_3Sn and Nb substitutes Ti in Ti_3Sn. This confirms the work of Velios and Tsakiropoulos [19] and Wang et al. [154] who reported the substitution of Ti on the Nb site in Nb-Ti-Si-Sn and Nb-Ti-Sn alloys, respectively. However the substitution of Nb in Ti_3Sn conflicts with the results of Holleck et al. [155].

In the IP9-AC the primary phase formed was Nb_3Sn. As this phase formed the melt became richer in Ti, and thus Ti_3Sn would subsequently form. Hence the suggested solidification path is $L \rightarrow L+Nb_3Sn \rightarrow L+Nb_3Sn+Ti_3Sn \rightarrow Nb_3Sn+Ti_3Sn+$ Nb-rich Ti_3Sn with Nb-rich Ti_3Sn being formed by the reaction $L+Nb_3Sn \rightarrow$ Nb-rich Ti_3Sn.

In IP10 it is suggested that the equilibrium phases at 900 and 1200 °C are Nb_3Sn, Ti_3Sn and Nb-rich Ti_6Sn_5. After heat treatment at 900 and 1200 °C the Ti content in the Nb_3Sn decreased by ~1 at. % and ~4.5 at. %, respectively. Furthermore, Ti_3Sn always formed at the grain boundaries of Nb_3Sn. These results indicate that Ti partitioning occured from Nb_3Sn to Nb-rich Ti_6Sn_5 leading to the formation of Ti_3Sn at the grain boundaries. In both Nb_3Sn and Ti_3Sn the Sn content was approximately 26 at. %, which again suggests that Ti substitutes Nb in Nb_3Sn and Nb substitutes Ti in Ti_3Sn. Niobium substitutes primarily Ti and secondarily Sn in Ti_6Sn_5. In IP10-AC the Nb_3Sn phase formed first, followed by the formation of Nb-rich Ti_6Sn_5 and as the melt was still rich in Ti the Ti_6Sn_5 was formed in some areas. The proposed solidification path was $L \rightarrow L+Nb_3Sn \rightarrow L+Nb_3Sn+$Nb-rich $Ti_6Sn_5 \rightarrow Nb_3Sn+$ Nb-rich $Ti_6Sn_5+Ti_6Sn_5$ with Ti_6Sn_5 being formed by the reaction L+ Nb-rich $Ti_6Sn_5 \rightarrow Ti_6Sn_5$.

11.4. Conclusions

The as cast and heat treated alloys Nb-10Ti-18Sn (IP7), Nb-13Ti-3Sn (IP8), Nb-40Ti-23Sn (IP9) and Nb-39Ti-40Sn (IP10) were investigated. The conclusions of this study are as follows:

- In IP7 at 900 °C the equilibrium consisted of Nb_{ss}, Nb_3Sn and Ti_3Sn, while at 1200 °C it consisted of Nb_{ss}, Nb_3Sn and Ti_{ss}. It is suggested that Ti moved from the solid solution to the grain boundaries to form the Ti_3Sn phase at 900 °C. In Ti_3Sn Nb substituted Ti and in Nb_3Sn Ti substituted Nb. Also in the solid solution the Ti/Sn ratio increased as the temperature of heat treatment increased, mainly due to the decrease in Sn content.
- The suggested solidification path of IP7-AC was $L \rightarrow L+Nb_{ss} \rightarrow Nb_{ss}+Nb_3Sn$.
- In IP8, at both 900 and 1200 °C, the equilibria consisted of Nb_{ss} and Ti_{ss}. Titanium moved from Nb_{ss} to the grain boundaries to form Ti_{ss}. It can be concluded that despite its low content, Sn caused Ti to partition from Nb_{ss}.
- In IP9, at both temperatures under the current study the equilibria consisted of Nb_{ss} and Nb_3Sn. Titanium moved from Nb_3Sn to Ti_3Sn after the heat treatment process. Titanium substitutes Nb in Nb_3Sn and Nb substitutes Ti in Ti_3Sn.
- The suggested solidification path of IP9-AC was $L \rightarrow L+Nb_3Sn \rightarrow L+Nb_3Sn+Ti_3Sn \rightarrow Nb_3Sn+Ti_3Sn+$ Nb-rich Ti_3Sn with Nb-rich Ti_3Sn formed by the reaction $L+Nb_3Sn \rightarrow$ Nb-rich Ti_3Sn.
- In IP10, at 900 °C and at 1200 °C the equilibria consisted of Nb_3Sn, Ti_3Sn and Ti_6Sn_5. Titanium partitioning took place from Nb_3Sn to Nb-rich Ti_6Sn_5 leading to the formation of Ti_3Sn. In Nb_3Sn Ti substitutes Nb, whereas in Ti_3Sn Nb substitutes Ti. In Ti_6Sn_5 Nb substitutes both Ti and Sn, with primary preference to the former.
- The proposed solidification path of IP10-AC was $L \rightarrow L+Nb_3Sn \rightarrow L+Nb_3Sn+$Nb-rich $Ti_6Sn_5 \rightarrow Nb_3Sn+$ Nb-rich $Ti_6Sn_5+Ti_6Sn_5$ with Ti_6Sn_5 formed by the reaction L+ Nb-rich $Ti_6Sn_5 \rightarrow Ti_6Sn_5$.

12

Phase equilibria in the Nb-Ti-Si-Sn quaternary system

12.1. Introduction

The microstructure of the Nb-24Ti-18Si-5Sn (IP1) alloy was studied in the as cast (NV6-AC) and heat treated at 1200 ^{0}C for 100 hours (NV6-HT) alloy in [19]. Overall, the microstructure of the as cast and heat treated alloy consisted of the $(Nb,Ti)_{ss}$, $(Nb,Ti)_3Sn$ and $(Nb,Ti)_5Si_3$ phases (Fig. 12.1). There were areas of Ti-rich and very Ti-rich 5-3 silicide observed, while macrosegregation of Ti and Si was evident. The co-existence of the $\alpha(Nb,Ti)_5Si_3$, $\beta(Nb,Ti)_5Si_3$ and $\gamma(Nb,Ti)_5Si_3$ was confirmed in the as-cast alloy by XRD [19], while in the heat-treated only the $\alpha(Nb,Ti)_5Si_3$ and $\gamma(Nb,Ti)_5Si_3$ phases were evident. Only the $\alpha(Nb,Ti)_5Si_3$ and $\beta(Nb,Ti)_5Si_3$ intermetallics are stable in the Nb-Si system, while the $\gamma(Nb,Ti)_5Si_3$ is considered metastable. Lamellar structures between $(Nb,Ti)_5Si_3$ and $(Nb,Ti)_{ss}$ were observed in as cast (NV6-AC) and heat treated (NV6-HT) alloy (Fig. 12.1).

The motivation of the research described in this chapter was to verify the stable phases and the phase equilibria in the above alloy at 1000, 1100 and 1300 ^{0}C.

12.2 Results

As cast. The EBSD analysis of the cast alloy (NV6-AC in [19]) is shown in Fig.12.2 and 12.3. From the phase map (Fig. 12.2 (b)) it can be seen that the present phases were Nb, Nb_3Sn, αNb_5Si_3, βNb_5Si_3 and γNb_5Si_3. The αNb_5Si_3 silicide formed bulk dendrites throughout the specimen, while remnants of the β where found where the Nb_3Sn grains were of a specific orientation. The Ti-rich and very Ti-rich areas reported in [19] were αNb_5Si_3 and γNb_5Si_3 respectively. Furthermore the orientation maps of the as cast alloy (Fig. 12.3) showed that all the phases (except the γNb_5Si_3) and especially the α silicide exhibited large regions with similar orientation extending over several hundreds of micrometers.

Heat treated. The IP1 alloy was heat treated for 100 hours at 1000 °C or 1100 °C or 1300 °C. The chemical analysis data and the typical microstructures of all the heat treated alloys are given in Table 12.1 and Fig. 12.4 to 12.6, respectively. Table 12.1 includes data from [19] for NV6-AC and NV6-HT (the alloy compositions of IP1 and NV6 were the same). The X-ray element maps and X-ray line-scans of the IP1-HT 1000 °C are shown in Fig. 12.9 and 12.10.

Table 12.1

EPMA data of the NV6-AC [19] and NV6-HT 1200 ^{0}C alloy [19], and EDS data (at. %) of the IP1-HT 1000 ^{0}C, IP1-HT 1100 ^{0}C, IP1-HT 1300 ^{0}C alloy.

	Nb	Ti	Si	Sn	Si+Sn	Si/Sn
NV6-AC [19]						
$(Nb,Ti)_{ss}$	56.7 ± 2.1	35.6 ± 2.1	1.6 ± 0.4	6.1 ± 0.3	7.7	0.26
$(Nb,Ti)_3Sn$	61.6 ± 0.7	20.2 ± 1.0	7.6 ± 0.4	10.6 ± 0.7	18.2	0.72
$(Nb,Ti)_5Si_3$	46.6 ± 0.7	16.6 ± 0.5	35.3 ± 0.7	1.5 ± 0.4		
Ti-rich $(Nb,Ti)_5Si_3$	42.3 ± 1.2	21.0 ± 1.2	35.5 ± 0.4	1.2 ± 0.2		
very Ti-rich $(Nb,Ti)_5Si_3$	34.0 ± 4.1	30.4 ± 3.8	34.2 ± 0.9	1.4 ± 0.6		
IP1-HT 1000 °C						
$(Nb,Ti)_{ss}$	66.2 ± 1.1	29.9 ± 1.2	0.4 ± 0.1	3.6 ± 0.6	3.9	0.10
$(Nb,Ti)_3Sn$	55.7 ± 0.9	28.5 ± 1.2	5.5 ± 0.6	10.4 ± 0.3	15.8	0.53
$(Nb,Ti)_5Si_3$	48.0 ± 0.8	15.1 ± 0.9	35.5 ± 0.5	1.4 ± 0.5		
Ti-rich $(Nb,Ti)_5Si_3$	40.7 ± 1.5	24.2 ± 1.6	33.9 ± 0.6	1.2 ± 0.3		
very Ti-rich $(Nb,Ti)_5Si_3$	33.4 ± 2.2	30.8 ± 2.9	34.9 ± 0.8	0.9 ± 0.5		
IP1-HT 1100 °C						
$(Nb,Ti)_{ss}$	66.9 ± 1.5	29.1 ± 2.1	0.6 ± 2.1	3.4 ± 0.2	4.0	0.16
$(Nb,Ti)_3Sn$	54.1 ± 1.0	28.4 ± 0.5	7.4 ± 0.3	10.1 ± 0.8	17.5	0.74
$(Nb,Ti)_5Si_3$	48.5 ± 0.8	19.0 ± 0.6	31.3 ± 0.6	1.2 ± 0.3		
Ti-rich $(Nb,Ti)_5Si_3$	39.0 ± 1.2	25.1 ± 1.3	34.4 ± 0.8	1.5 ± 0.2		
very Ti-rich $(Nb,Ti)_5Si_3$	31.4 ± 1.3	32.5 ± 2.2	35.8 ± 1.0	0.4 ± 0.1		
NV6-HT 1200 ^{0}C/100h [19]						
$(Nb,Ti)_{ss}$	66.5 ± 0.7	29.2 ± 0.7	0.3 ± 0.3	4.0 ± 0.2	4.3	0.08
$(Nb,Ti)_3Sn$	55.5 ± 1.5	28.2 ± 1.1	5.3 ± 0.5	11.0 ± 0.8	16.3	0.48
$(Nb,Ti)_5Si_3$	47.3 ± 0.2	16.2 ± 0.2	34.7 ± 0.1	1.8 ± 0.1		
Ti-rich $(Nb,Ti)_5Si_3$	41.9 ± 2.3	21.9 ± 2.	35.0 ± 0.3	1.2 ± 0.2		
very Ti-rich $(Nb,Ti)_5Si_3$	32.7 ± 1.5	32.1 ± 1.2	34.9 ± 1.1	0.3 ± 0.2		
IP1-HT 1300 °C						
$(Nb,Ti)_{ss}$	64.0 ± 1.1	31.1 ± 2.1	0.4 ± 0.1	4.5 ± 0.1	5.0	0.10
$(Nb,Ti)_3Sn$	53.0 ± 0.6	29.3 ± 0.7	4.1 ± 0.5	13.6 ± 1.0	17.8	0.30
$(Nb,Ti)_5Si_3$	46.7 ± 0.8	16.0 ± 0.6	36.4 ± 0.6	1.0 ± 0.4		
Ti-rich $(Nb,Ti)_5Si_3$	40.7 ± 1.3	23.9 ± 1.2	34.5 ± 0.4	0.9 ± 0.3		
very Ti-rich $(Nb,Ti)_5Si_3$	31.0 ± 1.3	32.6 ± 1.1	36.0 ± 1.2	0.5 ± 0.2		

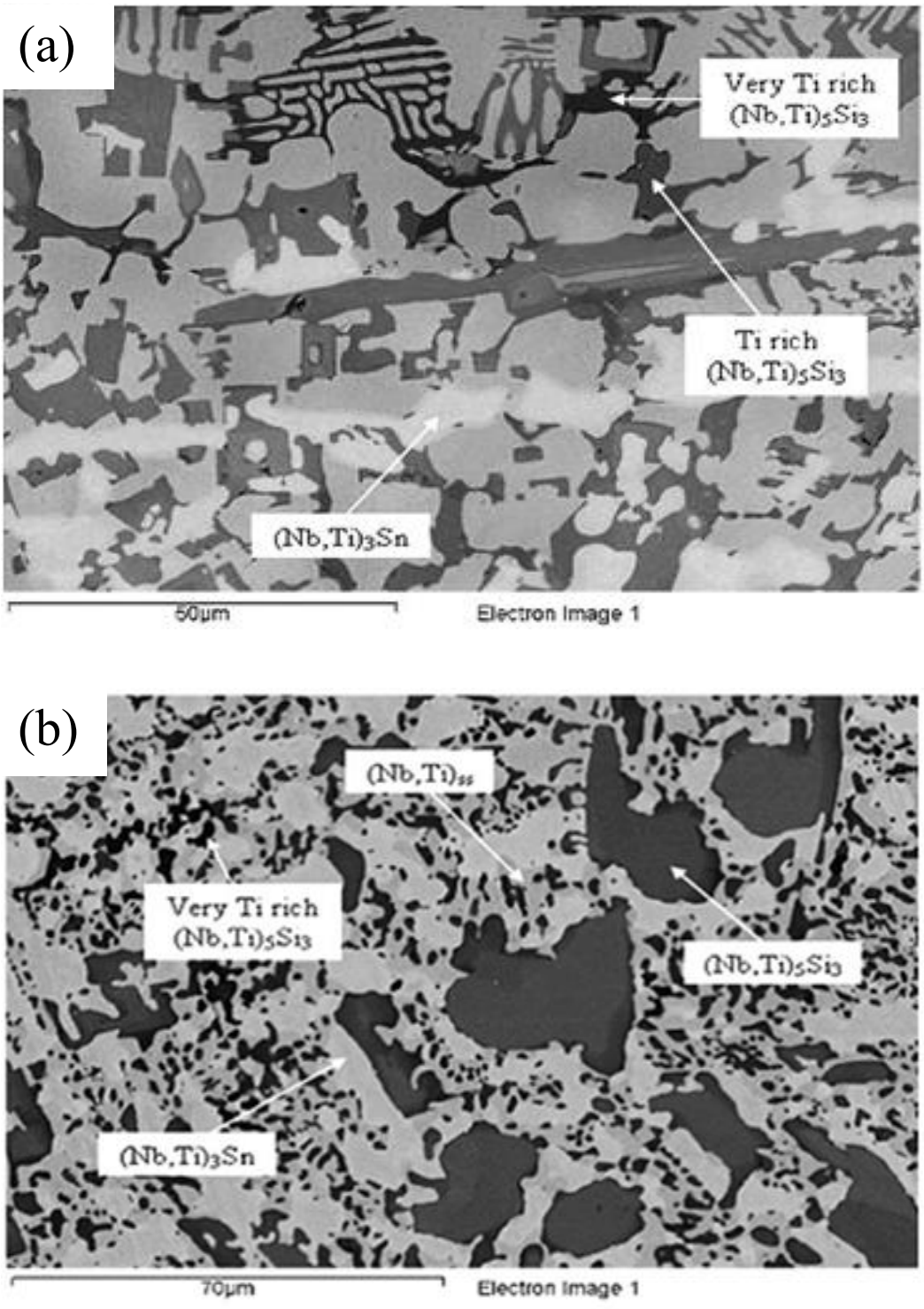

Fig. 12.1. BSE images of (a) the as cast and (b) the heat treated at 1200 ^{0}C alloy NV6 as reported in [19].

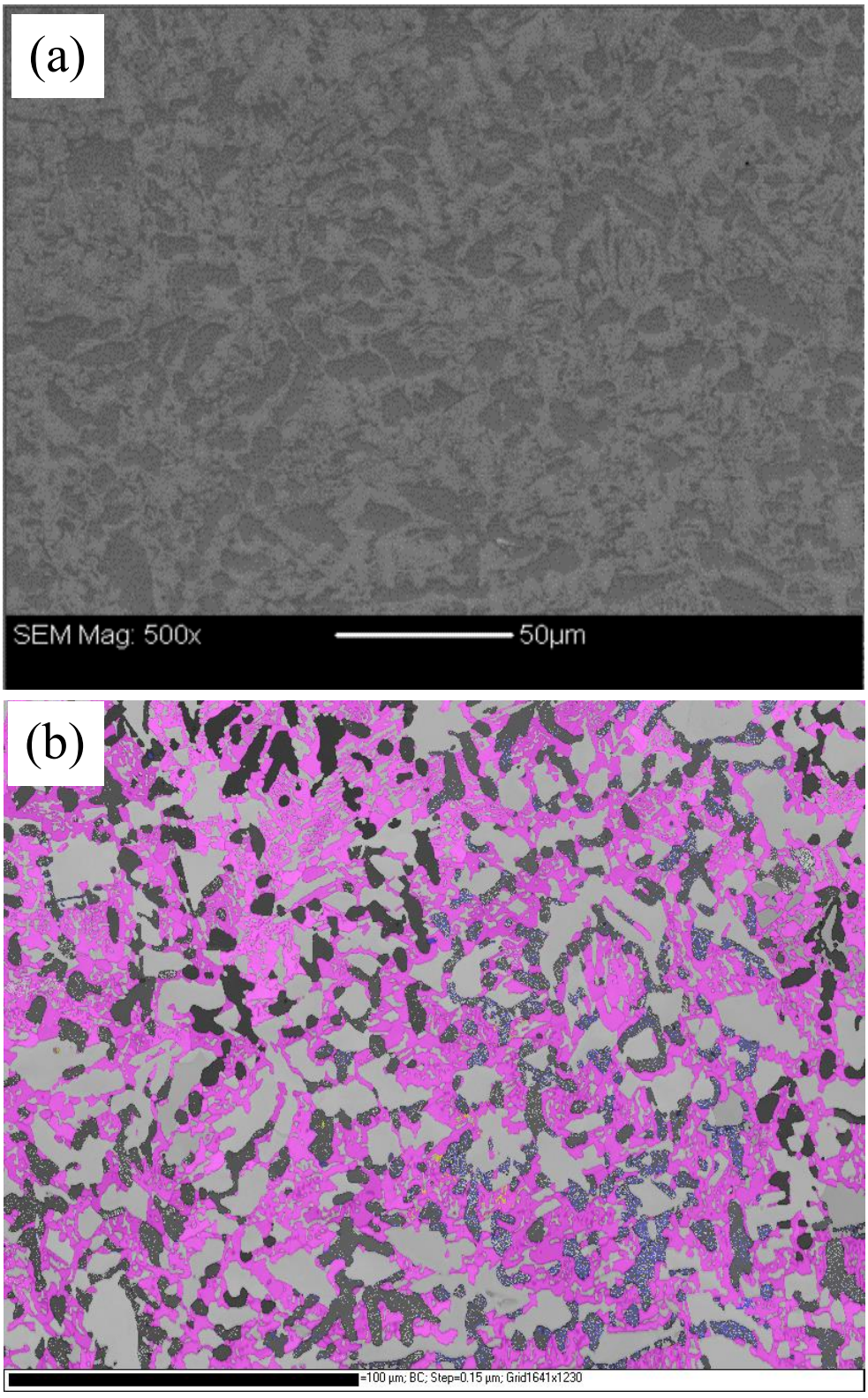

Fig. 12.2. SE image (a) and EBSD phase map (b) of IP1- AC (i.e. NV6-AC). The fuchsia, black, grey, blue and yellow areas denote Nb, Nb_3Sn, αNb_5Si_3, βNb_5Si_3 and γNb_5Si_3.

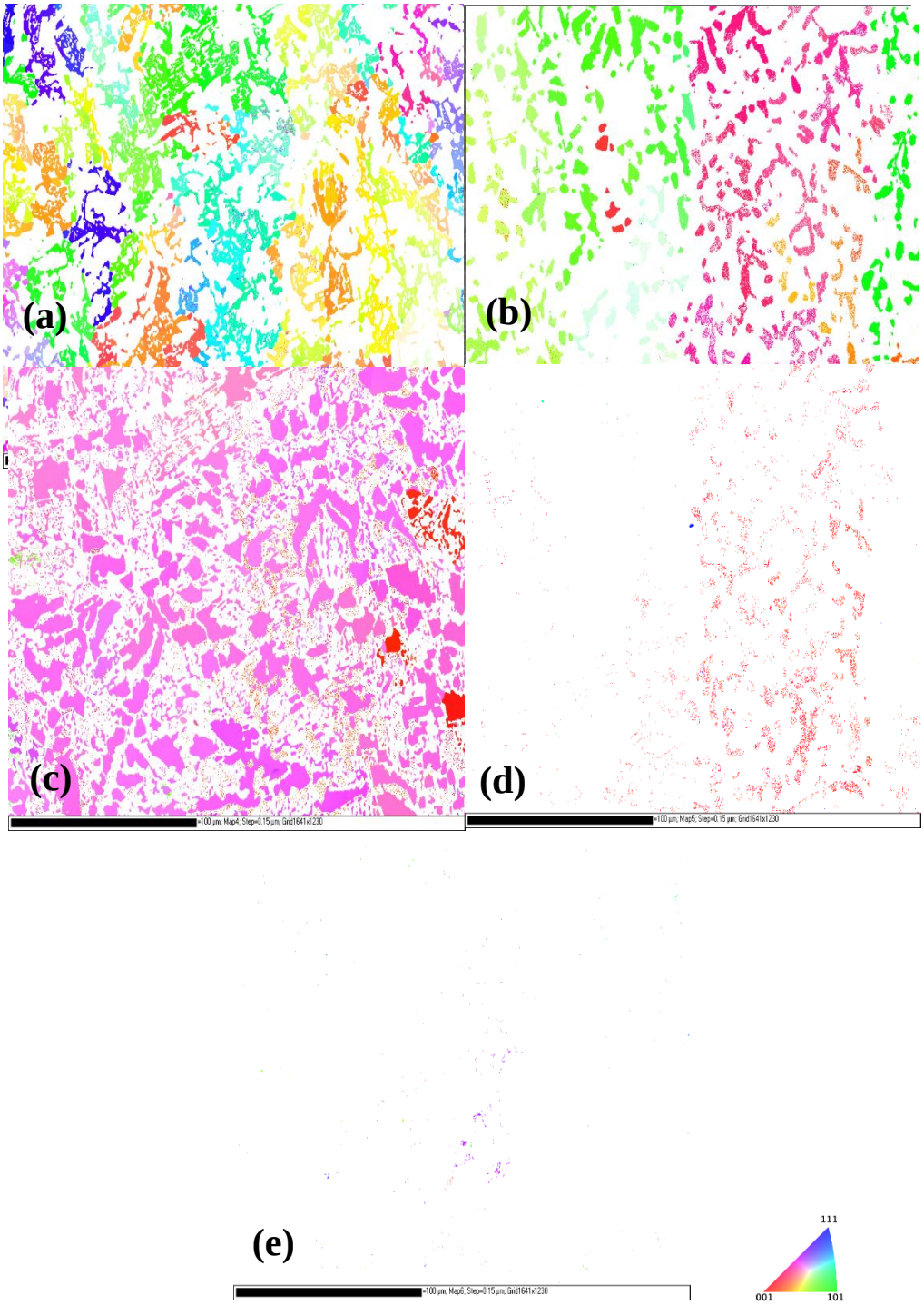

Fig. 12.3. Inverse pole figure (IPF) maps for Nb (a), Nb_3Sn (b), αNb_5Si_3 (c), βNb_5Si_3 (d) and γNb_5Si_3 (e) in IP1 – AC (i.e. NV6-AC) showing the orientation of each phase within the sample.

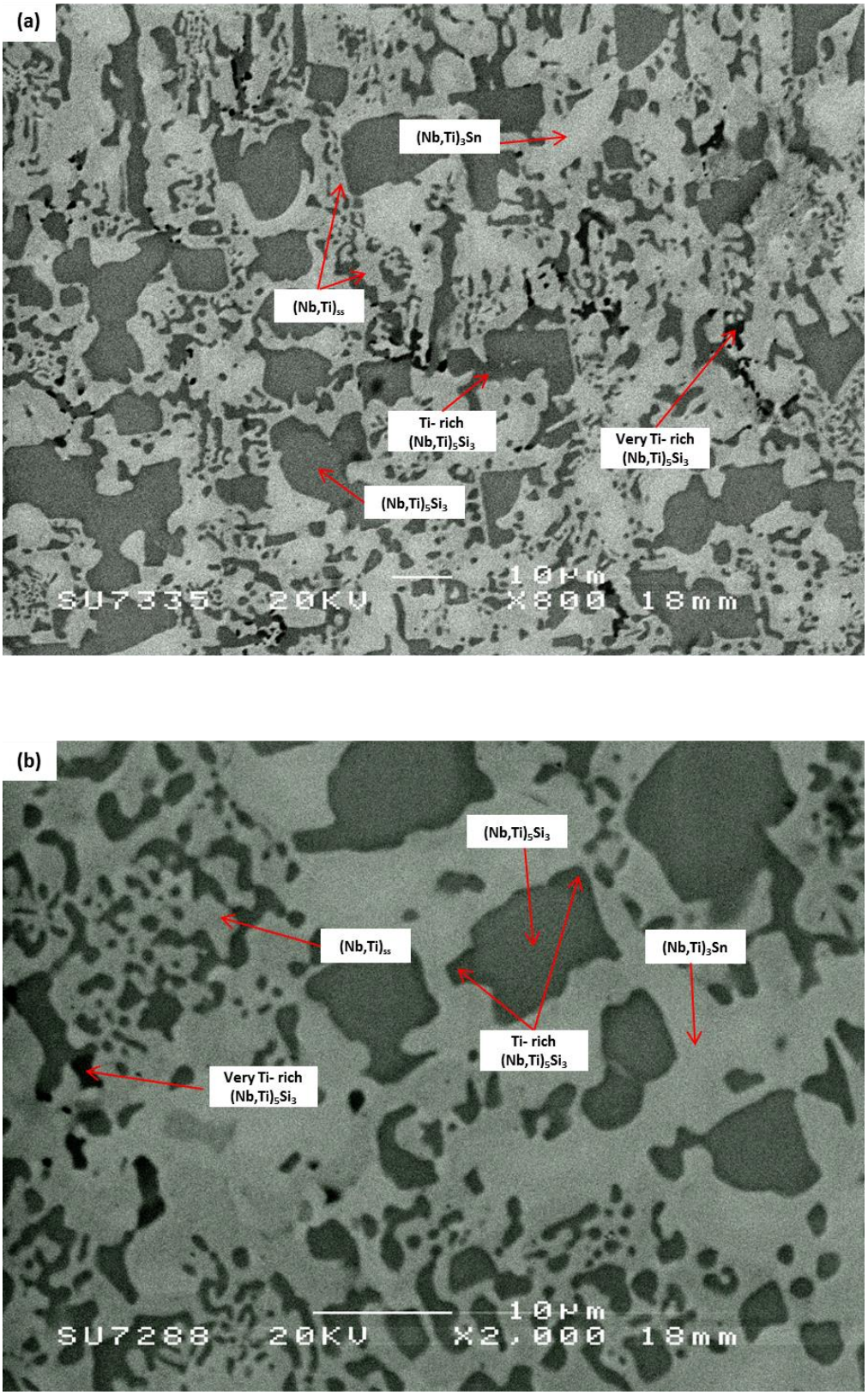

Fig.12.4. BSE images (a-b) of the IP1-HT 1000 ^{0}C.

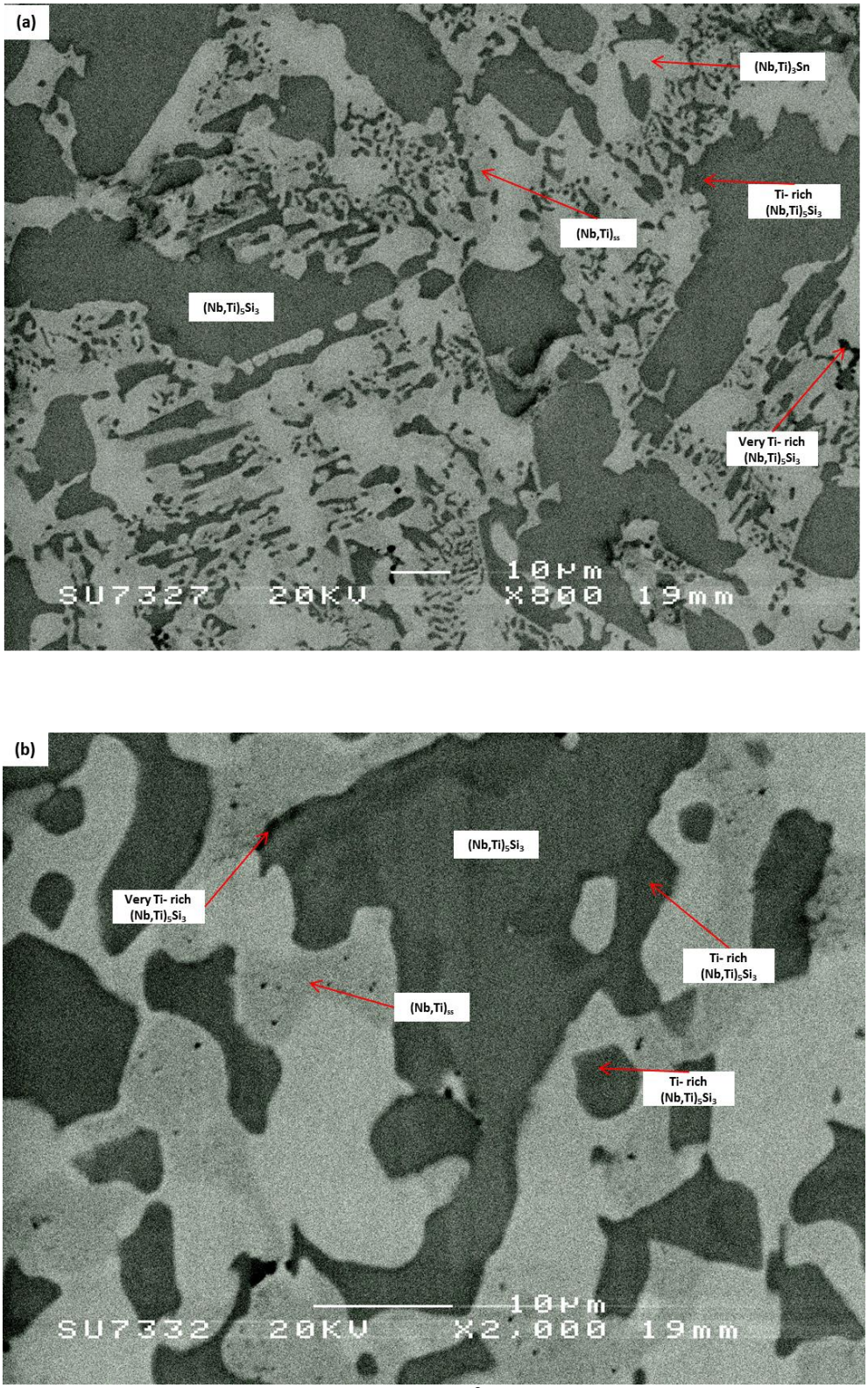

Fig.12.5. BSE images (a-b) of the IP1-HT 1100 ^{0}C. In (b) notice the presence of second phase in the $(Nb,Ti)_{ss}$ (see also Fig. 12.12).

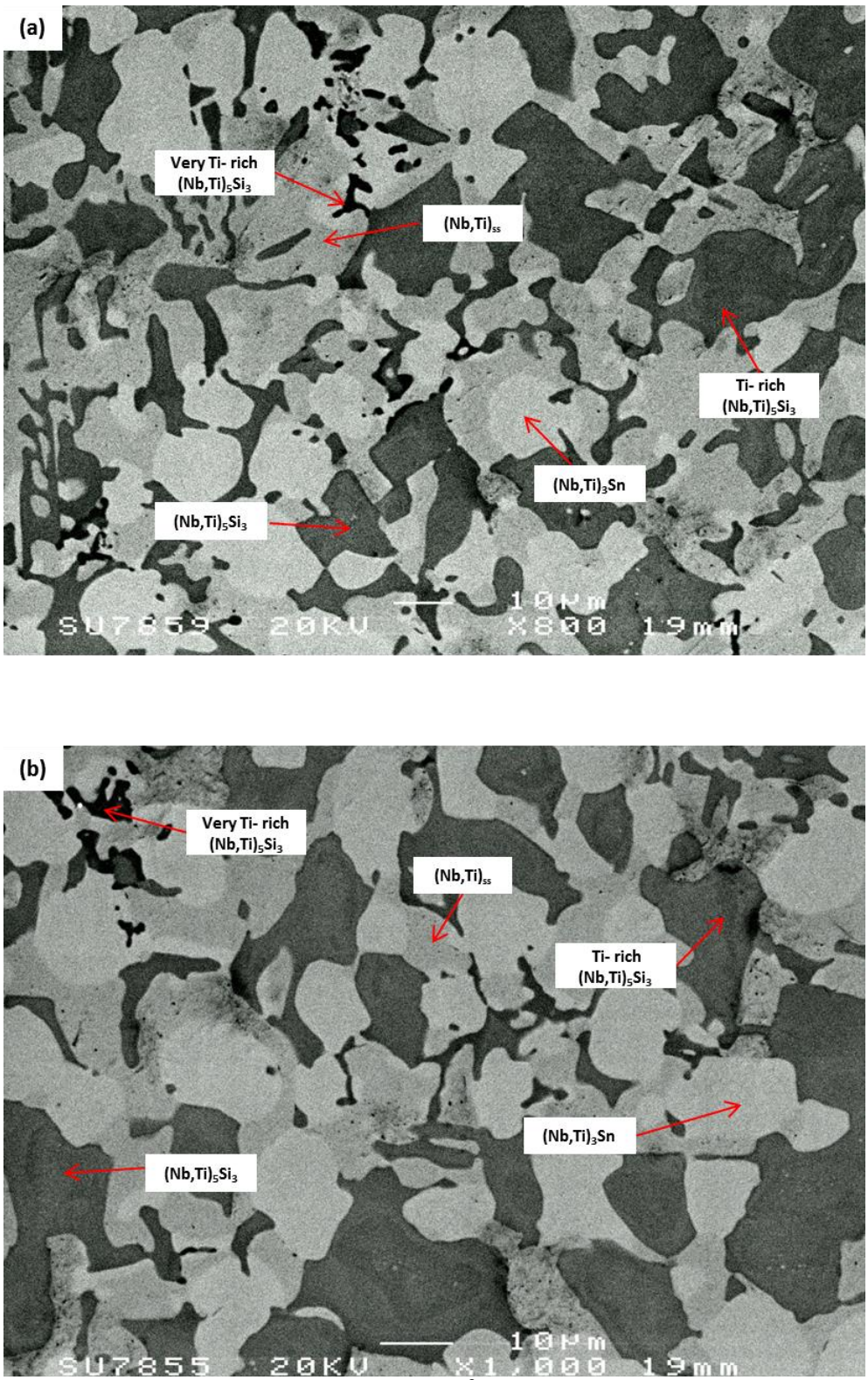

Fig.12.6. BSE images (a-b) of the IP1-HT 1300 ^{0}C. There is evidence of precipitation of a second phase in the $(Nb,Ti)_{ss}$ (see also Fig. 12.12)

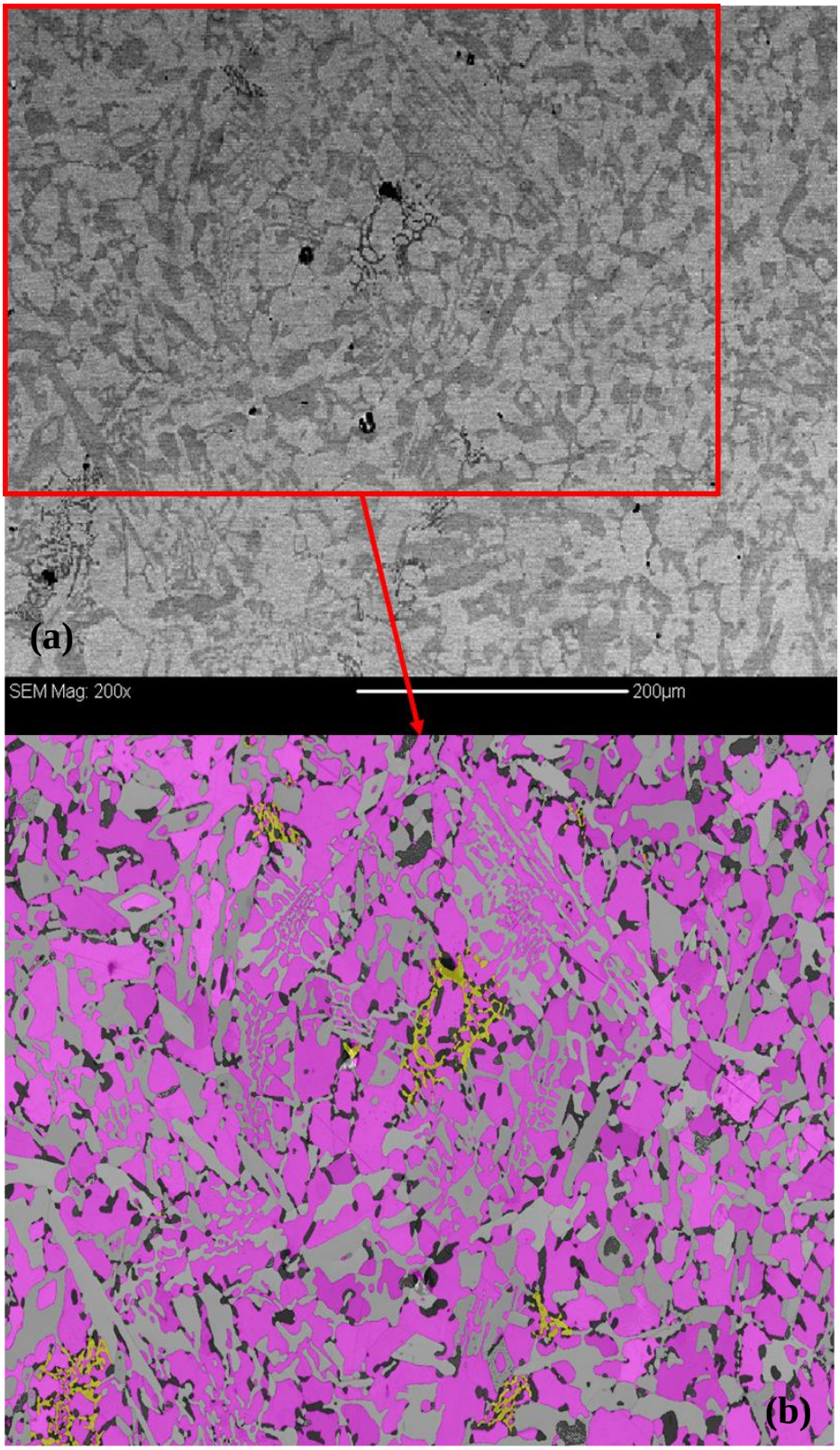

Fig. 12.7. SE image (a) and EBSD phase map (b) of IP1- HT 1300 ^{0}C. The fuchsia, black, grey and yellow areas denote Nb, Nb_3Sn, αNb_5Si_3 and γNb_5Si_3. (See Fig. 12.8 for IPF map).

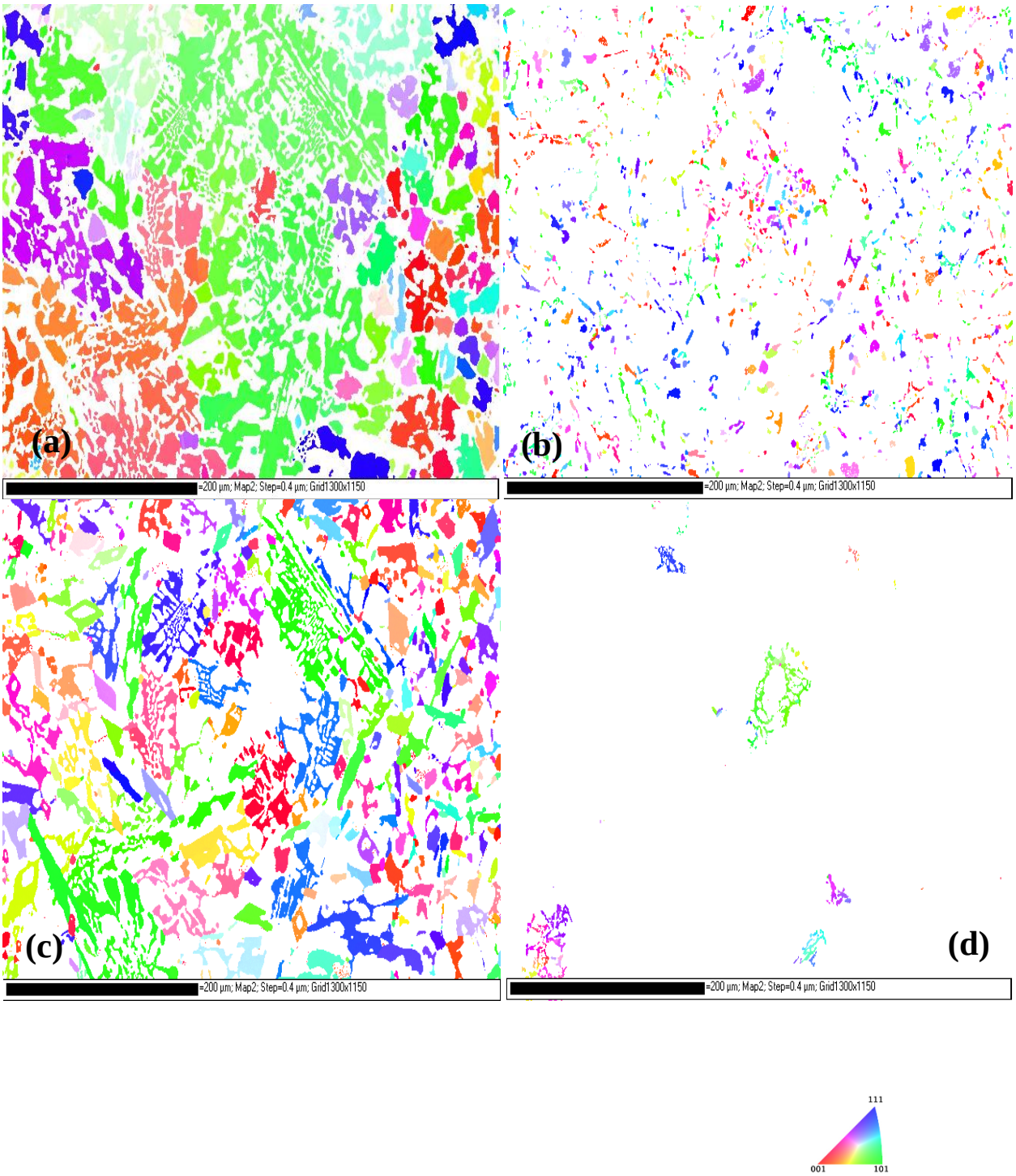

Fig. 12.8. Inverse pole figure (IPF) maps for Nb (a), Nb_3Sn (b), αNb_5Si_3 (c) and γNb_5Si_3 (d) in IP1- HT 1300 ^{0}C showing the orientation of each phase within the sample.

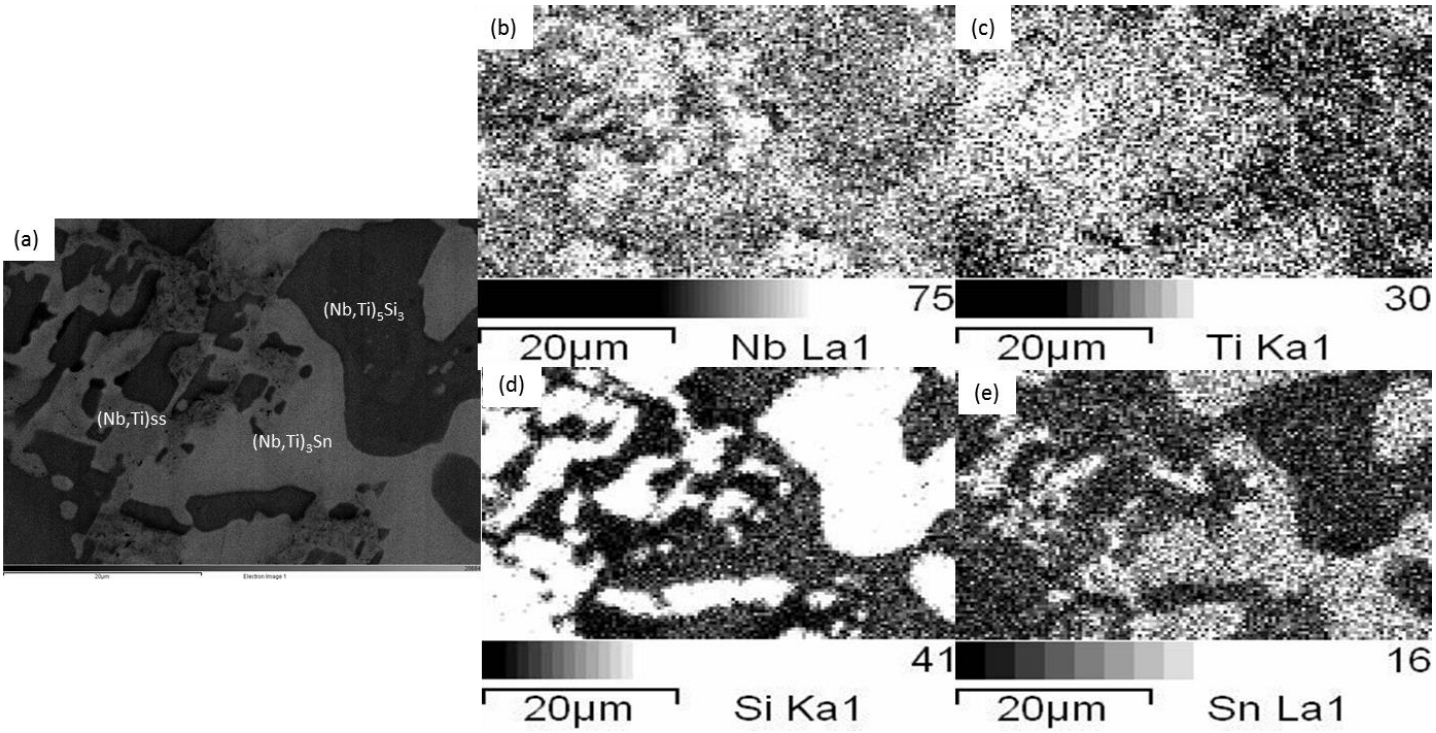

Fig. 12.9 (a) BSE image of IP1-HT/1000 and (b),(c),(d),(e) X-ray element maps of Nb, Ti, Si and Sn respectively.

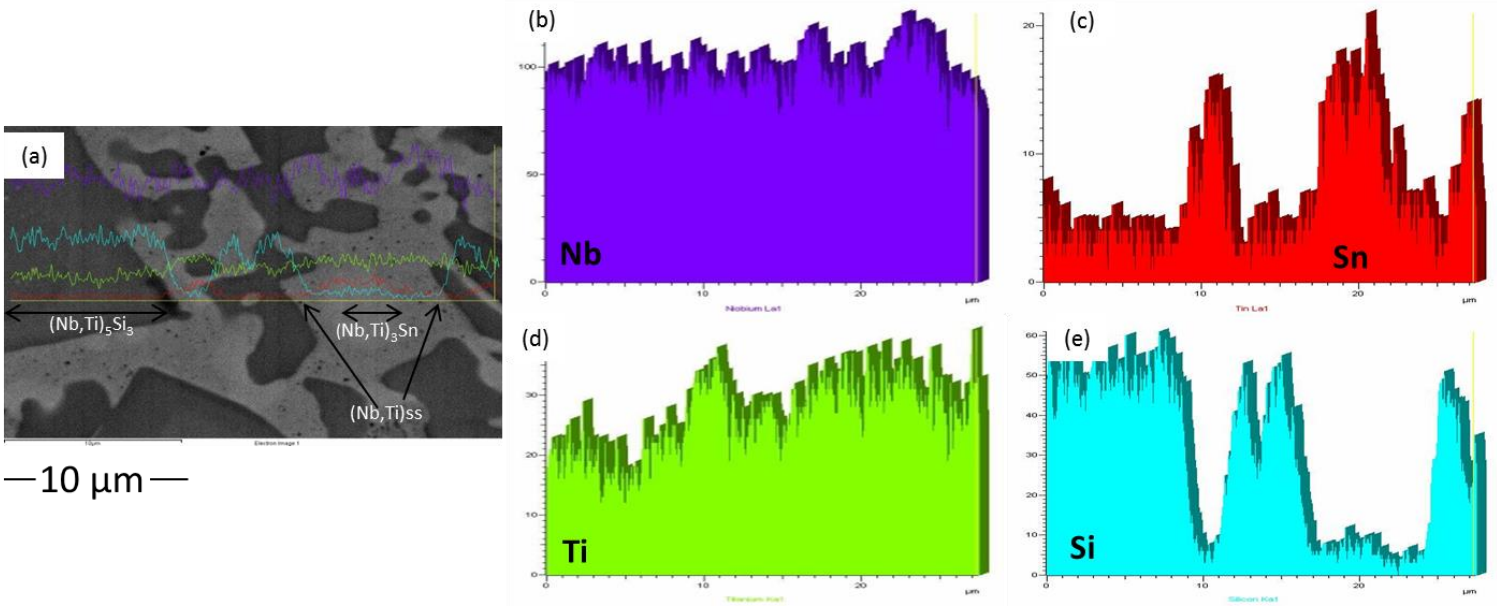

Fig. 12.10 (a) BSE image of IP1-HT/1000 and (b),(c),(d),(e) X-ray line scan patterns of Nb, Ti, Si and Sn respectively.

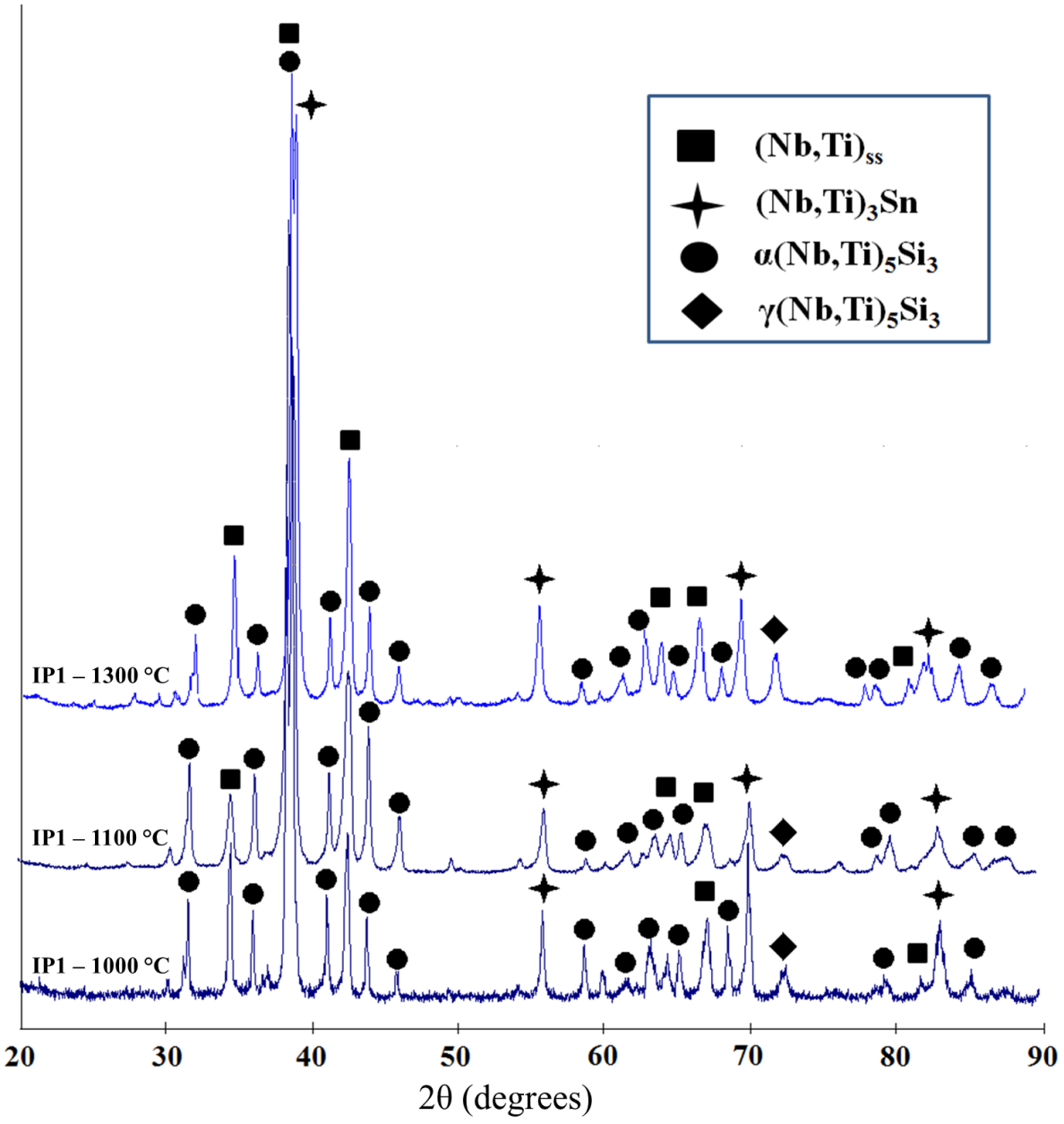

Fig. 12.11. X-Ray diffractograms patterns of the IP1-HT/1000, IP1-HT 1100 ^{0}C and IP1-HT 1300 ^{0}C alloys.

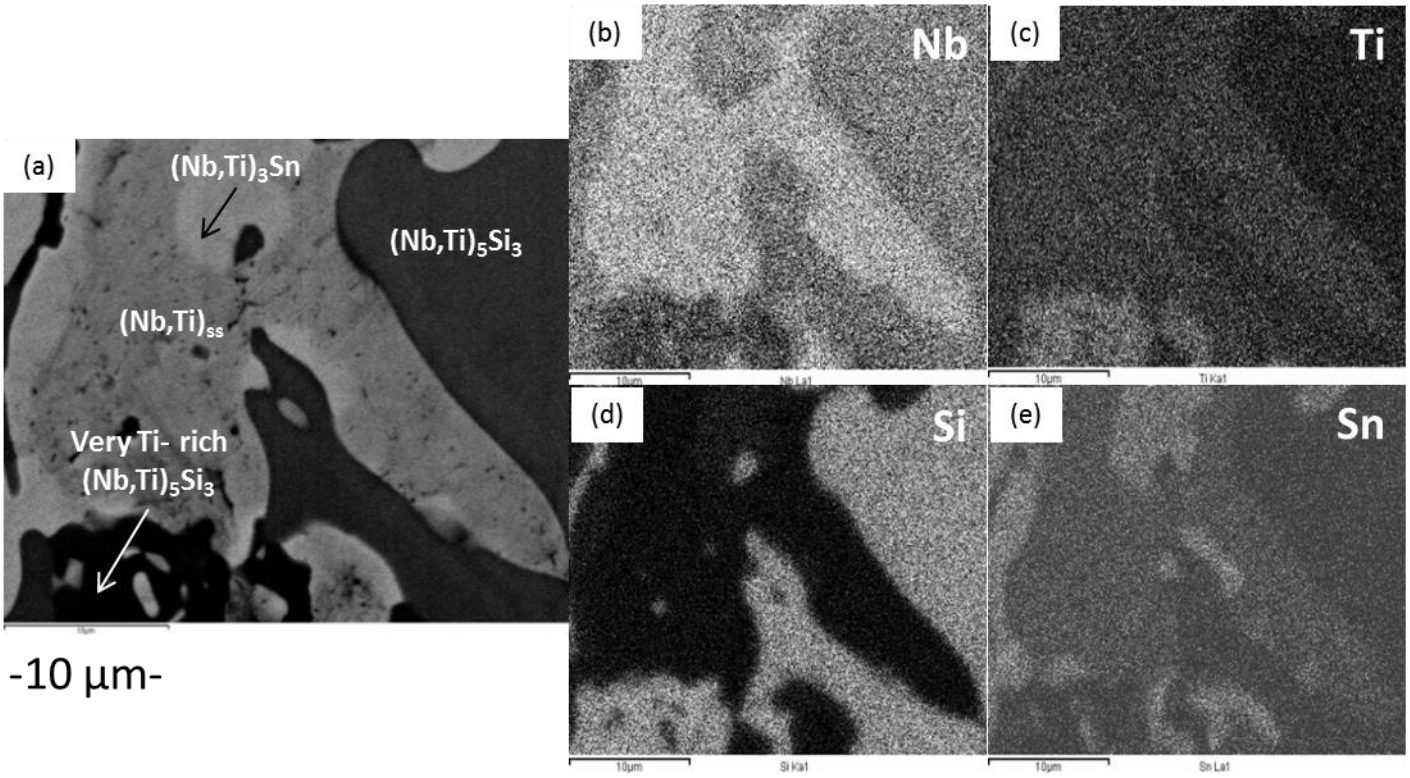

Fig. 12.12. (a) BSE image of the IP1-HT 1300 ^{0}C alloy and (b),(c),(d),(e) X-ray element map of Nb, Ti, Si and Sn, respectively. The Si map (d) would suggest the precipitation of a Si-rich phase in the $(Nb,Ti)_{ss}$.

In Fig. 12.7 and 12.8 the EBSD phase map and orientation maps of each phase of the IP1-HT 1300 °C respectively are presented. It was confirmed the βNb_5Si_3 was absent from the microstructure with the αNb_5Si_3 still forming bulk dendrites throughout the sample and the γNb_5Si_3 occupying the very Ti-rich areas of the ingot. The solid solution still exhibited large regions of similar orientation while the Nb_3Sn and the γ 5-3 intermetallic did not show any preferred orientation compared with the as cast alloy. Also, smaller areas with similar orientation were preserved for the α silicide. In Figure 12.12 the X-ray element maps of the IP1-HT 1300 °C are presented, while the XRD data of all the heat treated conditions of the present study is shown in Fig. 12.11. According to the EBSD and XRD data the microstructure of the heat treated alloy consisted of the $\alpha(Nb,Ti)_5Si_3$, $\gamma(Nb,Ti)_5Si_3$, $(Nb,Ti)_3Sn$ and the $(Nb,Ti)_{ss}$ phases at 1000 ^{0}C, 1100 ^{0}C and 1300 ^{0}C. Lamellar microstructure of $(Nb,Ti)_5Si_3$ and $(Nb,Ti)_{ss}$ was present in all heat treatment temperatures. Areas of Ti-rich and very Ti-rich 5-3 silicide were observed (Table 12.1), with the size of the latter increasing as the heat treatment temperature increased, while partitioning of Sn and Ti was evident in all samples. The Ti concentration in the $(Nb,Ti)_{ss}$ in all the heat treatment temperatures was approximately 30 at. %, which indicates a reduction of about 6 at. % compared with the as cast alloy (35.6 at. % Ti), whereas in the $(Nb,Ti)_3Sn$ it was increased (~ 29 at. % as compared with ~ 20 at. % in the as cast alloy). At the 1000 ^{0}C and 1100 ^{0}C heat treatment temperatures the Si + Sn concentration in the $(Nb,Ti)_{ss}$ was approximately 4 at. % and for the IP1-HT 1300° it was ~ 5 at. %, whereas in the as cast alloy it was 7.7 at. %. In the $(Nb,Ti)_3Sn$ the Si + Sn concentration was 15.8, 17.5 and 17.8, at 1000 ^{0}C, 1100 ^{0}C and 1300 ^{0}C, respectively.

12.3 Discussion

In all three heat treatment temperatures of this study the compositions of the phases present in the microstructure of IP1 were about the same with the results for the heat treated alloy at 1200 ^{0}C in the work of Velios and Tsakiropoulos [19]. Also, it was confirmed by the XRD and the EBSD analysis that the βNb_5Si_3 was absent from all of the heat treated alloys and that only αNb_5Si_3 and γNb_5Si_3 were present. Moreover, the lamellar eutectic structure of solid solution and $(Nb,Ti)_5Si_3$ was observed to be present in all the heat treatment temperatures. The ratio Si/Sn in the $(Nb,Ti)_3Sn$ phase in the NV6-AC [19], IP1-HT 1000 ^{0}C, IP1-HT 1100 ^{0}C, NV6-HT 1200 ^{0}C [19] and IP1-

HT 1300 ^{0}C alloys did not exceed 0.7 and the solubility of Si in $(Nb,Ti)_3Sn$ was not significantly affected by the heat treatment temperatures. Compared with the IP2 and IP3 alloys (see chapter 9) the presence of Ti in IP1 reduced the solubility of Si in the Nb_3Sn phase.

12.4 Conclusions

The Nb-24Ti-18Si-5Sn (IP1) alloy was investigated in the as cast and heat treated conditions at 1000 ^{0}C, 1100 ^{0}C and 1300 ^{0}C. The conclusions of this study are as follows:

- The microstructure of IP1 consisted of $(Nb,Ti)_{ss}$, $(Nb,Ti)_3Sn$ and $(Nb,Ti)_5Si_3$ in all the heat treatment temperatures. Only the $\alpha(Nb,Ti)_5Si_3$ was present in the heat treated microstructures and Ti-rich $(Nb,Ti)_5Si_3$ and very Ti-rich $(Nb,Ti)_5Si_3$ areas were evident in all the conditions.
- The presence of lamellar eutectic between the solid solution and $(Nb,Ti)_5Si_3$ was confirmed in all IP1 heat treated specimens.
- The Ti-rich areas were αNb_5Si_3.
- The very Ti-rich areas were γNb_5Si_3.
- The presence of Ti in the alloy reduced the solubility of Si in the Nb_3Sn phase.

13

Phase equilibria in Nb-Cr-Sn ternary alloys at 900 °C and 1200 °C

13.1. Introduction

The Nb-Cr-Sn system is of interest for the development of Nb silicide based alloys as the phases $NbCr_2$ and Nb_3Sn are reported to benefit oxidation resistance. To date the binary phase diagrams of the constituent elements have been thoroughly investigated. The Nb-Sn system consists of the $NbSn_2$, Nb_6Sn_5 and Nb_3Sn intermetallics [28] (see also chapters 5 and 9). Two intermetallics exist in the Nb-Cr system [156], the $NbCr_2$ with the C15 fcc-based structure (Pearson symbol *cF*24) which is stable until about 1850 K, above which it undergoes a transformation to C14 hexagonal structure (Pearson symbol *hP*12). In the Cr-Sn system no intermetallic compounds are reported [157]. Ternary systems containing Nb and Cr that have been investigated are the Nb-Cr-Si [13, 158] and Nb-Cr-Al [148]. To the author's knowledge there is no data about ternary phase equilibria in the Nb-Cr-Sn system to date.

The alloys IP11 (Nb-15Cr-11Sn) and IP12 (Nb-65Cr-18Sn) were manufactured for the current study are described in Chapter 3. The motivation of the current work was to investigate stable phases and phase equilibria in the Nb-Cr-Sn ternary system.

13.2. Results

13.2.1. Alloy Nb-15Cr -11Sn (IP11)

As cast. The microstructure and the compositions of the phases present in the Nb-15Cr-11Sn as cast alloy (IP11-AC) can be seen in Fig. 13.1 (a-b) and Table 13.1, respectively. The EDS data of the IP11-AC confirm that the Nb_{ss} and Nb_3Sn phases were formed, with the Nb_{ss} having the largest volume fraction. Areas of Cr-rich solid solution were observed throughout the microstructure. Dark areas near the Nb_3Sn phase were evident (Fig. 13.1 (a)). Judging from the contrast of the phases in these areas (Fig. 13.1 (b)) they consisted of Nb_3Sn and a Cr-rich phase. The EDS analysis was not accurate enough to allow the measurement of the stoichiometry of the Cr-rich phase owing to its size and volume fraction. XRD (Fig. 13.2) confirmed only Nb_3Sn and Nb_{ss}. In the Nb_3Sn phase the Cr content was ~7.8 at. %, and the ratio Cr/Sn was 0.44. In the Nb_{ss} the Cr content was 9.9 at. % and the Cr/Sn ratio was 1.13 and the Cr+Sn sum was equal to 18.54. The Cr-rich areas

of the solid solution contained about 17.2 at. % of Cr, with the Cr/Sn ratio and the Cr+Sn sum reaching ~2.2 and ~25 at. %, respectively (Table 13.1).

Heat treated. Three heat treatments were performed at 900 °C for 200h, at 1200 °C for 100h and at 1200 °C for 200h. In Fig. 13.1(c-d) the microstructure of IP11-AC after 200 hours at 900 ^{0}C is shown (IP11-HT-900 ^{0}C/ 200h). The same phases were present, however the dark areas underwent significant coarsening. As such the phase corresponding to these areas was detectable by XRD (Fig. 13.2) and analysed by EDS. It was concluded that this phase was $NbCr_2$ with ~2at. % Sn and ~59 at. % Cr content. In the Nb_3Sn and Nb_{ss} the Cr content was ~7.2 at. % and ~9.8 at. %, respectively. The Cr/Sn ratio was 0.42 and 0.99 in Nb_3Sn and Nb_{ss} respectively. The Cr+Sn sum was ~19.7 at. % in the Nb_{ss}. No significant difference was noted in the composition of the Cr-rich solid solution areas (Table 13.1).

The IP11 alloy was heat treated at 1200 ^{0}C for 100 hours. The microstructure consisted primarily of the Nb_{ss}, Nb_3Sn and $NbCr_2$ phases, (Fig. 13.1 (e-f) and 13.2. In addition to the large grains of Nb_3Sn, new smaller grains of Nb_3Sn formed inside the Nb_{ss}. Significant coarsening of $NbCr_2$ was observed. The Cr content in Nb_3Sn was ~5.3 at. % with the Cr/Sn ratio being 0.3 and Cr+Sn sum being 23 at. %. The corresponding values for the solid solution were about 11.8 at. %, 1.3 and 20.9 at. %. In the Laves phase the Sn content was approximately 2.2 at. % while the Nb concentration was ~39.7 at. % (Table 13.1).

The IP11 was heat treated at 1200 ^{0}C for a further 100 hours. The same constituent phases were evident in the alloy (Fig. 13.1 (g-h) and Fig. 13.2). No significant changes occurred in the microstructure or in the composition of the constituent phases. The Sn content in the $NbCr_2$ phase was about 1.9 at. % whereas the Nb content was ~38.5 at. %. In the Nb_3Sn on the other hand the Cr content was ~5.9 at. % with the Cr/Sn ratio being ~0.3 and the Cr+Sn sum being 23.1 at. %. In the Nb_{ss} the corresponding values for the solid solution were about 11.7 at. %, 1.23 and 21.1 at. % (Table 13.1).

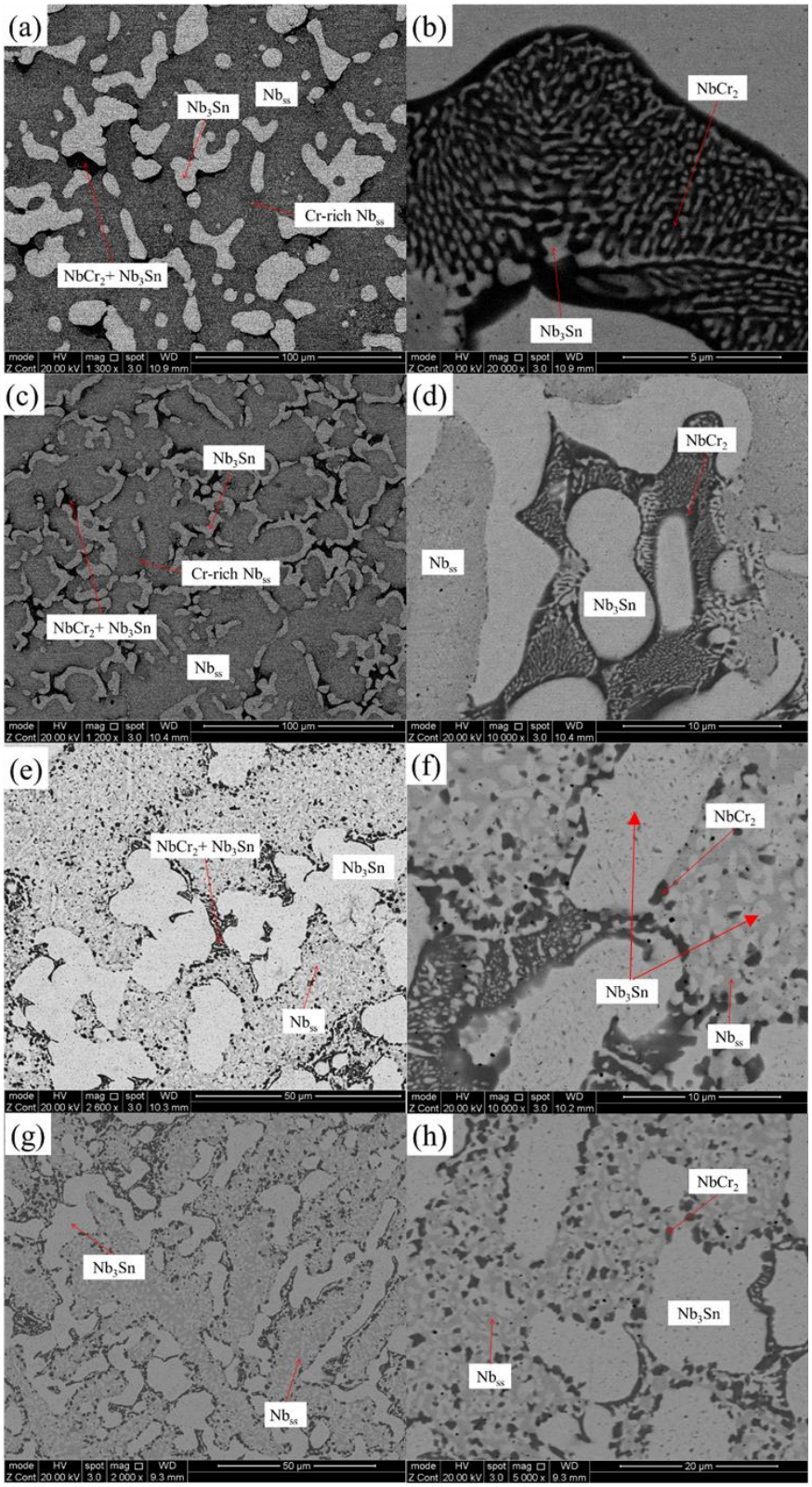

Fig. 13.1. BSE images of IP11-AC (a-b), IP11-HT-900 ^{0}C/200h (c-d), IP11-HT-1200 ^{0}C/100h (e-f) and IP11-HT-1200 ^{0}C/200h (g-h)

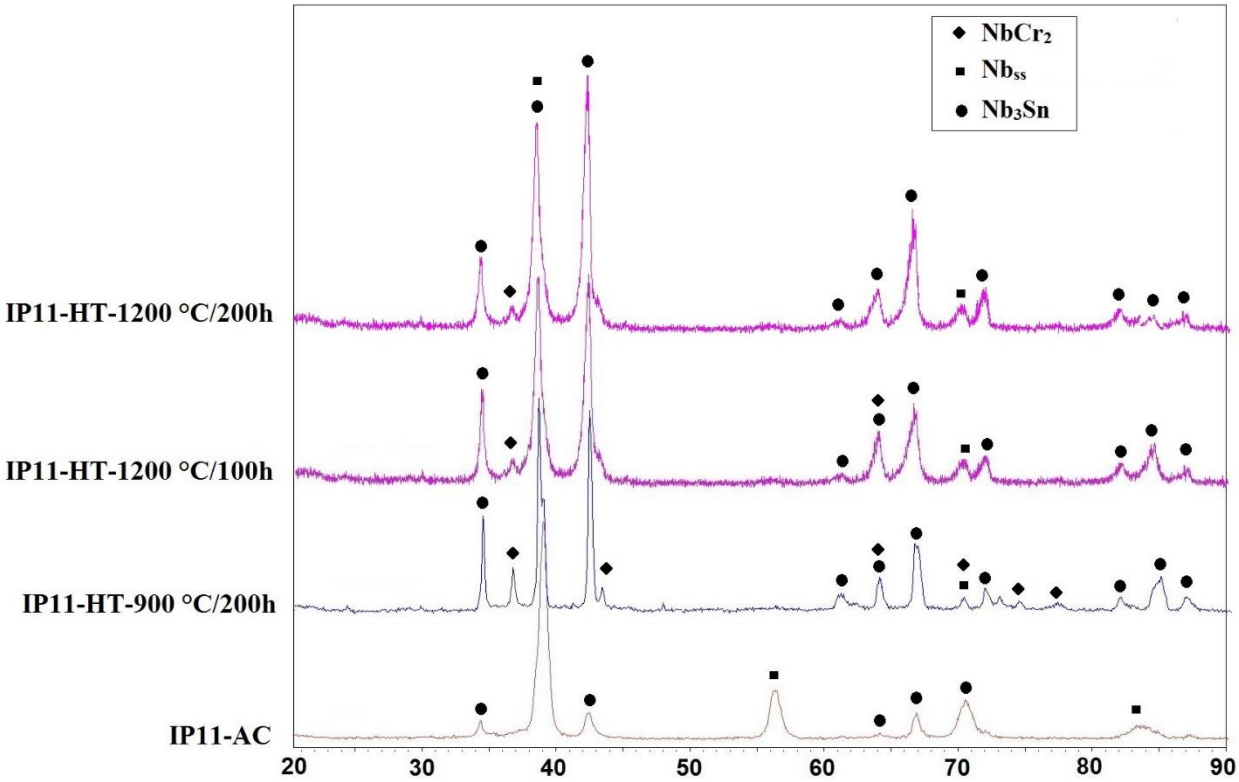

Fig. 13.2. XRD diffractograms of IP11-AC, IP11-HT-900 ^{0}C/200h, IP4-HT-1200 ^{0}C/100h and IP4-HT-1200 ^{0}C/200h

Table 13.1.

EDS data for the phases in IP11-AC, IP11-HT-900 ^{0}C/200h, IP4-HT-1200 ^{0}C/100h and IP4-HT-1200 ^{0}C/200h alloys.

	Nb (at. %)	Cr (at. %)	Sn (at. %)
IP11-AC			
Nb_3Sn	74.7 ± 0.7	7.8 ± 0.3	17.5 ± 0.4
Nb_{ss}	81.4 ± 1.1	9.9 ± 0.7	8.7 ± 0.4
IP11-HT-900 °C/200h			
Nb_3Sn	75.5 ± 0.5	7.2 ± 0.3	17.2 ± 0.4
Nb_{ss}	80.3 ± 0.9	9.8 ± 0.5	9.9 ± 0.4
Cr-rich Nb_{ss}	75.0 ± 1.4	17.3 ± 0.9	7.7 ± 0.5
$NbCr_2$	38.9 ± 2.7	59.0 ± 2.5	2.1 ± 0.7
IP11-HT-1200 °C/100h			
Nb_3Sn	77.0 ± 0.2	5.3 ± 0.1	17.7 ± 0.3
Nb_{ss}	79.1 ± 1.6	11.8 ± 1.0	9.1 ± 1.1
$NbCr_2$	39.7 ± 1.9	58.1 ± 1.3	2.2 ± 0.8
IP11-HT-1200 °C/200h			
Nb_3Sn	76.9 ± 0.2	5.4 ± 0.1	17.7 ± 0.2
Nb_{ss}	78.9 ± 0.9	11.7 ± 1.0	9.4 ± 0.9
$NbCr_2$	38.5 ± 1.0	59.7 ± 0.9	1.8 ± 0.5

13.2.2. Alloy Nb-65Cr-18Sn (IP12)

As cast. The microstructure of the Nb-65Cr-18Sn as cast alloy (IP12-AC) can be seen in Fig. 13.3 (a-b), and the data of the compositions of the constituent phases is shown in Table 13.2. Large areas of the $NbCr_2$ phase were primarily observed. The Laves phase was often surrounded by Nb_6Sn_5 and in between the Cr solid solution and Nb_3Sn were formed. The Nb_3Sn was formed amongst the Nb_6Sn_5 grains. These phases were confirmed by XRD (Figure 13.4). The Nb_3Sn was difficult to distinguish in the microstructure. The X-ray element maps (Fig. 13.5) of IP12-AC show

evidence of this phase. The Sn and Nb contents in $NbCr_2$ were approximately 5.5 and 28.3 at. %, respectively, while in the Cr solid solution the corresponding values were both less than 1 at. %. Furthermore the Cr and Nb contents in Nb_6Sn_5 were 12.6 and 42.2 at. %, respectively, whereas in the Nb_3Sn the corresponding values were approximately 10.8 and 64.4 at. %.

Heat treated. The IP12 alloy was heat treated at 900 °C for 100h, 300h and 400h and at 1200 °C for 100h and 300h. After heat treatment at 900 ^{0}C for 100 hours the $NbCr_2$ was still the primary phase. The Cr_{ss} was still present with the Nb_6Sn_5 (Fig. 13.3 (c)). A fine structure consisting of Cr_{ss} and Nb_6Sn_5 formed around the grain boundaries between Nb_6Sn_5 and $NbCr_2$ where the $NbCr_2$ was in the as cast alloy. This can be clearly seen in Fig. 13.3 (d). The XRD data of the IP12-HT-900 ^{0}C/ 100h alloy suggested that the Nb_3Sn was still present (Fig. 13.4) but this phase was not confirmed by the EDS. As it is shown in Table 13.2, the Sn and Nb contents in $NbCr_2$ were ~6.6 and ~30.2 at. %, respectively, whereas the Cr and Nb concentrations in the Nb_6Sn_5 were 11 and ~44 at. %, respectively. The Cr_{ss} contained less Nb and Sn, with both elements adding up to approximately 0.6 at. %.

The compositions of the constituent phases were approximately the same after heat treating the IP12-HT-900 ^{0}C/ 100h alloy at the same temperature for a further 200 hours (Table 13.2). The microstructure was significantly altered as the volume fraction of the Nb_6Sn_5 increased and the volume fraction of the Laves phase decreased (Fig. 13.3 (e)). In Fig. 13.3 (f) it appears that the Laves phase transformed to Nb_6Sn_5 and the Cr solid solution. The $NbCr_2$ was surrounded by an area of Nb_6Sn_5 and Cr_{ss}. The boundary between these two regions appeared to be progressing inwards, consuming the Laves phase. Still some remnants of the Nb_3Sn were confirmed by the XRD (Fig. 13.4) but not by the EDS. To see the progress of the above transformation the IP12-HT-900 ^{0}C/ 300h alloy was annealed at 900 ^{0}C for an additional 100 hours. A further coarsening of the Nb_6Sn_5 phase was observed. The $NbCr_2$ phase was no longer present and was replaced by the Cr solid solution and the Nb_6Sn_5 (Fig. 13.3 (g-h)). The compositions of the constituent phases are given in Table 13.2. In the Cr_{ss} the Nb+Sn content was ~1 at. %. The Cr and Nb contents in Nb_6Sn_5 were 11.4 and 44.6 at. %, respectively. The XRD data of the IP12-HT-900 ^{0}C/ 400h confirmed the presence of only the Cr_{ss} and Nb_6Sn_5 (Fig. 13.4).

The IP12 alloy was heat treated at 1200 ^{0}C for 100 hours (IP12-HT-1200 ^{0}C/ 100h). The Nb_6Sn_5, Cr_{ss} and the Laves phase were observed, along with some traces of the Nb_3Sn phase confirmed only by the XRD. The Laves phase formed between the areas that contained the Nb_6Sn_5 and the

solid solution (Fig. 13.3 (i)). A fine structure consisting of these phases was observed in the same areas as in the alloys heat treated at 900 ^{0}C (Fig. 13.3 (j)). The XRD data and the compositions of the phases are shown in Fig. 13.4 and Table 13.2 respectively. The Sn and Nb contents in the Laves phase was about 8.8 and 27.7 at. % whereas in the Nb_6Sn_5 phase the Cr and Nb contents were approximately 10.4 and 44.8 at. % respectively. The Nb+Sn sum in the solid solution was less than 1 at. %.

The IP12-HT-1200 ^{0}C/ 100h was heat treated for a further 200 h at 1200 ^{0}C (IP12-HT-1200 ^{0}C/ 300h). The alloy consisted mainly of the Cr solid solution and the Nb_6Sn_5 phase. As it can be seen in Fig. 13.3 (k) some remnants of the Laves phase were still present, confirmed by XRD (Fig. 13.4). The composition of the Laves phase was ~8.1 at. % Sn and ~28.4 at. % Nb. The Nb+Sn sum in the solid solution was ~0.8 at. %, while in the Nb_6Sn_5 the Nb and Cr concentrations were approximately 10.9 and 44.7 at. %, respectively.

Table 13.2.

EDS data for the composition of the phases in IP12-AC, IP12-HT-900 ^{0}C/100h, IP12-HT-900 ^{0}C/300h, IP12-HT-900 ^{0}C/400h, IP12-HT-1200 ^{0}C/100h and IP12-HT-1200 ^{0}C/300h alloys.

	Nb (at. %)	Cr (at. %)	Sn (at. %)
IP12-AC			
$NbCr_2$	28.3 ± 0.6	66.2 ± 0.7	5.5 ± 0.5
Cr_{ss}	0.6 ± 0.2	99.0 ± 0.1	0.4 ± 0.1
Nb_6Sn_5	42.2 ± 0.4	12.6 ± 0.4	45.2 ± 0.2
Nb_3Sn	64.4 ± 0.7	10.8 ± 0.6	24.8 ± 0.3
IP12-HT-900 °C/100h			
$NbCr_2$	30.2 ± 0.6	63.3 ± 0.2	6.5 ± 0.2
Cr_{ss}	0.5 ± 0.1	99.4 ± 0.2	0.1 ± 0.1
Nb_6Sn_5	44.0 ± 0.4	11.0 ± 0.5	45.0 ± 0.2
IP12-HT-900 °C/300h			
$NbCr_2$	30.8 ± 0.5	63.7 ± 0.5	5.5 ± 0.3
Cr_{ss}	0.4 ± 0.1	99.4 ± 0.3	0.2 ± 0.1
Nb_6Sn_5	43.8 ± 0.6	11.7 ± 0.6	44.5 ± 0.6
IP12-HT-900 °C/400h			
Cr_{ss}	0.7 ± 0.1	99.0 ± 0.3	0.3 ± 0.1
Nb_6Sn_5	44.6 ± 0.6	11.4 ± 0.5	44.0 ± 0.4
IP12-HT-1200 °C/100h			
$NbCr_2$	27.7 ± 0.6	63.4 ± 0.2	8.9 ± 0.4
Cr_{ss}	0.6 ± 0.1	99.1 ± 0.2	0.3 ± 0.1
Nb_6Sn_5	44.8 ± 0.4	10.4 ± 0.5	44.7 ± 0.4
IP12-HT-1200 °C/300h			
$NbCr_2$	28.4 ± 0.6	63.5 ± 0.5	8.1 ± 0.2
Cr_{ss}	0.6 ± 0.1	99.2 ± 0.1	0.2 ± 0.1
Nb_6Sn_5	44.7 ± 0.3	10.9 ± 0.3	44.5 ± 0.2

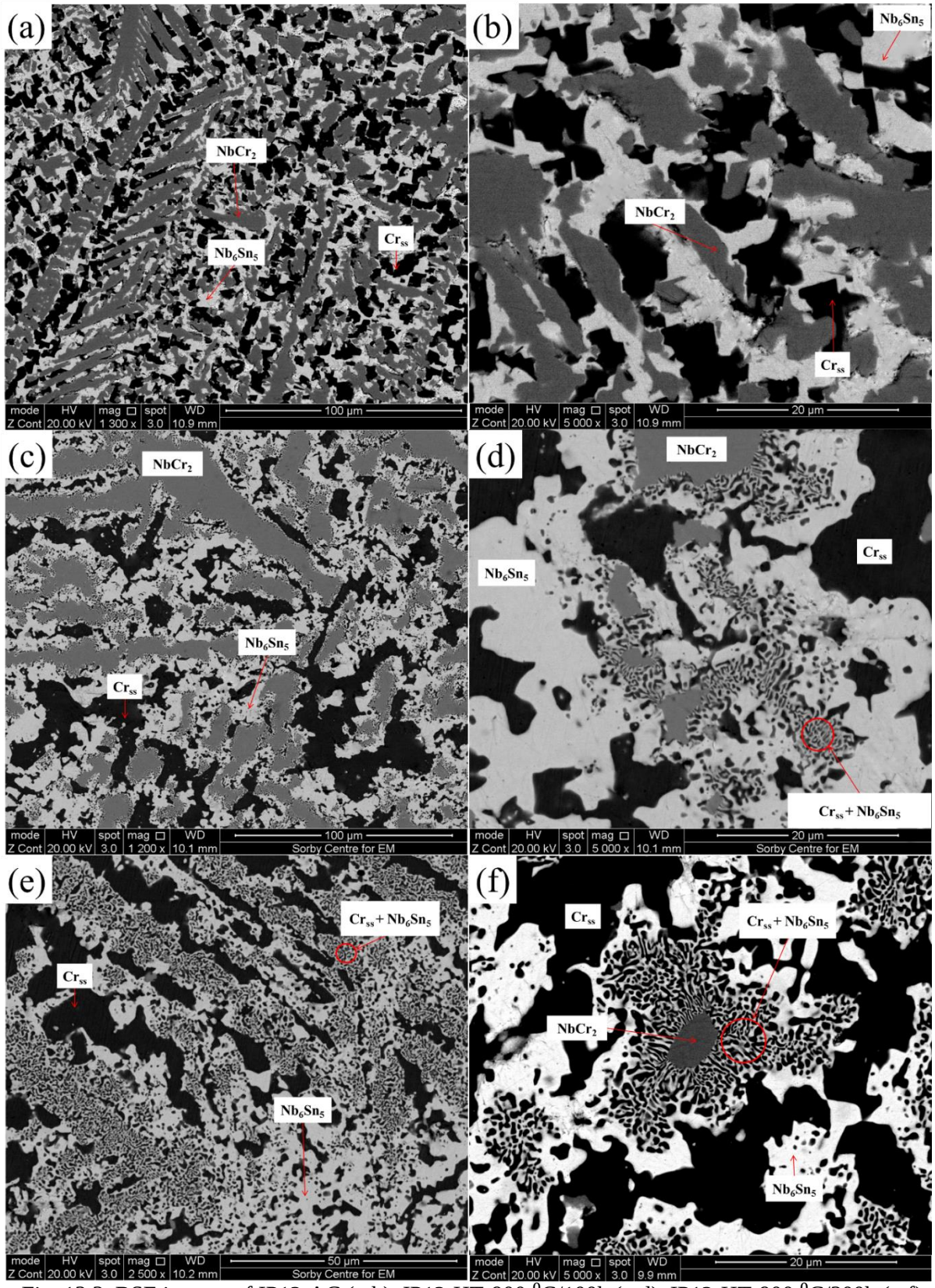

Fig. 13.3. BSE images of IP12-AC (a-b), IP12-HT-900 ^{0}C/100h (c-d), IP12-HT-900 ^{0}C/300h (e-f)

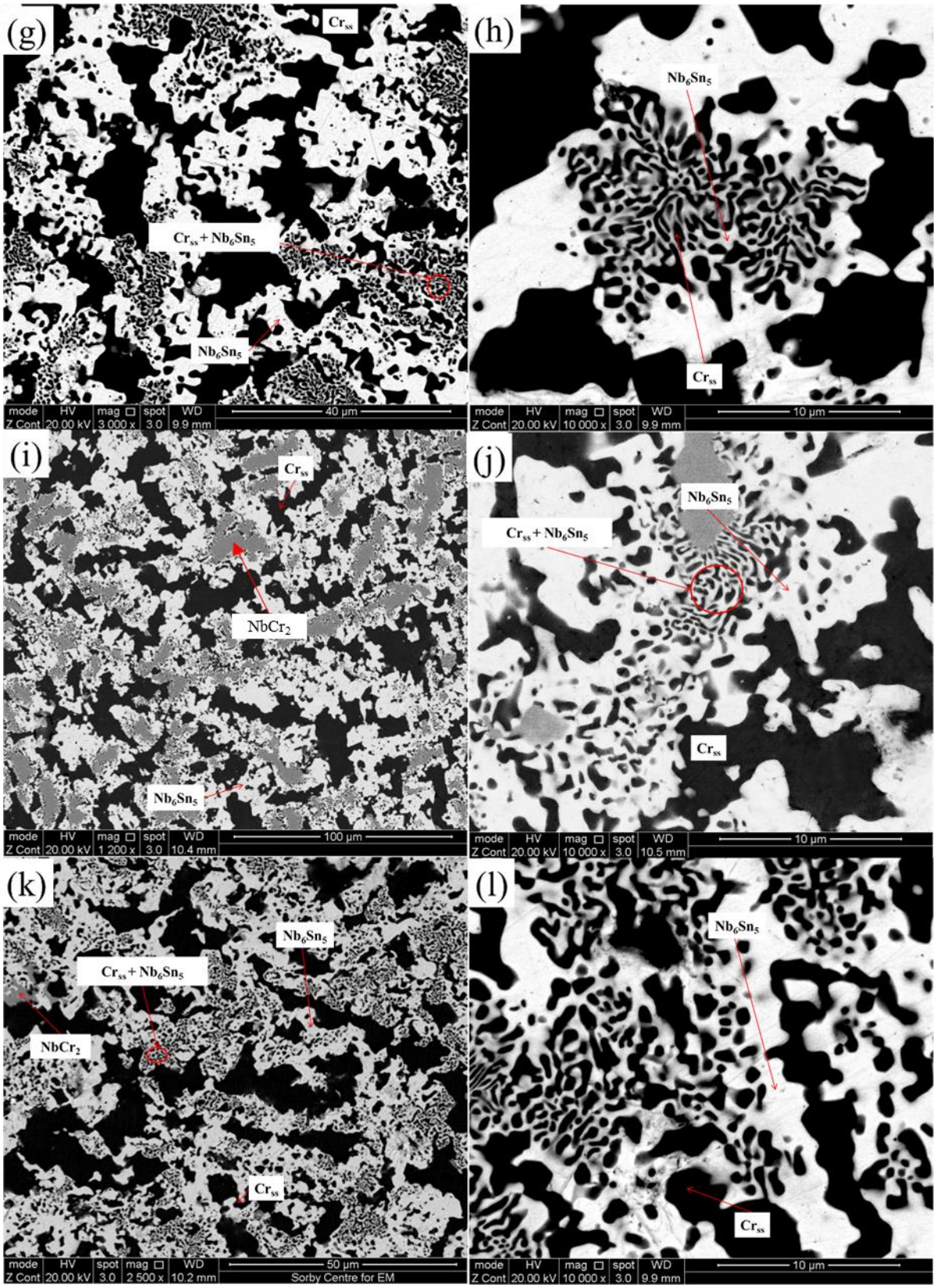

Fig. 13.3. BSE images of IP12-HT 900 ^{0}C/400h (g-h), IP12-HT-1200 ^{0}C/100h (i-j) and IP12-HT-1200 ^{0}C/300h (k-l)

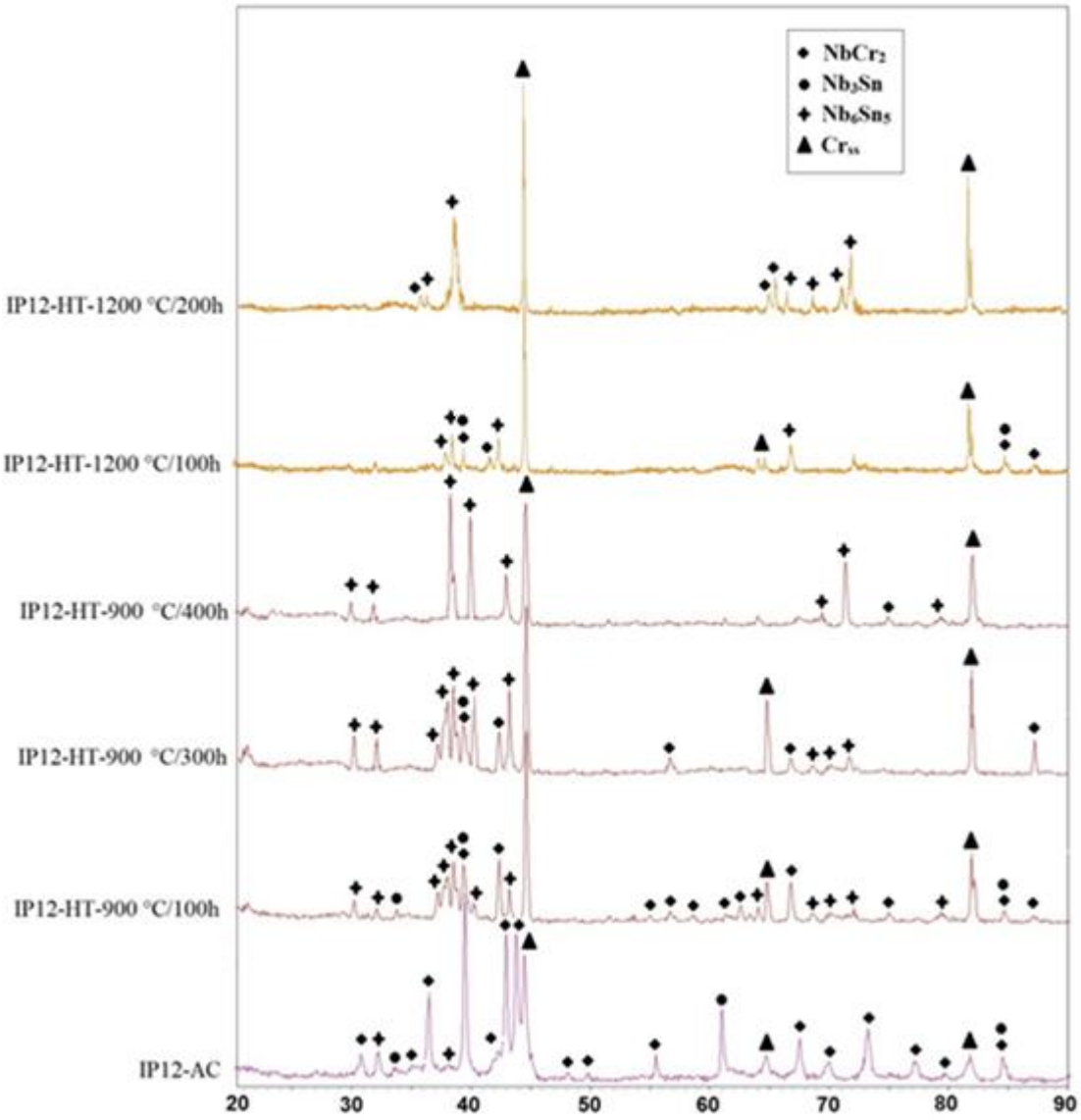

Fig. 13.4. XRD diffractogramm of IP12-AC, IP12-HT-900 ^{0}C/100h, IP12-HT-900 ^{0}C/300h, IP12-HT-1200 ^{0}C/400h, IP12-HT-1200 ^{0}C/100h and IP12-HT-1200 ^{0}C/300h

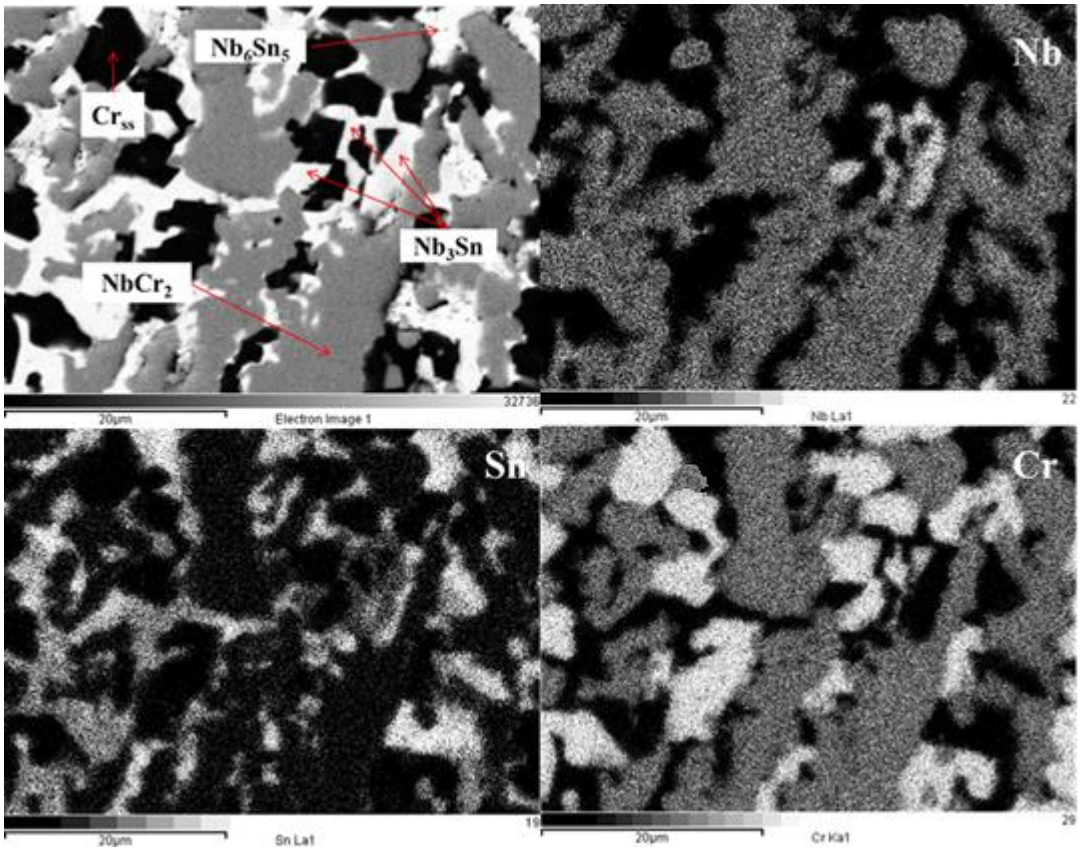

Fig. 13.5. X-ray element maps of IP12-AC

13.3. Discussion

The as cast IP11 alloy consisted of the Nb_{ss}, $NbCr_2$, and Nb_3Sn phases. The Nb_{ss} should be surrounded by the Nb_3Sn, consistent with the peritectic reaction $L+Nb_{ss}\rightarrow Nb_3Sn$. This was not the case in IP11-AC, where the Nb_3Sn was surrounded by the Nb_{ss}. Within the solid solution Cr-rich areas were observed. The Nb_3Sn phase was decorated by layers of Cr-rich solid solution and a structure resembling a fine eutectic that consisted of $NbCr_2$ and Nb_3Sn. The solidification path was $L\rightarrow L+Nb_3Sn\rightarrow L+Nb_3Sn+Nb_{ss}\rightarrow L+Nb_3Sn+Nb_{ss}+NbCr_2+(NbCr_2+Nb_3Sn)_{eutectic}$. In the cast alloy the Nb_3Sn was primarily formed from the melt. The surrounding melt became rich in Cr and lean in Nb and the Nb_{ss} was formed. As the Nb_{ss} formed, the surrounding liquid became rich in Cr, forming the $NbCr_2$. After 200 hours of heat treatment at 900 °C the composition of the phases was not significantly altered. However, the morphology of the microstructure changed and the $NbCr_2$ had considerably coarsened. In the Nb_3Sn the Cr substituted Nb as the Nb+Cr sum was ~82 at. % and the Sn content

was 18 at. %, which is in good agreement with the typical composition of the Nb_3Sn phase [28]. In the Laves phase Sn and Nb substitute Cr. In the solid solution, the Cr and Sn contents were about the same, however in the Cr-rich areas, the Cr content was more than two times the content of Sn. The Cr-rich areas were approximately 5.2 at. % poorer in Nb compared with the "normal" solid solution.

After 100 hours at 1200 °C the constituent phases were the same. The $NbCr_2$ and Nb_3Sn had coarsened compared with the as cast alloy. The Nb_3Sn was poorer in Cr by about 2.5 at. % and the Nb_{ss} was richer in Cr by about 2 at. % which would suggest partitioning of Cr between the two phases. After an additional 100 h heat treatment there were no significant alterations in the composition of phases, except for the Laves phase which was richer in Cr by ~1.5 at. %. In the microstructure it was observed that the $NbCr_2$ and Nb_3Sn coarsened considerably at the expense of the volume fraction of solid solution. The above data suggests that at both 900 ^{0}C and 1200 ^{0}C the equilibrium phases of the IP11 alloy were Nb_3Sn, Nb_{ss} and $NbCr_2$.

The IP12-AC alloy consisted of Cr solid solution, Nb_6Sn_5, $NbCr_2$ and a low volume fraction of the Nb_3Sn phase. In the Laves phase the Sn and Nb contents were 5.5 and 28.3 at. %, respectively, indicating that Sn substitutes for Nb. The Cr and Nb contents in the Nb_6Sn_5 (12.6 and 42.2 at. % respectively) suggested that Cr substitutes for Nb. Furthermore, it must be noted that Sn and Nb had very low solubility in the Cr_{ss} adding up less than 1 at. % in all the conditions studied for the IP12 alloys. At 900 °C after 300 hours only traces of the Nb_3Sn phase were present while after 400 hours no Nb_3Sn was found, indicating that it is a metastable phase at this composition and temperature. In the $NbCr_2$ the concentration of Nb and Cr was similar after 100 and 300 hours (~30.2 at. % Nb and 63.3 at. % Cr, and 30.8 and 63.7 at. %, respectively). Hence it is deduced that Sn substitutes for Nb and Cr. After 400 hours the $NbCr_2$ was not present and it is thus suggested that it is not an equilibrium phase at 900 °C. On the other hand the Nb_6Sn_5 was present for all heat treatment times at 900 °C with Cr content varying from 11 (100 hours) to ~11.7 at. % (300 hours) and Nb content ranging from 43.8 (300 hours) to 44.6 at. % (400 hours). It is hence deduced that Cr substitutes Nb in the Nb_6Sn_5.

At 1200 ^{0}C the observed phases were the same as at 900 ^{0}C up to 300 hours. The $NbCr_2$ phase was observed after 100 hours of heat treatment and contained ~27.7 at. % Nb and ~63.4 at. % Cr. After 300 hours, remnants of the phase were present and contained ~28.4 at% Nb and ~63.5 at. % Cr, respectively. Hence it is deduced that Sn substitutes Nb and Cr. Comparing the two heat treatments, the solubility of Sn in $NbCr_2$

increased between 900 °C and 1200 °C. The Nb_6Sn_5 phase was present in both alloys at 1200 °C with Cr content varying from ~10.4 (100 hours) to ~10.9 at. % (300 hours) and Nb content being ~44.7 at. %. It is therefore confirmed that Cr substitutes Nb in the Nb_6Sn_5 at 1200 ^{0}C as was the case at 900 ^{0}C. Compared with the 900 ^{0}C heat treatment conditions it is suggested that the solubility of Cr in Nb_6Sn_5 decreases with increasing temperature.

Microstructural changes occurred during annealing. The volume fraction of a fine lamellar structure consisting of Cr_{ss} and Nb_6Sn_5 increased and the volume fraction of $NbCr_2$ decreased. The amount of $NbCr_2$ consumed was correlated to the annealing time and temperature. Most of $NbCr_2$ was consumed with only remnants of it remaining in IP12-HT-1200 ^{0}C/ 300h. It is suggested that the following solid state transformation reaction took place: $NbCr_2 + Nb_3Sn \rightarrow Cr_{ss} + Nb_6Sn_5$.

In the cast alloy the primary phase was Cr_{ss}. Following formation of the Cr_{ss}, the melt became poor in Cr and rich in Nb and Sn, allowing Nb_3Sn solid solution to form. After the formation of the Nb_3Sn and as the melt became richer in Cr the $NbCr_2$ phase was formed. The melt was poor in Cr and richer in Nb and Sn, thus the last phase that solidified was Nb_6Sn_5 (it must be noted that it is also the phase with the lowest melting temperature). Therefore the proposed solidification route was $L \rightarrow L + Cr_{ss} \rightarrow L + Cr_{ss} + Nb_3Sn \rightarrow L + Cr_{ss} + Nb_3Sn + NbCr_2 \rightarrow L + Cr_{ss} + Nb_3Sn + NbCr_2 + Nb_6Sn_5$. At both 900 ^{0}C and 1200 ^{0}C the equilibrium phases of IP12 were Nb_6Sn_5 and Cr_{ss}.

13.4. Conclusions

- The primary phase in IP11 was the Nb_3Sn. The phase equilibria of the alloy IP11 at both 900 ^{0}C and 1200 ^{0}C consisted of Nb_3Sn, Nb_{ss} and $NbCr_2$.
- Chromium substituted Nb in Nb_3Sn, while Sn and Nb substituted Cr in the Laves phase in the IP11 alloy.
- The primary phase in IP12 was the Cr_{ss}. The phase equilibria of the alloy IP12 at both 900 ^{0}C and 1200 ^{0}C consisted of Nb_6Sn_5 and Cr_{ss}, with a fine structure between the former and the latter phases forming in the areas that the $NbCr_2$ initially occupied.
- The solid state transformation reaction $NbCr_2 + Nb_3Sn \rightarrow Cr_{ss} + Nb_6Sn_5$ took place in the heat treated IP12 alloy.

- Chromium substituted Nb in Nb_6Sn_5, while Sn substituted Cr and Nb in the Laves phase in the IP12 alloy.
- Tin and Nb showed very small solubility in Cr_{ss} in the IP12 alloy, as their sum was less than 1 at. %.

14

Conclusions and suggestions for future work

14.1 Conclusions

The aim of this study was to obtain data for the Nb-Ti-Si-Sn-Al-Cr system to support the design of Nb silicide based alloys. The objectives of the current study were to investigate phase equilibria and phase stabilities in the Nb-Ti-Si-Sn-Al-Cr subsystems, which have not been reported in the past as well as investigate the elastic and thermodynamic properties (enthalpy of formation versus temperature, Debye temperature) of the intermetallics in selected binary systems. The use of clean melting for alloy making, heat treatments and XRD, SEM/EDS, EBSD and ab initio calculations was employed.

The Nb-Si binary system intermetallics were investigated using ab initio calculations and their elastic and thermodynamic properties were. It was concluded that the most ductile phases are the βNb_5Si_3 and Nb_3Si with the latter being the most ductile while the less ductile are αNb_5Si_3 and $NbSi_2$ (with the latter being the most brittle). The $NbSi_2$ compound was investigated for the first time using ab initio calculations. Also the transition temperatures for $Nb_3Si \rightarrow Nb + \alpha Nb_5Si_3$ and $\beta Nb_5Si_3 \rightarrow \alpha Nb_5Si_3$ and the stability of the $NbSi_2$ at low and elevated temperatures were confirmed and were in good agreement with the Nb-Si phase diagram.

The intermetallics in the Nb-Sn system were investigated using ab initio calculations. Their enthalpy of formation versus temperature, Debye temperatures and elastic properties were obtained. The Nb_6Sn_5 was found to be the less brittle compound, while the temperature dependence of its moduli and Poisson's ratio, along with the corresponding properties of Nb, were calculated using the quasistatic approximation and the low temperature values were found to be in good agreement with the literature. The high temperature elastic properties of Nb_3Sn and the elastic properties at 0 K of $NbSn_2$ and Nb_6Sn_5 were investigated for the first time.

The intermetallics of the Nb-Al binary system were studied using ab initio calculations. Their elastic properties and Debye temperatures were calculated. The temperature dependence of their enthalpy of formation, along with the temperature dependence of the elastic properties of the Nb_3Al were calculated and reported for the first time. The elastic properties of the Nb_2Al were also reported for the first time. It was concluded that the Nb_3Al has the highest bulk modulus value, while the $NbAl_3$ is the stiffest and most brittle phase.

A comparative study of the A15 intermetallics containing Nb and Sn, Si, Al, Ge was also made using ab initio calculations. Their linear thermal expansion coefficients were obtained and found to be in good agreement with the available literature. The temperature dependence of their enthalpy of formation along with their Debye temperatures were also calculated. It was concluded that the A15 Nb_3Si phase has the highest bulk, shear and Young's modulus values and that it is the stiffest and less ductile of the four binary intermetallics of the present study and that alloying with Al and Sn would improve ductility. The enthalpy of formation results suggest that the Sn and Al additions in the Nb_3Si stabilise the A15 structure over the competing *tP*32, while the Ge addition has the opposite effect.

Ab initio theory was used to investigate ternary W_5Si_3 type $TMSn_2X$ compounds (TM=Nb, Ti and X=Al,Si). Data for the temperature dependence of their enthalpies of formation that would allow the construction and optimisation of the Nb-Si-Sn, Nb-Al-Sn, Ti-Si-Sn, Ti-Al-Sn phase diagrams, along with Debye temperature data, were obtained and reported for the first time (with the exception of Ti_5Sn_2Si) . After obtaining their elastic properties, it was found that Al and Nb improve ductility, while Ti and Si enhance brittleness. It was concluded that when the transition metal is Nb the moduli of the ternary phase are considerably higher compared with the case of Ti. The elastic properties of Nb_5Sn_2Si, Nb_5Sn_2Al, Ti_5Sn_2Si and Ti_5Sn_2Al were investigated for the first time.

An experimental investigation of the phase equilibria in Nb-Si-Sn ternary alloys at 900 °C and 1200 °C was made. The alloys (IP2/Nb-16Si-13Sn and IP3/Nb-18Si-17Sn) were studied. The phase equilibria at 900 °C and 1200 °C and the solidification paths of the latter alloys were reported. It was concluded that the Nb_5Sn_2Si is stable below 900 °C phase and that it is formed possibly by the substitution of Nb by Sn in the Nb_3(Sn,Si) phase. Experimental data regarding the ternary Nb_5Sn_2Si phase was reported for the first time.

An experimental study of phase equilibria in the Nb-Al-Sn system at 900 °C and 1200 °C was made. The alloys (IP4/Nb-17Al-17Sn, IP5/Nb-33Al-13Sn and IP6/Nb-16Al-20Sn) were studied. It was concluded that Sn shows high solubility in Nb_2Al, reaching up to 21 at. % in the Sn-rich areas and that it substitutes Al atoms. Also Sn and Al substitute each other in the A15 phase (Nb_3Al and Nb_3Sn), while Sn shows limited solubility in $NbAl_3$, not exceeding ~3.6 at. % as it substitutes Al atoms as was the case in the Nb_2Al. The solubility of Al in $NbSn_2$ varies from ~4.8 to ~6.8 at. %. Furthermore,

it was verified that the Nb_5Sn_2Al is a ternary intermetallic stable in the range ~900 °C to ~1200 °C and it can be treated as a line compound. Experimental data of the ternary Nb_5Sn_2Al phase was reported for the first time.

Phase equilibria in the Nb-Ti-Sn system at 900 °C and 1200 °C was also studied. The alloys IP7 (Nb-10Ti-18Sn), IP8 (Nb-13Ti-3Sn), IP9 (Nb-40Ti-23Sn) and IP10 (Nb-39Ti-40Sn) were studied. It was concluded that in Nb_3Sn the Ti substitutes Nb, whereas in Ti_3Sn Nb substitutes Ti. In Ti_6Sn_5 the Nb substitutes both Ti and Sn, with primary preference to the former. Phase equilibria data in the Nb-Ti-Sn system was obtained for the first time.

Phase equilibria in the Nb-Ti-Si-Sn quaternary system was studied at 1000, 1100 and 1300 °C using the alloy IP1 (Nb-24Ti-18Si-5Sn). It was concluded that over a certain content of Ti (possibly 25-30 at. %) the γNb_5Si_3 phase becomes stable. Titanium shows higher solubility in the γNb_5Si_3 intermetallic of all the Nb_5Si_3 silicides and reduces the solubility of Si in the Nb_3Sn.

Finally, the phase equilibria in the Nb-Cr-Sn system was studied at 900 °C and 1200 °C using the alloys IP11 (Nb-15Cr-11Sn) and IP12 (Nb-65Cr-18Sn). The solidification paths of the latter alloys were deduced. It was concluded that Cr substitutes Nb in the Nb_3Sn and the Nb_6Sn_5 phases. Tin on the other hand substitutes Cr and Nb in the Laves phase. Finally, Nb and Sn show very small solubility in Cr_{ss}.

Overall, the present study provided the valuable data on phase equilibria, phase stability of key phases and the effects of additional alloying elements on the phases. Thermodynamic data such as enthalpy of formation and the elastic properties were also computationally obtained for the first time for some phases, which would be difficult and costly if experimentally approached.

14.2 Suggestions for future work

The findings from the present study regarding phase equilibria and thermodynamic properties, such as enthalpies of formation, can be used to create a robust thermodynamic database starting from the Nb-Si-Sn, Nb-Ti-Sn, Nb-Al-Sn and Nb-Cr-Sn ternary systems to gradually build up to higher than ternary order systems. The ternary systems investigated in the present study can now be assessed with the use of Calculation of Phase Diagrams method (CALPHAD). The construction of a larger database, namely the Nb-Ti-Si-Sn-Al-Cr, can be accomplished by both experimental

and theoretical approaches. No phase equilibria exist for quaternary systems such as the Nb-Al-Cr-Sn, Nb-Al-Si-Sn, Nb-Cr-Si-Sn and Nb-Cr-Al-Sn.

Also the good agreement of the data obtained from the current study with the help of the ab initio method with available experimental data in the literature should encourage research of alloying additions in phases that are considered important for high temperature application materials. To that end, the Nb_5Si_3, the Nb_3Si, the Nb_3Sn and the $NbCr_2$ (Laves) phases are considered to be very important. After acquiring elastic and thermodynamic properties data of those phases in the present work, studies of the effect of different alloying elements (for example Ge, Ti, Mo, Al, Cr etc.) on their elastic and thermodynamic properties, phase stability and coefficients of thermal expansion would provide valuable data, which would be otherwise very difficult to be obtained experimentally. This data combined with phase equilibria in ternary, quaternary or higher order systems would significantly aid the design of Nb based alloys.

Acknowledgments

At this point I would like to thank the man who I had the opportunity to be supervised by, a highly regarded and experienced supervisor (Professor P. Tsakiropoulos) that helped me with his vast knowledge in the field of Materials Science. He was a valuable advisor, but also allowed me to retain my independency as a researcher within reasonable boundaries. I would also like to thank Dr Claire Utton for her valuable help and for always being there whenever needed.

The support of this work by the FP-7 "Accelerated Metallurgy" project and the EPSRC-Rolls Royce research partnership and useful discussions with Dr A. Scott and especially Dr Keith Refson are gratefully acknowledged.

Last but definitely not least, I would like to thank the people that stood by me throughout my PhD. The people that kept supporting me throughout this wonderful journey.

15

Appendices

APPENDIX A

Appendix

Elastic properties*

Cubic structures

Reuss's shear modulus (lower bound)

$$G_R = \frac{5(C_{11}-C_{12})C_{44}}{4C_{44}+3(C_{11}-C_{12})} \quad (1)$$

Voigt's shear modulus (upper bound)

$$G_V = \frac{1}{5}(C_{11} - C_{12} + 3C_{44}) \quad (2)$$

Reuss's (lower bound) and Voigt's (upper bound) bulk modulus

$$B_R = \frac{1}{3}(C_{11} + 2C_{12}) \quad (3)$$

Tetragonal structures

Reuss's shear modulus (lower bound)

$$G_R = \frac{15}{\frac{18B_V}{C^2}+\frac{6}{C_{11}-C_{12}}+\frac{6}{C_{44}}+\frac{3}{C_{66}}} \quad (4)$$

Voigt's shear modulus (upper bound)

$$G_V = \frac{1}{30}(M + 3C_{11} - 3C_{12} + 12C_{44} + 6C_{66}) \quad (5)$$

Reuss's bulk modulus (lower bound)

$$B_R = \frac{C^2}{M} \quad (6)$$

Voigt's bulk modulus (upper bound)

$$B_V = \frac{1}{9}[2(C_{11} + C_{12}) + C_{33} + 4C_{13}] \quad (7)$$

where $C^2 = (C_{11} + C_{12})C_{33} - 2{C_{13}}^2$ (8)

and M= $C_{11} + C_{12} + 2C_{33} - 4C_{13}$ (9)

Orthorhombic structures

Reuss's shear modulus (lower bound)

$$G_R = 15\{4[C_{11}(C_{22}+C_{33}+C_{23})+C_{22}(C_{33}+C_{13})+C_{33}C_{12}-C_{12}(C_{23}+C_{12})-C_{13}(C_{12}+C_{13})-C_{23}(C_{13}+C_{23})]/\Delta+3[\left(\frac{1}{C_{44}}\right)+\left(\frac{1}{C_{55}}\right)+\left(\frac{1}{C_{66}}\right)]\}\ s^{-1} \quad (10)$$

Voigt's shear modulus (upper bound)

$$G_V = \frac{1}{15}[C_{11}+C_{22}+C_{33}+3(C_{44}+C_{55}+C_{66})-(C_{12}+C_{13}+C_{23}) \quad (11)$$

Reuss's bulk modulus (lower bound)

$$B_R = \Delta[C_{11}(C_{22}+C_{33}-2C_{23})+C_{22}(C_{33}-2C_{13})-2C_{33}C_{12}+C_{12}(C_{23}-C_{12})+C_{13}(2C_{12}-C_{13})+\ C_{23}(C_{13}-C_{23})]^{\ -1} \quad (12)$$

Voigt's bulk modulus (upper bound)

$$B_V = \frac{1}{9}[C_{11}+C_{22}+C_{33}+2(C_{12}+C_{13}+C_{23}] \ (13)$$

where Δ is defined as

$$\Delta = C_{13}(C_{12}C_{23}-C_{13}C_{22})+C_{23}(C_{12}C_{13}-C_{23}C_{11})+C_{33}\left(C_{11}C_{22}-{C_{12}}^2\right) \ (14)$$

Bulk modulus

$$B = \frac{(B_V+B_R)}{2} \quad (15)$$

Shear Modulus

$$G = \frac{(G_V+G_R)}{2} \quad (16)$$

Young's Modulus

$$E = \frac{9GB}{(3B+G)} \quad (17)$$

Poisson's ratio

$$v = \frac{E}{2G} - \ 1 \quad (18)$$

Debye Temperature

$$\theta_D = \frac{h}{k}\left[\frac{3n}{4\pi}\left(\frac{N_A\rho}{M}\right)\right]^{1/3} u_m \quad (19)$$

where M is the molecular weight, N_A is the Avogadro's number, n is the number of atoms per formula unit and ρ is the density.

$$u_m = \left[\frac{1}{3}\left(\frac{2}{u_t^3} + \frac{1}{u_l^3}\right)\right]^{-1/3} \quad (20)$$

where u_t and u_l are the traverse and longitudinal elastic wave velocities of the polycrystalline material, respectively:

$$u_t = \sqrt{\frac{G}{\rho}} \quad (21) \qquad u_l = \sqrt{\frac{B+\frac{4G}{3}}{\rho}} \quad (22)$$

Birch–Murnaghan equation of state:

$$E(V) = E_0 + \frac{9V_0B_0}{16}\left\{\left[\left(\frac{V_0}{V}\right)^{\frac{2}{3}} - 1\right]^3 B_0' + \left[\left(\frac{V_0}{V}\right)^{\frac{2}{3}} - 1\right]^2 \left[6 - 4\left(\frac{V_0}{V}\right)^{\frac{2}{3}}\right]\right\} \quad (23)$$

where E_0 and B_0 are the equilibrium energy and bulk modulus respectively, while B'_0 is the first pressure derivative of the bulk modulus.

Quasiharmonic approximation*

$$E(T) = \frac{1}{2}\int f(\omega)\hbar\omega d\omega + \int \frac{\hbar\omega}{exp\left(\frac{\hbar\omega}{kT}\right)-1} f(\omega)d\omega \quad (24)$$

$$F(T) = \frac{1}{2}\int f(\omega)\hbar\omega d\omega + kT\int f(\omega) ln\left[1 - exp\left(-\frac{\hbar\omega}{kT}\right)\right] d\omega \quad (25)$$

$$C_v(T) = k\int \frac{\left(\frac{\hbar\omega}{kT}\right)^2 exp\left(\frac{\hbar\omega}{kT}\right)}{\left[exp\left(\frac{\hbar\omega}{kT}\right)-1\right]^2} f(\omega)d\omega \quad (26)$$

$$C_v(T) = 9Nk\left(\frac{T}{\Theta_D}\right)^3 \int_0^{\frac{T}{\Theta_D}} \frac{\chi^4 e^x}{\left(e^x-1\right)^2} dx \quad (27)$$

where k is the Boltzmann's constant, $\hbar$ is the reduced Planck's constant, N is the number of atoms per cell f(ω) the phonon density of states, E is the vibrational

internal energy, F is the vibrational free energy, C_v is the heat capacity and Θ_D is the Debye temperature.

Heat of formation

$$\Delta H_f^0 = [E^{A_mB_n} - mE^A - nE^B]/(m+n) \quad (28)$$

with ΔH_f^0 and $\Delta H_f(T)$ being the static (T=0 K) and temperature dependent enthalpy of formation of the given intermetallic respectively, $E^{A_mB_n}$, $E^A$and E^B are the total energies of the intermetallic, A and B element unit cell respectively, while m and n are the number of A and B are atoms in the compound respectively,

$$\Delta H_f(T) = [F^{A_mB_n}(T) - mF^A(T) - nF^B(T)]/(m+n) \quad (29)$$

$$\text{where:} \quad F^{A_mB_n}(T) = E^{A_mB_n} + F^{phon}(T) \quad (30)$$

After fitting the enthalpy of formation curves versus temperature for each intermetallic studied in this work the equations 31 to 44 were obtained:

$$\Delta H_f^{Nb_3Si}(T) = 1.11 * 10^{-8} * T^2 + 0.00126 * T - 37.4 \quad (31)$$

$$\Delta H_f^{NbSi_2}(T) = -4.1 * 10^{-8} * T^2 + 0.00173 * T - 50.4 \quad (32)$$

$$\Delta H_f^{\alpha Nb_5Si_3}(T) = 5.5 * 10^{-8} * T^2 + 0.00537 * T - 62.7 \quad (33)$$

$$\Delta H_f^{\beta Nb_5Si_3}(T) = 1.51 * 10^{-8} * T^2 + 0.00395 * T - 59.6 \quad (34)$$

$$\Delta H_f^{Nb_6Sn_5}(T) = 3.59 * 10^{-8} * T^2 + 0.00428 * T - 26 \quad (35)$$

$$\Delta H_f^{NbSn_2}(T) = 3.45 * 10^{-8} * T^2 + 0.00397 * T - 18.7 \quad (36)$$

$$\Delta H_f^{Nb_3Sn}(T) = 2.8 * 10^{-8} * T^2 + 0.00428 * T - 16.8 \quad (37)$$

$$\Delta H_f^{NbAl_3}(T) = -1.45 * 10^{-8} * T^2 + 0.00856 * T - 48.2 \quad (38)$$

$$\Delta H_f^{Nb_2Al}(T) = 6.69 * 10^{-8} * T^2 + 0.00401 * T - 29.2 \quad (39)$$

$$\Delta H_f^{Nb_3Al}(T) = 3.11 * 10^{-8} * T^2 + 0.00186 * T - 22.6 \quad (40)$$

$$\Delta H_f^{Nb_5Sn_2Si}(T) = 3.6 * 10^{-8} * T^2 + 0.00576 * T - 30.7 \quad (41)$$

$$\Delta H_f^{Nb_5Sn_2Al}(T) = 7.23 * 10^{-8} * T^2 + 0.00723 * T - 20.3 \quad (42)$$

$$\Delta H_f^{Ti_5Sn_2Si}(T) = 5.13 * 10^{-8} * T^2 + 0.0062 * T - 51.1 \quad (43)$$

$$\Delta H_f^{Ti_5Sn_2Al}(T) = 6.35 * 10^{-8} * T^2 + 0.00645 * T - 37 \quad (44)$$

APPENDIX B

Table B.1 JCPDS cards used for the phases observed in the current study.

Phase	Structure	JCPDS Reference
Nb_{ss}	cubic	34-0370
Nb_3Sn	cubic	19-0875
Nb_6Sn_5	orthorhombic	19-0877
$NbSn_2$	orthorhombic	15-0481
Sn_{ss}	cubic	86-2265
aNb_5Si_3	tetragonal	30-0874
bNb_5Si_3	tetragonal	65-2785
gNb_5Si_3	hexagonal	65-3599
Nb_5Sn_2Si	tetragonal	24-0813
Nb_3Al	cubic	12-0085
Al_3Nb	hexagonal	13-0146
Nb_2Al	tetragonal	14-0458
Ti_6Sn_5	orthorhombic	65-6932
Ti_3Sn	hexagonal	10-0226
Cr_{ss}	cubic	88-2323
C14 Cr_2Nb	hexagonal	65-9006

Table B.2 Reflections of the Nb_5Sn_2Al intermetallic.

h	k	l	d	θ	2Θ
0	0	2	0.2608	17.178	34.356
1	1	0	0.751584	5.882204	11.76441
1	1	2	0.246388	18.21701	36.43402
2	0	0	0.53145	8.333438	16.66688
2	0	2	0.234128	19.20728	38.41456
2	2	2	0.214258	21.0693	42.1386
2	1	1	0.351336	12.66408	25.32817
2	2	0	0.375792	11.82758	23.65515
2	1	3	0.163287	28.1458	56.29159
3	2	1	0.256643	17.46515	34.93029
3	3	0	0.250528	17.90567	35.81134
3	1	0	0.336118	13.24764	26.49528
3	1	2	0.206049	21.95136	43.90272
3	3	2	0.180672	25.23452	50.46903
3	2	3	0.14976	30.95222	61.90445
4	0	0	0.265725	16.85001	33.70003
4	2	0	0.237672	18.90994	37.81988
4	1	1	0.231106	19.46849	38.93698
4	4	0	0.187896	24.20071	48.40142
4	0	2	0.18613	24.44522	48.89044
4	1	3	0.144146	32.3001	64.60021
5	2	1	0.184601	24.66116	49.32231
5	3	0	0.182286	24.99572	49.99145
6	0	0	0.17715	25.77263	51.54527
6	2	0	0.168059	27.27879	54.55757
6	3	1	0.151607	30.53447	61.06894
7	1	0	0.150317	30.82502	61.65004
4	2	4	0.114323	42.3569	84.71381
7	1	2	0.130233	36.2591	72.5182

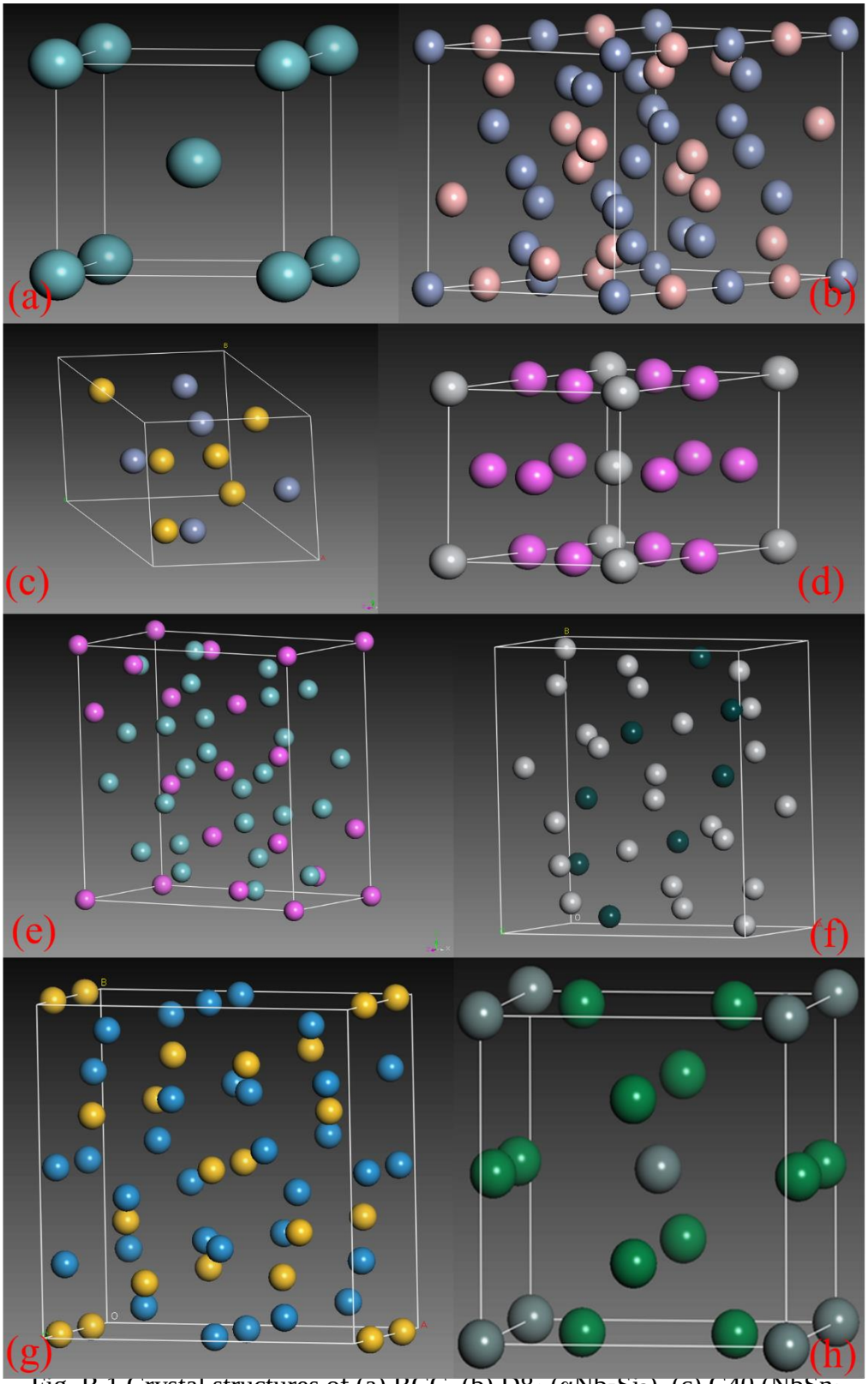

Fig. B.1 Crystal structures of (a) BCC, (b) $D8_1$ (αNb_5Si_3), (c) C40 ($NbSn_2$, $NbSi_2$), (d) $D0_{22}$ ($NbAl_3$), (e) $D8_b$ (Nb_2Al), (f) tetragonal Nb_3Si), (g) $D8_m$ (βNb_5Si_3, Nb_5Sn_2Si, Nb_5Sn_2Al, Ti_5Sn_2Si, Ti_5Sn_2Al) and (h) A15 (Nb_3Sn, Nb_3Al, Nb_3Ge).

APPENDIX C

Publications made from this study

[1] Papadimitriou I., Utton C., Scott A., Tsakiropoulos P., Ab initio study of the intermetallics in Nb–Si binary system, Intermetallics 2014;54:125

[2] Papadimitriou I., Utton C., Scott A., Tsakiropoulos P., Ab initio study of binary and ternary $Nb_3(X,Y)$ A15 intermetallic phases (X,Y= Al, Ge, Si, Sn), Metallurgical and Materials Transactions A 2015;46A:566

[3] Papadimitriou I., Utton C., Tsakiropoulos P., Ab initio study of the intermetallics in Nb–Sn binary system, Acta Materialia 2015;86:23

REFERENCES

[1] P. Tsakiropoulos, Beyond Nickel Based Superalloys. in: B. R., S. W. (Eds.), John Wiley & Sons, Ltd, Encyclopedia of Aerospace Engineering, 2010.

[2] S.J. Balsone, B.P. Bewlay, M.R. Jackson, P.R. Subramanian, J.C. Zhao, A. Chatterjee, T.M. Heffernan, in: K.J. Hemker, D.M. Dimiduk, H. Clemens, R. Darolia, M. Inui, J.M. Larsen, V.K. Sikka, Thomas, J.D. Whittenberger (Eds.) Structural Intermetallics 2001, TMS, Warrendale, 2001, pp. 99-108.

[3] J. Geng, P. Tsakiropoulos, Intermetallics, 15 (2007) 382-395.

[4] D.M. Shah, D.L. Anton, D.P. Pope, S. Chin, Materials Science Engineering, A192/193 (1995) 658-672.

[5] J. Geng, P. Tsakiropoulos, G. Shao, Materials Science and Engineering A, 441 (2006) 26-38.

[6] Jackson MR, Bewlay BP, Zhao JC. vol. US patent 6,913,655 B2, July 5, 2005.

[7] K. Zelenitsas, P. Tsakiropoulos, Materials Science and Engineering A, 416 (2006) 269-280.

[8] B.P. Bewlay, M.R. Jackson, J.C. Zhao, P.R. Subramanian, Metallurgical and Materials Transactions A: Physical Metallurgy and Materials Science, 34 A (2003) 2043-2052.

[9] D.M. Dimiduk, P.R. Subramanian, M.G. Mendiratha, Acta Metallurgica Sinica Series A, Physical Metallurgy & Materials Science, 8 (1995) 519-530.

[10] M.G. Mendiratta, D.M. Dimiduk, Metallurgical Transactions A, 24 (1993) 501-504.

[11] M.G. Mendiratta, J.J. Lewandowski, D.M. Dimiduk, Metallurgical Transactions A, 22 (1991) 1573-1583.

[12] R. Grill, A. Gnadenberger, Int. J. Refract. Met. Hard Mater., 24 (2006) 275-282.

[13] N. David, Y. Cartigny, T. Belmonte, J.M. Fiorani, M. Vilasi, Intermetallics, 14 (2006) 464-473.

[14] M.E. Schlesinger, H. Okamoto, A.B. Gokhale, R. Abbaschian, Journal of Phase Equilibria, 14 (1993) 502-509.

[15] H. Okamoto, J. Phase Equilib. Diffus., 33 (2012) 250-251.

[16] T. Geng, C.R. Li, Z.M. Du, C.P. Guo, X.Q. Zhao, H.B. Xu, J. Alloys Compd., 509 (2011) 3080-3088.

[17] P.B. Fernandes, G.C. Coelho, F. Ferreira, C.A. Nunes, B. Sundman, Intermetallics, 10 (2002) 993-999.

[18] I. Grammenos, P. Tsakiropoulos, Intermetallics, 18 (2010) 242-253.

[19] N. Vellios, P. Tsakiropoulos, Intermetallics, 15 (2007) 1518-1528.

[20] I. Grammenos, P. Tsakiropoulos, Intermetallics, 19 (2011) 1612-1621.

[21] W.B. Pearson, A Handbook of Lattice Spacings and Structures of Metals and Alloys, Pergamon, Oxford, 1967.

[22] H. Nowotny, A.W. Searcy, J.E. Orr, J. Phys. Chem., 60 (1956) 677-678.

[23] Y. Chen, T. Hammerschmidt, D.G. Pettifor, J.-X. Shang, Y. Zhang, Acta Materialia, 57 (2009) 2657-2664.

[24] B.P. Bewlay, M.R. Jackson, M.F.X. Gigliotti, Intermetallic Compounds: Principles and Practice, 3 (2002) 541-560.

[25] M.R. Jackson, B.P. Bewlay, R.G. Rowe, D.W. Skelly, H.A. Lipsitt, JOM, 48 (1996) 39-44.

[26] B.P. Bewlay, J.J. Lewandowksi, M.R. Jackson, JOM, 49 (1997) 44-45, 67.

[27] T. Geng, C. Li, J. Bao, X. Zhao, Z. Du, C. Guo, Intermetallics, 17 (2009) 343-357.

[28] C. Toffolon, C. Servant, J.C. Gachon, B. Sundman, Journal of Phase Equilibria, 23 (2002) 134-139.

[29] K. Zelenitsas, P. Tsakiropoulos, Intermetallics, 13 (2005) 1079-1095.

[30] N. Vellios, P. Tsakiropoulos, Intermetallics, 15 (2007) 1529-1537.

[31] J.C. Zhao, M.R. Jackson, L.A. Peluso, Materials Science and Engineering: A, 372 (2004) 21-27.
[32] Z. Li, P. Tsakiropoulos, Intermetallics, 26 (2012) 18-25.
[33] K.S. Chan, Materials Science and Engineering: A, 329–331 (2002) 513-522.
[34] K.S. Chan, Materials Science and Engineering: A, 409 (2005) 257-269.
[35] E. Wainer, United States Patent Office, Patented April 21,1959.
[36] J. Geng, P. Tsakiropoulos, G. Shao, Intermetallics, 15 (2007) 270-281.
[37] N. Vellios, P. Tsakiropoulos, Intermetallics, 18 (2010) 1729-1736.
[38] J. Geng, P. Tsakiropoulos, G. Shao, Intermetallics, 15 (2007) 69-76.
[39] F.G. Meng, H.S. Liu, L.B. Liu, Z.P. Jin, J. Alloys Compd., 431 (2007) 292-297.
[40] A.K. Sinha, Prog. Mater. Sci., 15 (1972) 79-179.
[41] D. Dew-Hughes, Cryogenics, 15 (1975) 435-454.
[42] J.P. Charlesworth, Physics Letters, 21 (1966) 501-502.
[43] Z. Fisk, G.W. Webb, Physical Review Letters, 36 (1976) 1084-1086.
[44] G.W. Webb, Z. Fisk, J.J. Engelhardt, S.D. Bader, Phys. Rev. B, 15 (1977) 2624-2629.
[45] B.M. Klein, L.L. Boyer, D.A. Papaconstantopoulos, Physical Review Letters, 42 (1979) 530-533.
[46] W. Rehwald, M. Rayl, R.W. Cohen, G.D. Cody, Phys. Rev. B, 6 (1972) 363-371.
[47] G.S. Knapp, S.D. Bader, Z. Fisk, Phys. Rev. B, 13 (1976) 3783-3789.
[48] M. Sundareswari, S. Ramasubramanian, M. Rajagopalan, Solid State Communications, 150 (2010) 2057-2060.
[49] P. Soderlind, O. Eriksson, J.M. Wills, A.M. Boring, Phys. Rev. B, 48 (1993) 5844-5851.
[50] J. Moon, K. Cho, M. Cho, Int. J. Precis. Eng. Manuf., 13 (2012) 1191-1197.
[51] C. Kittel, Introduction to Solid State Physics. 8th ed. New York:Wiley;, (2005) 116.
[52] J.A. Rayne, B.S. Chandrasekhar, Physical Review, 120 (1960) 1658-1663.
[53] G. Shao, Intermetallics, 12 (2004) 655-664.
[54] P.R. Subramanian, M.G. Mendiratta, D.M. Dimiduk, M.A. Stucke, Materials Science and Engineering A, 239-240 (1997) 1-13.
[55] K. Zelenitsas, P. Tsakiropoulos, Intermetallics, 14 (2006) 639-659.
[56] T. Kumagai, S. Hanada, Materials Science and Engineering: A, 152 (1992) 349-355.
[57] P.P. Smith, B.F. Oliver, R.D. Noebe, Scripta Metallurgica Materialia, 26 (1992) 1365-1370.
[58] T. Tabaru, S. Hanada, Intermetallics, 6 (1998) 735-739.
[59] C.D. Bencher, A. Sakaida, K.T.V. Rao, R.O. Ritchie, Metallurgical and Materials Transactions A, 26 (1995) 2027-2033.
[60] R. Gnanamoorthy, S. Hanada, K. Kamata, Scripta Materialia, 34 (1996) 999-1003.
[61] Y. Murayama, S. Hanada, Scripta Materialia, 37 (1997) 949-953.
[62] S.V. Meschel, O.J. Kleppa, J. Alloys Compd., 191 (1993) 111-116.
[63] I. Shilo, H.F. Franzen, R.A. Schiffman, Journal of the Electrochemical Society, 129 (1982) 1608-1613.
[64] C. Paduani, Braz. J. Phys., 37 (2007) 1073-1076.
[65] Z. Nong, J. Zhu, X. Yang, Y. Cao, Z. Lai, Y. Liu, Physica B: Condensed Matter, 407 (2012) 3555-3560.
[66] M.H. Robert, S.L.U. Filho, Journal of Materials Processing Technology, 64 (1997) 335-341.
[67] M. Steinhorst, H.J. Grabke, Materials Science and Engineering: A, 120–121, Part 1 (1989) 55-59.
[68] H. Liang, Y.A. Chang, Intermetallics, 7 (1999) 561-570.

[69] H.J. Seifert, H.L. Lukas, G. Petzow, Zeitschrift fuer Metallkunde/Materials Research and Advanced Techniques, 87 (1996) 2-13.
[70] Y. Zhang, H. Liu, Z. Jin, CALPHAD, 25 (2001) 305.
[71] Z. Sun, X. Guo, C. Zhang, CALPHAD, 36 (2012) 82-88.
[72] R.M. Waterstrat, J. Müller, Journal of The Less-Common Metals, 52 (1977) 271-277.
[73] R. Horyn, K. Lukaszewicz, Bull. Acad. Pol. Sci.,Ser. Sci. Chim, 18 (1970) 59-64.
[74] Dinsdale, A.T., CALPHAD, 15 (1991) 317-425.
[75] M.A. Pietzka, J.C. Schuster, J. Alloys Compd., 230 (1995) L10-L12.
[76] F.J. Bachner, J.B. Goodenough, H.C. Gatos, Journal of Physics and Chemistry of Solids, 28 (1967) 889-895.
[77] F. Yin, J.C. Tedenac, F. Gascoin, Calphad: Computer Coupling of Phase Diagrams and Thermochemistry, 31 (2007) 370-379.
[78] V.T. Witusiewicz, A.A. Bondar, U. Hecht, S. Rex, T.Y. Velikanova, J. Alloys Compd., 465 (2008) 64-77.
[79] V.T. Witusiewicz, A.A. Bondar, U. Hecht, T.Y. Velikanova, J. Alloys Compd., 472 (2009) 133-161.
[80] C. Brukl, H. Nowotny, F. Benesovsky, Monatshefte für Chemie, 92 (1961) 967-980.
[81] V.M. Pan, V.I. Latysheva, O.G. Kulik, A.G. Popov, L.E.N. Izuvestiya, Metally, 3 (1982) 167-177.
[82] T. Murakami, S. Sasaki, K. Ichikawa, A. Kitahara, Intermetallics, 9 (2001) 621-627.
[83] L. Zifu, P. Tsakiropoulos, Intermetallics, 18 (2010) 1072-1078.
[84] Y. Murayama, S. Hanada, Science and Technology of Advanced Materials, 3 (2002) 145-156.
[85] D.W. Woodard, G.D. Cody, Physical Review a-General Physics, 136 (1964) A166-168.
[86] M. Bulanova, L. Tretyachenko, K. Meleshevich, V. Saltykov, V. Vereshchaka, O. Galadzhyj, L. Kulak, S. Firstov, J. Alloys Compd., 350 (2003) 164-173.
[87] C. Colinet, J.-C. Tedenac, CALPHAD, 35 (2011) 643-647.
[88] P. Hohenberg, W. Kohn, Phys. Rev. B, 136 (1964) B864.
[89] W. Kohn, L.J. Sham, Physical Review, 140 (1965) A1133-A1138.
[90] Y. Chen, J.X. Shang, Y. Zhang, Journal of Physics-Condensed Matter, 19 (2007) 016215 1-8.
[91] S.J. Clark, M.D. Segall, C.J. Pickard, P.J. Hasnip, M.J. Probert, K. Refson, M.C. Payne, Z. Kristall., 220 (2005) 567-570.
[92] S. De Gironcoli, Phys. Rev. B, 51 (1995) 6773-6776.
[93] D.R. Bates, A. Fundaminsky, H.S.W. Massey, J.W. Leech, Philosophical Transactions of the Royal Society of London Series a-Mathematical and Physical Sciences, 243 (1950) 93-143.
[94] J.P. Perdew, J.A. Chevary, S.H. Vosko, K.A. Jackson, M.R. Pederson, D.J. Singh, C. Fiolhais, Phys. Rev. B, 46 (1992) 6671-6687.
[95] J.P. Perdew, K. Burke, M. Ernzerhof, Physical Review Letters, 77 (1996) 3865-3868.
[96] H.J. Monkhorst, J.D. Pack, Phys. Rev. B, 13 (1976) 5188-5192.
[97] D. Vanderbilt, Phys. Rev. B, 41 (1990) 7892-7895.
[98] S. Baroni, S. de Gironcoli, A. Dal Corso, P. Giannozzi, Rev. Mod. Phys., 73 (2001) 515-562.
[99] X. Gonze, J.C. Charlier, D.C. Allan, M.P. Teter, Phys. Rev. B, 50 (1994) 13035-13038.
[100] X. Gonze, Abstr. Pap. Am. Chem. Soc., 213 (1997) 312.
[101] R. Hill, Proceedings of the Physical Society of London Section A, 65 (1952) 349-355.
[102] A. Reuss, Z. Angew. Math. Mech., 9 (1929) 49-58.
[103] O.L. Anderson, Journal of Physics and Chemistry of Solids, 24 (1963) 909-917.
[104] S.F. Pugh, Philosophical Magazine, 45 (1954) 823-843.

[105] B.G. Pfrommer, M. Cote, S.G. Louie, M.L. Cohen, J. Comput. Phys., 131 (1997) 233-240.
[106] M.C. Payne, M.P. Teter, D.C. Allan, T.A. Arias, J.D. Joannopoulos, Rev. Mod. Phys., 64 (1992) 1045-1097.
[107] M. Born, K. Huang, Dynamical Theory of Crystal Lattices, Oxford, 1956.
[108] F. Birch, Phys Rev 71 (1947) 809-824.
[109] Y. Wang, C. Woodward, S.H. Zhou, Z.K. Liu, L.Q. Chen, Scripta Materialia, 52 (2005) 17-20.
[110] B. Montanari, N.M. Harrison, Chemical Physics Letters, 364 (2002) 528-534.
[111] S.L. Shang, H. Zhang, Y. Wang, Z.K. Liu, J. Phys.: Condens. Matter, 22 (2010) 375403.
[112] Y. Wang, J.J. Wang, H. Zhang, V.R. Manga, S.L. Shang, L.Q. Chen, Z.K. Liu, J. Phys.: Condens. Matter 22 (2010) 225404.
[113] O. Gulseren, R.E. Cohen, Phys. Rev. B, 65 (2002) 064103.
[114] G. Simmons, H. Wang, Single Crystal Elastic Constants and Calculated Aggregate Properties: A Handbook, 1971.
[115] F. Chu, M. Lei, S.A. Maloy, J.J. Petrovic, T.E. Mitchell, Acta Materialia, 44 (1996) 3035-3048.
[116] M.E. Straumanis, E.Z. Aka, J. Appl. Phys., 23 (1952) 330-334.
[117] Y.A. Kocherzhinskiy, L.M. Yupko, E.A. Shishkin, Russian Metallurgy, 1 (1980) 184-188.
[118] R.M. Waterstrat, K. Yvon, H.D. Flack, E. Parthe, Acta Crystallographica B, 31 (1975) 2765-2769.
[119] C.J. Smithells, Metal References Book, 5th Edition Butterworth, London, 1976.
[120] W.A. Brantley, J. Appl. Phys., 44 (1973) 534-535.
[121] D.G. Pettifor, Mater. Sci. Technol., 8 (1992) 345-349.
[122] C. Kittel, Introduction to Solid State Physics, 7th edition John Wiley & Sons, New York, 1996.
[123] G.R. Stewart, B. Olinger, L.R. Newkirk, Solid State Communications, 39 (1981) 5-9.
[124] S.V. Meschel, O.J. Kleppa, J. Alloys Compd., 274 (1998) 193-200.
[125] J.S. Lin, A. Qteish, M.C. Payne, V. Heine, Phys. Rev. B, 47 (1993) 4174-4180.
[126] M. Born, J Phys Chem Solids, 7 (1939) 591-601.
[127] F. deBoer, R. Boom, W.C. Mattens, A.R. Miedema, A.K. Niessen, Cohesion in Metals, Transition Metal Alloys, North Holland, Amsterdam, the Netherlands, (1988).
[128] A.R. Miedema, P.F. Dechatel, F.R. Deboer, Physica B & C, 100 (1980) 1-28.
[129] R.A. Schiffman, D.M. Bailey, High Temp. Sci., 15 (1982) 165-177.
[130] R. Grill, A. Gnadenberger, International Journal of Refractory Metals and Hard Materials, 24 (2006) 275-282.
[131] D.P. Boso, M. Lefik, B.A. Schrefler, Cryogenics, 46 (2006) 569-580.
[132] J.R. Ogren, T.G. Ellis, J.F. Smith, Acta Crystallographica, 18 (1965) 968-973.
[133] T. Wölpl, W. Jeitschko, Journal of Alloys and Compounds, 210 (1994) 185-190.
[134] C.J. Smithells, Metal References Book, 5th Edition Butterworth, London, (1976) p975.
[135] W.P. Mason, H.E. Bommel, J. Acoust. Soc. Am., 28 (1956) 930.
[136] V.M. Mathew, C.S. Menon, K.P. Jayachandran, J. Phys. Chem. Solids, 63 (2002) 1835-1838.
[137] R.J. Wasilewski, Journal of Physics and Chemistry of Solids, 26 (1965) 1643-1647.
[138] K.R. Keller, J.J. Hanak, Physics Letters, 21 (1966) 263-264.
[139] P.W. Brown, F.J. Worzala, J. Mater. Sci., 11 (1976) 760-766.
[140] H.E. Swanson, E. Tatge, National Bureau of Standards (U.S.), 539 (1953) 1-95.
[141] H.H. Pham, M.E. Williams, P. Mahaffey, M. Radovic, R. Arroyave, T. Cagin, Phys. Rev. B, 84 (2011) 064101.

[142] H. Kawamura, K. Tachikawa, K. Takemura, S. Minomura, Journal of the Physical Society of Japan, 47 (1979) 1365-1366.
[143] C. Filippi, D.J. Singh, C.J. Umrigar, Phys. Rev. B, 50 (1994) 14947-14951.
[144] W.K. Wang, H. Iwasaki, C. Suryanarayana, T. Masumoto, N. Toyota, T. Fukase, F. Kogiku, J. Mater. Sci., 17 (1982) 1523-1532.
[145] F. Galasso, B. Bayles, S. Soehle, Nature, 198 (1963) 984-988.
[146] K. Schubert, in W. Koster (ed.), Kristallstrukturen Zweikomponentiger Phasen, 1964.
[147] M. Arita, H.U. Nissen, W. Schauer, J. Solid State Chem., 84 (1990) 386-400.
[148] K. Mahdouk, J.-C. Gachon, J. Alloys Compd., 321 (2001) 232-236.
[149] D.M. Ceperley, B.J. Alder, Physical Review Letters, 45 (1980) 566-569.
[150] C.P. Umbach, L.E. Toth, A.M. Goldman, Journal of the Less-Common Metals, 69 (1980) 319-326.
[151] S. Knittel, S. Mathieu, L. Portebois, M. Vilasi, Intermetallics, 47 (2014) 43-52.
[152] E. Scheil, Z Metallkd, 34 (1942).
[153] J.O. Andersson, T. Helander, L.H. Hoglund, P.F. Shi, B. Sundman, Calphad-Computer Coupling of Phase Diagrams and Thermochemistry, 26 (2002) 273-312.
[154] J.L. Wang, L.B. Liu, X.D. Zhang, W.M. Bai, C.P. Chen, J. Phase Equilib. Diffus., 35 (2014) 223-231.
[155] H. Holleck, F. Benesovsky, H. Nowotny, Monatshefte Fur Chemie, 94 (1963) 359-365.
[156] J.G. Costa Neto, S.G. Fries, H.L. Lukas, S. Gama, G. Effenberg, Calphad, 17 (1993) 219-228.
[157] R.J. Pérez, B. Sundman, CALPHAD, 25 (2001) 59-66.
[158] J.C. Zhao, M.R. Jackson, L.A. Peluso, Acta Materialia, 51 (2003) 6395-6405.